Spin Dynamics at Fast MAS in ^{1}H – ^{14}N Double Cross Polarization and TRAPDOR – HMQC Experiments Involving Spin 3/2 Nuclei

A thesis submitted
in partial fulfilment for the award of the degree of

Doctor of Philosophy
in
Physics
by
Sajith V S

Department of Physics
Indian Institute of Space Science and Technology
Thiruvananthapuram, India
June 2023

Certificate

This is to certify that the thesis titled ***'Spin Dynamics at Fast MAS in ^{1}H–^{14}N Double Cross – Polarization and TRAPDOR – HMQC Experiments Involving Spin 3/2 Nuclei'***, submitted by ***Sajith V S,*** to the Indian Institute of Space Science and Technology, Thiruvananthapuram, in partial fulfilment for the award of the degree of **Doctor of Philosophy** in **Physics**, is a bonafide record of research work carried out by him under my supervision. The contents of this thesis, in full or in parts, have not been submitted to any other Institute or University for the award of any degree or diploma.

Dr S Jayanthi	**Dr Sudheesh Chethil**
Associate Professor	Professor & Head
Department of Physics	Department of Physics

Place: Thiruvananthapuram
Date: June 2023

Declaration

I declare that this thesis titled **‘*Spin Dynamics at Fast MAS in ^{1}H–^{14}N Double Cross – Polarization and TRAPDOR – HMQC Experiments Involving Spin 3/2 Nuclei*’**, submitted in partial fulfilment for the award of the degree of Doctor of Philosophy in Physics is a record of original work carried out by me under the supervision of Dr S Jayanthi, and has not formed the basis for the award of any degree, diploma, associateship, fellowship, or other titles in this or any other Institution or University of higher learning. In keeping with the ethical practice in reporting scientific information, due acknowledgments have been made wherever the findings of others have been cited.

Place: Thiruvananthapuram Sajith V S
Date: June 2023 (SC18D007)

Acknowledgments

Firstly, I would like to thank my supervisor Dr S Jayanthi for her constant support and guidance over the last five years. Words cannot express my gratitude to her for building me as a responsible researcher and a well-organized person. This endeavour would not have been complete without the invaluable assistance and discussions with Dr Adonis Lupulescu, Extreme Light Infrastructure—Nuclear Physics, Bucharest-Măgurele, Romania. I cherish the innumerable organized discussions online with the research group during the pandemic times that uplifted my confidence to continue with the projects.

Discussions with Prof. Shimon Vega were priceless, and memorable. Chapter 3 and its subsequent publication is a humble dedication to him, as a token of his ever loving memory, everlasting enthusiasm towards science, and for his constant support throughout.

Thanks are due to the doctoral committee members (Dr. Resmi Lakshmi, ESS, IIST; Prof. Narayan D Kurur, Department of Chemistry, IIT Delhi; Prof. C. S. Narayanamurthy, and Dr. Naveen Surendran:- Physics, IIST) for their constant support and timely suggestions.

This journey would not have been possible without a cheerful and supporting lab-mates. Thanks are due to Dr. V. S. Veena and Mr. Praveen Kumar K for being there for me. I remember all those scientific discussions in the evenings that helped me a lot in the initial days to build confidence in the field.

As IIST lack NMR facility, it was hard to correlate at times the theory and its outcome. Thanks are due to Prof. P. K. Madhu, Dr. Kausthubh, Dr. Rajalakshmi, and Dr. Vipin Agarwal at the National Facility for High Field NMR at TIFR Hyderabad for the fruitful training sessions on solid-state NMR spectrometers, lectures, and discussions. The experience I gained was an additional benefit to my understanding of the field.

My heartfelt thanks to all faculties and staff at the department of physics for all official support. University Grants Commission- India is gratefully acknowledged for the financial assistance in the form of fellowship. I sincerely appreciate the assistance of Dr. V. Sennaraj (deputy registrar), and his team for the efficient disbursal of the fellowship amount, and other contingencies. Shri. Abdunnasar A (library officer) and his team is acknowledged for their assistance especially for retrieving journal articles.

I am extremely thankful to Prof. Anil Kumar, department of Mathematics; Prof. Lakshmi V Nair, department of Humanities, the staff members of department of Mathematics and Humanities for the technical support provided during several doctoral committee meetings and also during the presynopsis presentation.

I would like to appreciate the partial financial support that I have received from IIST that helped me attend the '***Alpine Conference on Magnetic Resonance in Solids, Chamonix-Mont-Blanc, France'***. Thanks are also due to the administration (especially Ms. Bindhya K. R. and Shri. Pradeep Kumar K. R.) for their extended support.

Many thanks to the current head of the department, Prof. Sudheesh Chethil and the former heads Prof. Umesh R Kadhane and Prof S. Murugesh for rendering all official support during my stay. Thanks are due to Prof. Sudheesh Chethil for the support provided in the initiation and subsequent organization of the monthly seminar series in the department "Let's Talk Physics @ IIST".

Thanks to all those friends who made my stay at IIST memorable. The warmth and support you have provided was my strength and stepping stone. I take this opportunity to wish you all the very best for your future endeavours.

I am deeply indebted to the Hostel Managers (especially Mr. Rajkumar and Mr. Praveen) and other staff for their valuable help especially during the COVID time. A deepest appreciation to the cleaning and gardening staff for maintaining IIST as an eco-friendly campus and a beautiful dwelling place. Their smiling faces whenever I pass near them are forever cherished.

In closing, I would like to express my gratitude to my parents, rest of my family members, relatives and well-wishers, and my friends, for the overwhelming support and love they have showered upon me.

Abstract

Experiments probing correlations between spin-1/2 nuclei (*I*) and nuclear spins (*S*) with large anisotropic interactions (quadrupolar or chemical shift anisotropy) often offer valuable access routes to molecular structure and dynamics. In such experiments, development of efficient correlation schemes is not trivial and constitutes an ever-evolving theme of research. As these experiments are performed routinely under MAS, interference between the RF field and the large time-dependent quadrupolar or chemical shift anisotropic interaction leads to complex spin dynamics, often leading to poor and orientation-dependent transfer efficiency.

The work presented in this thesis is a theoretical and numerical investigation of the spin-dynamics in two recently demonstrated experiments involving long periods of RF irradiation on the quadrupolar nuclei channel, the ^{1}H - ^{14}N double cross polarization (double CP) under fast MAS experiment by Carnevale et al. and the ^{1}H - ^{35}Cl TRAPDOR-HMQC experiment of Hung et al. Creation and evolution of various coherences generated in these proton-detected experiments are explored. To analyse the rich and complex spin dynamics due to the interference between the large time-dependent quadrupolar interaction and the radio-frequency (RF) field, an exact effective Hamiltonian is constructed numerically using the *matrix logarithm* approach. Structure of the effective Hamiltonian is connected with transfer amplitudes to various coherences, the output signal, etc. and, when possible, features of the spin dynamics are derived theoretically. The analysis also provides insight on the efficiency of these experiments under different experimental conditions.

Contents

1 Introduction

2 Spin Dynamics of ^{1}H-^{14}N Cross Polarization and Double Cross Polarization at fast MAS

3 Spin Dynamics in Fast MAS TRAPDOR-HMQC Experiments Involving Spin-3/2 Quadrupolar Nuclei

Appendix 1

Appendix 2

Appendix 3

List of Figures

Chapter 1

Chapter 2

Chapter 3

Appendix 1

Appendix 2

Appendix 3

List of Tables

List of Abbreviations

NMR	Nuclear Magnetic Resonance
XRD	X-Ray Diffraction
MAS	Magic Angle Spinning
DOR	Double Rotation
DAS	Dynamic Angle Spinning
MQMAS	Multiple Quantum Magic Angle Spinning
STMAS	Satellite-Transition Magic Angle Spinning
CP	Cross-Polarization
RIACT	Rotationally Induced Adiabatic Coherence Transfer
TRAPDOR	TRAnsfer of Populations In DOuble Resonance
HMQC	Heteronuclear Multiple Quantum Correlation
CPMAS	Cross Polarization under Magic Angle Spinning
RF	Radio-Frequency
FID	Free Induction Decay
FWHM	Full Width at Half Maximum
PAF	Principal Axis Frame
LAB	Laboratory frame
CSA	Chemical Shift Anisotropy
SNR	Signal-to-Noise Ratio
AHT	Average Hamiltonian Theory
SQ	Single-Quantum
DQ	Double-Quantum
MQ	Multiple-Quantum
CT	Central Transition
ST	Satellite Transition
TQ	Triple Quantum
BRAIN	Broadband Adiabatic-Inversion
WURST	Wideband Uniform Rate Smooth Truncation

CPMG	Carr-Purcell Meiboom-Gill
R3	Rotary Resonance Recoupling
REDOR	Rotational Echo at Double Resonance
RESPDOR	Rotational Echo Saturation Pulse Double Resonance
PM	Phase Modulated
RESPIRATION	Rotor Echo Short Pulse IRrAdiaTION
ZQ	Zero Quantum
COMPUTE	Computation over One Modulation Period Using Time Evolution
API	Active Pharmaceutical Ingredients

1

Introduction

1.1 Introduction to Solid State NMR

Nuclear magnetic resonance (NMR)[1,2] spectroscopy is an important tool, apart from the X-Ray Diffraction (XRD) techniques,[3] for investigating at atomic level the chemical structure and dynamics of complex biomolecules and numerous organic and inorganic compounds. However, the information content strongly depends on how well resonances corresponding to distinct chemical sites can be resolved in NMR spectra of the systems under investigation.

When the sample under study is in solution, structural studies of complex molecules using NMR is possible due to spectral simplification resulting from the time averaging of anisotropic interactions due to rapid tumbling in liquids. However, for polycrystalline solid samples, since molecular motions are restricted, anisotropic NMR interactions are not averaged out and result in broad spectral lines and low sensitivity. This hinders the determination of structural features of the system under study. The inherent low resolution and sensitivity for solids has been addressed by new experimental techniques involving multi-pulse irradiation or (and) by mechanically spinning the sample (Magic Angle Spinning - MAS).[4–7] In this way, by manipulating the spin or (and) spatial parts of the Hamiltonian, complete or partial averaging of anisotropic interactions can be achieved. With advanced NMR hardware technologies currently available, solution-like spectra can be recorded under fast MAS.[8] With the advent of current ultra-fast MAS rates (>100 kHz)[9]; solid state NMR has opened new avenues for the determination of molecular structure and dynamics of solid samples.

Solid-state NMR of nuclei with spin quantum number greater than $1/2$, which are the most numerous among the NMR-active nuclei in the periodic table, is particularly challenging in many cases due to low gyromagnetic ratio and the quadrupolar interaction which can reach magnitudes in the MHz range. The quadrupolar interaction originates from the interaction of nuclear quadrupole moments (eQ), with the electric field gradient generated by the surrounding electrons. The large anisotropic quadrupolar interaction results in spectral broadening and overlap, thereby leading to poor spectral resolution and sensitivity. Since MAS alone is unable to average out completely the anisotropic quadrupolar interactions, various schemes have been proposed to regain isotropic resolution in quadrupolar systems. Among the methods which have contributed to the conceptual development of the field, double rotation (DOR),[10] dynamic angle spinning (DAS),[11] multiple quantum MAS (MQMAS),[12] and satellite-transition MAS (ST-MAS),[13] are noteworthy. Incorporating techniques such as cross-polarization (CP),[14,15] rotationally induced adiabatic coherence transfer (RIACT),[16] etc., a variety of new experiments were further developed, leading to sensitivity and resolution gains. The work presented in this thesis is a theoretical and numerical investigation of the spin dynamics in two recently demonstrated experiments involving long periods of RF irradiation on the quadrupolar nuclei channel, the ^{1}H-^{14}N double cross-polarization (double CP) experiment by Carnevale et al.[17–19] and the ^{1}H-^{35}Cl TRAnsfer of Populations in DOuble Resonance - Heteronuclear Multiple Quantum Correlation (TRAPDOR-HMQC or T-HMQC)[20,21] experiment of Hung et al. Creation and evolution of various coherences generated in these proton-detected experiments are explored. To analyse the rich and complex spin dynamics due to the interference between the large time-dependent quadrupolar interaction and the radio-frequency (RF) field, an exact effective Hamiltonian is constructed numerically using the *matrix logarithm* approach.[22] Structure of the effective Hamiltonian is connected with the transfer amplitudes to various coherences, the output signal, etc. and, when possible, features of the spin dynamics are derived theoretically. The analysis also provides insight on the efficiency of these experiments under different experimental conditions.

The thesis is organized as follows. A brief introduction to NMR phenomena in the semi-classical and quantum-mechanical frameworks, the origin of various anisotropic interactions together with their corresponding Hamiltonian operators, and the widely used sensitivity enhancement techniques MAS and CP under MAS (CPMAS)[23,24] is provided in the initial sections. Within the context of the current study, various analytical and numerical approaches that are used frequently in solid state NMR for understanding spin dynamics, are discussed. Basics of the quadrupolar interactions and the respective corresponding Hamiltonians are finally provided, thereby setting stage to the 2nd and 3rd chapters which include the research results. The thesis ends with a summary of the work presented, and possible future applications.

1.1.1 Basics of Nuclear Magnetic Resonance (NMR)

(i) The semi-classical framework

NMR phenomena are based on the existence of the nuclear spin and the resulting magnetic moment.[25,26] Nuclear spin or intrinsic nuclear angular momentum is characterized by the spin operator, $\hbar\boldsymbol{I}$. The components I_X, I_Y, I_Z of the dimensionless spin operator $\boldsymbol{I}$ obey the general commutation rules of angular momentum, and have eigenvalues $m_I = -I, -I + 1/2\,, \dots, I$ where the number I is integer or half-integer and depends on the atomic number and atomic mass number of the nucleus. If nuclear spin is non-zero, the nucleus also possesses a magnetic moment $\boldsymbol{\mu}$[27–32]

$$\boldsymbol{\mu} = \gamma\hbar\boldsymbol{I}, \qquad [1.1]$$

where γ is the gyromagnetic ratio of the nucleus. The sensitivity of NMR experiments involving a certain isotope depends on the natural abundance and gyromagnetic ratio of the isotope. The NMR-relevant properties of some of the NMR active isotopes are listed in Table 1.1.[32,33]

Isotope	**Spin**	**Natural abundance (%)**	**Gyromagnetic ratio (10^6 rad s^{-1} T^{-1})**	**Quadrupole moment (fm^2)**
^{1}H	1/2	99.988	267.522	0
^{2}H	1	0.0115	41.066	0.286
^{13}C	1/2	1.07	67.238	0
^{14}N	1	99.632	19.338	2.044
^{15}N	1/2	0.368	-27.126	0
^{35}Cl	3/2	75.78	26.242	-8.165
^{37}Cl	3/2	24.22	21.84368	-6.435

Table 1.1 NMR properties of some of the important spin ½ and quadrupolar nuclei are listed.

A few examples are given as follows. As nuclei with an even number of protons and neutrons have a nuclear spin value of zero, highly-abundant and biologically-important nuclei such as ^{12}C and ^{16}O are unfortunately NMR inactive. On the other hand, protons (^{1}H) are highly abundant and have the largest gyromagnetic ratio, resulting in good NMR sensitivity. Biologically-important nuclei ^{13}C, and ^{15}N are much less abundant (known as dilute) and their gyromagnetic ratio is low, resulting in poor NMR sensitivity. When possible, isotopic enrichment is used in order to boost the sensitivity. More than 70% of NMR active nuclei in the periodic table have spin larger than ½ and possess a non-zero electric quadrupole moment. The electric quadrupolar moment interacts with the electric field gradients produced by the surrounding electrons. Such nuclei are therefore termed as quadrupolar. Due to small gyromagnetic ratios and often very large quadrupolar interactions (^{14}N, ^{17}O, etc.) NMR of quadrupolar nuclei suffers from low sensitivity and resolution.

The classical energy (E) of a magnetic moment $\boldsymbol{\mu}$ placed in an external magnetic field **B** is,

$$E = -\boldsymbol{\mu} \cdot \boldsymbol{B}. \qquad [1.2]$$

If the static magnetic field is applied along the Z direction ($\boldsymbol{B} = B_0\hat{z}$), and considering the quantization of the spin angular momentum along the direction of the external magnetic field, the energy of the magnetic moment is quantized according to $E_m = -\mu_z B_0 = -\gamma m_I \hbar B_0$ where m_I is the eigenvalue of z component of the spin operator, I_Z. Spin quantum number m_I can take values from $-I$ to I. For I = 1/2, the corresponding spin-up and spin-down eigenstates of I_Z are labelled as ($|\alpha\rangle = |+1/2\rangle$ and ($|\beta\rangle = |-1/2\rangle$). The energy difference between adjacent levels is $\Delta E = -\gamma\hbar B_0$, and the associated frequency $\omega_0 = \Delta E/\hbar$ is known as the Larmor frequency.[31] The sign of the gyromagnetic ratio can be positive or negative as shown in Table 1.1.

The nuclear spins present are not isolated and interact among themselves and with the lattice. Therefore, the description of magnetic resonance phenomena is usually based on statistical considerations. At thermal equilibrium, the spin energy levels become populated as per Boltzmann distribution such that the population for the m^{th} level is $N_m \propto e^{-\frac{E_m}{k_B T}}$, where k_B is the Boltzmann constant and T is the absolute temperature. The population difference between the energy levels is directly related to the intensity of the NMR transitions between them. Under thermal equilibrium, the lower energy levels have a slight excess of population, and this results in a bulk magnetization along the direction of the external magnetic field whereas the transverse components of magnetization average to zero as they are randomly oriented. For all external magnetic fields encountered in NMR the thermal energy $k_B T$ is much higher than the energy difference between the Zeeman levels. As consequence, a simple expression can be derived for the equilibrium magnetization for spin$-1/2$ nuclei[29]

$$M_0 = \frac{N\gamma^2\hbar^2 B_0}{4k_B T}. \qquad [1.3]$$

As the total number of spins in the sample, N, is directly related to the natural abundance of the isotope, the bulk magnetization and hence the sensitivity of NMR signal will depend upon the natural abundance of the isotope, gyromagnetic ratio, the magnitude of the external magnetic field, and the temperature.

Under the action of an external magnetic field, the ensemble of spins constitutes towards an average nuclear magnetic moment along the direction of the applied field. If a radio frequency field with frequency close to Larmor frequency is switched on, it can bring the magnetization in the XY-plane. After RF field is switched off, the magnetization will precess around the static magnetic field and thereby induce an oscillating current in the coil,[28–30] according to Faraday's induction law. The spin dynamics sketched above can be described more quantitatively with the phenomenological Bloch equations.[29] In the presence of a magnetic field, the bulk magnetic moment $\boldsymbol{M}$ experiences a torque $\boldsymbol{\tau}$ which is the time rate of change of the bulk spin angular momentum $\boldsymbol{J}$,

$$\boldsymbol{\tau} = \frac{d\boldsymbol{J}}{dt} = \boldsymbol{M} \times \boldsymbol{B} \qquad [1.4]$$

where, $\boldsymbol{M} = \sum_j \boldsymbol{\mu_j}$ and $\boldsymbol{J} = \sum_j \boldsymbol{I_j}$. Equivalently

$$\frac{d\boldsymbol{M}}{dt} = \gamma \boldsymbol{M} \times \boldsymbol{B} = \boldsymbol{M} \times \boldsymbol{\Omega} \qquad [1.5]$$

as $\boldsymbol{M} = \gamma \boldsymbol{J}$ in analogy to $\boldsymbol{\mu} = \gamma \boldsymbol{I}$. Here $\boldsymbol{\Omega} = \gamma \boldsymbol{B}$. At equilibrium $\boldsymbol{M}$ is parallel to the static magnetic field and $d\boldsymbol{M}/dt$. However, if an RF field (or RF pulse) with frequency close to Larmor frequency γB_0 is applied Eq. [1.5] predicts a precession and tilt of $\boldsymbol{M}$ towards X-Y plane. With an appropriate duration of the RF field the magnetization can be brought completely in the X-Y plane.

Assuming that at the end of the RF pulse equilibrium magnetization is tilted along X direction, it will start to precess around the large static magnetic field. At the same time the system will start relaxing towards thermal equilibrium in which magnetization is again aligned along the static magnetic field. This can happen through two kinds of relaxation processes, the longitudinal and transverse relaxations.[29–31] (i) The spin-lattice/longitudinal/T_1 relaxation is due to the interaction of the spins with the lattice (all other degrees of freedom in the sample). Longitudinal relaxation tends to bring bulk magnetization to its equilibrium value and orientation. The speed of this relaxation process is characterised by the relaxation time T_1. (ii) The spin-spin/transverse/T_2 relaxation arises because of dephasing/loss of coherence of the bulk magnetization in the transverse plane as a result of interaction between the spins or due to the inhomogeneity of the static magnetic field. It is characterized by a time constant T_2 which characterizes rate of decay of the transverse components of bulk magnetization. Incorporating the relaxation phenomena into Eq. [1.5] the Bloch equations are

$$\frac{dM_X}{dt} = \gamma(\boldsymbol{M} \times \boldsymbol{B})_X - \frac{M_X}{T_2}, \frac{dM_Y}{dt} = \gamma(\boldsymbol{M} \times \boldsymbol{B})_Y - \frac{M_Y}{T_2}, \frac{dM_Z}{dt} = \gamma(\boldsymbol{M} \times \boldsymbol{B})_Z + \frac{M_0 - M_Z}{T_1} \qquad [1.6]$$

Solving Eq. [1.6] with the initial condition $\boldsymbol{M}(0) = M_0\hat{z}$, evolution of the magnetization is given by

$$M_X(t) = M_0\, cos(\omega_0 t)\left(e^{-\frac{t}{T_2}}\right), M_Y(t) = M_0\, sin(\omega_0 t)\left(e^{-\frac{t}{T_2}}\right), M_Z(t) = M_0(1 - e^{-\frac{t}{T_1}}). \quad [1.7]$$

The precession of the transverse components induces a current in the detection coil. This current also called free induction decay (FID)[29–31] is amplified and recorded in the form of the NMR signal in the time domain. The NMR signal has the form $S(t) \propto M_X(t) + iM_Y(t) = M_0 e^{i\Omega t}\ e^{-R_2 t}$. The spectrometer can detect from both transverse components, $M_X(t)$ and $M_Y(t)$, through quadrature detection.[29–31] Fourier transform of the FID results in the NMR spectrum in the frequency domain[34] represented as,

$$S(\omega) = \int_0^\infty S(t)\, e^{i\omega t} dt = \frac{S_0 R_2}{R_2^2 + (\omega - \omega_0)^2} + i\,\frac{-S_0(\omega - \omega_0)}{R_2^2 - (\omega - \omega_0)^2} \qquad [1.8]$$

where $R_2 = 1/T_2$. The real part of Eq. [1.8] results in an absorption-mode Lorentzian spectral lineshape, centered at ω_0 for which the maximum height of the Lorentzian is $1/R_2$, and full width at half maximum (FWHM) is at R_2/π, while the imaginary part is a dispersion-mode Lorentzian spectral lineshape.

Though semi-classical picture can provide a basic understanding of the NMR phenomenon by visualizing the spin dynamics of isolated spins in terms of the magnetization vectors obeying Bloch's equation, it is not sufficient to describe complex NMR phenomena due to interaction between spins. A more accurate and detailed picture of spin dynamics taking into consideration all NMR interactions is provided by quantum mechanical treatment.

(ii) The quantum-mechanical description

In the quantum-mechanical description, the state of a quantum system is described by a state vector, $|\psi(t)\rangle$. The state vector is expressed in terms of a density operator by considering the spin system as a statistical ensemble. The quantum state described by $|\psi(t)\rangle$ can be represented in terms of the Zeeman basis, $|n\rangle$ as[29,35]

$$|\psi(t)\rangle = \sum_n c_n\, |n\rangle \qquad [1.9]$$

such that the expectation value of a quantum mechanical operator, $\hat{O}$ is given by:

$$\langle\hat{O}\rangle = \langle\psi(t)|\hat{O}|\psi(t)\rangle = \sum_{m,n} c_n c_m^*\, \langle m|\hat{O}|n\rangle. \qquad [1.10]$$

The density operator/matrix, ρ, is described in the Zeeman basis in terms of the ensemble-averaged $c_n c_m^*$ coefficients and the corresponding matrix elements are given by

$$\rho_{nm} = \overline{c_n c_m^*} \qquad [1.11]$$

For any density operator and any basis of the Hilbert space we have,

$$\langle\hat{O}\rangle = \sum_{m,n} \rho_{nm}\, O_{mn} = \sum_n (\rho O)_{nn} = \mathrm{Tr}(\rho\hat{O}) \qquad [1.12]$$

In general, for a system in thermal equilibrium with the environment at temperature T, the equilibrium density operator is, $\hat{\rho}_{eq} = \frac{1}{Z} e^{\frac{-\widehat{\mathcal{H}}}{k_B T}}$, where $Z = \mathrm{Tr}\{\exp\,(-\widehat{\mathcal{H}}/k_B T)\}$. In NMR, by far, the dominant contribution to $\widehat{\mathcal{H}}$ is given by the interaction with the static magnetic field, $\widehat{\mathcal{H}} \cong -\hbar\omega_0 I_Z$. For temperatures and magnetic fields occurring in NMR experiments, $\hbar\omega_0 \ll k_B T$, and the equilibrium density operator can be approximated by $\hat{\rho}_{eq} = \frac{1}{N_Z}(1_{N_Z} + \frac{\hbar\omega_0}{k_B T}\hat{I}_Z)$, where N_Z is the dimension of the Hilbert space and 1_{N_Z} is the unit operator. For a single spin-1/2 nucleus $N_Z = 2$ corresponding to the spin-up and spin-down basis. For a system of n spin-1/2 nuclei of the same kind $I_Z = \sum_{k=1}^{n} I_{Z,k}$ and $N_Z = 2^n$, etc.

The temporal evolution of the density operator, $\rho(t)$ is expressed in terms of the Liouville-Von Neumann- equation[29,35]

$$i\hbar\frac{d\rho}{dt} = [\mathcal{H}, \rho]. \qquad [1.13]$$

A very important operator for the dynamic quantum-mechanical description is the propagator $U(t,0)$ which connects any initial state of the system with the state at a later time, $|\psi(t)\rangle = U(t,0)|\psi(0)\rangle$. The propagator $U(t,0)$ corresponding to Hamiltonian $\mathcal{H}$ satisfies $i\hbar\frac{dU}{dt} = \mathcal{H}U$. Similar to the pure case, the density operator, $\rho(t)$ can be evaluated from the prior knowledge of the propagator, $U(t,0)$.

$$\rho(t) = U(t,0)\rho(0)U(t,0)^{\dagger} \qquad [1.14]$$

where $\rho(0)$ is the initial density operator. Since magnetization is the expectation value of the bulk magnetic moment of the sample and since $\boldsymbol{\mu} = \gamma\hbar\boldsymbol{I}$ we have that the NMR signal must be proportional to $S(t) = S_X(t) + iS_Y(t)$ where $S_X(t) = Tr\big(I_X\rho(t)\big)$ and $S_Y(t) = Tr\big(I_Y\rho(t)\big)$. In most NMR experiments the nuclear spin system starts from thermal equilibrium, $\rho(0) = \hat{\rho}_{eq}$. However, the unit operator in $\hat{\rho}_{eq}$ has no contribution to the NMR signal and is omitted from now onwards. For homonuclear systems the proportionality coefficient $\hbar\omega_0/(k_BTN_Z)$ is often omitted in density operator calculations, such that we will write $\rho(0) = I_Z$ instead of $\rho(0) = \frac{1}{N_Z}(1_{N_Z} + \frac{\hbar\omega_0}{k_BT}I_Z)$. For a heteronuclear system, composed from spins *I* of gyromagnetic ratio γ_I and spins *S* of gyromagnetic ratio γ_S, $\hat{\rho}_{eq} = \frac{1}{N_Z}(1_{N_Z} + \frac{\hbar\omega_{0I}}{k_BT}I_Z + \frac{\hbar\omega_{0S}}{k_BT}S_Z)$ therefore we can write $\rho(0) = \gamma_I I_Z + \gamma_S S_Z$ since $\omega_{0I} = \gamma_I B_0$ and $\omega_{0S} = \gamma_S B_0$. Experiments in which spins *S*, for example, are not brought out of equilibrium during experiment or do not contribute to the NMR signal, it is safe to start with $\rho(0) = \gamma_I I_Z$ or $\rho(0) = I_Z$.

If the Hamiltonian $\mathcal{H}$ is constant in time, then the corresponding propagator during a given time interval, T, can be calculated as

$$U(T,0) = exp(-i\mathcal{H}\,T/\hbar). \qquad [1.15]$$

If the Hamiltonian is time-dependent and inhomogeneous[7] (where the Hamiltonian is commuting at different time instants inside the time interval *T*), the propagator can be obtained as

$$U(t,0) = exp\left(-i\int_0^t \mathcal{H}(t')\,dt'/\hbar\right) \qquad [1.16]$$

For many NMR experiments the spin Hamiltonian does not commute with itself at different instants of time, $[\mathcal{H}(t'),\mathcal{H}(t)] \neq 0$. In such cases, the propagator can be symbolically expressed as

$$U(t_2,t_1) = \hat{T}exp\left(-i\int_{t_1}^{t_2} \mathcal{H}(t')\,dt'/\hbar\right) \qquad [1.17]$$

where $\hat{T}$ is the time ordering operator[36] such that the Hamiltonians appear in chronological order. In most cases this makes the study of spin dynamics complex as an explicit exact expression for the propagator cannot be obtained and approximate methods are required. Spin dynamics arising corresponding to Eq. [1.17] are discussed in detail in section 1.2. The following section discusses the various interactions and the corresponding Hamiltonians in

NMR. In NMR the Hamiltonian is usually expressed in angular frequency units and the reduced Planck constant $\hbar$ does not appear in Eq. [1.13-1.17] or in any other expressions derived from them.

1.1.2 The interaction Hamiltonians

Nuclear spin interactions are categorized as external and internal. The external interactions are between individual nuclear spins and the applied magnetic fields. Internal interactions are either interactions of nuclear spins among themselves or interactions with other, *non-nuclear*, degrees of freedom. The mathematical representation of various interactions is presented below.

External interactions

The external interactions couple nuclear spins with the large static magnetic field and the radiofrequency magnetic field. The interaction with the static magnetic field is called Zeeman interaction. Both interactions stem from quantization of the classical expression for the energy of a dipole moment in a magnetic field, $E = -\boldsymbol{\mu} \cdot \boldsymbol{B} \rightarrow \widehat{\boldsymbol{\mathcal{H}}} = -\widehat{\boldsymbol{\mu}} \cdot \boldsymbol{B}$.

(i) Zeeman interaction

This is the interaction of the nuclear spins with the externally applied static magnetic field, $B = B_0\hat{z}$. The interaction results in the lifting of the degeneracy of the spin states by splitting them into $2I + 1$ number of levels, thereby inducing a population difference among them. The Zeeman Hamiltonian in angular frequency units is[27]

$$\boldsymbol{\mathcal{H}}_z = -\widehat{\boldsymbol{\mu}} \cdot \boldsymbol{B}/\hbar = -\gamma I_Z B_0 = \omega_0 I_Z \qquad [\,1.18]$$

where $\omega_0 = -\gamma B_0$. It is by far the strongest of all interactions, of the order of hundreds of MHz up to about 1 GHz.[37] Therefore, internal interactions can be considered as perturbations to the Zeeman Hamiltonian and perturbation theory up to second order is enough to predict all eigen-energy and eigenstate corrections. To first order within perturbation theory, only those terms in the internal interactions Hamiltonian which commute with Zeeman interaction are retained. This approximation is known as the secular or high-field approximation.[27]

(ii) Interaction with radiofrequency fields

Similar to Zeeman interaction, we consider the interaction with the RF magnetic field. The linearly-polarized magnetic field produced by the coil, $\boldsymbol{B}_1(t) = B_1(cos(\omega_{RF}t + \phi)\hat{x})$, can be decomposed into two circularly polarized RF fields as,

$$\boldsymbol{B}_1(t) = B_1 \frac{(cos(\omega_{RF}t + \phi)\hat{x} + sin(\omega_{RF}t + \phi)\hat{y})}{2} + B_1 \frac{(cos(\omega_{RF}t + \phi)\hat{x} - sin(\omega_{RF}t + \phi)\hat{y})}{2}.$$

It can be shown[32] that only the right circularly-polarized component affects the spin dynamics. The corresponding Hamiltonian is given by,

$$\boldsymbol{\mathcal{H}}_{rf} = -\boldsymbol{\hat{\mu}} \cdot \boldsymbol{B_1(t)}/\hbar = \boldsymbol{\omega_1}\big(I_X cos(\omega_{RF}t + \phi) + I_Y sin(\omega_{RF}t + \phi)\big) \quad [1.19]$$

where the nutation frequency is $\omega_1 = -\gamma B_1/2$ whereas ω_{RF} and ϕ are the frequency and phase of the RF pulse, respectively. The analysis of RF irradiation effects can be considerably simplified by transferring the Hamiltonian into a frame rotating around $\boldsymbol{B}_0$ with frequency ω_{RF}. In this rotating frame [Appendix A1.1], the Hamiltonian representing the external interactions is time independent,[27]

$$\widetilde{\mathcal{H}}_{RF} = \Omega I_Z + \omega_1\big(I_X cos(\phi) + I_Y sin(\phi)\big), \quad [1.20]$$

where $\Omega = \omega_0 - \omega_{RF}$ is known as the offset frequency. For an on-resonance pulse, $\omega_{RF} = \omega_0$ yielding offset frequency, $\Omega = 0$. Choosing $\phi = 0$, we get $\widetilde{\mathcal{H}}_{RF} = \omega_1 I_X$ known as the x-pulse, which is capable of rotating the bulk magnetization created along the Z-axis about the X-axis towards the YZ-plane. Starting with the thermal equilibrium density operator $\rho(0) = AI_Z$ it can be shown [Appendix A1.1] that at time *t* during on-resonance irradiation the state of the system is described by: $\rho(t) = A(I_Z \cos(\omega_1 t) - I_Y \sin(\omega_1 t))$.

By choosing the duration of irradiation τ_{90} such that $\omega_1\tau_{90} = \pi/2$ we have $\rho(\tau_{90}) = -AI_Y$, which shows that initial longitudinal magnetization $M_Z^0\hat{z} \propto \langle I_Z\rangle\hat{z}$ nutates towards the X-Y plane and is converted fully into transverse magnetization $-M_Y^0\hat{y} \propto \langle I_Y\rangle\hat{y}$ at the end of the RF pulse of duration τ_{90}.

Internal Spin Interactions

The internal spin interactions have their origin in the coupling of the nuclear spin to the chemical, magnetic or electrical environment of the nucleus. The strength of various internal spin interactions depends on the type of nuclei involved and on molecular structure and dynamics. Because of their anisotropic nature, the Hamiltonians of various internal interactions are best represented using the spherical tensor formalism[26–28] which is discussed in Appendix

A1.2. The internal interactions are commonly dealt with in the principal axis frame (PAF) in which the tensor has only diagonal components. As measurements are done in the laboratory frame (LAB), proper frame transformations from PAF to the laboratory frame are needed. These transformations are achieved with the aid of Wigner rotation matrices. A description of Wigner rotation matrices and their properties is given in Appendix A1.2. The internal interactions which are relevant to the study are described below.

(i) Chemical shift

When a static external magnetic field, B_0 is applied to the sample, the electron orbitals surrounding the nucleus will be perturbed and as a consequence generate an induced local magnetic field, B_{ind}. As a result, the magnetic field felt by the nucleus and the corresponding Larmor frequency experience a shift, termed *chemical shift*, which depends on the electronic environment of the nucleus and on the orientation of the molecular frame with respect to laboratory frame. This dependence on orientation results in the anisotropy of the total effective magnetic field felt by the nuclear spin, $B_{eff} = B_0 + B_{ind}$. Chemical shift[26–28,32] is a measure of the degree of magnetic shielding or deshielding of nuclear spin when the molecule is placed in an external magnetic field. In the tensorial form (Appendix A1.2), the interaction between the nuclear spins and the induced local magnetic field can be expressed as[27]

$$\mathcal{H}_{CS} = \gamma \vec{\boldsymbol{I}} \cdot \overleftrightarrow{\boldsymbol{\sigma}} \cdot \vec{\boldsymbol{B}} = -\omega_0 \vec{\boldsymbol{I}} \cdot \overleftrightarrow{\boldsymbol{\sigma}} \cdot \hat{\boldsymbol{z}} = -\,\omega_0 \sigma_{zz} I_z \qquad [1.21]$$

where $\overleftrightarrow{\boldsymbol{\sigma}}$ is the chemical shift tensor. The last equality is due to the secular approximation, which is excellent in all cases. In the PAF, $\overleftrightarrow{\boldsymbol{\sigma}}$ is represented as shown in Eq. [1.22] and the diagonal elements are termed as *principal values*

$$\overleftrightarrow{\boldsymbol{\sigma}} = \begin{bmatrix} \sigma_{XX} & 0 & 0 \\ 0 & \sigma_{YY} & 0 \\ 0 & 0 & \sigma_{ZZ} \end{bmatrix}. \qquad [1.22]$$

From Eq. [1.22], the isotropic value, σ_{iso}, the asymmetry, η_{cs} defining the shape of the spectrum, and the anisotropy, Δ_{cs} defining the width of the spectrum, are defined as

$$\sigma_{iso} = \frac{1}{3}(\sigma_{XX} + \sigma_{YY} + \sigma_{ZZ}),\ \Delta_{cs} = \sigma_{ZZ} - \sigma_{iso},\ \eta_{cs} = \frac{\sigma_{XX} - \sigma_{YY}}{\Delta_{cs}},\ 0 \le \eta_{cs} \le 1. \qquad [1.23]$$

Second rank interaction tensors can be represented in terms of an ellipsoid as shown in Figure 1.1 in which its principal axes coincide with the PAF axes. Asymmetry measures the deviation of the ellipsoid from the circular cross section whereas anisotropy measures the magnitude of the tensor in different orientations of the ellipsoid.

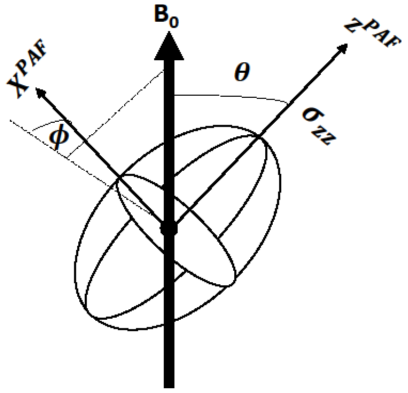

Figure 1.1 The orientation of the chemical shift tensor in the principal axis frame is represented in terms of the polar angles (θ,ϕ) with respect to the laboratory frame.

The transformation of $\overleftrightarrow{\boldsymbol{\sigma}}$ from the principal axis frame to the laboratory frame (Figure 1.1) is defined by Euler angles, $\Omega_{PL}(\alpha=\phi,\beta=\theta,\gamma=0)$ allows to express σ_{zz}^{LAB} in terms of the principal values of $\overleftrightarrow{\boldsymbol{\sigma}}$ as

$$\sigma_{zz}^{LAB}(\theta,\phi)=\sigma_{XX}\,sin^2\,\theta\,cos^2\,\phi+\sigma_{YY}\,sin^2\,\theta\,sin^2\,\phi+\sigma_{ZZ}\,cos^2\,\theta$$

$$=\sigma_{iso}+\sigma_{aniso}(\theta,\phi) \qquad [1.24]$$

where $\sigma_{aniso}(\theta,\phi)=\Delta_{cs}\left(\frac{3\,cos^2\,\theta-1}{2}+\frac{\eta_{cs}}{2}sin^2\,\theta\,cos\,2\phi\right)$ is the anisotropic part. Thus, the Hamiltonian in the laboratory frame is:

$$\mathcal{H}_{CS}^{LAB}=-\omega_0\sigma_{zz}^{LAB}I_z=-\omega_0(\sigma_{iso}+\sigma_{aniso}(\theta,\phi))I_z$$

or alternatively:

$$\mathcal{H}_{CS}^{LAB}=\omega_{CS}(\theta,\phi)I_z=\big(\omega_{iso}+\omega_{aniso}(\theta,\phi)\big)I_z \qquad [1.25]$$

where $\omega_{iso}=-\omega_0\sigma_{iso}$ is the isotropic chemical shift frequency and $\omega_{aniso}(\theta,\phi)$ denotes frequency corresponding to the chemical shift anisotropy (CSA). Immediately after the application of a 90^o pulse $\rho(0)=I_X$ and the time evolution of the density matrix under the chemical shift Hamiltonian corresponding to Eq. [1.25] can be calculated as:

$$\rho(t)=U(t,0)\rho(0)U(t,0)^{\dagger}=I_X\cos(\omega_{CS}(\theta,\phi)t)+I_Y\sin(\omega_{CS}(\theta,\phi)t) \qquad [1.26]$$

with $U(t,0)=e^{-iH_{CS}^{LAB}t}$. Accordingly, the NMR signal is given by:

$$S(t,\theta,\phi)=S_X(t)+iS_Y(t)=\frac{1}{2}\exp(i\omega_{CS}(\theta,\phi)t) \qquad [1.27]$$

where the quadrature signals are estimated with $S_X(t)=\mathrm{Tr}\big(I_X\rho(t)\big)$ and $S_Y(t)=\mathrm{Tr}\big(I_Y\rho(t)\big)$.

For a powder sample, the contribution to the intensity from different crystallite orientations results in a powder pattern (Figure 1.2) and the signal from a powder is obtained by averaging over all crystallite orientations

$$S_{powder}(t) = \frac{1}{4\pi}\int_0^{2\pi}\int_0^{\pi} S(t,\theta,\phi)\, sin\theta d\theta d\phi. \qquad [1.28]$$

In NMR experiments, the chemical shift is measured in parts per million (ppm) with respect to a reference compound and can be represented as: $\delta = \delta_{iso} + \delta_{aniso}$

where $$\delta_{aniso} = \frac{1}{2}\Delta_{cs}\{3cos^2\theta - 1 + \eta_{cs} sin^2\theta cos2\phi\} \qquad [1.29]$$

$$\delta_{iso} = \frac{\sigma_{iso}(ref) - \sigma_{iso}}{1 - \sigma_{iso}(ref)} = \frac{\nu - \nu_{ref}}{\nu_{ref}} \approx \sigma_{iso}(ref) - \sigma_{iso} = \frac{1}{3}(\delta_{11} + \delta_{22} + \delta_{33}) \qquad [1.30]$$

Here $\sigma_{iso}(ref)$ represents the isotropic chemical shift of the reference, ν and ν_{ref} are the spectral frequencies of the signal from the sample and the reference, respectively.

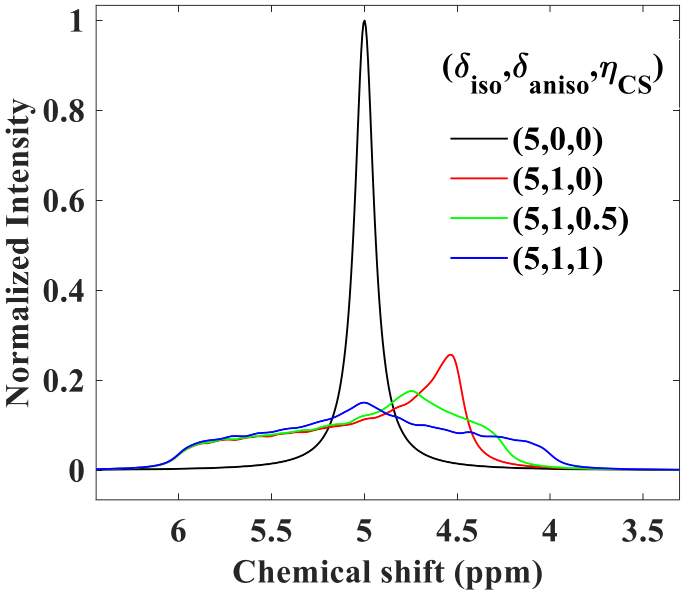

Figure 1.2 ^{1}H Simulated powder spectra using SIMPSON software as a function of different chemical shift parameters, at $\nu_0 = 400\ MHz$. δ_{iso} and δ_{aniso} are expressed in ppm. Intensity is normalized with respect to the maximum. The crystal file used was ZCW986.

Usually, anisotropy associated with protons (≃ up to 12 ppm) is smaller when compared with ^{13}C (up to 250 ppm). Simulated spectra using SIMPSON[38] are shown in Figure 1.2 for different values of δ_{aniso} (ppm) and η_{cs} and a given δ_{iso} (ppm). As seen from Eq. [1.27,1.28], the anisotropic NMR frequency depends on the orientation of the second-rank tensor with respect to the static magnetic field. In a powder sample, the orientation of each spatial tensor of the spins in a rigid molecular fragment may be associated with orientation of crystal with respect to the magnetic field. The spatial tensor changes when the orientation of the crystal changes. In powder samples, there are large number of randomly oriented crystallites (~10^7). A powder averaged NMR signal is thus the sum of the signals deriving from each orientation, weighted by the probability of finding that particular orientation. If the orientation Ω with respect to the static magnetic field (or the laboratory frame) is described through Euler angles by $\Omega = \{\alpha, \beta, 0\}$, the probability $\wp(\alpha, \beta)$ is calculated to be the ratio between the solid angle and the surface of the unit sphere, as can be seen from Eq. [1.28]. To implement this concept using numerical simulation software like SIMPSON, different powder averaging schemes have been developed in the form of crystal files that contain various possible Euler angle sets and weight factors corresponding to the different crystallite orientations.[39] With respect to the change in the above parameters, the spectral features changes in terms of intensity, lineshape, and linewidth.

(ii) Spin-spin interactions

A. Dipolar interaction

Dipolar interaction is a direct, through-space interaction between the magnetic moments of two nuclear spins. Within a classical picture, a local magnetic field is generated by the magnetic moment of the nucleus, and this local field affects the magnetic moment of a neighbouring spin, resulting in shifting of the Zeeman energy levels. The corresponding Hamiltonian can be obtained from the classical expression for the interaction energy of two magnetic moments, by replacing the magnetic moments with the magnetic moment operators, $\boldsymbol{\mu_I} = \gamma_I \hbar \boldsymbol{I}$ and $\boldsymbol{\mu_S} = \gamma_S \hbar \boldsymbol{S}$ for nuclear spins I and S. In tensorial form (Appendix A1.2) it assumes the form[26–28,32]

$$\mathcal{H}_D = \boldsymbol{I} \cdot \overleftrightarrow{\boldsymbol{D}}_{\boldsymbol{IS}} \cdot \boldsymbol{S} \qquad [1.31]$$

The PAF is any coordinate system with Z axis parallel to the internuclear position vector $\boldsymbol{r}_{IS}$. In the PAF,

$$\overleftrightarrow{\boldsymbol{D}}_{\boldsymbol{IS}} = \begin{bmatrix} \omega_{D,IS} & 0 & 0 \\ 0 & \omega_{D,IS} & 0 \\ 0 & 0 & -2\omega_{D,IS} \end{bmatrix} \qquad [1.32]$$

The quantity $\omega_{D,IS} = -\left(\frac{\mu_0}{4\pi}\right)\frac{\gamma_I \gamma_S \hbar}{r^3}$, is the dipolar coupling constant, alternatively expressed in kHz as $d = \omega_D/2\pi$, $\hbar = h/2\pi$, where h is Planck's constant, and μ_0 is the permeability of free space. The dipolar coupling constant gives access to the internuclear distance, r, expressed in Å. The strength of the dipolar interaction is directly proportional to the product of the gyromagnetic ratios of the coupled nuclei and is inversely proportional to the internuclear distance. For example, for $r(1\text{H} - 13\text{C})$ = 1.125 Å we have $d(1\text{H} - 13\text{C}) = 21.13$ kHz for ^{1}H coupled to ^{13}C in Histidine. Since the trace of $\overleftrightarrow{\boldsymbol{D}}_{\boldsymbol{IS}}$ is zero, the isotropic part of the dipolar coupling vanishes. As the anisotropic part averages to zero in liquids due to the random molecular motion, the dipolar coupling has no direct effect on the position of the resonances in

NMR spectra of liquids. However, it contributes towards relaxation.[32,35] In addition, $\overleftrightarrow{\boldsymbol{D}}_{\boldsymbol{IS}}$ is axially symmetric, with the internuclear vector parallel to one of the principal axes as shown in Figure 1.3.

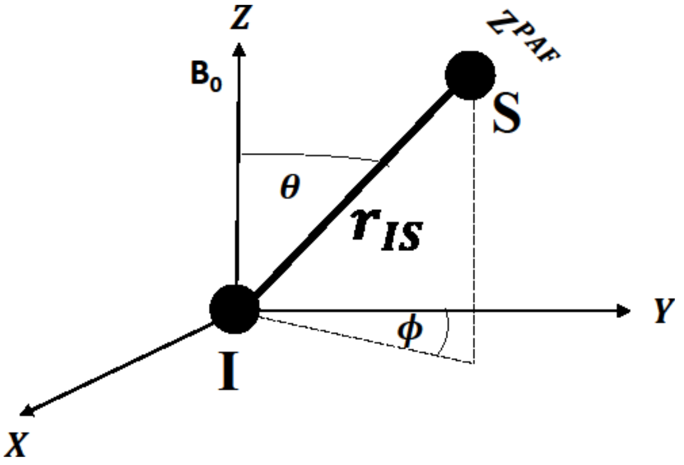

Figure 1.3 Dipolar coupled spins I and S seperated by a distance, r_{IS} in the principal axis frame is represented in terms of the polar angles (θ,ϕ) with respect to the laboratory frame.

As mentioned above, the Hamiltonian for the dipolar interaction between two spins *I* and *S* is obtained by quantizing the classical expression for the interaction energy between two classical dipoles to give

$$\mathcal{H}_D = -\frac{\mu_0}{4\pi}\hbar\gamma_I\gamma_S\left\{\frac{\boldsymbol{I}\cdot\boldsymbol{S}}{r^3} - 3\frac{(\boldsymbol{I}\cdot\boldsymbol{r})(\boldsymbol{S}\cdot\boldsymbol{r})}{r^5}\right\} \qquad [1.33]$$

In the laboratory frame, the dipolar Hamiltonian can be written as the so-called dipolar alphabet[28]:

$$\mathcal{H}_D = -\left(\frac{\mu_0}{4\pi}\right)\frac{\gamma_I\gamma_S\hbar}{r^3}[A+B+C+D+E+F] \qquad [1.34]$$

where $A = I_zS_z(3\cos^2\theta - 1), B = -\frac{1}{4}[I_+S_- + I_-S_+](3\cos^2\theta - 1),$

$\mathrm{C} = \frac{3}{2}[I_zS_+ + I_+S_z]\sin\theta\cos\theta e^{-i\phi}, D = \frac{3}{2}[I_zS_- + I_-S_z]\sin\theta\cos\theta e^{+i\phi},$

$E = \frac{3}{4}[I_+S_+]\sin^2\theta e^{-2i\phi}$ and $F = \frac{3}{4}[I_-S_-]\sin^2\theta e^{+2i\phi}.$ [1.35]

Under the secular approximation, only terms *A* and *B* are retained and the dipolar interaction Hamiltonian for a homonuclear spin pair $((I_z \to I_{1z}, S_z \to I_{2z}, \gamma_I = \gamma_S)$ in the laboratory frame is:

$$\begin{aligned}\mathcal{H}^{LAB}_{D,I_1I_2} &= -\frac{\mu_0}{4\pi}\frac{\hbar\gamma_I 2}{r^3_{I_1I_2}}\left(\frac{3cos^2\theta - 1}{2}\right)(3I_{1z}I_{2z} - I_1\cdot I_2)\\ &= \omega_{D,I_1I_2}(\theta)(3I_{1z}I_{2z} - I_1\cdot I_2)\end{aligned} \qquad [1.36]$$

where $\omega_{D,I_1I_2} = -\frac{\mu_0}{4\pi}\frac{\hbar\gamma_I^2}{r_{I_1I_2}^3}$, $\omega_{D,I_1I_2}(\theta) = -\frac{\mu_0}{4\pi}\frac{\hbar\gamma_I^2}{r_{I_1I_2}^3}\left(\frac{3cos^2\theta-1}{2}\right)$ and $(3I_{1z}I_{2z} - I_1 \cdot I_2) = 2A + 2B$. Here, term A represents the first-order correction to the energy levels, whereas term $B \propto I_{1_+}I_{2_-} + I_{1_-}I_{2_+}$ is responsible for spin diffusion in the solid-state through the flip-flop term, $I_{1_+}I_{2_-} + I_{1_-}I_{2_+}$. For a heteronuclear spin pair, under secular approximation only A is retained and the dipolar interaction Hamiltonian is

$$\mathcal{H}_{D,IS}^{LAB} = -\frac{\mu_0}{4\pi}\frac{\hbar\gamma_I\gamma_S}{r_{IS}^3}\left(\frac{3cos^2\theta-1}{2}\right)2I_zS_z = \omega_{D,IS}(\theta)2I_zS_z. \qquad [1.37]$$

where $\omega_{D,IS} = -\frac{\mu_0}{4\pi}\frac{\hbar\gamma_I\gamma_S}{r_{IS}^3}$ and $\omega_{D,IS}(\theta) = -\frac{\mu_0}{4\pi}\frac{\hbar\gamma_I\gamma_S}{r_{IS}^3}\left(\frac{3cos^2\theta-1}{2}\right)$. Hence, the dipolar contribution to the energy levels for a heteronuclear spin pair is,

$$E_{m_I,m_s} = \omega_{D,IS}(\theta)\langle m_I m_S|2I_zS_z|m_I m_S\rangle = 2\omega_{D,IS}(\theta)m_I m_S. \qquad [1.38]$$

The time evolution of the density matrix immediately after a 90^o pulse on I spin ($\rho(0) = I_X$) under the Hamiltonian given in Eq. [1.37] can be calculated as

$$\begin{aligned}\rho(t) &= U(t,0)\rho(0)U(t,0)^\dagger = e^{-i\mathcal{H}_{D,IS}^{LAB}t}(I_X)e^{i\mathcal{H}_{D,IS}^{LAB}t}\\ &= I_X\cos\big(\omega_{D,IS}(\theta)t\big) + 2I_YS_Z\sin\big(\omega_{D,IS}(\theta)t\big) \qquad [1.39]\end{aligned}$$

with $U(t,0) = e^{-i\mathcal{H}_{D,IS}^{LAB}t}$. The NMR signal is $S_X(t) = Tr((I_X)\rho)$= $\cos\big(\omega_{D,IS}(\theta)t\big)\,Tr\{(I_X)^2\}$= $\propto \cos\big(\omega_{D,IS}(\theta)t\big)$, $S_Y(t) = 0$, and leads after Fourier transform to a doublet with splitting $2\omega_{D,IS}(\theta)$. For a powder sample, this splitting varies such that spectrum containing contributions from different orientations (through angle θ) will have the appearance of a powder pattern with a characteristic lineshape which depends on the dipolar coupling parameters. This particular lineshape shown in Figure 1.4 is known as the *Pake doublet or Pake pattern*,[40] and the splitting of the horns is equal to the dipolar coupling constant, *d*=$\omega_{D,IS}/2\pi$. The horns represent the intensity contribution from the crystal orientations for which the internuclear vector is perpendicular to the applied field.

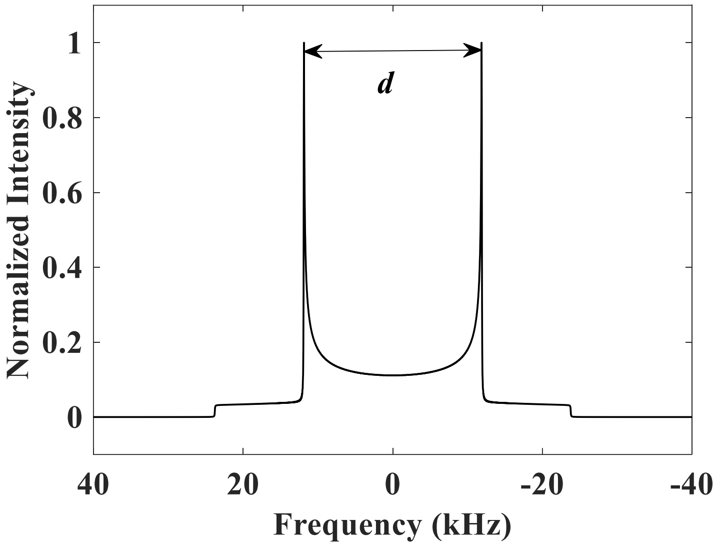

Figure 1.4 Powder lineshape (Pake pattern) for dipolar interaction for a ^{1}H-^{13}C spin system in Histidine (d= 21.13 kHz). Isotropic chemical shifts are not considered. Simulations are performed with SIMPSON software and utilize crystal file ZCW4180.

B. Indirect coupling

The indirect coupling or *J*-coupling is a through-bond interaction between two nuclear spins, mediated by the electrons around the nucleus.[29,31] It is independent of the static magnetic field. This interaction is responsible for the multiplet structure of resonances in solution NMR. The multiplet structure gives information about the bond connectivity between different nuclei such that indirect coupling is helpful in the determination of chemical/molecular structure with solution NMR. The indirect coupling Hamiltonian between two spins, j and k, is represented by

$$\mathcal{H}_J = 2\pi \boldsymbol{I_j} \cdot \overleftrightarrow{\boldsymbol{J}} \cdot \boldsymbol{I_k} \qquad [1.40]$$

where $\overleftrightarrow{\boldsymbol{J}}$ is the coupling tensor. It is a second-rank tensor, which is not symmetric and has a non-vanishing trace. However, the anisotropic part of the coupling tensor is very small as compared to the dipolar coupling interaction and can be ignored in the solid-state, whereas it averages in solution. Taking into consideration only the isotropic component, Hamiltonian of the indirect coupling for a homonuclear spin pair is

$$\mathcal{H}_J = 2\pi J_{iso} \boldsymbol{I_j} \cdot \boldsymbol{I_k} \qquad [1.41]$$

where $J_{iso} = \frac{1}{3}(J_{XX} + J_{YY} + J_{ZZ})$. Compared to other interactions, J_{iso} is very small, from a few Hertz among proton spins, up to less than 200 Hz for bonded ^{1}H and ^{13}C nuclei. If in a homonuclear spin system the chemical shift difference for two spins $I_1$and I_2 is considerably larger than the *J* coupling, the Hamiltonian can be approximated as,

$$\mathcal{H}_{J,I_1I_2} = 2\pi J_{iso} I_{1Z} I_{2Z}. \qquad [1.42]$$

The same expression is valid for a heteronuclear *I-S* spin pair, regardless of the chemical shifts,

$$\mathcal{H}_{J,IS} = 2\pi J_{iso} I_z S_z. \qquad [1.43]$$

(iii) Quadrupolar interaction

The quadrupolar interaction Hamiltonian, the corresponding energy levels as well as the respective transitions for integer and half-integer spin nuclei will be dealt in detail in section 1.3.

1.1.3 Resolution/Sensitivity Enhancement Techniques in Solid State NMR

As compared to solids which have only very restricted molecular motion, molecules in solution tumble rapidly resulting in averaging out of the anisotropic part of all interactions. Therefore, the solution NMR spectra will contain narrow resonances at frequencies determined by the isotropic chemical shift and the indirect coupling. In the case of solids, since molecular motions are restricted, the various interactions discussed above have a strong dependence on the crystallite orientation. The resultant NMR spectra (see Figure 1.2 and 1.4), arising from the superposition of various orientations in a powder sample, are generally broad. Additionally, with multiple sites present, the resultant powder spectra will be complex. Both features lead to poor resolution and sensitivity in solid-state NMR, making structural determination extremely challenging. Therefore, much effort has been made to develop different experimental techniques leading to spectra with better resolution and sensitivity. These experimental techniques involve manipulation of the spatial and/or spin parts of the interaction Hamiltonians. Two important and widely-used techniques are discussed below:

(i) Magic Angle Spinning (MAS)

Magic Angle Spinning (MAS)[4–7] involves physical spinning of the sample kept in a rotor spinning with axis of rotation making an angle, $\theta_m = 54.7^0$ with respect to the direction of the static magnetic field (θ_m is the angle between the Z axis and the body diagonal of a unit cube, known as the magic angle). The geometry of MAS is schematically shown in Figure 1.5.

Inspection of the form of the Hamiltonians of various internal interactions indicates that there is a factor proportional to the Legendre polynomial $P_2 = \frac{1}{2}(3\cos^2\theta - 1)$, where θ represents the orientation dependence of the respective interaction with respect to the static magnetic field. Under rotation of the sample at any angle, θ becomes time dependent resulting in (partial) time averaging of P_2 terms in the interaction Hamiltonian. However, when the rotation is at magic angle the time averaging is complete as $\langle 3\cos^2\theta(t) - 1\rangle = 0$ for any crystallite orientation. The averaging of the anisotropic parts of internal interaction results in considerable narrowing of the broad powder patterns and hence to significant increase in sensitivity and resolution of solid-state NMR spectra.

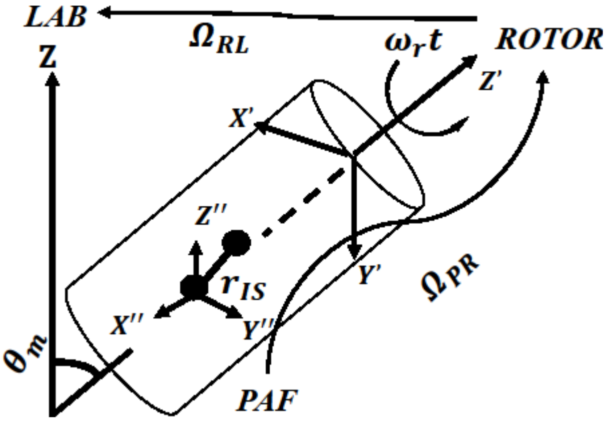

Figure 1.5 Geometrical sketch of dipolar interaction under Magic Angle Spinning. The different reference frames involved are indicated (PAF, ROTOR and LAB). The corresponding Euler angles for rotations involved, are indicated.

In order to understand the principle of MAS, the explicit time dependence of internal interactions has to be evaluated. An additional reference frame, the so-called rotor frame which rotates with the rotor, is introduced. Transformation from laboratory frame to PAF is performed in two steps: from laboratory frame to rotor frame and from rotor frame to PAF. The framework of irreducible spherical tensors is specifically used to represent the Hamiltonians. It has a spatial part and a spin part with characteristics that correspond to each interaction. The general derivation of the time-dependent Hamiltonians using spherical tensor formalism is provided in Appendix A1.2.

As an important case we consider the heteronuclear dipolar coupling under MAS. The space part of the secular heteronuclear dipolar Hamiltonian in Eq. [1.37] becomes time dependent, $\mathcal{H}_D(t) = \omega_{D,IS}\big(\theta(t)\big)2I_Z S_Z$. Using spherical tensor formalism to express $\omega_{D,IS}\big(\theta(t)\big)$, the Hamiltonian can be written as,

$$\mathcal{H}_D(t) = \omega_D\left[\frac{\sin(2\beta_D)}{2\sqrt{2}}\cos(\omega_R t + \gamma_D) - \frac{\sin^2(\beta_D)}{4}\cos(2\omega_R t + 2\gamma_D)\right]2I_Z S_Z$$

$$= \omega_D(t)2I_Z S_Z, \qquad [1.44]$$

where β_D and γ_D are the polar angles of the internuclear vector $\boldsymbol{r}_{IS}$ in the rotor frame, and

$$\omega_D(t) = \omega_D \left[\frac{\sin(2\beta_D)}{2\sqrt{2}}\cos(\omega_R t + \gamma_D) - \frac{\sin^2(\beta_D)}{4}\cos(2\omega_R t + 2\gamma_D)\right]. \qquad [1.45]$$

As mentioned above, to obtain Eq. [1.44] two successive transformations are utilized to express the spatial part under MAS in the laboratory frame.

$$\begin{aligned}[A_{20}^D]^{LAB} &= \sum_{m=-2}^{2} R_{2m}^{D,PAF} D_{0m}^2(\Omega_{PR}) D_{m0}^2(\Omega_{RL}) \\ &= \sum_{m=-2}^{2} R_{2m}^{D,PAF} d_{0m}^2(\beta_D)\, exp\{-i\gamma_D\}\, d_{m0}^2(\theta_m)\, exp\{im\omega_r t\} \qquad [1.46]\end{aligned}$$

The Euler angles employed by the two transformations are $\Omega_{PR} = (\alpha = 0, \beta = \beta_D, \gamma = \gamma_D), \Omega_{RL}(t) = (\alpha = \omega_R t, \beta = \theta_m = 54.7^0, \gamma = 0)$, and $\omega_D = -\mu_o\gamma_I\gamma_S\hbar/4\pi r_{IS}^3$. Dipolar interactions are symmetric, hence, the α angle for the transformation from the principal axis frame to the laboratory frame is not necessary. Also, under high field approximation, the Hamiltonian is invariant with respect to rotations about Z-axis. Therefore, the γ angle for the transformation from the rotor frame to the laboratory frame can be omitted.[32]

As $\mathcal{H}_D(t)$ commutes with itself at different times the corresponding propagator is $U(t,0) = \exp[-i\int_0^t dt\mathcal{H}_D(t)] = \exp[-i\int_0^t dt\omega_D(t)\, 2I_Z S_Z] = \exp[-i\Omega_\mathrm{D}(t,0)2I_Z S_Z]$ with $\Omega_\mathrm{D}(t,0) = \int_0^t dt\omega_D(t)$. Similarly to the static case, starting with the density operator $\rho(0) = I_X$ the state of the system at time t is $\rho(t) = U(t,0)\rho(0)U(t,0)^\dagger = I_X\cos(\Omega_\mathrm{D}(t,0)t) + 2I_Y S_Z\sin(\Omega_\mathrm{D}(t,0)t)$. Since $\Omega_\mathrm{D}(nT_R,0) = 0$, density operator refocuses at multiples of the rotor period $T_R, \rho(nT_R) = \rho(T_R)$ and generally $\rho(nT_R + \tau) = \rho(\tau)$. As a consequence, the signal refocuses at multiples of T_R, a phenomenon known as rotational echoes.[27,28,32] The fact that $\rho(nT_R + \tau) = \rho(\tau)$ implies that the NMR signal is periodic and ultimately leads to the breaking of the static powder pattern into narrow peaks of frequencies $n\omega_R, (n = \pm 1, \pm 2, \ldots)$, termed as spinning sidebands. The intensities of the spinning sidebands decreases at large ω_R and, if ω_R exceeds the dipolar frequency ω_D, the NMR spectrum contains only one peak at zero frequency, the so-called centerband. Herzfeld and Berger have described the calculation of intensities of the spinning sidebands arising due to chemical shift anisotropy as well as the determination of isotropic parameters in detail.[41] However, the same approach can also be extended to describe spinning sidebands arising due to dipolar interactions. The dependence of the spinning sidebands on MAS frequency is illustrated in Figure 1.6.

Similar rotational echoes are predicted with evolution under chemical shift or homonuclear dipolar interaction. Therefore, increased sensitivity and resolution is expected under MAS conditions. However, in many instances the rotational echoes are not perfect, resulting in broad spinning sidebands and hence in loss of resolution and sensitivity. The reason for this is that, when several interactions are present, the total Hamiltonian may not commute with itself at different times. This is the case with proton NMR where strong proton-proton dipolar couplings are present in most samples. In proton-proton networks the dipolar Hamiltonians corresponding to different spin pairs do not commute with each other, nor with chemical shift terms. The result is that very broad center- and spinning sidebands (line-widths in the kHz range) are produced at moderate MAS frequencies. Since for proton NMR line narrowing is predicted at considerably large ω_R, sustained efforts to obtain large MAS frequencies have been made over decades. Thanks to this efforts, reasonable resolution in proton NMR spectra can be currently achieved at MAS frequencies in the 50-150 kHz,[42] depending on the sample.

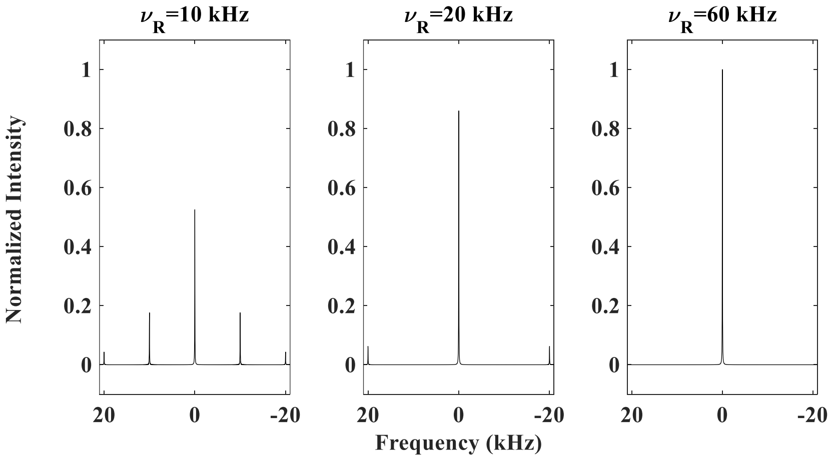

Figure 1.6 MAS spectra of a ^1H-^{13}C spin-pair with d= 21.13 kHz (r_{HC} =1.125 Å) and for different spin rates. The corresponding static spectrum was shown in Figure 1.4. SIMPSON software was utilized and the crystal file is ZCW4180.

(ii) Cross-Polarization (CP)

Natural abundance and magnitude of the gyromagnetic ratio of NMR active isotopes are two important factors that affect the sensitivity of an NMR experiment. Isotopes having low natural abundance as well as smaller gyromagnetic ratios are, in general, termed as dilute. The solid-state NMR detection of dilute nuclei through conventional pulse-acquire experiments results usually in spectra with very low sensitivity. The experiments in such cases have to be repeated many times and signals from individual scans have to be co-added in order to increase the signal-to-noise ratio (SNR). Between consecutive scans a relaxation delay of the order of T_1 is needed to ensure that the nuclear spin system starts again from thermal equilibrium. On the other hand, T_1 can be very large for dilute nuclei, as the non-secular homonuclear dipolar interactions, which contribute to the spin-lattice relaxation, are very feeble. As consequence, in order to obtain reasonable sensitivity (SNR) one needs to acquire a large number of scans with large relaxation delays in between, leading to excessively long experiments.

Among other methods, Cross-Polarization (CP),[14,15,24] introduced by Pines, Gibby, and Waugh, stands out as a widely used technique to enhance the signal-to-noise ratio in NMR spectra of dilute nuclei. It involves the transfer of magnetization from abundant spins, *I*, (such as ^{1}H, ^{19}F, etc.) to dilute spins, *S*, (such as ^{13}C, ^{15}N, etc.) through the dipolar interaction. The pulse sequence starts (Figure 1.7) with excitation of the abundant nuclei with an on resonance 90^0 pulse of phase Y on the I channel. Immediately after, spin-lock pulses of strengths ω_{1I} and ω_{1S} of phase X are applied on *I* and *S* channels respectively for a duration τ_{CP}, known as the contact time, during which the magnetisation on *I* spins is transferred to *S* spins if a certain condition, known as Hartmann-Hahn match[14] condition, is satisfied. At the end of the contact time the signal on *S* channel is acquired. A further boost in sensitivity is achieved by irradiating the *I* channel during acquisition[43–48] using a technique, known as heteronuclear decoupling, which removes line broadening due to interference between *I*-*S* heteronuclear dipolar interaction and the *I*-*I'* homonuclear dipolar interaction among the abundant spins.

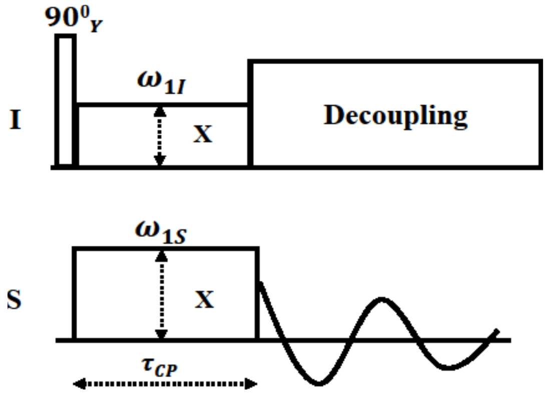

Figure 1.7 Cross polarization pulse sequence. ω_{1I} *and* ω_{1S} *represent the RF amplitudes of the CP pulses which are applied for a duration* τ_{CP} *known as the contact time. Heteronuclear decoupling is achieved by irradiation on the I channel during the acquisition.*

An enhancement of the signal by γ_I / γ_S, i.e. the ratio of the gyromagnetic ratios between the abundant spins and the dilute spins, can be achieved[49,50] by the CP mechanism as compared to direct excitation, since in an optimal CP transfer we have $\rho(0) = \gamma_I I_X$

$\xrightarrow{\tau_{CP}} \rho(\tau_{CP}) = \gamma_I S_X$ while with direct excitation $\rho(0) = \gamma_S S_X$. Further, since CP involves magnetization transfer from abundant spins, the relaxation delay between consecutive scans has to be of the order of T_1^I of the abundant spins, which is, in most cases, much shorter than T_1^S which dictates the relaxation delay in direct excitation experiments. The ability to pulse faster in CP experiments results in a considerable additional increase in sensitivity since during the same experimental time many more scans can be performed.

The analysis of the CP sequence, under static condition, can be simplified by treating the problem in a doubly rotating frame.[50,51] The transformation to the doubly rotating frame is achieved by the unitary transformation $\rho(t) = \exp[-i\omega_I t I_Z] \exp[-i\omega_S t S_Z] \rho'(t) \exp[+i\omega_I t I_Z] \exp[+i\omega_S t S_Z]$ where ρ and ρ' are the density operators in the laboratory and doubly rotating frame respectively whereas ω_I and ω_S represent the frequencies of the RF pulses applied during CP on the *I* and *S* channels. In the doubly rotating frame (dropping ' from all operators) the Hamiltonian of a dipolar-coupled heteronuclear *I-S* spin pair with *I*=1/2 and *S*=1/2 and subjected to irradiation on both *I* and *S* channels is

$$\mathcal{H} = \omega_{1I} I_X + \omega_{1S} S_X + \omega_D 2 I_Z S_Z \qquad [1.47]$$

For convenience, $\mathcal{H}$ is expressed in a tilted reference frame according to

$$\mathcal{H}_T = e^{i\frac{\pi}{2}(I_Y+S_Y)} \mathcal{H} e^{-i\frac{\pi}{2}(I_Y+S_Y)},$$

giving

$$\mathcal{H}_T = \omega_{1I} I_Z + \omega_{1S} S_Z + \omega_D 2 I_X S_X \qquad [1.48]$$

$\mathcal{H}_T$ can be represented as a sum of two commuting terms

$$\mathcal{H}_T = \mathcal{H}_{14} + \mathcal{H}_{23} = (\Sigma I_Z^{14} + \omega_D\, I_X^{14}) + (\Delta I_Z^{23} + \omega_D I_X^{23}) \qquad [1.49]$$

where $\Delta = \omega_{1I} - \omega_{1S}, \Sigma = \omega_{1I} + \omega_{1S}$ and I_Z^{14}, I_X^{14}, I_Z^{23}, I_X^{23} are fictitious spin-1/2 operators[52] associated with the basis $|1\rangle \equiv |1/2,1/2\rangle, |2\rangle \equiv |1/2,-1/2\rangle, |3\rangle \equiv |-1/2,1/2\rangle, |4\rangle \equiv |-1/2,-1/2\rangle$.

We now consider time evolution starting with an initial density operator $\rho(0) = \gamma_I I_X$ for which $\rho_T(0) = I_Z = I_Z^{14} + I_Z^{23}$. If $\Sigma \gg \omega_D$ the effect of ω_D in the 1-4 subspace is truncated such that the term I_Z^{14} in $\rho_T(0)$ remains unaffected. On the other hand, we see that rotation in 2-3 subspace around I_X^{23} becomes effective when $\Delta = \omega_{1I} - \omega_{1S} \sim 0$. This is the Hartmann-Hahn condition. At $\Delta = 0$

$$\rho_T(t_{CP}) \cong \gamma_I[I_Z^{14} + \cos(\omega_D t_{CP})\ I_Z^{23} - \sin(\omega_D t_{CP})\ I_Y^{23}] \qquad [1.50]$$

Utilizing $S_Z = I_Z^{14} - I_Z^{23}$ and coming back to the double rotating frame the expectation value of S-spin polarization, $\langle S_Z \rangle$, is

$$\langle S_Z \rangle(t_{CP}) = \mathrm{Tr}\{\rho_T(t_{CP}) S_Z\} = \gamma_I[1/2 - 1/2 \cos \omega_D t_{CP}]. \qquad [1.51]$$

Thus, maximal transfer $\langle I_Z \rangle \rightarrow \langle S_Z \rangle$ would be achieved by having a CP contact time $t_{CP} = \pi/\omega_D$. Since in a direct excitation experiment the relevant part of the density operator is $\rho_S(0) = \gamma_S S_Z$, the ratio of the signals acquired with optimal CP and direct excitation is γ_I/γ_S. However, due to the dependence of ω_D on θ, the maximum transfer in a powder is lower and is achieved at a different t_{CP} which corresponds to an averaging over crystallite orientations.

Under MAS, due to variation with time of the dipolar interaction, the Hamiltonian becomes time dependent and in the tilted frame

$$\mathcal{H}_T(t) = \omega_{1I} I_Z + \omega_{1S} S_Z + \omega_D(t) 2 I_X S_X \qquad [1.52]$$

where $\omega_D(t)$ is given by

$$\omega_D(t) = \omega_D \left[\frac{\sin(2\beta_D)}{2\sqrt{2}} \cos(\omega_R t + \gamma_D) - \frac{\sin^2(\beta_D)}{4} \cos(2\omega_R t + 2\gamma_D) \right]$$

and has the general form $\omega_D(t) = \sum_{m=-2}^{2} \omega_D^m e^{im\omega_R t}$ with $m \neq 0$. Similar to the static case, $\mathcal{H}_T(t)$ can be expressed as the sum of two commuting terms,

$$\mathcal{H}_T(t) = [\Sigma I_Z^{14} + \omega_D(t)\ I_X^{14}] + [\Delta I_Z^{23} + \omega_D(t) I_X^{23}] \qquad [1.53]$$

If $U(t, 0)$ is the propagator associated with $\mathcal{H}_T(t)$ we first define the unitary transformation,

$U(t, 0) = \exp[-ik\omega_R t I_Z^{23}]\, \widetilde{U}(t, 0)$, where the new propagator, $\widetilde{U}(t, 0)$, is associated with the Hamiltonian,

$$\widetilde{\mathcal{H}}_T(t) = \Sigma I_Z^{14} + \omega_D(t)\ I_X^{14} + (\Delta - k\omega_R) I_Z^{23}$$

$$+\omega_D(t)(I_X^{23} \cos(k\omega_R t) - I_Y^{23} \sin(k\omega_R t)). \qquad [1.54]$$

We see that $\widetilde{\mathcal{H}}_T(t)$ contains time-independent terms of the form $\omega_D^{\pm k} I_X^{23}$and $\omega_D^{\pm k} I_Y^{23}$. The remaining oscillating terms do not contribute significantly to the time evolution and can be neglected. The resulting time-independent Hamiltonian is

$$\widetilde{\mathcal{H}}_T \cong \Sigma I_Z^{14} + (\Delta - k\omega_R) I_Z^{23} + \mathrm{Re}(\omega_D^k) I_X^{23} - \mathrm{Im}(\omega_D^k) I_Y^{23}. \qquad [1.55]$$

The dipolar terms can produce an efficient rotation in the 2-3 subspace if $(\Delta - k\omega_R) \cong 0$ or $\omega_{1I} - \omega_{1S} \cong k\omega_R$. At this modified Hartmann-Hahn condition efficient polarization transfer occurs and it is found that

$$\langle S_Z\rangle(t) = \mathrm{Tr}\{\rho_T(t)S_Z\} = 1/2 - 1/2\cos\left|\omega_D^k\right|t, \qquad [1.56]$$

in analogy with the static case.

A different Hartmann-Hahn condition can be reached by the transformation generated by $U(t,0) = \exp[-ik\omega_R tI_Z^{14}]\widetilde{U}(t,0)$. Proceeding in the same way as above it is found that polarization transfer can occur if $\omega_{1I} + \omega_{1S} = k\omega_R$. In summary, optimal CP transfer can occur at the modified Hartmann-Hahn conditions $\omega_{1I} \pm \omega_{1S} = k\omega_R$, where $k = \pm 1$ or ± 2.

The theoretical approach utilized above is valid only at relatively short contact times. At longer contact times all the dipolar network of I spins surrounding the rare I spin has to be considered. As a result the spin system becomes very large and an explicit solution of Liouville-von Neumann is not possible. However, at long contact times, the evolution of the system can be still described within a thermodynamical approach. It predicts a similar enhancement of about γ_I/γ_S.

Several modified CP sequences such as ramped amplitude CP,[53] adiabatic CP,[54] etc. have been developed to further improve the efficiency of CP transfer in a powder. The ramped amplitude CP, in which the RF fields are swept across the matching condition by linearly incrementing one or both RF amplitudes over the contact time, is most widely used, especially under MAS. A short description of ramp-CP in the context of ^{1}H-^{14}N CPMAS at fast MAS is provided in Chapter 2, section 2.3.

1.2 Time-Dependent Hamiltonians in Solid-State NMR

It was shown above that MAS introduces a time dependence to the Hamiltonians connected to anisotropic interactions. In cases, an exact calculation of the propagator is not possible as the total Hamiltonian does not commute with itself at different times. Therefore, alternate methods are needed to address the evolution of the density matrix under a time dependent Hamiltonian in order to get an approximate understanding of the underlying spin dynamics. This section discusses various analytical and numerical methods to address this problem.

1.2.1 Effective Hamiltonian approach

The effective Hamiltonian associated with the periodic time-dependent Hamiltonian $\mathcal{H}(t)$ is defined as a time-independent Hamiltonian, $\mathcal{H}_{\mathrm{eff}}$ which satisfies the relation $U(T,0) = \exp\left(-i\mathcal{H}_{\mathrm{eff}}T\right)$, where $U(T,0)$ is the propagator over one modulation period, T, associated with the Hamiltonian $\mathcal{H}(t)$. Under MAS where the spinning frequency is $\nu_R = \omega_R/2\pi$, the modulation period is therefore $T_R = 1/\nu_R$. An effective Hamiltonian, capable of describing the state of the system at multiples of the modulation period, can be obtained with different methods, most notably average Hamiltonian theory[55–57] and Floquet theory.[58–62] A less frequently used numerical method, which we utilized in the work presented here, is the matrix logarithm method.[63–69] These three methods are discussed in the following sections according to their relevance to the work presented in the thesis.

(i) Average Hamiltonian theory

The concept of average Hamiltonian theory (AHT) to investigate the spin dynamics during cyclic multi-pulse periods was developed by Haeberlen and Waugh.[55] Later, P. Mansfield utilized the method for analysing symmetrized pulse sequences.[70] The performance of many solid-state NMR decoupling sequences (homonuclear multi-pulse sequences such as Lee-Goldburg (LG),[43] Waugh-Huber-Haeberlen (WAHUHA),[44] MREV8,[45] BR-24,[46] BLEW-12,[47] etc.), as well as recoupling sequences under MAS[71] (both homonuclear and heteronuclear such as Rotational Echo at Double Resonance (REDOR),[72] Rotary Resonance Recoupling (R^3) [73] etc.), can be predicted within the framework of AHT. It is also used for the description of spin-lock and CP under MAS.[27]

In average Hamiltonian theory, an average (effective) Hamiltonian is constructed for a periodic Hamiltonian ($i.e.\ \mathcal{H}(t) = \mathcal{H}(t+T)$) as a series of approximations called the Magnus expansion.[56]

$$\mathcal{H}_{ave} = \bar{\mathcal{H}}^{(1)} + \bar{\mathcal{H}}^{(2)} + \bar{\mathcal{H}}^{(3)} + \cdots \qquad [1.57]$$

The method is efficient if only few terms are significant in Eq. [1.57]. With higher order terms in $\mathcal{H}_{ave}$ discarded, spin dynamics can be determined with the approximate propagator,

$$U(T,0) = \hat{T}exp\left(-i\int_0^T \mathcal{H}(t')\,dt'\right) \cong exp[-i(\mathcal{H}_{ave})T].$$

The initial three terms, which are Hermitian, are listed below

$$\bar{\mathcal{H}}^{(1)} = \frac{1}{T}\int_0^T \mathcal{H}(t')dt'$$

$$\bar{\mathcal{H}}^{(2)} = -\frac{i}{2T}\int_0^T dt' \int_0^{t'} [\mathcal{H}(t'), \mathcal{H}(t)]dt$$

$$\bar{\mathcal{H}}^{(3)} = -\frac{1}{6T}\int_0^T dt'' \int_0^{t''} dt' \int_0^{t'} \left([\mathcal{H}(t''), [\mathcal{H}(t'), \mathcal{H}(t)]] + [[\mathcal{H}(t''), \mathcal{H}(t')], \mathcal{H}(t)]\right)dt$$

[1.58]

Alternatively, any periodic, time-dependent Hamiltonian can be represented utilizing the Fourier series expansion as $\mathcal{H}(t) = \sum_n \mathcal{H}_n e^{in\omega t}$, where $\omega = 2\pi/T$ is the characteristic frequency of $\mathcal{H}(t)$. Using this, the above terms can be rewritten as,[60]

$$\bar{\mathcal{H}}^{(1)} = \mathcal{H}_0$$

$$\bar{\mathcal{H}}^{(2)} = -\frac{1}{2}\sum_{n\neq 0}\frac{[\mathcal{H}_{-n}, \mathcal{H}_{+n}]}{n\omega} + \sum_{n\neq 0}\frac{[\mathcal{H}_0, \mathcal{H}_{+n}]}{n\omega} = \frac{1}{2}\sum_{n\neq 0}\frac{[\mathcal{H}_{+n}, \mathcal{H}_{-n}]}{n\omega} + \sum_{n\neq 0}\frac{[\mathcal{H}_0, \mathcal{H}_{+n}]}{n\omega}$$

$$\bar{\mathcal{H}}^{(3)} = \frac{1}{3}\sum_{n\neq 0}\sum_{n'\neq n\neq 0}\frac{[\mathcal{H}_{+n'}, [\mathcal{H}_{n-n'}, \mathcal{H}_{-n}]]}{nn'\omega^2} + \frac{1}{2}\sum_{n\neq 0}\frac{[\mathcal{H}_{+n}, [\mathcal{H}_0, \mathcal{H}_{-n}]]}{n^2\omega^2} - \frac{1}{2}\sum_{n\neq 0}\frac{[\mathcal{H}_0, [\mathcal{H}_0, \mathcal{H}_{+n}]]}{n^2\omega^2} + \sum_{n\neq 0}\sum_{n'\neq 0}\frac{[\mathcal{H}_{+n'}, [\mathcal{H}_{-n'}, \mathcal{H}_{+n}]]}{nn'\omega^2} + \frac{1}{2}\sum_{n\neq 0}\sum_{n'\neq 0}\frac{[\mathcal{H}_{+n'}, [\mathcal{H}_{+n}, \mathcal{H}_0]]}{nn'\omega^2}$$ [1.59]

Since only $U(T, 0)$ can be determined from H_{ave} the state of the system can be predicted only at multiples of the modulation period T. This may be sometimes not sufficient as in some experiments prediction of the state at arbitrary times is important. While applying AHT, it is very often needed to treat the problem in a convenient interaction frame in order to ensure fast convergence. However, if the Hamiltonian under study involves multiple time-dependencies which are incommensurate the approach as defined above fails. One way to address such situations is to consider successive averaging if the respective time scales are far apart.[74] There are also cases where AHT may not converge at all, even if we consider higher order terms, due to the complexity of the interaction Hamiltonian under study, discussed in Chapter 2.

(ii) Floquet theory

The utilization of the Floquet theorem for investigating the spin dynamics of quantum systems stems from the theoretical studies carried out by Shirley[59] for problems involving a periodic, time-dependent Hamiltonian. Later it has been extended to NMR by Vega,[75] Kubo and McDowell,[76] Levante et al.[77] and others. Subsequently, Floquet theory has been applied for the analysis of line shapes of single spins and dipolar coupled spin pairs under MAS.[78,79] Boender et al. proposed a physical interpretation of MAS phenomena using Floquet theory.[80] Bain and Dumont used Floquet theory to calculate spinning-sideband intensities under MAS.[81] The theoretical framework as well as various applications of Floquet theory are described in detail in references [60] and [62].

A periodic time-dependent Hamiltonian $\mathcal{H}(t)$, which is defined in Hilbert space, can be expanded as a Fourier series $\mathcal{H}(t) = \sum_n \mathcal{H}_n e^{in\omega t}$ where ω is the characteristic frequency of $\mathcal{H}(t)$. $\mathcal{H}_n$ are time-independent operators defined in Hilbert space. For homonuclear spin systems the dimension of Hilbert space is $(2I+1)^N$,where N is the number of spins, and I is the spin quantum number. In Fourier space, a time-dependent Hamiltonian is introduced as

$$\mathcal{H}^F(t) = \sum_n \mathcal{H}_n F_n \, e^{in\omega t}, \qquad [1.60]$$

in terms of the ladder operators $\boldsymbol{F_n}$, defined as

$$\langle m+n|\boldsymbol{F_n}|m\rangle = \mathbf{1}$$

where $|m\rangle$ are 'Fourier' states and $\mathbf{1}$ is a unit matrix with the dimension of the Hilbert space. The *time-independent* Floquet Hamiltonian, $\mathcal{H}_F$ [59,60,82–84] is defined in the basis $\{|i,n\rangle\}$, where $|i\rangle$ is a basis in the Hilbert space and $\{|n\rangle\}_{n\in Z}$, represents the Fourier basis as,

$$\mathcal{H}_F = N\omega + \sum_{n=-\infty}^{\infty} \mathcal{H}_n \, F_n. \qquad [1.61]$$

where

$$\langle m|\boldsymbol{N}|m'\rangle = \nu\delta_{m,m'}\mathbf{1}, \qquad [1.62]$$

The matrix structure of $\mathcal{H}_F, F_n, and\ N$ is displayed below.

$$\boldsymbol{N} = \begin{bmatrix} \ddots & & & & \\ & \begin{bmatrix} 1 & \\ & 1 \end{bmatrix} & \begin{bmatrix} & \\ & \end{bmatrix} & \begin{bmatrix} & \\ & \end{bmatrix} & \\ & \begin{bmatrix} & \\ & \end{bmatrix} & \begin{bmatrix} 0 & \\ & 0 \end{bmatrix} & \begin{bmatrix} & \\ & \end{bmatrix} & \\ & \begin{bmatrix} & \\ & \end{bmatrix} & \begin{bmatrix} & \\ & \end{bmatrix} & \begin{bmatrix} -1 & \\ & -1 \end{bmatrix} & \\ & & & & \ddots \end{bmatrix}, \mathbf{1} = \begin{bmatrix} \ddots & & & & \\ & \begin{bmatrix} 1 & \\ & 1 \end{bmatrix} & \begin{bmatrix} & \\ & \end{bmatrix} & \begin{bmatrix} & \\ & \end{bmatrix} & \\ & \begin{bmatrix} & \\ & \end{bmatrix} & \begin{bmatrix} 1 & \\ & 1 \end{bmatrix} & \begin{bmatrix} & \\ & \end{bmatrix} & \\ & \begin{bmatrix} & \\ & \end{bmatrix} & \begin{bmatrix} & \\ & \end{bmatrix} & \begin{bmatrix} 1 & \\ & 1 \end{bmatrix} & \\ & & & & \ddots \end{bmatrix},$$

$$\boldsymbol{F_1} = \begin{bmatrix} \ddots & & & & \\ & [\quad] & \begin{bmatrix}1 & \\ & 1\end{bmatrix} & [\quad] & \\ & [\quad] & [\quad] & \begin{bmatrix}1 & \\ & 1\end{bmatrix} & \\ & [\quad] & [\quad] & [\quad] & \\ & & & & \ddots \end{bmatrix}, \boldsymbol{F_{-1}} = \begin{bmatrix} \ddots & & & & \\ & [\quad] & [\quad] & [\quad] & \\ & \begin{bmatrix}1 & \\ & 1\end{bmatrix} & [\quad] & [\quad] & \\ & [\quad] & \begin{bmatrix}1 & \\ & 1\end{bmatrix} & [\quad] & \\ & & & & \ddots \end{bmatrix},$$

$$\mathcal{H}^{\boldsymbol{F}}(\boldsymbol{t}) = \begin{bmatrix} \ddots & & & & \\ & [\mathcal{H}_0] & [\mathcal{H}_1 e^{i\omega t}] & [\mathcal{H}_2 e^{i2\omega t}] & \\ & [\mathcal{H}_{-1} e^{-i\omega t}] & [\mathcal{H}_0] & [\mathcal{H}_1 e^{i\omega t}] & \\ & [\mathcal{H}_{-2} e^{-i2\omega t}] & [\mathcal{H}_{-1} e^{-i\omega t}] & [\mathcal{H}_0] & \\ & & & & \ddots \end{bmatrix},$$

$$\boldsymbol{\mathcal{H}_F} = \begin{bmatrix} \ddots & & & & \\ & [\mathcal{H}_0 + \omega] & [\mathcal{H}_1] & [\mathcal{H}_2] & \\ & [\mathcal{H}_{-1}] & [\mathcal{H}_0] & [\mathcal{H}_1] & \\ & [H_{-2}] & [\mathcal{H}_{-1}] & [\mathcal{H}_0 - \omega] & \\ & & & & \ddots \end{bmatrix}$$

In order to obtain an effective Hamiltonian, the Floquet Hamiltonian is first diagonalized, $\Lambda_F = D_F^{-1}\mathcal{H}_F D_F = \Lambda_0 F_0 + N\omega$, where Λ_0 is diagonal in the Hilbert space, and D_F is the diagonalization matrix. If Λ_F and D_F can be determined, the propagator in the Hilbert space can be evaluated as

$$U(t,0) = \textstyle\sum_n \langle n | D_F e^{-i\Lambda_F t} D_F^{-1} | 0 \rangle e^{in\omega t} \qquad [1.63]$$

and the density operator can be obtained at arbitrary times. An effective Hamiltonian can be also computed as

$$\mathcal{H}_{\text{eff}}^{\mathcal{F}} = D\Lambda_0 D^{-1}. \qquad [1.64]$$

where the Hilbert-space unitary matrix D is constructed from D_F.

Floquet theory is more general than average Hamiltonian theory in the sense that it allows the calculation of expectation values of any observable at arbitrary times without restricting to multiples of the modulation period. It can also deal with multiple, time-dependent, incommensurate frequencies corresponding to MAS as well as application of RF pulses sequences involved in decoupling, recoupling, etc.[60,62] Some of the work presented in this thesis has made use of Floquet theory. As one has to deal with infinite-dimensional Floquet matrices, applying Floquet theory may be very challenging from an analytical point of view. Hence, sometimes Floquet-based numerical approaches are utilized, in which the infinite-dimensional Floquet Hamiltonian is truncated to some finite dimension, sufficiently large enough to ensure convergence. The diagonalization of $\mathcal{H}_F$ is performed numerically, and the elements of Λ_0 are confined within the $(-\omega/2, \omega/2]$ interval.[85] The evolution of the system can then be predicted numerically with Eq. [1.63] or with $\mathcal{H}_{\mathrm{eff}}^{\mathcal{F}}$ in Eq. [1.64].

One of the important works in relation to the thesis (Chapter 2) was provided by Marks, Zumbulyadis, and Vega[86] on the quantitative description of ^{2}H CPMAS experiments and spin dynamics under spin lock within the Floquet formalism. For spin-1 nuclei, subjected to quadrupolar interactions in the 100 kHz range, under RF irradiation, and MAS rates of less than 10 kHz, it was shown that the eigenstates and eigenvalues of the Floquet Hamiltonian, as well as the Floquet effective Hamiltonian, exhibit a strong dependence on crystallite orientation. Therefore, CP matching conditions were also found to strongly depend on crystallite orientation. Nevertheless, with more complex spin dynamics in the system, Floquet theory sometimes fails in providing an accurate analytical picture. With the invention of the operator-based formulation of the Floquet Hamiltonian,[61] approximate Floquet Hamiltonians can be calculated based on the Van-Vleck perturbation theory, and can be used to derive a time-independent, effective Hamiltonian in the Hilbert space. This formalism can also be applied to solve non-resonant multi-mode problems.[61] Recently, the Floquet formalism has been generalized to *non-periodic* Hamiltonians by introducing a continuous frequency space.[87]

(iii) Matrix logarithm

Matrix logarithm method is yet another approach to compute effective Hamiltonians. Liu et al. used this method to derive the effective Hamiltonian for homonuclear decoupling sequences involving multi-pulse propagators.[64] Robyr et al. applied it to calculate the effective Hamiltonian which is used further to evaluate the off-resonance performance of the WALTZ17 sequence for decoupling.[67] Mehta et al. used the matrix logarithm method to derive an effective Hamiltonian to calculate the evolution of the spin system under the windowless, homonuclear dipolar recoupling (DRAWS) pulse sequence for the distance measurements in nucleic acids.[88,89] Recently it has been utilized in the SPINACH simulation library to derive the expression for the exact rotating frame Hamiltonian.[90]

Consider any operator, O, which has eigenstates and eigenvalues $|o_k\rangle$ and o_k. For any function $f(z)$, defined over the complex domain, the operator $f(O)$ is, by definition, constructed as $f(O) = \sum_k f(o_k)\, |o_k\rangle\langle o_k|$, where $f(o_k)$ are generally complex numbers. For $f(z) = \ln z$, the coefficients $\ln(o_k)$ are calculated according to the definition of the logarithm of a complex number, $z = rexp(i\phi)$, as $\ln z = \ln r + i(\phi + 2n\pi)$ (with $n = 0, \pm 1, \pm 2, \ldots$). This function is multivalued and in practice n is chosen such that $\phi + 2n\pi$ lies in the $(-\pi, \pi]$.

Only if all eigenvalues of O are real and positive, the standard definition of the logarithm function can be applied. This is clearly not the case when O is a *unitary* operator.

The matrix logarithm method proceeds in two steps.[68] (A) First, the propagator $U(T,0)$ is numerically calculated and (B) an effective Hamiltonian $\mathcal{H}_{\text{eff}}^{ln}$ is subsequently constructed by taking the *matrix logarithm* of $U(T,0)$

$$\mathcal{H}_{\text{eff}}^{ln} = \ln\big(U(T,0)\big)/(-iT). \qquad [1.65]$$

We have employed matrix logarithm method to determine the effective Hamiltonian in association with the work presented in Chapters 2 and 3. More details about the matrix logarithm are given in Chapter 2, section 2.1, where also a comparison of the effective Hamiltonians derived using the matrix logarithm and Floquet theory is provided. The potential of matrix logarithm approach is demonstrated in a heteronuclear dipolar coupled spin half pair under rotary resonance recoupling[73] and is provided in Appendix A1.3.

1.2.2 Brute force approach

The brute force approach, is a numerical method to calculate the propagator for a time dependent Hamiltonian. A few simulation packages including SIMPSON[38] utilizes this scheme. In this approach, the modulation time period of the Hamiltonian, T is divided into many small intervals, Δt, during which $\mathcal{H}(t)$ can be approximately treated as a constant. This is schematically shown in Figure 1.8.

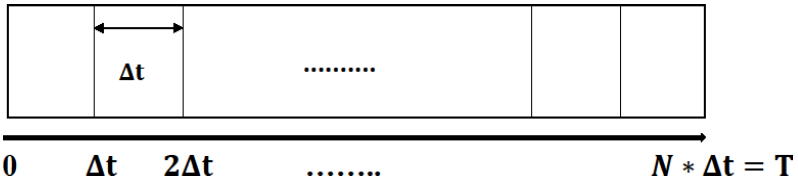

Figure 1.8 The modulation period, T has been divided into N equal parts of length Δt in such a way that the Hamiltonian can be considered as approximately constant over each of the Δt intervals.

The propagator $U(T,0)$ is then computed numerically as

$$U(T,0) \cong \prod_k exp(-i\mathcal{H}(t_k)\Delta\text{t}). \qquad [1.66]$$

There are various algorithms which can be used for the calculation of the exponential matrices in Eq. [1.66], the simplest (but not very efficient) being Taylor expansion. Once $U(T,0)$ computed, the propagator $U(kT,0)$ is simply obtained as a power, $U(kT,0) = U(T,0)^k$, such that density operator can be efficiently obtained at multiples of the modulation period. The method is also utilized in step (A) of the matrix logarithm method. The approach can be used also with non-periodic Hamiltonians, but then numerical evaluation of $U(t,0)$, where t is arbitrary, becomes more time consuming. The brute-force method, often associated with the matrix logarithm approach, has been employed extensively in the following chapters to understand the complex spin dynamics associated with RF irradiation on quadrupolar spins.

Having set a stage about the basics of NMR, solid state NMR in particular, and various theoretical tools associated with the work presented in the thesis, the concluding section of the chapter focuses on the quadrupolar interaction, its mathematical formulation and challenges. This part also provides an introduction and a smooth transition to Chapters 2 and 3.

1.3 Solid State NMR of Quadrupolar Nuclei

1.3.1 Quadrupolar interaction

Quadrupolar interaction[25,27,28,32] manifests with nuclei having a spin value greater than 1/2. More than 70% of NMR active nuclei are quadrupolar. The quadrupole moment, eQ, is an intrinsic property of a quadrupolar nucleus originating from the non-spherical ellipsoidal nuclear electric charge distribution, where 'e' is the charge of the electron. Quadrupole moment can interact with the electric field gradients generated by the surrounding electrons or by the charges of other nuclei present in the sample. Electric field gradients indicate the deviation of the electronic charge clouds around the nucleus from the spherical symmetry. The quadrupolar interaction Hamiltonian in the tensorial form (Appendix A1.2) is given by

$$\mathcal{H}_Q = \frac{eQ}{2I(2I-1)\hbar} \boldsymbol{S} \cdot \overleftrightarrow{\boldsymbol{V}} \cdot \boldsymbol{S} \qquad [1.67]$$

where eQ is the quadrupole moment, $\overleftrightarrow{\boldsymbol{V}}$ is the electric field gradient tensor for a spin, S . The interaction of a quadrupole moment with a field gradient in the PAF can be represented using the Hamiltonian,[91]

$$\mathcal{H}_Q^{PAS} = \frac{e^2qQ}{4S(2S-1)\hbar}\left[3S_Z^2 - S(S+1) + \eta_Q(S_X^2 + S_Y^2)\right]. \qquad [1.68]$$

where $S_X, S_Y, and\ S_Z$ are the spin components in the PAF. Here, the asymmetry parameter is defined as $\eta_Q = \frac{(V_{XX}-V_{YY})}{V_{ZZ}}$, where (V_{XX}, V_{YY}, V_{ZZ}) are the principal components of the electric field gradient tensor. As the trace of $\overleftrightarrow{\boldsymbol{V}}$ is zero, it has no isotropic part. The anisotropy, eq is given in terms of Z- component of the electrical field gradient tensor in the principal axes frame, V_{ZZ}. The strength of quadrupolar interactions is sometimes represented in terms of the quadrupole coupling constant, $C_Q = \frac{e^2qQ}{h}$ which can range up to a few MHz. In terms of the polar angles (θ, ϕ), the transformation of spin operators from PAF to the laboratory frame (LAB) is given by Euler angles $\Omega_{PL}(\alpha = \phi, \beta = \theta, \gamma = 0)$ (Appendix A1.2). A detailed description about the visualization of electric field tensor is provided by C. Bonhomme and J. Livage.[92.,93] The Hamiltonian in the laboratory frame takes the form,[28]

$$\mathcal{H}_Q{}^{LAB} = \frac{e^2qQ}{4S(2S-1)\hbar}\Bigg\{\Bigg(\frac{1}{2}(3cos^2\theta - 1)(3S_z^2 - S(S+1)) \\ + \frac{3}{2} sin\theta \, cos\theta \left[S_z(S_+ + S_-) + (S_+ + S_-)S_z + \frac{3}{4} sin^2\,\theta(S_+^2 + S_-^2)\right]\Bigg)\Bigg\} + \\ \frac{e^2qQ}{4S(2S-1)\hbar}\Bigg\{\eta_Q\left[\frac{1}{2} cos\,2\phi\,[(sin^2\,\theta)(3S_z^2 - S(S+1)) + (cos^2\,\theta + 1)(S_+^2 + S_-^2)]\right. \\ + \frac{1}{2} sin\,\theta[(cos\,\theta\,cos\,2\phi - i\,sin\,2\phi)(S_+S_Z + S_ZS_+) \\ \left. + (cos\,\theta\,cos\,2\phi + i\,sin\,2\phi)(S_-S_Z + S_ZS_-)] + \frac{i}{4} sin\,2\phi\,cos\,\theta(S_+^2 - S_-^2)\right]\Bigg\}$$

[1.69]

where now $S_X, S_Y, and\ S_Z$ are the spin components in the laboratory frame.

Under the secular approximation only terms which commute with the Zeeman interaction are retained such that

$$\mathcal{H}_Q{}^{LAB(1)} = \frac{\omega_Q}{4}\left[3\,cos^2\,\theta - 1 + \eta_Q\,sin^2\,\theta cos\;\,2\phi\right][3S_z^2 - S(S+1)] \qquad [1.70]$$

where $\omega_Q = \frac{e^2qQ}{2S(2S-1)\hbar}$ is called the quadrupolar coupling frequency. As the quadrupolar coupling can vary up to several MHz, besides $\mathcal{H}_Q{}^{LAB(1)}$ second-order perturbation theory corrections should be added resulting in the second order quadrupolar interaction Hamiltonian,[28,91,94]

$$\mathcal{H}_Q{}^{LAB(2)} = -\left(\frac{e^2qQ}{4S(2S-1)}\right)^2 \frac{S_z}{\omega_0}\{-\frac{1}{5}(S(S+1) - 3S_z^2)\left(3 + \eta_Q^2\right) \\ +\frac{1}{28}(8S(S+1) - 12S_z^2 - 3)[\left(\eta_Q^2 - 3\right)(3\,cos^2\,\theta - 1) + 6\eta_Q\,sin^2\,\theta\,cos\,2\phi] \\ + \frac{1}{8}(18S(S+1) - 34S_z^2 - 5)[\frac{1}{140}\left(8 + {\eta_Q}^2\right)(35\,cos^4\,\theta - 30\,cos^2\,\theta + 3) \\ + \frac{3}{7}\eta_Q \sin^2\theta(7\cos^2\theta - 1)\cos 2\phi + \frac{1}{4}\eta_Q^2 \sin^4\theta \cos 4\phi]\} \qquad [1.71]$$

Under MAS and for $\eta_Q = 0$, the first order and the second order quadrupolar interaction Hamiltonians can be written as:

$$\mathcal{H}_Q^{LAB^{(1)}}(t, \beta_Q, \gamma_Q) = \omega_Q(t, \beta_Q, \gamma_Q)[3S_Z^2 - S(S+1)] \quad [1.72]$$

where $\omega_Q(t, \beta_Q, \gamma_Q) = \frac{\omega_Q}{3}\left[\frac{1}{8}\sin^2(\beta_Q) cos(2\omega_R t + 2\gamma_Q) - \frac{1}{4\sqrt{2}}\sin(2\beta_Q)\cos(\omega_R t + \gamma_Q)\right]$.

where $\omega_Q = \frac{3\pi C_Q}{2S(2S-1)}$, and $\mathcal{H}_Q^{LAB^{(2)}}(t, \beta_Q, \gamma_Q) = \frac{2(\omega_Q^2)}{9\omega_{0S}}(L + M + N)$, [1.73]

$L = \frac{3}{5} S_Z \left\{3{S_z}^2 - S(S+1)\mathbf{1}_S\right\}$,

$M = \frac{3}{56} S_Z \left\{12{S_z}^2 - 8S(S+1)\mathbf{1}_S + 3\mathbf{1}_S\right\}\{M_1\, cos(\omega_R t + \gamma_Q) + M_2\, cos(2\omega_R t + 2\gamma_Q)\}$, and

$N = \frac{9}{4480} S_Z \{-34{S_z}^2 + 18S(S+1)\mathbf{1}_S - 5\mathbf{1}_S\}\{N_0 - 40N_1 cos(\omega_R t + \gamma_Q) +$
$20N_2\, cos(2\omega_R t + 2\gamma_Q) - 280N_3\, cos(3\omega_R t + 3\gamma_Q) + 35N_4\, cos(4\omega_R t + 4\gamma_Q)\}$,

$M_1 = -3(sin\, 2\beta_Q)(sin\, 2\theta_M), \; M_2 = 3\,(sin^2\beta_Q)(sin^2\theta_M)$,

$N_0 = (35\, cos^4\beta_Q - 30\, cos^2\beta_Q + 3)(35\, cos^4\theta_m - 30\, cos^2\theta_m + 3)$,

$N_1 = sin\,\beta_Q\,(7\, cos^3\beta_Q - 3\, cos\,\beta_Q)\, sin\,\theta_M\,(7\, cos^3\theta_M - 3\, cos\,\theta_M)$,

$N_2 = sin^2\beta_Q\,(7\, cos^2\beta_Q - 1)\, sin^2\theta_M\,(7\, cos^2\theta_M - 1)$,

$N_3 = cos\,\beta_Q\, sin^3\beta_Q\, cos\,\theta_M\, sin^3\theta_M, N_4 = sin^4\beta_Q\, sin^4\theta_M$. [1.74]

In the equations above $\mathbf{1}_S$ represents the S –spin unit operator, ω_{0S} represents the Larmor frequency of the S –spin and θ_m denotes the magic angle. It can be noticed from Eq. [1.73] that the second order correction is inversely proportional to the Larmor frequency and hence its magnitude reduces upon increasing the magnetic field strength. It has an isotropic part and an anisotropic part, consisting of second and fourth order Legendre polynomials. The presence of fourth order Legendre polynomials prevents the complete averaging of second order quadrupolar interaction by MAS, and special techniques are required which are briefly mentioned in the next section. The energy corrections also depend upon the spin system under consideration. The quadrupolar nuclei considered in this work are ^{14}N and ^{35}Cl which are spin 1 and 3/2 respectively. Hence the energy levels, transitions, energy corrections, spin dynamics, and spectral properties will be different.

1.3.2 Solid-state NMR of spin 1 and spin 3/2 nuclei

Spin-1 nuclei ($S = 1$; e.g.:- ^{1}H, ^{6}Li, ^{14}N, etc.) in the presence of an external magnetic field have $2S + 1 = 3$ energy levels corresponding to $m_S = 0, \pm 1$. The transitions between two adjacent m_S levels with $\Delta m_S = \pm 1$ are known as single-quantum (SQ) transitions. Single-quantum transitions are connected with single-quantum coherences in the density operator. Transitions with $\Delta m_S = \pm 2$ are termed as double-quantum (DQ) transitions. Double-quantum coherences cannot be directly detected in pulse-acquire experiments but can be indirectly detected after conversion into single-quantum coherences. The frequency of single-quantum transitions depend on the energy corrections of the Zeeman energy levels under the influence of the first and second order quadrupolar interactions. The corrections to the energy levels due to first and second order quadrupolar interactions are sketched in Figure 1.9.

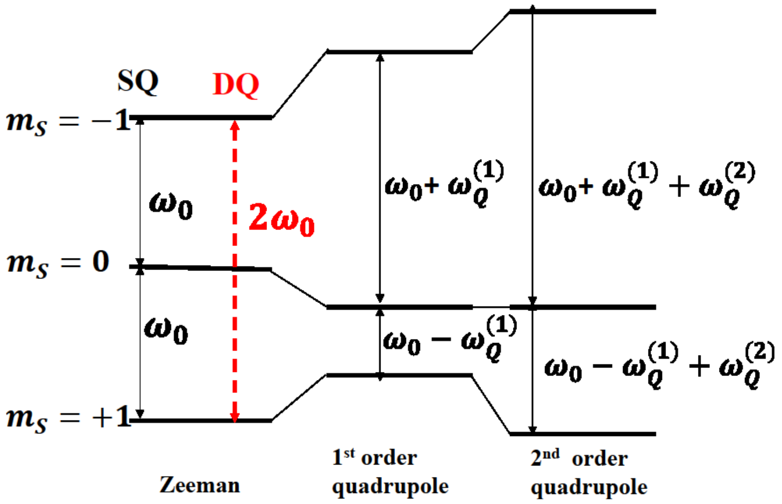

Figure 1.9 Corrections to the Zeeman energy levels for a spin 1 nucleus under the influence of first and second order quadrupolar interactions are shown, where $\omega_Q^{(j)} = \Delta E_Q^{(j)}/\hbar$, *as well as the frequencies of single and double-quantum transitions.*

Starting with $\rho(0) = S_X$, the time evolution of the spin system under static conditions can be obtained as[95]

$$\rho(t) = U(t,0)\rho(0)U(t,0)^\dagger = e^{-i\mathcal{H}_Q^{LAB(1)}t} S_X e^{i\mathcal{H}_Q^{LAB(1)}t}$$

$$= (S_X)\cos\big(\omega_Q(\theta)t\big) + 2(S_Y S_Z + S_Z S_Y)\sin\big(\omega_Q(\theta)t\big) \qquad [1.75]$$

with $\omega_Q(\theta) = \frac{\omega_Q}{4}[3\cos^2\theta - 1]$ for $\eta_Q = 0$ (axial symmetry). The NMR signal is:

$$S(t,\ \theta) = Trace\big((S_X)\rho(t)\big) = \cos\big(\omega_Q(\theta)t\big)\, Tr\{(S_X)^2\} \propto \cos\big(\omega_Q(\theta)t\big) \qquad [1.76]$$

since the second term in $\rho(t)$ does not contribute, as $Tr(S_X(S_YS_Z + S_ZS_Y)) = 0$. For a powder sample, the contribution to the intensity from different crystallite orientations in terms of $'\theta'$ results in a powder pattern in which the lineshape depends on the quadrupolar coupling parameters and can be obtained by Fourier transform of time domain signal,

$$S_{powder}(t) = \frac{1}{4\pi}\int_0^{2\pi}\int_0^{\pi} S(t,\theta)\, sin\theta d\theta d\phi. \qquad [1.77]$$

The splitting of the horns at $\theta = 90^0$ in the resulting powder lineshape corresponds to a value $3C_Q/4$ for a spin-1 nucleus. The horns represent the intensity contributions from crystal orientations for which the internuclear vector is perpendicular to the applied field, which is more probable. These features are illustrated in Figure 1.10. Double-quantum transitions are not affected by the first-order quadrupolar interaction. This can be seen by noting that double-quantum coherences of the form $|m_S = 1\rangle\langle m_S = -1|$ commute with the first order-quadrupolar interaction $\mathcal{H}_Q^{LAB\,(1)}$.

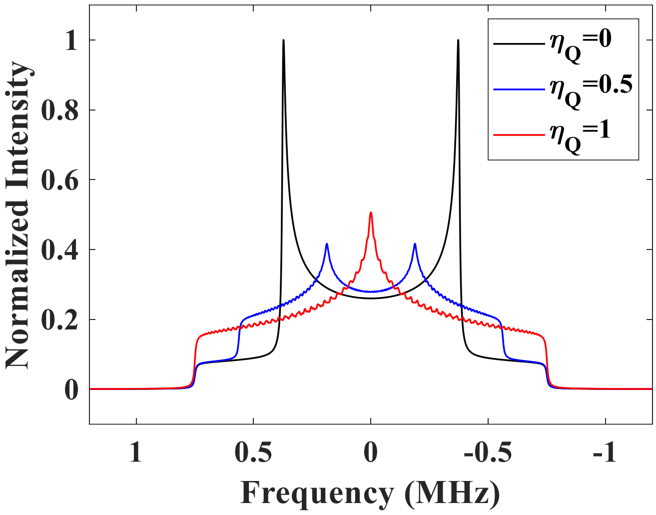

Figure 1.10 ^{14}*N static spectrum simulated with first order quadrupolar interaction only. The quadrupolar parameters are* C_Q*= 1 MHz and* $\eta_Q = 0$. *Simulations are performed with SIMPSON software using crystal file ZCW 28656. (The wiggles are a result of insufficient powder averaging.)*

Single-quantum transitions ($m_S = \pm1$) can be divided into a central transition (CT) between energy levels with $m_S = -\frac{1}{2}$ and $\frac{1}{2}$ and satellite transitions (ST) between energy levels with $m_S = \frac{3}{2}$ and $\frac{1}{2}$; $m_S = \frac{-1}{2}$ and $\frac{-3}{2}$. It is seen that the frequency of central transition is not affected by first-order quadrupolar interaction (MHz). Due to this, spin dynamics associated with central transition coherences is sometimes similar to that of a spin-1/2 system. This feature differentiates half-integer spins from integer spins quadrupolar nuclei. The frequency of central transition is affected by the second order quadrupolar interaction resulting in a specific powder lineshape which can span up to a few kHz, depending on the quadrupolar coupling constant and the Larmor frequency.

Spin-3/2 nuclei ($S = 3/2$ e.g. ^{7}Li, ^{11}B, ^{35}Cl, etc.) in the presence of external magnetic field have $2S + 1 = 4$ energy levels corresponding to $m_S = \pm1/2, \pm3/2$ as shown in Figure 1.11.

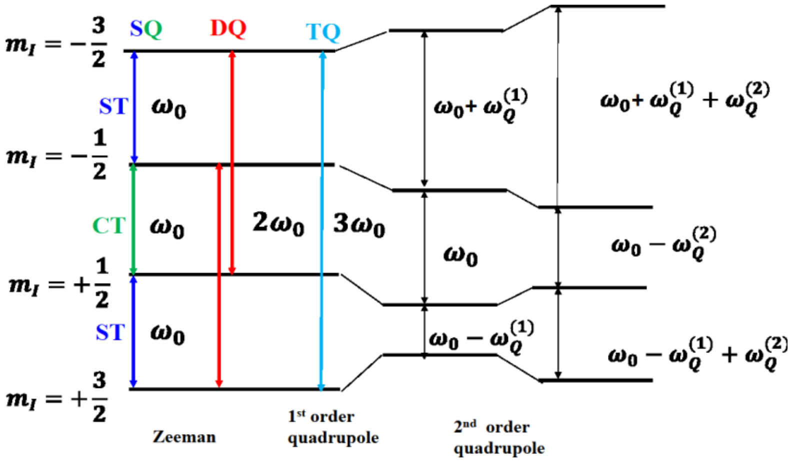

Figure 1.11 The corrections to the Zeeman energy levels for a spin 3/2 nucleus under the influence of the quadrupolar interaction are shown, where $\omega_Q^{(j)} = \Delta E_Q^{(j)}/\hbar$. *Central, Satellite, Double and Triple quantum transitions are represented as CT* ($\Delta m_I = \pm1$), *ST* ($\Delta m_I = \pm1$), *DQ* ($\Delta m_I = \pm2$) *and TQ* ($\Delta m_I = \pm3$) *respectively.*

On the other hand, since single-quantum satellite transitions are perturbed by first-order quadrupolar interactions in nuclei with half-integer spin, the resulting powder spectrum is dominated by the first order quadrupolar interaction and can span up to MHz, depending on the quadrupolar coupling constant. As a result, for *large* quadrupolar couplings and even with ideal excitation of both central and satellite transitions, the contribution of the central transition to the powder lineshape is dominant when compared with the contribution of satellite transitions. An illustration of these features for a spin-3/2 nucleus and ideal excitation is provided in Figure 1.12. In reality it is not possible experimentally to have ideal excitation of the satellite transitions due to limited excitation bandwidth of the probe. As a result, satellite transitions contributions to the static spectrum are in most cases invisible, for large quadrupolar couplings. However, both quadrupolar coupling and asymmetry parameter can be determined from analysis of the central transition spectrum, as the characteristic lineshape depends on these parameters. Acquiring nuclei with very large quadrupolar interaction (~ MHz) by employing frequency stepped excitation,[96] piecewise acquisition,[97] and so on, has been demonstrated by Schurkho, Bryce, etc. A brief reference of this in the context of ^{14}N is given in section 1.3.3.

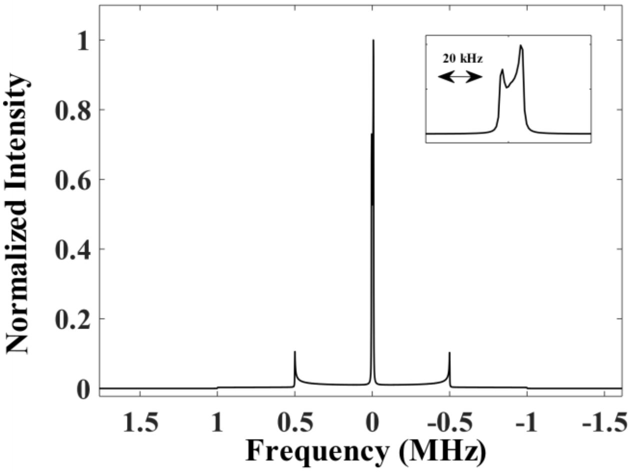

Figure 1.12 Static spectrum of a spin-3/2 nucleus for C_Q= 2 *MHz,* $\eta_Q = 0$ *and* $B_0 = 400\ MHz$. *The inset shows the central transition region with the characteristic second-order quadrupolar lineshape. Satellite transitions appear as mirror images on both sides of CT and are spread over 1MHz. The simulation was performed with SIMPSON software and crystal file ZCW4180 was utilized.*

Under MAS, the satellite transition contributions to the spectrum breaks into spinning sidebands which are typically spread over many hundreds of kHz, with intensities one or more orders of magnitude lower than the intensity of the central transition, hence satellite transitions are usually difficult to observe under direct detection. Each sideband has a characteristic lineshape due to second-order quadrupolar interaction which is not averaged completely by MAS. The central transition contribution to the spectrum also consists of spinning sidebands with lineshapes due to second-order quadrupolar interaction. However, the intensity of centerband is much larger than that of sidebands. The central transition centerband has a smaller linewidth than in the static case due to partial averaging of second-order quadrupolar interaction by MAS. As a result, an increase in sensitivity and resolution is achieved by rotation at magic angle. As for the static case, analysis of the MAS lineshape of the centerband can yield both quadrupolar coupling and asymmetry parameter. Spectral lines resulting from both CT and ST exhibit specific line shapes resulting from second-order quadrupolar interaction. Though the line width arising from CT confines within a kHz range, ST give rise to spinning sideband manifold that spread about ~ MHz range, which pose challenge as it exceeds the RF excitation and detection bandwidth of the probe.

Forbidden transitions with $\Delta m_S = \pm 2$ and ± 3 are termed as double and triple quantum (DQ, TQ) transitions respectively, collectively known as multiple quantum (MQ) transitions. The corresponding coherences can be detected only indirectly, by conversion into detectable single-quantum coherences. The following section deals with the solid-state NMR studies, techniques and challenges of ^{14}N, and ^{35}Cl NMR. For both nuclei the quadrupolar interactions can range up to a few MHz.

Triple-quantum transitions are not affected by the first-order quadrupolar interaction. This can be seen by noting that triple-quantum coherences of the form $|m_S = 3/2\rangle\langle m_S = -3/2|$ commute with the first order-quadrupolar interaction $\mathcal{H}_Q^{LAB^{(1)}}$.

1.3.3 Solid-state NMR studies of ^{14}N (S=1) and ^{35}Cl (S=3/2) systems and their challenges

Experiments probing correlations between spin- 1/2 nuclei (*I*) and nuclear spins (*S*) with large anisotropic interactions (quadrupolar or chemical shift anisotropy) often offer valuable access routes to molecular structure and dynamics. In such experiments, development of efficient correlation schemes is not trivial and constitutes an ever-evolving theme of research. As these experiments are performed routinely under MAS, interference between the RF field and the large time-dependent quadrupolar interaction leads to complex spin dynamics and often results in poor and orientation-dependent transfer efficiency. Nevertheless, with even the strongest insufficient RF fields currently available, sensitivity poses a challenge to such correlation experiments. Apart from hyperpolarization techniques,[98] higher MAS rates[9] currently available provides additional advantage in designing new experiments, where sensitivity and resolution can be improved through proton detection in the direct dimension and correlation to the low sensitive quadrupolar nuclei is achieved via indirect dimension. Compared with direct-detection correlation schemes, proton-detected correlation experiments under fast and ultra-fast MAS usually offer substantial gains in sensitivity.

Nitrogen is an important element in many areas of chemistry, biology, and materials. Solid state NMR of ^{14}N has potential in providing structural information, nearest neighbour proximities etc. in biological systems, and material science. Though ^{14}N is highly naturally abundant (99.6%), it is not a nucleus routinely used in solid-state NMR studies. Static ^{14}N NMR spectra are often very broad, as illustrated in Figure 1.10, due to the large first-order quadrupolar interaction ($1 - 5\ MHz$), resulting in extremely poor sensitivity and resolution Though there are excitation techniques meant for acquisition of ^{14}N spectra under static conditions, the use of MAS increases considerably the sensitivity and resolution. Still the anisotropic interactions will not be averaged out completely resulting in many spinning sidebands, hence still poor sensitivity, as shown in Figure 1.13.

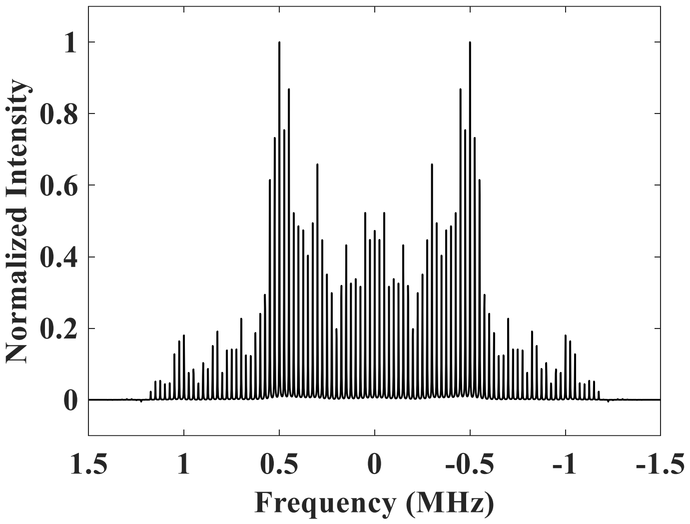

Figure 1.13 The powder lineshape for quadrupolar interaction under MAS with a spinning speed of 25 kHz is demonstrated using SIMPSON software for ^{14}N *nucleus in Histidine having* C_Q*= 1.14 MHz and* $\eta_Q = 0$ *using crystal file REP678 and* $B_0 = 400\ MHz$*.*

Current NMR methods applied to ^{14}N systems rely on piecewise acquisition, frequency swept excitation,[97] overtone irradiation,[99] low power single-sideband selective irradiation under MAS for broadband excitation,[100] broadband adiabatic-inversion CP (BRAIN CP),[101] Wideband Uniform Rate Smooth Truncation (WURST)[102] based Carr-Purcell Meiboom-Gill (CPMG)[103,104] schemes for acquiring ultra-wideline spectra,[105] $DANTE$ excitation,[106] and, most notably, various indirect detection schemes of ^{14}N spectra via ^{13}C or ^{1}H (HMQC)[107] such as J-HMQC,[108] D-HMQC,[109] etc. The indirect detection scheme introduced by Bodenhausen and coworkers has in fact opened up various possibilities for correlation experiments involving spin -1/2 nuclei dipolar-coupled to ^{14}N nuclear spins.

Following this, it was demonstrated that in dipolar-coupled ^{1}H-^{14}N systems, polarization transfer could be achieved through various recoupling schemes, e.g., rotary resonance recoupling (R^{3}),[110] REDOR, [72] symmetry-based recoupling schemes[111] such as $SR4_1^2$-Rotational Echo Saturation Pulse DOuble Resonance (S-RESPDOR) and phase modulated-S-RESPDOR (PM-S-RESPDOR),[112] Rotor Echo Short Pulse IRrAdiaTION mediated cross polarization (RESPIRATION CP),[113] TRAPDOR-HMQC,[114] etc. Sensitivity is still not outstanding, especially at low or moderate MAS rates (< 60 kHz). In addition, due to non-uniform excitation or transfer, resulting line-shapes are far from ideal, hence posing challenge in retrieving the quadrupolar coupling constant and asymmetry parameter accurately.

^{35}Cl is a highly abundant (75.78 %) half-integer quadrupolar nucleus having spin value $3/2$. It possesses comparatively higher gyromagnetic ratio than the ^{37}Cl isotope which has the same spin. Because of the large quadrupolar interaction~~s~~, the resolution of the resulting spectrum is hampered irrespective of the type of transitions involved, due to the second order broadening. The ability to excite or select CT, ST, or MQ transitions opened avenues towards resolution and sensitivity enhancement in NMR of half-integer quadrupolar nuclei.

Among the methods which have contributed to the conceptual development of the solid-state NMR of half-integer quadrupolar nuclei, double rotation (DOR),[10] dynamic angle spinning (DAS),[11] multiple quantum magic angle spinning (MQMAS),[12] and satellite-transition MAS (STMAS)[13] are noteworthy. Out of them, it is important to refer to MQMAS,[12] which revolutionized the field of solid-state NMR of quadrupolar nuclei compared to any previously existing techniques. For a spin-3/2, MQMAS involves excitation of triple-quantum coherences, their evolution in the indirect dimension, conversion into single-quantum central transition coherence followed by detection. A refocusing of the anisotropic part of the second-order quadrupolar interaction leaves only isotropic second-order quadrupolar shifts in the indirect dimension, hence high spectral resolution is achieved. STMAS[13] which followed, works on similar principles, but selects the satellite transitions in the indirect dimension. STMAS experiments are more demanding, requiring an accurate setting of the magic angle and highly stable spinning speeds. Various options for recoupling of homonuclear and heteronuclear dipolar interaction have been introduced later and often incorporate MQMAS or STMAS blocks in CP or HMQC-type experiments.

Solid-state Heteronuclear Multiple-Quantum Coherence (HMQC)[107] experiments constitute an important class of indirect-detection correlation schemes. HMQC experiments involve transfer of I-spin polarization to heteronuclear coherences (excitation), time evolution of these coherences during indirect dimension, transfer back to I-spin single-quantum coherences (reconversion), and finally detection. Initially introduced and developed for ^{14}N ($S = 1$) indirect detection,[107] HMQC experiments have been later extended to half-integer spins.[115] Usually, excitation and reconversion periods contain a train of pulses or pulses and delays, with well-defined phases and durations, applied on I channel with the purpose of recoupling the I-S dipolar interaction. However, Jarvis et al.[114] introduced an S-channel recoupling scheme, involving indirect detection of ^{14}N through ^{1}H or ^{13}C signals at moderate to high MAS. Through long periods of RF irradiation on the ^{14}N channel, the polarization transfer is achieved from ^{1}H or ^{13}C to heteronuclear coherences involving single and double quantum ^{14}N terms. They have demonstrated that such a scheme affords good transfer efficiency and allows extraction of quadrupolar parameters via numerical simulation.

Outline of the thesis

The first part of the thesis deals with a comprehensive investigation of $1H(I) \rightarrow 14N(S)$ CP spin dynamics and in particular the efficient $1H \rightarrow 14N \rightarrow 1H$ CP transfer in double CP experiments in the context of Ref. [17]. A detailed analytical solution of the associated time-dependent problem is challenging due to the interference between the large ^{14}N time-dependent quadrupolar interaction and ^{14}N RF irradiation. Towards this, an effective Hamiltonian is calculated numerically using the matrix logarithm approach and in parallel Floquet theory. The structure of the effective Hamiltonian is investigated. Employing RF strengths and MAS rates similar to the experimental studies in Ref. [17], various features specific to efficient transfer under CPMAS are addressed. A proof is given for the important observation that the sign of double CP signal is largely independent on crystallite orientation. The theoretical observations are substantiated with the experimental observations presented in Ref. [17].

In the second part, we study the spin dynamics associated with the TRAPDOR- HMQC type experiment (T-HMQC) implemented by Hung and Gan on active pharmaceutical ingredients (API) where remote ^{1}H (I) spins are dipolar coupled to ^{35}Cl (S) nuclei.[20] They have demonstrated that such a scheme affords good transfer efficiency and allows extraction of quadrupolar parameters via numerical simulation. Subsequently, Bayzou et al.[21] have presented an extensive experimental and theoretical study of T-HMQC. Experiments were demonstrated on ^{1}H-^{135}Pt/^{14}N/^{35}Cl systems with nuclear spin $S = 1/2, 1$ and $3/2$ respectively. In this work, we offer additional insights into the machinery of T-HMQC experiments for $S = 3/2$. Analytical conclusions are derived and confronted with numerical simulations in which the exact effective Hamiltonian is evaluated with the *matrix logarithm* approach and its structure was investigated. Subsequently, for the full T-HMQC experiment, the truncation approximation is utilized to derive analytically the dependence of the sign (phase) of the I-spin signal on the coherence type created by TRAPDOR irradiation. Different conditions driving the coherence transfer mechanism are explored.

The thesis concludes with a brief chapter on summary and discussion of the work carried out.

2

Spin Dynamics of ^{1}H-^{14}N Cross Polarization and Double Cross Polarization at fast MAS

2.1 Introduction

Cross Polarization under magic angle Spinning (CPMAS) is a technique which mediates transfer of polarization from abundant nuclei (*I*) to any dipolar coupled nuclei (*S*) which are less abundant and/or have low gyromagnetic (γ), yielding sensitivity enhancements in the order of γ_I/γ_S.[14,15] Magnetization transfer is achieved, through application of simultaneous RF irradiation on both *I* and *S* channels, when the RF strengths satisfy a certain condition called the Hartmann–Hahn match. Magnetization transfer in CPMAS experiments may have low efficiency either due to the presence of large chemical shift anisotropy (CSA) of the *S* nucleus or due to its large first order quadrupolar coupling (~ MHz). Sensitivity enhancement via CP under static conditions can be achieved by employing frequency modulated pulses on the *S* channel.[8,116-120] However, under MAS these techniques usually are less efficient due to the multiple time dependencies of the spin Hamiltonian and the resulting interference with the transfer process. In the case of half-integer quadrupolar nuclei, reasonable CPMAS efficiency may be achieved by transfer of magnetization to the central transition which is not affected by the first order quadrupolar interaction.[121,122] The feasibility of magnetization transfer from protons to spin 1 nuclei under MAS and the spin dynamics associated with the transfer process was investigated in various contexts, as discussed below.

Proton-deuterium CP dynamics under slow MAS was considered theoretically and demonstrated experimentally by L. Müller, in partially deuterated and perdeuterated polycrystalline solids.[123] Based on a spin temperature approach, an efficient CP match was predicted under adiabatic conditions and demonstrated experimentally when the sample was spun at very slow MAS. In the context of rotational echo (^{14}N/^{13}C/^{1}H) triple resonance experiments, Grey et al. have investigated the relation between ^{14}N spin lock and the adiabaticity of the spin dynamics.[124] A quantitative description of ^{2}H CPMAS experiments and the spin dynamics under spin lock within the Floquet formalism was provided by Marks et al.[86] For a spin 1 nucleus subjected to quadrupolar interaction in the 100 kHz range and under RF irradiation, it was found that the eigenstates and eigenvalues of the Floquet Hamiltonian, as well as the effective Hamiltonian, exhibit a strong dependence on crystallite orientation. Spin states which commute with the Floquet Hamiltonian were termed as *locked in Floquet space*. For an $S - I_N$ system with N sufficiently large and under reasonable assumptions, it was shown that the state of the system is locked in Floquet space after a long CP contact.[125] Deuterium Spin lock and CPMAS dynamics under adiabatic conditions were revisited by Gopalakrishnan and Bodenhausen.[126] Adiabatic conditions were exploited to derive analytical expressions for the spin-lock propagator and the deuterium density operator. Spin-locked states were predicted for which the density operator would vary co-periodically with the MAS frequency, after initial decay of transient components in the density operator. CP matching conditions were derived which essentially depended on an effective nutation frequency of the deuterium spin. The CP transfer efficiency was found to depend on crystallite orientation. S. Wi et al. proposed and demonstrated ^{1}H - ^{2}H CPMAS experiments involving frequency-swept pulses applied on the deuterium channel at MAS rates of 60 kHz, and under sudden passage conditions.[127] Average Hamiltonian Theory (AHT)[55,56] and intensive numerical simulations showed that due to frequency sweep both zero quantum (ZQ) and double quantum (DQ) transfer processes would occur at different instants during CP contact time. Although not directly connected with CPMAS, Pell et al. provided a comprehensive theoretical description and experimental implementation of efficient excitation of ^{14}N double quantum coherences using low-power phase-modulated pulses at ultrafast MAS.[100] For low RF power, an AHT Hamiltonian comprising the first two terms in the Magnus expansion was sufficient to quantitatively describe spin dynamics for most crystallite orientations.[56]

In principle, solid state NMR of ^{14}N, a spin-1 nucleus 99.6 % abundant, has potential in providing structural information, nearest neighbour proximities etc. in biological systems, material science and so on. However, due to its large quadrupolar coupling (in the MHz range), direct excitation and detection are not efficient at currently available RF strengths and MAS rates. A considerable boost in sensitivity of ^{14}N NMR was achieved more than a decade ago through the invention of suitable indirect detection techniques by Bodenhausen and coworkers,[108,128,129] and by Z. Gan.[107,109] In these experiments ^{13}C-^{14}N or ^{1}H-^{14}N heteronuclear coherences are excited, evolve rotor-synchronously in the indirect dimension, and are converted into ^{13}C or ^{1}H single quantum coherences which are finally detected. Essentially, the efficiency of the indirect method is given by the folding of all first order quadrupolar spinning sidebands in the indirect dimension thanks to the rotor-synchronized evolution of the heteronuclear coherences.[130]

Subsequently, Bodenhausen and coworkers[17] reported an efficient ^{14}N indirect detection with a ^{1}H →^{14}N→^{1}H 2D double cross polarization (double CP) experiment at a magic angle spinning (MAS) rate of 60 kHz. The schematic of double CP pulse sequence is given in Figure 2.1.

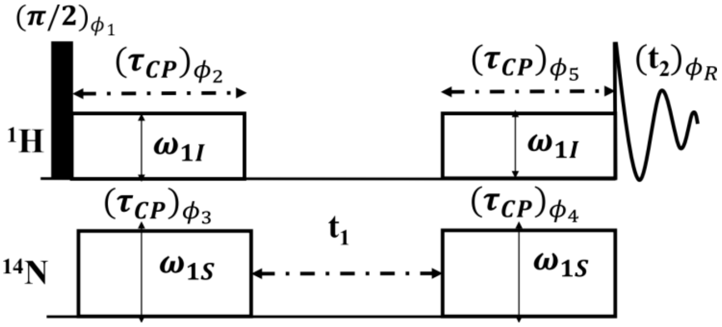

Figure 2.1: Schematic of the ^{1}H →^{14}N→^{1}H double-CP pulse sequence. ω_{1I} and ω_{1S} represent the RF amplitudes of the CP pulses which are applied for a duration τ_{CP}. The phase cycle used is: ϕ_1 = 4{y}, 4{–y}, 4{y}, 4{–y}, ϕ_2 = 8{x}, 8{–x}, ϕ_3 = 4{x, –x}, 4{–x, x}, ϕ_4 = 2{x}, 2{–x}, ϕ_5 = x, ϕ_R= x, –x, –x, x, –x, x, x, –x, –x, x, x, –x, x, –x, –x, x.

Double CP pulse sequence starts with a 90^{o} excitation pulse on the proton channel. The resulting proton magnetization is transferred to ^{14}N through ^{1}H-^{14}N CP transfer block of duration, τ_{CP} creating single quantum ^{14}N coherences. The coherences evolve under chemical shifts and second order quadrupolar interactions during t_1 evolution. The t_1 interval is incremented in steps of rotor periods in-order to refocus the first order quadrupolar interactions under MAS, under precise magic-angle setting. The evolved single quantum ^{14}N coherences are transferred back to the proton coherence by a reverse CP transfer. Finally, the proton magnetization is detected in the t_2 interval. The experiments were demonstrated on polycrystalline samples with ^{14}N quadrupolar couplings in the 1-4 MHz range. Subsequently, they have shown the potential of the ^{1}H-^{14}N double CP experiment by applying it to study amide functions in polypeptides[18] and guanine quartet self-assemblies.[19] The relatively straightforward implementation of ^{1}H-^{14}N double CP experiments is noteworthy.

In this work we provide a comprehensive investigation of $1H(I) \rightarrow 14N(S)$ CP spin dynamics and in particular the efficient $1H \rightarrow 14N \rightarrow 1H$ CP transfer in double CP experiments. A detailed analytical solution of the associated time-dependent problem is challenging due to the interference between large ^{14}N time-dependent quadrupolar interaction and ^{14}N RF irradiation. Spin dynamics of the CPMAS[15,131] process for spin-1 nuclei dipolar-coupled to protons was investigated in various contexts.[86,100,123,124,126,127] A few contributions relevant to the work presented here are mentioned below. Gan and coworkers[132] studied spin dynamics in ^{1}H/^{14}N HMQC[8,107-109,128-130] and double CP experiments under fast MAS. An insightful qualitative picture, employing AHT and Floquet theory in the jolting frame essentially within zeroth order approximation, was provided, showing that the effect of the large quadrupolar interaction is to introduce a scaling and a phase of the ^{14}N RF field which is dependent on crystallite orientation. The RF *phase spread* occurring for different crystallites causes cancellation of the CPMAS signal in a powder. It was predicted that, when two long ^{14}N pulses are used, like in HMQC and double CP experiments, the phase cancellation is nullified resulting in coherent signal addition in a powder.

Preliminary brute force simulations performed with many individual crystallite orientations confirmed the two important predictions of Gan and coworkers.[132] However, with parameters close to the experimental values of Ref. [17] we found that an average Hamiltonian computed in the jolting frame with first three terms in the Magnus expansion was not able to predict the S-spin dynamics under spin lock for a large number of crystallite orientations. Therefore, in order to understand in more detail the $1H(I) \rightarrow 14N(S)$ CP spin dynamics, and in particular the efficient $1H \rightarrow 14N \rightarrow 1H$ CP transfer, we have utilized in parallel the logarithm and Floquet approaches for numerical calculation of the effective Hamiltonian. Within the Floquet formalism an accurate *numerical* effective Hamiltonian can be obtained by numerical diagonalization of the Floquet Hamiltonian.[86] Within the matrix logarithm method a numerical effective Hamiltonian is obtained by evaluating numerically the propagator over one cycle time and subsequently computing its matrix logarithm.[63-69] Since the complex logarithm function is multivalued, the generated effective Hamiltonian may not be unique and its interpretation requires caution, depending on the problem under study. A powerful algorithm, COMPUTE (Computation Over one Modulation Period Using Time Evolution), which allows calculation of spectral frequencies and amplitudes without estimating signal for long acquisition times was introduced in Ref. [68]. It calculates numerically and utilizes both eigenvalues of the effective Hamiltonian and a set of intermediate propagators. The equivalence between effective Hamiltonians generated by the Floquet and multi-step approaches was proved by Ding and McDowell[133]: the eigenvalues of these effective Hamiltonians can differ only through multiples of the modulation frequency. The equivalence of the effective Hamiltonians generated by logarithm and Floquet approaches was tested for the problem considered here. We found that both approaches provided *identical* effective Hamiltonians, within inherent numerical errors. This equality is in fact general and it is shown that it follows from the fact that both methods confine the eigenvalues to the $(-\omega/2, \omega/2]$ interval, where ω is the modulation frequency. In order to obtain an interpretable effective Hamiltonian we have performed an additional rotating frame transformation with respect to the usual doubly rotating frame. We found that the effective Hamiltonian in the new rotating frame can be obtained by a simple *rearrangement* of eigenvalues of the effective Hamiltonian in the doubly rotating frame. We presume that this procedure may be extended to other time-dependent problems.

We found that the effective Hamiltonian thus computed contains virtually all possible spin operators in the chosen basis and the coefficients of these spin operators depend strongly on the crystallite orientation. Correlation between the structure of the effective Hamiltonian and the CP signal indicates that significant CP transfer occurs for a given crystallite orientation when (A) all pure ^{14}N spin terms in the effective Hamiltonian are small, except for S_X and S_Z, and simultaneously (B) the proton and the ^{14}N *effective* RF strengths, ω_{1I}^{eff} and ω_{1S}^{eff} satisfy $|\omega_{1S}^{eff}| \cong |\omega_{1I}^{eff}|$. For a given proton RF strength ω_{1I}, the above condition is satisfied only in certain ranges of crystallite orientations thereby resulting in non-uniform CP transfer in a powder. Furthermore, the sign of ω_{1S}^{eff} strongly depends on crystallite orientation and the sign of CPMAS signal follows the sign of ω_{1S}^{eff}. In terms of the proton RF strength the matching condition in (B) can be written as $|\omega_{1S}^{eff}| \cong \omega_{1I} - \omega_R$, ω_R is the MAS angular frequency. We also predict and verify other matching conditions employing multiples of the spinning frequency or involving other ^{14}N RF strengths. On the contrary, simulations show that the sign of double CP signal is largely independent of crystallite orientation. For this crucial feature, we provide an analytical proof which also allows us to calculate the ratios of transfer amplitude in $1H \rightarrow 14N$ and $14N \rightarrow 1H$ CP processes. The proof assumes only S_X or S_Y coherences during indirect dimension. However, we found that, besides S_X and S_Y, several other single-quantum coherences (which cannot be distinguished from S_X and S_Y by phase-cycling) are present in the indirect dimension and contribute to the double CP signal. Domination of these additional coherences at short contact times leads to a reversal of the double CP signal. This rather unusual behavior was observed experimentally by Bodenhausen and coworkers.[17] We also investigate the effect on sensitivity of a ramped ^{1}H RF strength during CP, second-order quadrupolar lineshapes in double CP experiments, the connection between ^{14}N spin-lock and CP transfer, etc.

All simulations presented in the manuscript are performed using home-written MATLAB® (The Mathworks, Inc.) code. In this context it is worth mentioning that the optimal control module of SIMPSON[38] simulation software offers the option of computing effective Hamiltonians numerically.

2.2 Effective Hamiltonian with logarithm and Floquet approaches

For a periodic time-dependent Hamiltonian $\mathcal{H}(t)$ with modulation frequency ω and period $T = 2\pi/\omega$, the time evolution of the system is given by

$$\rho(t) = U(t,0)\rho(0)U^{\dagger}(t,0), \qquad [2.1]$$

where the propagator $U(t,0)$ satisfies Schrödinger equation

$$idU/dt = \mathcal{H}(t)U. \qquad [2.2]$$

The propagator for one period, $U(T,0)$, is unitary and hence can be expressed as

$$U(T,0) = \exp\left(-i\mathcal{H}_{eff}T\right), \qquad [2.3]$$

where $\mathcal{H}_{eff}$ represents an effective Hamiltonian capable of predicting the density operator at any multiple of the period. If the Hamiltonian does not commute with itself at different times, an exact analytical expression of $U(t,0)$ is generally not accessible but approximate analytical or numerical methods are available. The propagator $U(T,0)$ can be obtained numerically as

$$U(T,0) \cong \prod_k exp(-i\mathcal{H}(t_k)\Delta \mathrm{t}), \qquad [2.4]$$

where Δt is sufficiently small such that $\mathcal{H}(t)$ is practically constant over the Δt interval.

The matrix logarithm and Floquet numerical procedures, used in this work for generating effective Hamiltonians, are briefly discussed below. The matrix logarithm method proceeds in two steps. (A) First the propagator $U(T,0)$ is numerically calculated and (B) an effective Hamiltonian H_{eff}^{ln} is subsequently constructed by taking the *matrix logarithm*[22] of $U(T,0)$

$$\mathcal{H}_{eff}^{ln} = \ln\left(U(T,0)\right)/(-iT). \qquad [2.5]$$

The Hamiltonian H_{eff}^{ln} can be written as

$$\mathcal{H}_{eff}^{ln} = \sum \epsilon_j |\epsilon_j\rangle\langle\epsilon_j|, \qquad [2.6]$$

where ϵ_j and $|\epsilon_j\rangle$ represent the corresponding eigenvalues and eigenvectors. The eigenvalues ϵ_j are not unique as the replacement $\epsilon_j \to \epsilon_j + k_j\omega$, where k_j are integers, leads to the same propagator $U(T,0)$. The matrix logarithm numerical algorithm automatically choses ϵ_j in the $(-\omega/2\,,\omega/2]$ interval.[22]

Within Floquet approach, from the periodic time-dependent Hamiltonian $\mathcal{H}(t) = \sum_n \mathcal{H}_n e^{in\omega t}$, an infinite dimensional time-independent Hamiltonian, $\mathcal{H}_F$ is constructed with which the evolution of the density operator can be predicted. The Floquet Hamiltonian corresponding to the time-dependent Hamiltonian can be written in the basis $\{|i,n\rangle\}$, where $|i\rangle$ constitute a basis of the Hilbert space and $\{|n\rangle\}_{n\in Z}$, is the Fourier basis. In terms of the number operator N and ladder operators F_n, defined as $\langle m+n|F_n|m\rangle = \mathbf{1}$, and $\langle m|N|m'\rangle = m\delta_{m,m'}\mathbf{1}$, where $\mathbf{1}$ is the Hilbert space unit matrix, the Floquet Hamiltonian $\mathcal{H}_F$ can be expressed as

$$\mathcal{H}_F = N\omega + \sum_{n=-\infty}^{\infty} \mathcal{H}_n\, F_n.$$

In order to obtain an effective Hamiltonian, the Floquet Hamiltonian is first diagonalized, $\Lambda_F = D_F^{-1}\mathcal{H}_F D_F = \Lambda_0 F_0 + N\omega$, where Λ_0 is diagonal in the Hilbert space, and D_F is the diagonalization matrix. From D_F a unitary matrix D in Hilbert space can be constructed and an effective Hamiltonian can be computed as

$$\mathcal{H}_{eff}^{\mathcal{F}} = D\Lambda_0 D^{-1}.$$

In a numerical approach, the infinite dimensional Floquet Hamiltonian is truncated to some finite dimension sufficiently large to ensure convergence. The diagonalization of $\mathcal{H}_F$ is performed numerically and the elements of Λ_0 are usually confined within the $(-\omega/2,\omega/2]$ interval.[59,82,83]

Since $\mathcal{H}_{eff}^{ln}$ and $\mathcal{H}_{eff}^{\mathcal{F}}$ correspond to the same propagator $U(T,0)$ their eigenvectors should be the same. If, in addition, eigenvalues of both effective Hamiltonians are constrained to the $(-\omega/2\,,\omega/2]$ interval, it follows that

$$\mathcal{H}_{eff}^{ln} = \mathcal{H}_{eff}^{\mathcal{F}}.$$

The relation between the $(-\omega/2\,,\omega/2]$ constraint and the structure of the effective Hamiltonian is discussed in the following sections.

2.3 Spin dynamics in ^{1}H-^{14}N CPMAS and double CP experiments

System Hamiltonian

We consider a dipolar-coupled $I-S$ spin pair ($S=1, I=1/2$), under magic angle spinning at angular frequency ω_R and subjected to irradiation at RF strengths ω_{1I} and ω_{1S} on I and S channels respectively. First and second-order nuclear quadrupolar interactions of S are included in the Hamiltonian. We consider an axially-symmetric quadrupolar interaction (asymmetry parameter, $\eta_Q = 0$) with Z axis of PAF of the quadrupolar tensor described by polar angles β_Q and γ_Q with respect to the rotor-frame coordinate system. The internuclear $I-S$ vector, $\boldsymbol{r}_{IS}$, is characterized by polar angles β_D and γ_D in the rotor frame. The angle between the Z principal axis of the quadrupolar tensor and internuclear $I-S$ vector is denoted by θ_{QD}.

The Hamiltonian of the system can be written as

$$\mathcal{H}(t) = \omega_{1I}I_X + \omega_{1S}S_X + \Delta\omega_Q(\beta_Q)S_Z + \omega_Q(t,\beta_Q,\gamma_Q)[3S_Z^2 - S(S+1)] + d(t,\beta_D,\gamma_D)2I_ZS_Z. \quad [2.7]$$

where $\omega_Q(t,\beta_Q,\gamma_Q)$ is the first-order quadrupolar frequency, $\Delta\omega_Q(\beta_Q)$ is the MAS-averaged second-order quadrupolar interaction, and $d(t,\beta_D,\gamma_D)$ is the dipolar coupling. Both ω_Q and $\Delta\omega_Q$ depends on quadrupolar coupling constant $C_Q = e^2Qq/\hbar$, where eQ is the quadrupole moment and eq is the principal component V_{ZZ} of electric field gradient tensor in the PAF. The second order quadrupolar interaction corresponds to a Larmor frequency of 43.36 MHz (^{1}H 600 MHz). The dipolar interaction is characterized by dipolar coupling, $\omega_D = -\mu_o\gamma_I\gamma_S\hbar/4\pi r_{IS}^3$, where γ_I and γ_S are gyromagnetic ratios of I and S. The expressions of these frequencies are provided in Appendix A2.1. When $\theta_{QD} = 0$, a common set of polar angles, β and γ, is used to characterize both quadrupolar and dipolar interactions. In numerical estimations, instead of angular frequency quantities, we utilize their frequency analogues, e.g. ν_{1S}, ν_R, ν_D.

In order to derive preliminary insight on ^{1}H-^{14}N CPMAS and double CP spin dynamics, numerical simulations were performed focusing on the dependence of CPMAS and double CP signals on crystallite orientation. With the propagator computed numerically according to Eq. [2.4], the density operator is evaluated at multiples of rotor period $T_R = 2\pi/\omega_R$. We have divided T_R into 500 discrete steps giving $\Delta t = T_R/500$ which ensured numerical convergence for our problem. For double CP experiments, a filtration of the density operator at the end of the first CP block is performed keeping only S_X or S_Y terms in order to mimic phase cycling. The parameters employed are similar to the experimental values utilized in Ref. [17] and are given in Figure 2.2.

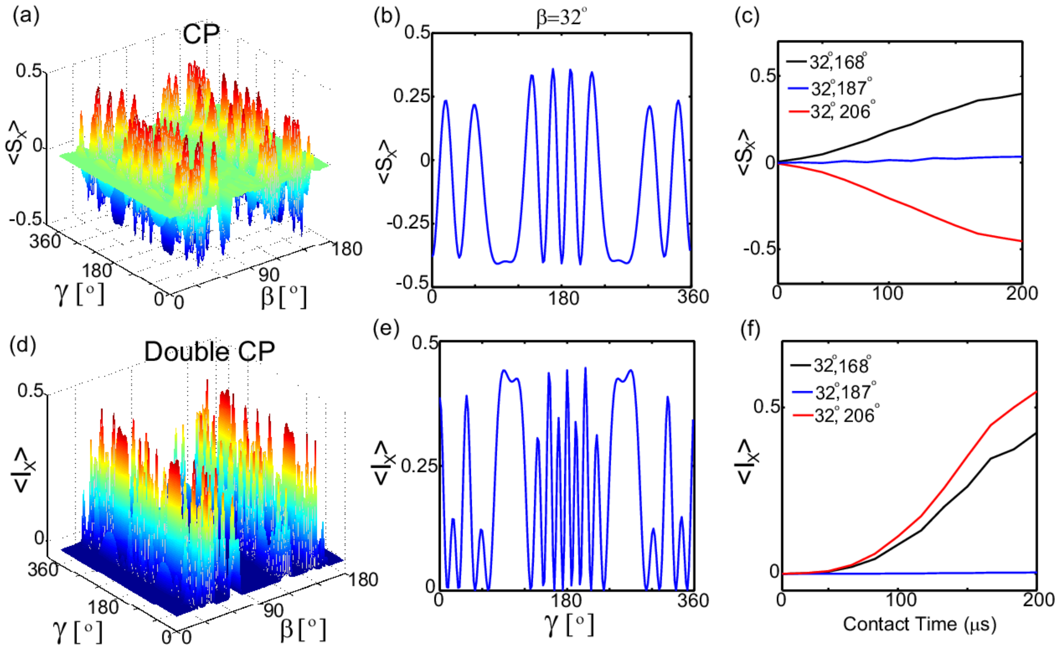

Figure 2.2 Brute force simulations showing (a) dependence of the CPMAS signal on crystallite orientation, (b) a slice of (a) displaying the dependence of CPMAS signal on γ for $\beta = 32^\circ$, (c) CPMAS signal buildup as function of time for 3 selected γ angles and $\beta = 32^\circ$. Brute force simulations showing (d) dependence of double CP signal on crystallite orientation, (e) a slice of (d) displaying the dependence of double CP signal on γ for $\beta = 32^\circ$, (f) double CP signal buildup as function of time for 3 selected γ angles and $\beta = 32^\circ$. Parameters employed are: $\nu_{1S} = 80\ kHz$, $\nu_{1I} = 46\ kHz$, $\nu_R = 60\ kHz$, $C_Q/2\pi = 1.5\ MHz$, $\eta_Q = 0$, $\nu_D = 10\ kHz$, $\theta_{QD} = 0$. For (a), (b), (d), (e) the contact time is 10 rotor periods. For (c) and (f), the CPMAS and double CP signals are calculated in steps of T_R up to $12T_R$.

The output of numerical simulations carried out for a CPMAS experiment at a spinning speed of 60 kHz is presented in Figure 2.2(a-c). From Figure 2.2(a) it can be seen that CP transfer occurs only for certain β-angle regions and $\langle S_X \rangle$ may be parallel or anti-parallel to the direction of the ^{14}N RF field depending on β and γ. For a given β, $\langle S_X \rangle$ has positive or negative values depending on γ resulting in destructive addition of CPMAS signals in a powder. The output of numerical simulations performed for a double CP experiment under similar conditions is presented in Figure 2.2(d-f). As before, the transfer occurs selectively for the same β-angle regions, however signals arising from different orientations have the same sign and hence add constructively in a powder. This addition may result in good transfer efficiency for double CP experiments, in contrast to CPMAS experiment. These features were predicted by Gan and co-workers.[132]

It is instructive to consider the CPMAS transfer in the absence of quadrupolar interaction, where polarization transfer occurs at the usual Hartmann-Hahn conditions, $|\nu_{1I}| \pm |\nu_{1S}| = n\nu_R$. In this case, it can be shown analytically that CPMAS signal is independent of γ, has smooth variation with respect to β, and the sign of the signal is independent of crystallite orientation. By applying one of the general bounds on polarization transfer introduced in Ref. [134], the smallest upper bound is found to be 0.5 for our system, a value which can also be obtained explicitly within AHT. The CPMAS signal, as a function of β and γ, is shown in Appendix A2.2. The maximum signal achieved (Appendix A2.2) is very close to 0.5.

2.3.2 Structure of the effective Hamiltonian

In this sub-section, numerical effective Hamiltonians are calculated with the logarithm and Floquet approaches and their structure is discussed. In order to facilitate interpretation, the effective Hamiltonians are expanded in terms of a set of Hermitian spin operators, O_p, which form a basis for the linear space of all 6×6 matrices. We choose to use a hybrid basis involving Hermitian linear combinations of spherical tensor operators.[95] This basis contains pure I operators, I_X, I_Y, I_Z, pure S operators, S_X, S_Y, S_Z, $S_XS_Z + S_ZS_X$, $S_YS_Z + S_ZS_Y$, $(3S_Z^2 - 2)$, $(S_+^2 + S_-^2)/2$, $(S_+^2 - S_-^2)/2i$, and IS terms like I_ZS_Z, $(S_YS_Z + S_ZS_Y)I_X$, etc. The matrix representations of these spin operators are provided in Appendix A 2.3. The coefficient ω_p^{eff} of a given operator O_p is calculated as $\omega_p^{eff} = \mathrm{Tr}\{\mathcal{H}_{eff}O_p\}/\mathrm{Tr}\{O_p^2\}$. Table 2.1 provides the labeling of ω_p^{eff} coefficients corresponding to different spin. The coefficients $\nu_p^{eff} = \omega_p^{eff}/2\pi$ are expressed in kHz wherever plotted.

	Spin operator	ω_p^{eff}	Spin operator	ω_p^{eff}
I terms	I_X, I_Y, I_Z	$\omega_{1I}^{eff}, \omega_{IY}^{eff}\ \omega_{IZ}^{eff}$		
S terms	S_X, S_Y, S_Z	$\omega_{1S}^{eff}, \omega_{SY}^{eff}\ \omega_{SZ}^{eff}$	$3S_Z^2 - 2$	ω_{SZ2}^{eff}
	$S_XS_Z + S_ZS_X$	ω_{SXZ}^{eff}	$(S_+^2 + S_-^2)/2$	ω_{SDQX}^{eff}
	$S_YS_Z + S_ZS_Y$	ω_{SYZ}^{eff}	$(S_+^2 - S_-^2)/2i$	ω_{SDQY}^{eff}
IS terms	$S_XI_{X,}S_XI_Y$, etc.	$\omega_{SXIX}^{eff}, \omega_{SXIY}^{eff}$, etc.	$(3S_Z^2 - 2)I_X$, etc	ω_{SZ2IX}^{eff}, etc.
	$(S_XS_Z + S_ZS_X)I_X$, etc.	ω_{SXZIX}^{eff}, etc.	$(S_YS_Z + S_ZS_Y)I_X$, etc.	ω_{SYZIX}^{eff}, etc.
	$I_X(S_+^2 + S_-^2)/2$, etc.	ω_{SDQXIX}^{eff}	$I_X(S_+^2 - S_-^2)/2i$, etc.	ω_{SDQYIX}^{eff}

Table 2.1 Spin-operators and the labelling of the corresponding coefficients, ω_p^{eff}.

To understand the appearance of various terms in the effective Hamiltonian, simulations were performed under three conditions.

Case 1: $\nu_{1S} = 80$ kHz, $\nu_{1I} = 0$, and $\nu_D = 0$. Pure S-spin coefficients, determined as a function of γ, are presented in Figure 2.3. Since $\nu_D = 0$, IS terms are absent, as expected. The coefficients determined by both methods (shown by solid and dashed lines) are identical within numerical errors. The main observations from Figure 2.3 are: (a) ν_{1S}^{eff} ($1S$) strongly depends on the γ angle and changes sign several times, (b) ν_{1S}^{eff} and the coefficient of $S_Y S_Z + S_Z S_Y$ (SYZ) are comparable, and (c) the coefficients ν_{SZ2}^{eff}, ν_{SDQX}^{eff} of $3S_Z^2 - 2$ and $(S_+^2 + S_-^2)/2$ are almost identical. It was shown for deuterium[86] that $\nu_{SZ2}^{eff} = \nu_{SDQX}^{eff}$ holds *exactly*, provided no S_Z term is present in the time-dependent Hamiltonian. With ^{14}N, due to second-order quadrupolar interaction, presence of $\Delta\omega_Q S_Z$ in the time-dependent Hamiltonian also leads to coefficients of $(S_+^2 - S_-^2)/2i$ and $S_X S_Z + S_Z S_X$, with smaller magnitude.

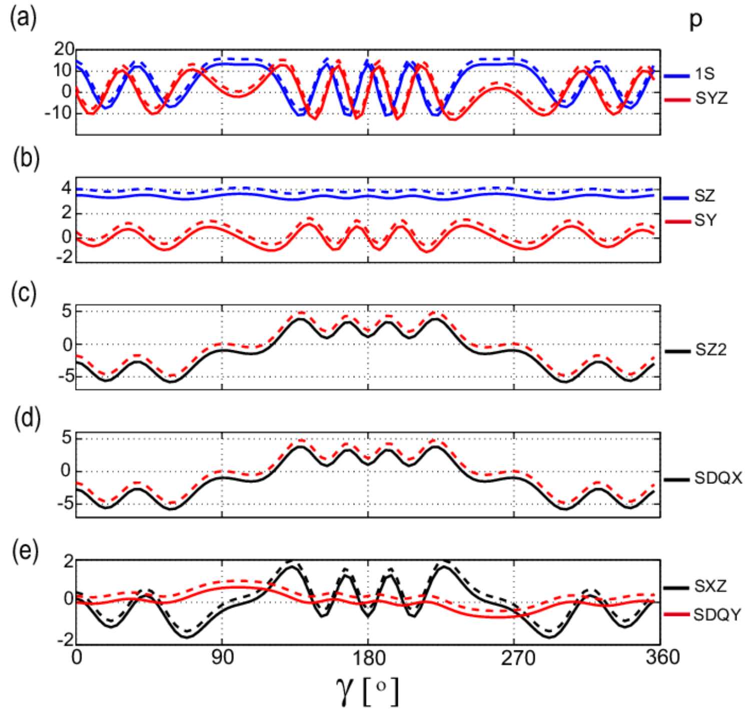

Figure 2.3 (a-e) Dependence of ν_p^{eff} coefficients on γ, calculated with Floquet theory (solid line) and the logarithm method (dashed line). For visibility the plots with dashed line are shifted vertically. Labeling of the coefficients is given in Table 2.1. The calculation assumes $\nu_D = 0\ kHz$ hence IS terms are not expected. Other parameters are: $\beta = 32^\circ$, $\nu_{1S} = 80\ kHz$, $\nu_{1I} = 0\ kHz$, $\nu_R = 60\ kHz$, $C_Q/2\pi = 1.5\ MHz$, $\eta_Q = 0$, and a contact time of 10 rotor periods. The dimension of the truncated Floquet Hamiltonian was set to 151 for all calculations. The coefficients ν_p^{eff} are expressed in kHz.

Case 2: $\nu_{1S} = 80$ kHz, $\nu_{1I} = 46$ kHz, and $\nu_D = 0$. It was again found (Appendix A2.4) that logarithm and Floquet effective Hamiltonians are identical within numerical errors and yield $\langle S_X \rangle = 0$ at multiples of the rotor period, as expected. However, $\mathcal{H}_{eff}$ contains a few large *IS* terms, a fact which is rather unexpected since $\nu_D = 0$. Though the presence of these *IS* terms is inconvenient, the effective Hamiltonian predicts correctly the evolution of density operator at multiples of the rotor period. However, it is convenient to find a procedure to remove them in order to simply further discussion. Below we discuss two procedures to achieve this.

With first procedure, we found that an effective Hamiltonian with no IS terms can be produced through a conventional rotating frame transformation according to

$$U(t,0) = \exp(-i\omega_R t I_X)\, \widetilde{U}(t,0). \qquad [2.8]$$

The Hamiltonian driving the new propagator, $\widetilde{U}(t,0)$, is

$$\widetilde{\mathcal{H}}(t) = (\omega_{1I} - \omega_R)I_X + \Delta\omega_Q(\beta_Q)S_Z + \omega_{1S}S_X + \omega_Q(t,\beta_Q,\gamma_Q)[3S_Z^2 - S(S+1)]$$

$$+ 2d(t,\beta_D,\gamma_D)S_Z \exp(+i\omega_R t I_X)\, I_Z \exp(-i\omega_R t I_X). \qquad [2.9]$$

With the newly defined $\widetilde{\mathcal{H}}(t)$, both $\widetilde{\mathcal{H}}_{eff}^{ln}$ and $\widetilde{\mathcal{H}}_{eff}^{\mathcal{F}}$ were computed and were found to be identical, and moreover *IS* terms are removed (Appendix A2.4). We note that a similar transformation has been utilized by Ernst and coworkers in order to remove ambiguity of the effective Hamiltonian obtained by logarithm method.[67] Taking into account the $(-\omega_R/2, \omega_R/2]$ eigenvalue constraint and that $U(T,0) = -\widetilde{U}(T,0)$, it is shown in Appendix A2.5 that $\widetilde{\mathcal{H}}_{eff}$ and $\mathcal{H}_{eff}$ are related by $\widetilde{\mathcal{H}}_{eff} = \sum_{\epsilon_j>0}(\epsilon_j - \omega_R/2)|\epsilon_j\rangle\langle\epsilon_j| + \sum_{\epsilon_j<0}(\epsilon_j + \omega_R/2)|\epsilon_j\rangle\langle\epsilon_j|$,

where ϵ_j and $|\epsilon_j\rangle$ are eigenvalues and eigenvectors of $\mathcal{H}_{eff}$.

From here a second procedure to remove IS terms suggests itself as follows. From the Floquet effective Hamiltonian in the old rotating frame, $\mathcal{H}_{eff}^{\mathcal{F}} = D\Lambda_0 D^{-1}$, we can obtain the Floquet effective Hamiltonian $\widetilde{\mathcal{H}}_{eff}^{\mathcal{F}}$ as

$$\widetilde{\mathcal{H}}_{eff}^{\mathcal{F}} = D\widetilde{\Lambda}_0 D^{-1},$$

where $\widetilde{\Lambda}_0$ is a new diagonal matrix, with elements

$$\tilde{\epsilon}_j = \begin{cases} \epsilon_j - \omega_R/2\,, \text{if } \epsilon_j > 0 \\ \epsilon_j + \omega_R/2\,, \text{if } \epsilon_j < 0 \end{cases} \qquad [2.10]$$

This *simple rearrangement* of the eigenvalues of the effective Hamiltonian in the old rotating frame leads directly to the effective Hamiltonian obtained in the new rotating frame. The connection between the two procedures is discussed in Appendix A2.5. It would be interesting to investigate whether this shifting procedure can be extended to more general frame transformations.

In the old rotating frame, when dipolar interaction is turned off or when one is away from any CP match condition, it is shown in Appendix A2.6 that IS terms are present in the effective Hamiltonian even in the absence of the quadrupolar interaction. However, if $S = 1/2$, it can be shown (Appendix A2.6) that no IS terms are present. Obviously, whether employment of a rotating frame transformation or rearrangement of eigenvalues is needed or not, depends on the spin system and the magnitudes of the external and internal interactions.

Case 3: After removing the IS terms through the transformation of Eq. [2.8], simulations were performed starting from Eq. [2.9] with $\nu_{1S} = 80$ kHz, $\nu_{1I} = 46$ kHz, and $\nu_D = 10$ kHz. The effective Hamiltonians $\widetilde{\mathcal{H}}_{eff}^{ln}$, and $\widetilde{\mathcal{H}}_{eff}^{\mathcal{F}}$ were again found to be identical within numerical errors. A few pure S, pure I, and IS ν_p^{eff} coefficients extracted from $\widetilde{\mathcal{H}}_{eff}^{ln}$ are show in Figure 2.4.

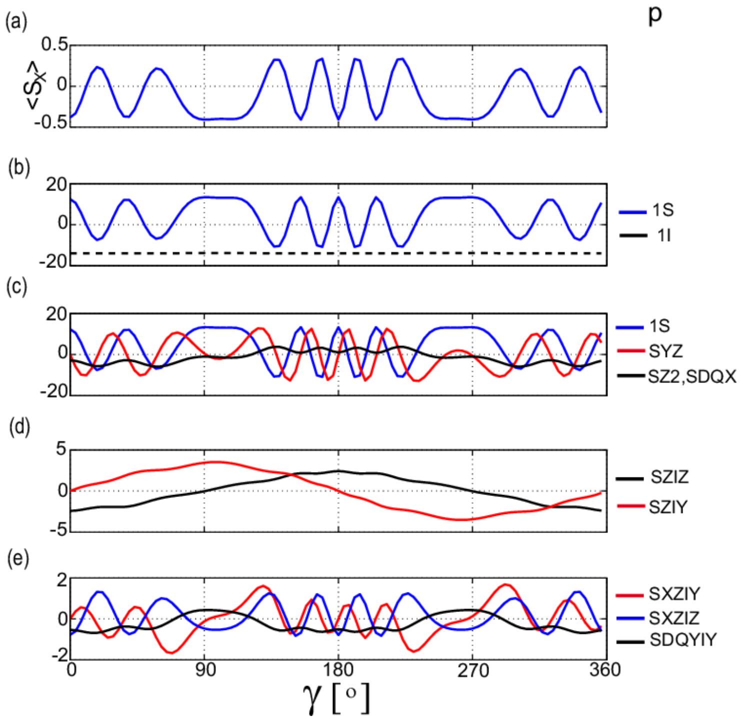

Figure 2.4 Dependence on γ of (a) CPMAS signal and of (b-e) ν_p^{eff} coefficients. Calculations start with the Hamiltonian of Eq. [2.9] and assume $\nu_D = 10\ kHz$, $\beta = 32^{\circ}$, $\nu_{1S} = 80\ kHz$, $\nu_{1I} = 46\ kHz$, $\nu_R = 60\ kHz$, $C_Q/2\pi = 1.5\ MHz$, $\eta_Q = 0$, $\theta_{QD} = 0$ and $\tau_{CP} = 10T_R$. Labeling of the coefficients is given in Table 2.1. The coefficients ν_p^{eff} are expressed in kHz.

The main features derived from Figure 2.4(a,b) are as follows. (i) Good CP transfer occurs for those γ angles for which $|\nu_{1I}^{eff}| \cong |\nu_{1S}^{eff}| \cong max|\nu_{1S}^{eff}|$, where $max|\nu_{1S}^{eff}|$ represents maximum value of the magnitude of ν_{1S}^{eff} for the given β, and $\nu_{1I}^{eff} \cong \nu_{1I} - \nu_R$, corresponds to the I_X term in Eq. [2.9]. (ii) Sign of the ^{14}N signal follows the sign of ν_{1S}^{eff}. Additional simulations (Appendix A2.7) show that a significant overall drop in signal occurs when the proton RF strength is varied such that $|\nu_{1I}^{eff}|$ becomes smaller than $max|\nu_{1S}^{eff}|$.

Detailed examination of the effective Hamiltonian reveals additional features of the CP transfer as shown in Figure 2.5, in which ν_p^{eff} coefficients of all pure S terms along with the CP signal are plotted.

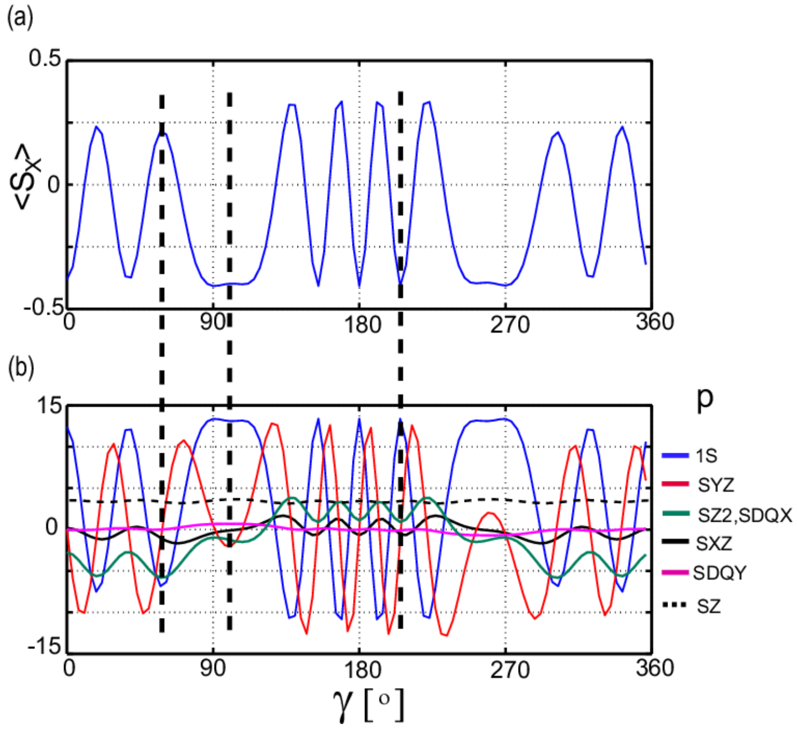

Figure 2.5 Dependence on γ *of (a) CPMAS signal and of (b) pure* S ν_p^{eff} *coefficients. Calculations start with the Hamiltonian of Eq. [2.9]. The calculation assumes* $\nu_D = 10\,kHz$, $\beta = 32^{\circ}$, $\nu_{1S} = 80\,kHz$, $\nu_{1I} = 46\,kHz$, $\nu_R = 60\,kHz$, $C_Q/2\pi = 1.5\,MHz$, $\eta_Q = 0$, $\theta_{QD} = 0$. *The contact time is 10 rotor periods. Labeling of the coefficients is given in Table 2.1. Vertical lines correspond to three gamma angles for which good CP transfer occurs. The coefficients* ν_p^{eff} *are expressed in kHz.*

From Figure 2.5(b), we note that, (iii) at γ angles for which $|\nu_{1S}^{eff}| \cong max|\nu_{1S}^{eff}|$ the coefficients of all pure S terms are small in the effective Hamiltonian except for ν_{1S}^{eff} and ν_{SZ}^{eff}. Combining this with observation (a) we arrive at a simple picture: when $|\nu_{1I}^{eff}| \cong |\nu_{1S}^{eff}| \cong max|\nu_{1S}^{eff}|$, the effective Hamiltonian is approximately

$$\widetilde{\mathcal{H}}_{eff} = \omega_{SZ}^{eff} S_Z + \omega_{1S}^{eff} S_X + \omega_{1I}^{eff} I_X + \widetilde{\mathcal{H}}_{eff}^{IS}, \qquad [2.11]$$

where $\widetilde{\mathcal{H}}_{eff}^{IS}$ represents IS terms. Such a Hamiltonian ensures an efficient CP transfer via $\widetilde{\mathcal{H}}_{eff}^{IS}$ under a static-like CP matching condition, $\left|\nu_{1I}^{eff}\right| \cong \left|\nu_{1S}^{eff}\right|$. The effect of S_Z term is to modify ω_{1S}^{eff} to $\sqrt{\left(\omega_{1S}^{eff}\right)^2 + \left(\omega_{SZ}^{eff}\right)^2}$ and tilt the quantization axis. For the parameters used here, for good CP transfer, the tilt angle and the change in the effective RF field are small (about 15° and 0.5 kHz), hence the S_Z term is omitted for a qualitative discussion below. With this approximation, when $\omega_{1S}^{eff} \cong \pm\,\omega_{1I}^{eff}$, two pairs of eigenvalues of $\omega_{1S}^{eff} S_X + \omega_{1I}^{eff} I_X$ are sufficiently close to each other such that IS terms in Eq. [2.11] can mix the corresponding eigenstates, ultimately resulting in polarization transfer between I and S spins. Assuming $\omega_{1I}^{eff} < 0$ and $\omega_{1S}^{eff} > 0$, the eigenstates involved in CPMAS transfer are $\{|1/2,1\rangle_X, |-1/2\,,0\rangle_X\}$ and $\{|1/2\,,0\rangle_X, |-1/2\,,-1\rangle_X\}$, where the subscript X indicates that they are eigenstates of I_X and S_X. For RF strengths and spinning speed considered here, $\omega_{1I}^{eff} \cong \omega_{1I} - \omega_R < 0$, and hence we recover the CPMAS matching condition, $\left|\omega_{1S}^{eff}\right| + \omega_{1I} \cong \omega_R$.

A smaller magnitude of CPMAS signal is always associated with the presence of larger S terms, other than ω_{1S}^{eff} as seen from Figure 2.5(a,b). For these γ angles the effective Hamiltonian is

$$\widetilde{\mathcal{H}}_{eff} = \omega_{1S}^{eff} S_X + \omega_{1I}^{eff} I_X + OPS + \widetilde{\mathcal{H}}_{eff}^{IS} = \widetilde{\mathcal{H}}_{eff}^{S} + \widetilde{\mathcal{H}}_{eff}^{I} + \widetilde{\mathcal{H}}_{eff}^{IS}, \qquad [2.12]$$

where OPS represents all other pure S terms. The larger S terms, besides altering the eigenvalues, mix the $|m_S\rangle_X$ spin states, resulting in less efficiency of the standard $I_X \rightarrow S_X$ CP transfer. It follows that for these γ angles change in ν_{1I} does not lead to significant CP transfer. However, mixing may lead to transfer from I_X to other coherences such as double-quantum S-spin coherences, etc., which are not detected in a CPMAS experiment but can be detected in a double CP experiment.

So far, the connection between CP dynamics and structure of the effective Hamiltonian has been discussed as a function of γ for a particular β angle. Below we investigate the relationship between CP transfer and the effective RF strengths as function of both β and γ. For better visualization, we define a parameter $\Delta = -\left|\left|\nu_{1I}^{eff}\right| - \left|\nu_{1S}^{eff}\right|\right|$ which indicates the deviation from the CP matching condition. Figure 2.6 shows the magnitude of CPMAS signal and Δ as function of β and γ. Although dependence of Δ on β and γ is complex, the correspondence between $|\langle S_X \rangle|$ and Δ is rather obvious.

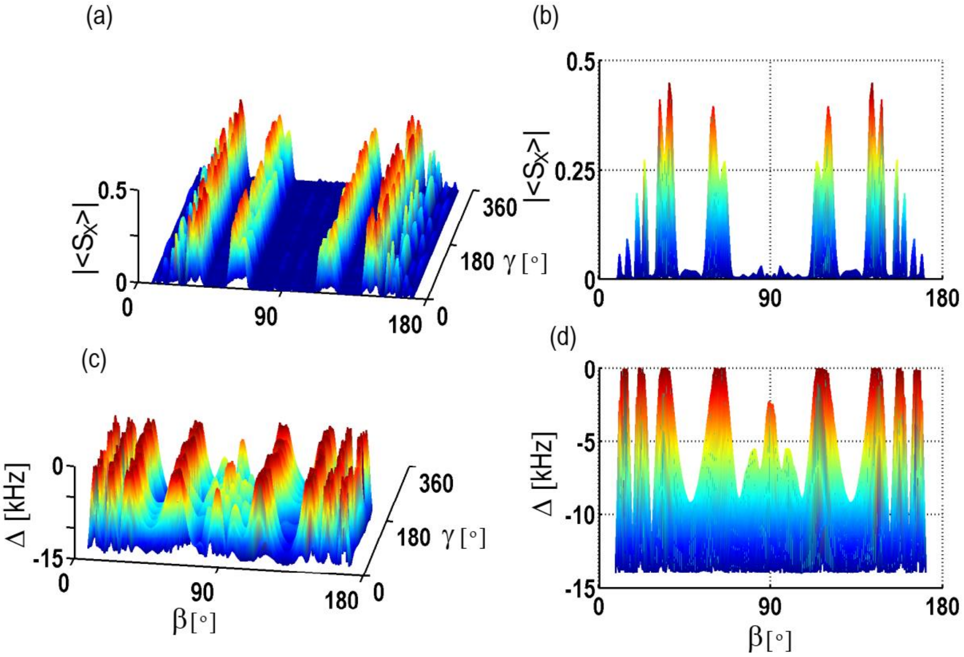

Figure 2.6 (a) Dependence of magnitude of CPMAS signal on β and γ. (b) Projection of (a) along γ. (c) Dependence on β and γ of the Δ parameter which reflects the difference between $\left|\nu_{1S}^{eff}\right|$ and $\left|\nu_{1I}^{eff}\right|$. (d) Projection of (c) along γ. Calculations start with the Hamiltonian of Eq. [2.9] and assume $\nu_D = 10\ kHz, \nu_{1S} = 80\ kHz,\ \nu_{1I} = 46\ kHz,\ \nu_R = 60\ kHz,\ C_Q/2\pi = 1.5\ MHz,\ \eta_Q = 0,\ \theta_{QD} = 0,$ and $\tau_{CP} = 10T_R$. β ranges for which signal is significant are {10^{o}-26^{o}}, {30^{o}-40^{o}}, {55^{o}-70^{o}}, and their mirror ranges in the {90^{o}-180^{o}} interval.

As seen from Figure 2.6(a,b), a reasonable CPMAS signal occurs for β belonging to certain ranges (ranges listed in figure caption). Figure 2.6(c,d) shows that good (poor) CP transfer occurs for small (large) $|\Delta|$. Since $\theta_{QD} = 0$, for β around $0, 90, \mathrm{and} 180^\circ$ CP transfer is poor because the dipolar term oscillating at ν_R vanishes. The dependence of Δ on β and γ implies dependence of $max\left|\nu_{1S}^{eff}\right|$ on β, therefore only those β regions for which $max\left|\nu_{1S}^{eff}\right| \cong \left|\nu_{1I}^{eff}\right|$ contribute significantly to signal. Accordingly, variation of ν_{1I} should be accompanied by changes in both position and width of the β regions contributing to the signal.

All calculations and resulting conclusions so far correspond to a particular choice of RF strengths for which $\nu_{1I} + \left|\nu_{1S}^{eff}\right| \cong \nu_R$, a choice which yields good overall CP transfer in simulations and is also close to the optimized conditions employed in the experiments of Ref. [17]. Following the same reasoning, other matching conditions can be predicted, for example $\nu_{1I} - \left|\nu_{1S}^{eff}\right| \cong \nu_R$, or other conditions employing multiples of spinning frequency or involving other ^{14}N RF strengths. Some of these matching conditions are illustrated in Appendix A2.8.

Following Ref. [132] where a linear ramp was applied to the ^{1}H RF field, we compare CP transfer with and without ramp as function of crystallite orientation. Figure 2.7 shows CPMAS signals projected along γ, obtained (a) without and (b) with a ± 3% linear ramp of the proton RF amplitude, with $\tau_{CP} = 20T_R$. It is evident that with ramp significant CP transfer occurs for more crystallite orientations hence sensitivity is expected to increase.

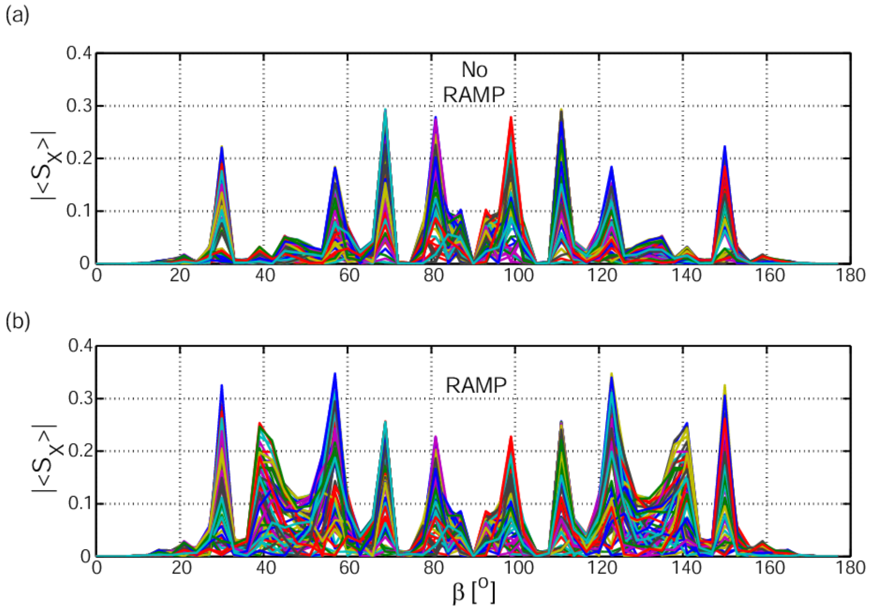

Figure 2.7 Dependence on β and γ of CPMAS signal, (a) without and (b) with a ±3% linear ramp of ^{1}H RF amplitude. Projection along γ direction is displayed. Calculations start with the Hamiltonian of Eq. [2.9] and assume $\nu_D = 10\ kHz$, $\nu_{1S} = 80\ kHz$, $\nu_{1I} = 50\ kHz$, $\nu_R = 60\ kHz$, $C_Q/2\pi = 1.5\ MHz$, $\eta_Q = 0$, $\theta_{QD} = 0$ and $\tau_{CP} = 20T_R$.

Straightforward application of the matrix logarithm in this case is not useful since the eigenvalues of the effective Hamiltonian are now confined to $(-\omega_R/40, +\omega_R/40] = (-1.5\text{ kHz}, +1.5\text{ kHz}]$ interval. With such small interval all ω_p coefficients in the effective Hamiltonian are of comparable magnitude and a simple analysis is not possible. In order to derive an interpretable effective Hamiltonian for $\tau_{CP} = NT_R$, the propagator is calculated for each rotor period during CP and the corresponding effective Hamiltonian is calculated with the matrix logarithm approach. Denoting by $\mathcal{H}_{eff}^k$ the effective Hamiltonian of kth rotor period, the total propagator is

$$U(NT_R, 0) = \prod_k exp(-i\mathcal{H}_{eff}^k T_R). \qquad [2.13]$$

Since $[\mathcal{H}_{eff}^k, \mathcal{H}_{eff}^m] \neq 0$, we construct the effective Hamiltonian for the whole CP process, $\mathcal{H}_{eff}$, by utilizing Baker-Campbell-Hausdorff (BCH)[56] equation. If we retain only the first two terms, we obtain

$$\mathcal{H}_{eff} \cong \frac{1}{N}\sum_{k=1}^{N}\mathcal{H}_{eff}^{k} - \frac{i}{NT_R}\sum_{k>m}\left[\mathcal{H}_{eff}^{k}, \mathcal{H}_{eff}^{m}\right]. \quad [2.14]$$

Comparison of CPMAS signals calculated with $U(NT_R, 0)$ and with $exp(-i\mathcal{H}_{eff}NT_R)$ shows (Appendix A2.9) that Eq. [2.14] is quite accurate for the relatively short contact time and mild slope of the ramp employed**.** For longer contact times and/or steeper slope higher order terms have to be added in Eq. [2.14]. Comparison of ω_p coefficients (Appendix A2.9) reveals that (a) pure *S* terms with and without ramp are identical, and (b) *IS* terms are generally larger with the ramp. The larger *IS* terms broaden the matching conditions, resulting in CP transfer for more crystallite orientations. As of now we do not have an analytical proof for (a).

2.4 Sign of the double CP signal

We have seen that the sign of CPMAS signal strongly depends on β and γ while sign of signal in the double CP experiment is invariant. This difference can be rationalized as follows. Double CP experiments involve two CP transfers,

$$I_X \to A_{IS}S_X + \text{other coherences} \xrightarrow{phase\ cycle} A_{IS}S_X \to A_{IS}A_{SI}I_X + \text{other coherences}. \quad [2.15]$$

where A_{IS} and A_{SI} are CP transfer amplitudes for the $I \to S$ and $S \to I$ processes, respectively. Since $\mathcal{H}_{eff}$ is the same in both CP processes, we conjecture that there exist a correlation between the signs of A_{IS} and A_{SI} which leads to invariance of the sign of double CP signal. We prove below that such a correlation exists and moreover $A_{IS} = 3A_{SI}/8$.

For convenience, the effective Hamiltonian of Eq. [2.12] is expressed in the tilted frame in which *I* and *S* spin operators are rotated by 90° around Y axis. In this frame,

$$\mathcal{H}_{eff} = \mathcal{H}_{eff}^{S} + \omega_{1I}^{eff}I_Z + \mathcal{H}_{eff}^{IS}, \quad [2.16]$$

To avoid cumbersome notation, we keep the label $'eff'$ only in $\omega_{1I}^{eff}I_Z$ and omit it in $\mathcal{H}_{eff}$, $\mathcal{H}_{eff}^{S}$, $\mathcal{H}_{eff}^{IS}$. The effective Hamiltonian $\mathcal{H}^S$ can be diagonalized as

$$\mathcal{H}^S = D\omega_S S_Z D^\dagger \quad [2.17]$$

$\mathcal{H}^S$, ω_S, and the diagonalization matrix *D* strongly depend on crystallite orientation and when *OPS* terms are negligible $\omega_S \cong \omega_{1S}^{eff}$. In principle, the diagonalized Hamiltonian may also contain an $\omega_{Z2}(3S_Z^2 - 2)$ term. If S_Z term is not present in the time-dependent Hamiltonian, Eq. [2.7], it can be shown rigorously that $\omega_{Z2} = 0$.[86] Due to the ^{14}N second-order quadrupolar shift, $\omega_{Z2} \neq 0$ and for the parameters considered here, ω_{Z2} is below 1 kHz. Inclusion of this term in Eq. [2.17] will not affect the proof presented below, hence we omit this term for simplicity. The total effective Hamiltonian can be rewritten as $\mathcal{H} = D\mathcal{H}'D^{\dagger}$ where

$$\mathcal{H}' = \omega_S S_Z + \omega_{1I}^{eff} I_Z + \mathcal{H}'_{IS}, \tag{2.18}$$

and $\mathcal{H}'_{IS} = D^{\dagger}\mathcal{H}^{IS}D$.

Taking into account that D commutes with I_Z, the transfer amplitude A_{IS} after CP contact nT_R is

$$A_{IS} = \mathrm{Tr}\{UI_Z U^{\dagger} S_Z\}/\mathrm{Tr}\{S_Z^2\} = \frac{1}{4}\mathrm{Tr}\{VI_Z V^{\dagger} D^{\dagger} S_Z D\}. \tag{2.19}$$

where $V = \exp(-i\mathcal{H}' nT_R)$ and $U = DVD^{\dagger}$. In order to obtain A_{IS}, we need to evaluate $VI_Z V^{\dagger}$ and hence the influence of $\mathcal{H}'_{IS}$ shall be taken into account. Due to the complicated structure of D, $\mathcal{H}'_{IS}$ may have off-diagonal matrix elements practically between any pair of eigenstates, $|m_I, m_S\rangle$ and $|m_I{}', m_S{}'\rangle$, of $\omega_S S_Z + \omega_{1I}^{eff} I_Z$. From Figure 2.4 we estimate that matrix elements $\mathcal{H}^{IS}(\mathcal{H}'_{IS})$ are of the order of 2 kHz or below hence considerably smaller than ω_{1I}^{eff}. If (a) $\omega_{1I}^{eff} > 0$, (b) ω_S is comparable to ω_{1I}^{eff}, and (c) matrix elements of $\mathcal{H}'_{IS}$ are smaller than ω_{1I}^{eff}, the eigenstates which may be significantly mixed are $|2\rangle \equiv |-1/2, 1\rangle$, $|3\rangle \equiv |1/2, 0\rangle$ and $|4\rangle \equiv |-1/2, 0\rangle$, $|5\rangle \equiv |1/2, -1\rangle$. The Hamiltonian $\mathcal{H}'$ is then approximately the sum of commuting terms each acting only in the (1,6), (2,3), and (4,5) subspaces, where $|1\rangle \equiv |1/2, 1\rangle$ and $|6\rangle \equiv |-1/2, -1\rangle$. Henceforth, we utilize fictitious spin-1/2 operators,[52] X_{pq}, Y_{pq}, Z_{pq}, to describe Hamiltonians, propagators, and density operators, where

$$Z_{pq} = \frac{1}{2}[|p\rangle\langle p| - |q\rangle\langle q|],\ X_{pq} = \frac{1}{2}[|p\rangle\langle q| + |q\rangle\langle p|],\ Y_{pq} = \frac{1}{2i}[|p\rangle\langle q| - |q\rangle\langle p|],$$

and $|p\rangle$ or $|q\rangle$ are any two states of the basis. It is shown in Appendix A2.10 that

$$\begin{aligned} VI_Z V^{\dagger} = {} & Z_{16} - Z_{23}[\cos^2\phi_Y^{23}\, cos(\Omega_{23} nT_R) + \sin^2\phi_Y^{23}] \\ & - Z_{45}[\cos^2\phi_Y^{45}\, cos(\Omega_{45} nT_R) + \sin^2\phi_Y^{45}] + \mathrm{A}_{23} + A_{45}, \end{aligned} \tag{2.20}$$

where angles $\phi_Z^{23}, \phi_Y^{23}, \phi_Z^{45}, \phi_Y^{45}$, and angular frequencies Ω_{23}, Ω_{45} depend on $\omega_S - \omega_{1I}^{eff}$ and on matrix elements of $\mathcal{H}'_{IS}$ in the corresponding subspaces. The terms A_{23} and A_{45} contain X_{23}, Y_{23} and X_{45}, Y_{45} operators respectively and depend on time as $\sin(\Omega_{23} nT_R)$ or $\cos(\Omega_{23} nT_R)$, etc. Since D acts only on the S part of the basis states, $D^{\dagger} S_Z D$ does not contain

X_{23}, Y_{23} or X_{45}, Y_{45} terms. Therefore, A_{23} and A_{45} terms *do not contribute* to the trace in Eq. [2.19] and hence

$$A_{IS} = \frac{1}{4}\mathrm{Tr}\Big\{\Big[Z_{16} - Z_{23}[\cos^2\phi_Y^{23}\, cos(\Omega_{23}nT_R) + \sin^2\phi_Y^{23}] \\ - Z_{45}[\cos^2\phi_Y^{45}\, cos(\Omega_{45}nT_R) + \sin^2\phi_Y^{45}]\Big]D^\dagger S_Z D\Big\}. \quad [2.21]$$

After some rearrangement, the inverse transfer amplitude A_{SI} for the same contact time nT_R can be expressed as

$$A_{SI} = \mathrm{Tr}\{US_ZU^\dagger I_Z\}/\mathrm{Tr}\{I_Z^2\} = \tfrac{2}{3}\mathrm{Tr}\{V^\dagger I_Z V D^\dagger S_Z D\}. \quad [2.22]$$

Since $V^+ = e^{+i\mathcal{H}'nT_R} = e^{-i\mathcal{H}'(-nT_R)}$, we infer from Eq. [2.20] that

$$V^+ I_Z V = Z_{16} - Z_{23}[\cos^2\phi_Y^{23}\, cos(\Omega_{23}nT_R) + \sin^2\phi_Y^{23}] \\ -Z_{45}[\cos^2\phi_Y^{45}\, cos(\Omega_{45}nT_R) + \sin^2\phi_Y^{45}] + B_{23} + B_{45},$$

where the term $B_{23} + B_{45}$ can be obtained by substituiting $\Omega_{23}nT_R \to -\Omega_{23}nT_R$ and $\Omega_{45}nT_R \to -\Omega_{45}nT_R$ in $A_{23} + A_{45}$. However, since $B_{23} + B_{45}$ does not contribute to the trace,

$$A_{SI} = \frac{2}{3}\mathrm{Tr}\Big\{\Big[Z_{16} - Z_{23}[\cos^2\phi_Y^{23}\, cos(\Omega_{23}nT_R) + \sin^2\phi_Y^{23}] \\ - Z_{45}[\cos^2\phi_Y^{45}\, cos(\Omega_{45}nT_R) + \sin^2\phi_Y^{45}]\Big]D^\dagger S_Z D\Big\}. \quad [2.23]$$

We see that the traces in Eq. [2.21] and [2.23] are equal, therefore

$$A_{IS} = \tfrac{3}{8}A_{SI}. \quad [2.24]$$

Eq. [2.24] implies that the double CP transfer amplitude, $A_{IS}A_{SI}$, is positive, a feature that holds regardless of the complex dependence of $\mathcal{H}_S^{eff}$ or D on crystallite orientation as long as conditions (a-c) are satisfied. With $\omega_S < 0$, mixing occurs within (1,4) and (3, 6) subspaces resulting again in Eq. [2.24] but with

$$A_{IS} = \frac{1}{4}\mathrm{Tr}\{[-Z_{25} + Z_{14}[\cos^2\phi_Y^{14}\, cos(\Omega_{14}nT_R) + \sin^2\phi_Y^{14}] \\ + Z_{36}[\cos^2\phi_Y^{36}\, cos(\Omega_{36}nT_R) + \sin^2\phi_Y^{36}]]D^\dagger S_Z D\}. \quad [2.25]$$

Maximum transfer amplitudes can be estimated by setting (i) $\phi_Y^{23} \cong \phi_Y^{45} \cong 0$, and (ii) $D \cong \mathbf{1}$ in Eq. [2.21, 2.23]. Condition (i) signifies (see Appendix A2.10) that levels corresponding to states $|2\rangle$ and $|3\rangle$, $|4\rangle$ and $|5\rangle$ are close to each other. Condition (ii) implies that $\omega_{1S}^{eff} \cong \omega_S$. If conditions (i, ii) are satisfied and using $S_Z = 2Z_{16} + Z_{23} + Z_{45} + \mathbf{1}_{23}/2 - \mathbf{1}_{45}/2$ we obtain

$$A_{IS} = \frac{1}{4}[1 - cos(\Omega_{23} nT_R)/2 - cos(\Omega_{45} nT_R)/2]. \qquad [2.26]$$

We see that A_{IS} is *positive* and if further $\Omega_{23} \cong \Omega_{45}$ it may reach up to 1/2. Using Eq. [2.24] we see that A_{SI} is also positive and may reach up to 4/3. If we consider $\omega_{1I}^{eff} > 0 > \omega_S$, then for maximal transfer ($\phi_Y^{14} \cong \phi_Y^{36} \cong 0$, and $D \cong \mathbf{1}$) we obtain from Eq. [2.25]

$$A_{IS} = \frac{1}{4}[-1 + cos(\Omega_{14} nT_R)/2 + cos(\Omega_{36} nT_R)/2] \qquad [2.27]$$

and we see that A_{IS} is *negative* and, if further $\Omega_{14} \cong \Omega_{36}$, it may reach down to -1/2. Eq. [2.26] and [2.27] confirm the assertion that sign of the CPMAS signal follows the sign of ω_{1S}^{eff}, at least in case of significant polarization transfer.

Since our derivation is based on certain approximations, it is expected that Eq. [2.24] holds only approximately. Generally, if the separation of V into parts operating on orthogonal two-dimensional subspaces is allowed, following the same mathematical reasoning, it can be shown that Eq. [2.24] still holds approximately. It is expected that this approximation breaks down when ω_S is sufficiently small in comparison with ω_{1I}^{eff}, a situation which may lead to complex mixing of the states.

The above proof also relies on the fact that the two CP contact times are equal and no conclusions can be drawn about the sign of the signal for unequal contact times. In order to get further insight for arbitrary contact times, brute force simulations were performed and the results are shown in Figure 2.8 which displays the buildup of amplitudes A_{IS} and A_{SI} as function of time and γ, for a constant β. It is seen that for any given γ (a) A_{IS} and A_{SI} have the same sign and (b) the sign of A_{IS} and A_{SI} does not depend on the contact time. From this it follows that the sign of double CP signal does not depend on crystallite orientation, even for *unequal* contact times.

With data available for Figure 2.8, we have computed A_{IS}/A_{SI} as a function of γ in order to test the theoretical value 3/8 (0.375) of Eq. [2.24]. For γ angles yielding A_{IS} larger than 0.1, 0.2, and 0.3, the average ratio A_{IS}/A_{SI} and the error are found to be 0.376 ± 0.01, 0.375 ± 0.005, and 0.375 ± 0.003 respectively. A figure showing the scattering of A_{IS}/A_{SI} as function of γ is shown in Appendix A2.11.

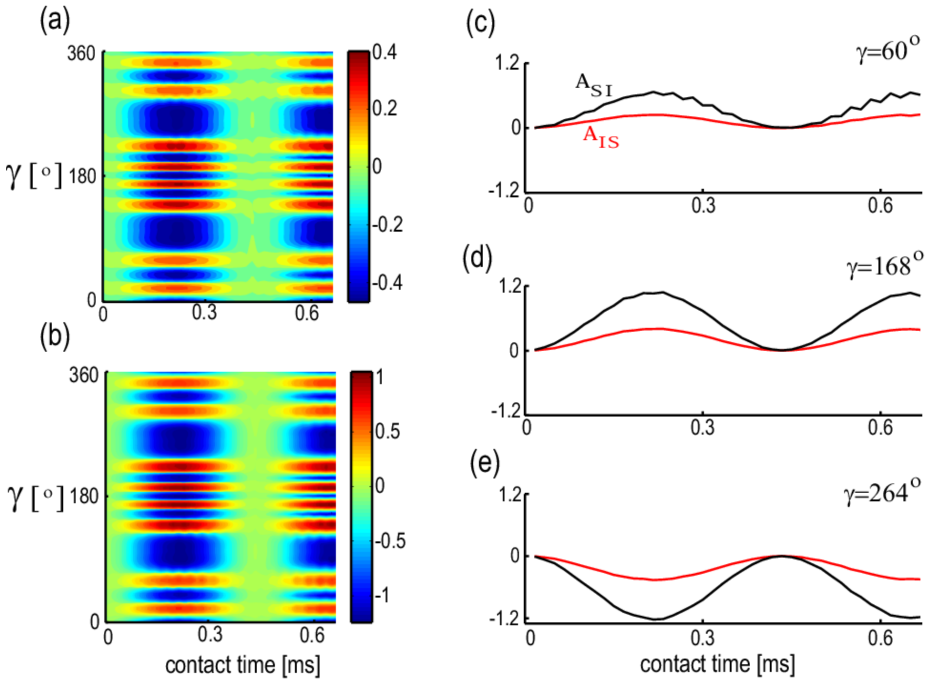

Figure 2.8 (a) Dependence of the $I \rightarrow S$ CP transfer amplitude, A_{IS}, on γ and contact time. (b) Dependence of the $S \rightarrow I$ CP transfer amplitude, A_{SI}, on γ and contact time. (c-e) Dependence of A_{SI} and A_{IS} on contact time for three selected γ angles. Calculations start from the Hamiltonian of Eq. [2.9] and assume $\beta = 32^{\circ}$, $\nu_D = 10\ kHz, \nu_{1S} = 80\ kHz$, $\nu_{1I} = 46\ kHz$, $\nu_R = 60\ kHz$, $C_Q/2\pi = 1.5\ MHz, \eta_Q = 0, \theta_{QD} = 0$, and $\tau_{CP} = 10T_R$.

2.5 Coherences during t_1 and double CP powder lineshapes

In this section, we discuss the contributions of various single-quantum coherences to the double CP signal, double CP ^{14}N lineshapes, and their connection with the experimental observations presented in Ref. [17].

In a ^{1}H-^{14}N double CP experiment, after the first CP transfer, single-quantum S-spin coherences evolve during t_1 and are converted back to single-quantum I-spin coherences which are detected during t_2. We assumed a process of filtration at the end of first CP block which retains only S_X or S_Y single-quantum coherences during t_1. However, if other S-spin single-quantum coherences are created by first CP block, experimental phase cycling alone is not capable to ensure such a filtration. In the discussion below, we include signal coming through all S-spin single-quantum coherences: $S_X, S_X I_Z, (S_X S_Z + S_Z S_X), (S_X S_Z + S_Z S_X) I_Z$, and their counterpart containing S_Y. Individual contributions to double CP signal due to various single-quantum coherences present at end of first CP block are shown in Figure 2.9(a) for CP contact times of 3 and 10 rotor periods. Signals are calculated as function of β after averaging over γ.

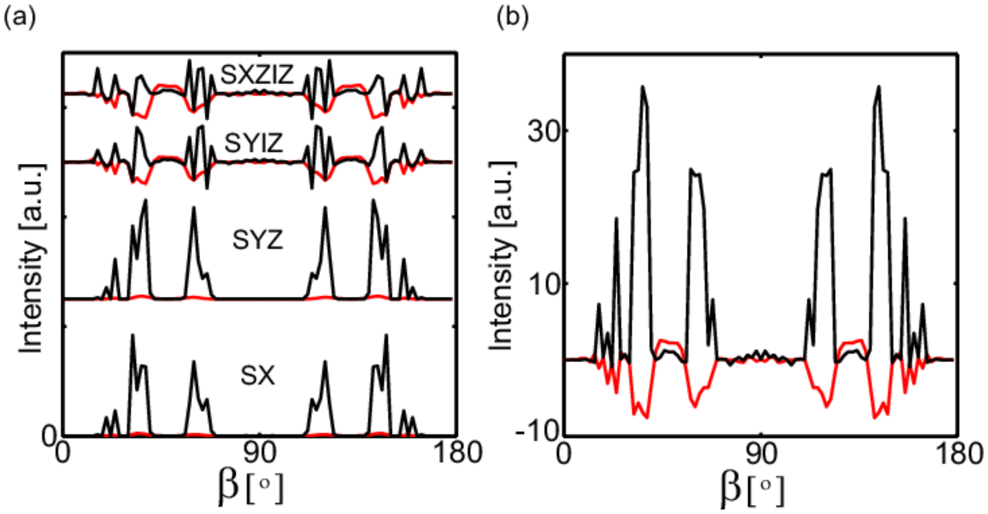

Figure 2.9 Contributions from various coherences to double CP signal as a funcion of β after averaging over γ for a CP contact times of (a) 3 rotor periods (red) and 10 rotor periods (black). (b) Sum of all contributions for 3 rotor periods (red) and 10 rotor periods (black). Other parameters are, $\nu_{1S} = 80\ kHz,\ \nu_{1I} = 46\ kHz,\ \nu_R = 60\ kHz,\ C_Q/2\pi = 1.5\ MHz,\ \ \eta_Q = 0,\ \nu_D = 10\ kHz,\ \theta_{QD} = 0.$ *For visibility, the signals due to different coherences are displaced vertically and are labeled as follows:* $S_X \rightarrow SX,\ S_Y I_Z \rightarrow SYIZ,\ S_Y S_Z + S_Z S_Y \rightarrow SYZ,\ (S_X S_Z + S_Z S_X) I_Z \rightarrow SXZIZ.$

We have observed that for both short and long contact times, the following coherences dominate: S_X, $(S_Y S_Z + S_Z S_Y)$, $S_Y I_Z$, and $(S_X S_Z + S_Z S_X) I_Z$. It can be seen from Figure 2.9(a,b) that, for the shorter contact time, the main contributions are coming from coherences involving I_Z and the sum of all contributions has predominantly a *negative* sign. On the other hand, for the longer contact time, the main contributions are coming via S_X and $(S_Y S_Z + S_Z S_Y)$ and the sum of all contributions has predominantly a *positive* sign, as seen from Figure 2.9(b). This change in sign of the double CP signal for very short contact times was noted experimentally in Ref. [17] and it may be attributed to the dominance of these additional coherences at shorter contact times. In the previous section it was shown that double CP signal passing through the S_X coherence is positive, regardless of β, γ, and the contact time. Additional simulations (not shown) indicate that the same property of the signal holds for $(S_Y S_Z + S_Z S_Y)$. However, we found that sign of signal passing through $S_Y I_Z$ or $(S_X S_Z + S_Z S_X) I_Z$ depends on β, γ, and the contact time. Therefore, the sign and magnitude of the total double CP signal acquires additional complexity due to the presence of different coherence pathways and their dependence on orientation and CP contact time. It has to be noted that $S_Y I_Z$ coherence may be created even in the absence of a quadrupolar interaction, in particular for dipolar-coupled spin-½ nuclei.[127]

^{1}H-^{14}N double CP experiments on powder samples result in ^{14}N second-order quadrupolar lineshapes in the first spectral dimension. The presence of β regions with poor transfer in a double CP experiment must lead to a certain degree of distortion of the lineshape. Analysis in previous sections indicates that ^{14}N lineshapes must also depend on duration of CP transfers and on the RF strengths. Simulated ^{14}N lineshapes for slightly different RF strengths, CP durations, and orientations of the quadrupolar and dipolar PAF's are displayed in Figure 2.10.

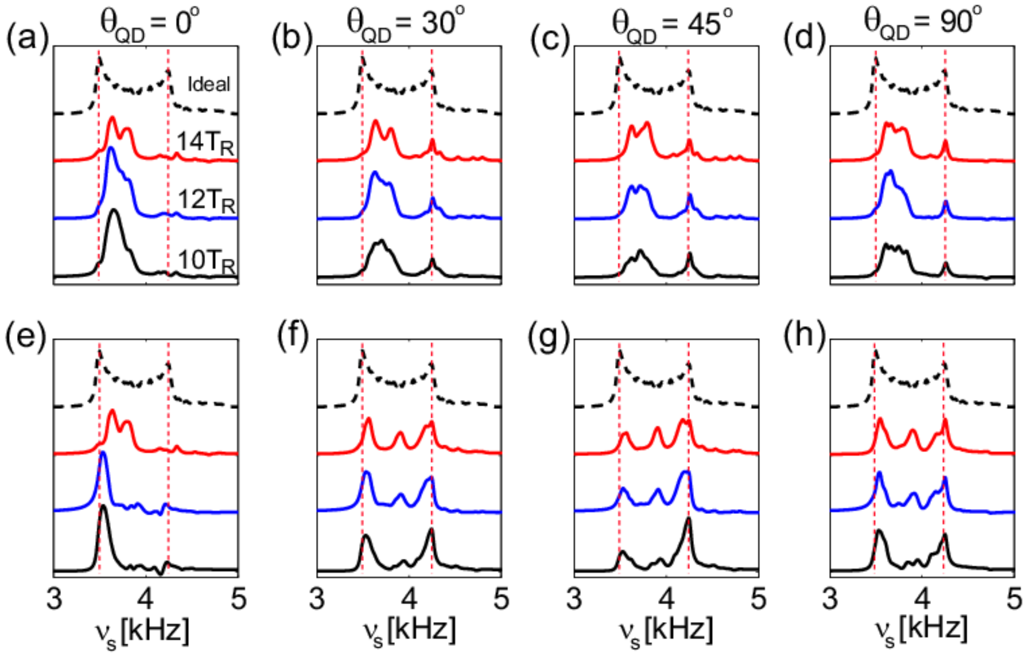

Figure 2.10 Double CP ^{14}N powder lineshapes simulated for different experimental conditions and with four different angles between the Z axes of the quadrupole and dipole PAFs. In (a-d) $\nu_{1S} = 80\ kHz$, $\nu_{1I} = 46\ kHz$ *while in (e-h)* $\nu_{1S} = 85\ kHz, \nu_{1I} = 50\ kHz$. *Contact times are 10 (black), 12 (blue), 14 (red) rotor periods. The 4 columns, from left to right, correspond to a* θ_{QD} *angle of* $0°, 30°, 45°$*, and* $90°$. *Common parameters are* $\nu_R = 60\ kHz$, $\frac{C_Q}{2\pi} = 1.5\ MHz$, $\eta_Q = 0$ $\nu_D = 10\ kHz$. *An ideal ^{14}N powder lineshape corresponding to the above quadrupolar parameters (dashed line) is displayed for comparison. For the ideal lineshape, the two singularities at 4.26 kHz and 3.48 kHz correspond to* $\beta_Q = 90°$ *and* $\beta_Q \cong 49°, 131°$ *respectively. Vertical lines passing through the singularities of the ideal lineshape are also shown. The spectra were obtained by Fourier transform of the time-domain signal after multiplication by an exponential decay function. The crystal file used was ZCW986 for all the spectra displayed. The ideal lineshape clearly indicates sufficient powder averaging and ensures the same for the double CP lineshapes.*

The lineshapes in Figure 2.10(a-d) are obtained with $\nu_{1S} = 80\ kHz, \nu_{1I} = 46\ kHz$ and with θ_{QD} angles of 0°, 30°, 45°, and 90°. Lineshape distortions are more prounced for $\theta_{QD} = 0°$ regardless of CP duration. The lineshapes in Figure 2.10(e-h), obtained with $\nu_{1S} = 85\ kHz$, $\nu_{1I} = 50\ kHz$, are less distorted since more crystallites satisfy the matching condition. The shift in the position of singularities is discussed in Appendix A2.12.

Simulations were also performed with different quadrupolar coupling constants (data not shown). Simulations indicate that it is possible to find a compromise RF configuration which gives reasonable resemblance between ideal and double CP lineshapes when several ^{14}N sites, with different quadrupolar coupling constants, are present. The nontrivial dependence of the lineshape on MAS, RF strengths, CP contact time, etc., was discussed in Ref. [17]. The lineshapes presented in Ref. [17-18] show less distortion when compared to our simulations. This may be due to proton-proton dipolar couplings which are not considered in this work.

2.6 Spin-lock and cross polarization

For an efficient CP transfer, a steady buildup of transferred magnetization is necessary and this requires that good spin lock is achieved on both channels, such that leaks from I_X and S_X to other coherences are as small as possible. We have seen that a necessary condition for good CP transfer is that all S terms in the effective Hamiltonian should be small, except ω_{1S}^{eff} and ω_{SZ}^{eff}. This condition also ensures an efficient spin-lock as presence of other pure S terms in the effective Hamiltonian leads to transfer of S_X to other coherences. This is confirmed in Figure 2.11 which investigates the connection between crystallite orientation, spin-lock, and CP transfer.

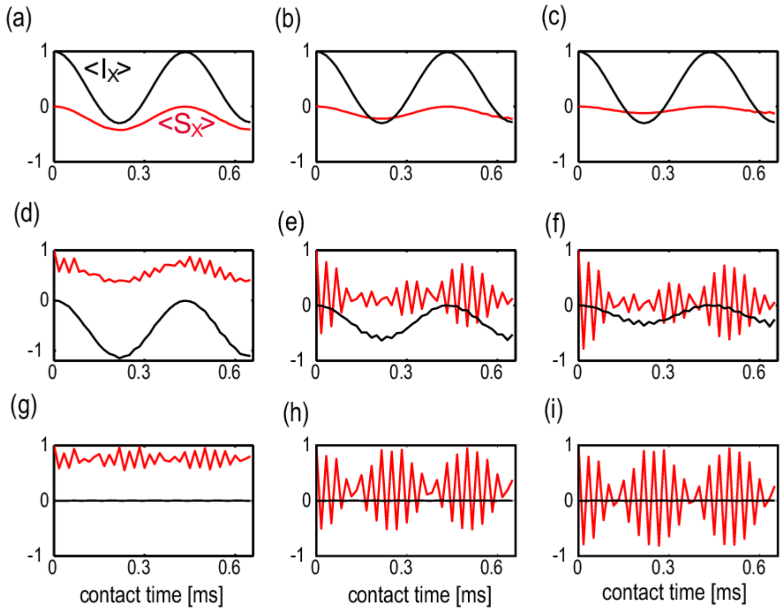

Figure 2.11 (a-c) Dependence of proton and nitogen polarizations, $\langle I_X\rangle$ and $\langle S_X\rangle$, on contact time during an $I \rightarrow S$ CP process, for three selected gamma angles. (d-f) Dependence of $\langle I_X\rangle$ and $\langle S_X\rangle$ on contact time during the inverse, $S \rightarrow I$, CP process, for the same gamma angles. (g-i) Dependence of $\langle S_X\rangle$ on time during a spin-lock experiment, for the same gamma angles. Calculations start from the Hamiltonian of Eq. [2.9] and assume $\beta = 32^{\circ}$, $\nu_{1S} = 80\ kHz$, $\nu_{1I} = 46\ kHz$ (a-f), $\nu_{1I} = 0\ kHz$ (g-i), $\nu_R = 60\ kHz$, $C_Q/2\pi = 1.5\ MHz$, $\eta_Q = 0$, $\nu_D = 10\ kHz$, and $\tau_{CP} = 10T_R$.

Figure 2.11 presents (a-c) $I \rightarrow S$ CP build up, (d-f) $S \rightarrow I$ CP build up, and (g-i) S spin lock as function of time, for three different crystallite orientations. These orientations were chosen as representatives for good (a,d), intermediate (b,e), and poor CP transfer (c,f). It can be seen that good (poor) efficiency of spin-lock is connected with good (poor) efficiency of $I \rightarrow S$ or $S \rightarrow I$ CP transfer. Of course, good spin lock is not a sufficient condition for establishing good CP transfer. Together with a good spin lock, a CP matching condition also needs to be satisfied.

2.7 Conclusions

Recently, Bodenhausen and coworkers[17] demonstrated that ^{1}H-^{14}N double CP experiments performed at fast magic angle spinning rates resulted in relatively high sensitivity as well as reasonable ^{14}N lineshapes in the indirect dimension. Employing AHT and Floquet theory in the jolting frame, essentially within zeroth order approximation, Gan and coworkers[132] found that the effect of the large quadrupolar interaction is to introduce a scaling and a phase of ^{14}N RF field which is dependent on crystallite orientation. The RF *phase spread* occurring for different crystallites causes cancellation of the CPMAS signal in a powder. They also predicted that, when two long ^{14}N pulses are used as in HMQC and double CP experiments, the phase cancellation is nullified resulting in coherent signal addition in a powder.

For investigating in detail the underlying spin-dynamics associated with ^{1}H-^{14}N double CP experiments, an effective Hamiltonian was calculated numerically using the matrix logarithm approach and in parallel Floquet theory. It is found that both methods lead to the same effective Hamiltonian, within numerical error differences (computationally the two methods are very different). We show that this equality is general and is related to the fact that both methods confine the eigenvalues to the $(-\omega_R/2, \omega_R/2]$ interval. We have investigated the relation between the effective Hamiltonians in two different rotating frames and we found that the effective Hamiltonian in the second rotating frame can be obtained by a simple *rearrangement* of the eigenvalues of the effective Hamiltonian in the first rotating frame. This procedure may be extended to other time-dependent problems.

The structure of the effective Hamiltonian was found to exhibit a strong dependence on crystallite orientation, with several spin terms of comparable magnitude present for most crystallite orientations. Employing RF field strengths and MAS rates close to those of Ref. [17] the following features are observed: (A) sign of the ^{14}N CPMAS signal follows the sign of the

^{14}N effective RF strength ω_{1S}^{eff}; significant CP transfer occurs when (B) the magnitudes of the proton and nitrogen effective RF strengths are comparable, and $|\omega_{1I}^{eff}| \cong |\omega_{1S}^{eff}| \cong max|\omega_{1S}^{eff}|$. This ensures that a CP matching condition is satisfied and, at the same time, the absence of large pure S terms in the effective Hamiltonian guarantees that the CP process proceeds unhindered. We have analyzed in detail the condition $\omega_{1I} + max|\omega_{1S}^{eff}| \cong \omega_R$ for arriving at the above conclusions. We would like to emphasize that for a given ω_{1I} the above condition is satisfied only by certain β angle regions thereby resulting in non-uniform CP transfer in a powder. Change in ν_{1I} results in alteration of both position and width of the β regions contributing to the signal. Following the same reasoning other matching conditions, employing multiples of the spinning frequency or involving other ^{14}N RF strengths were predicted and verified. These conclusions are simple, yet they involve a quantity, the effective ^{14}N RF strength ω_{1S}^{eff}, which depends in a non-trivial manner on crystallite orientation, ^{14}N RF strengths, MAS rate, and quadrupolar parameters. With a ramped ^{1}H RF amplitude we have observed that significant CP transfer occurs for more crystallite orientations resulting in improved sensitivity. Since in this case the eigenvalue window is very small, in order to obtain an interpretable effective Hamiltonian we have used a hybrid approach by combining the logarithm method and Baker-Campbell-Hausdorff expansion. The condition (B) is also the necessary and sufficient condition for good spin lock of the S nucleus. Although almost self-evident, the connection between efficiency of CP transfer and efficiency of spin lock was verified with additional simulations.

A proof is given for the important observation that the sign of double CP signal is largely independent on crystallite orientation. The proof also provides an estimate of 3/8 for the ratio of $I \rightarrow S$ and $S \rightarrow I$ transfer amplitudes and this estimate is further substantiated through simulations. Observation (A) is also proved in case of significant polarization transfer. The proof assumes only S_X or S_Y coherences during indirect dimension. However, we find that double CP signals include contributions from additional single-quantum coherences present after the first CP process. It is found that, due to uneven contribution of these coherences, the double CP signal is predominantly positive for larger contact times ($\sim 10T_R$) and predominantly negative for short contact times ($3 - 4T_R$). This feature was noticed experimentally in Ref. [17].

Second-order quadrupole powder lineshapes simulated with the double CP pulse sequence were found to depend significantly on RF strengths and contact times. Lineshape distortions are connected to the fact that a given RF configuration is unable to satisfy condition B for all crystallite orientations. The lineshapes presented in Ref. [17,18] show less distortion when compared to our simulations. This may be due to proton-proton dipolar couplings which were not considered in this work.

We hope that the comprehensive insight on ^{1}H-^{14}N CPMAS and double CP spin dynamics presented here may help in developing improved ^{1}H-^{14}N polarization transfer schemes.

3

Spin Dynamics in Fast MAS TRAPDOR-HMQC Experiments Involving Spin-3/2 Quadrupolar Nuclei

3.1 Introduction

Experiments probing correlations between spin-1/2 nuclei (*I*) and nuclear spins (*S*) with large anisotropic interactions (quadrupolar or chemical shift anisotropy) often offer valuable access routes to molecular structure and dynamics. In such experiments, development of efficient correlation schemes is not trivial and constitutes an ever-evolving theme of research. As these experiments are performed routinely under MAS, interference between the RF field and the large time-dependent quadrupolar interaction leads to complex spin dynamics, often leading to poor and orientation-dependent transfer efficiency. When compared with direct-detection schemes,[121] proton-detected correlation experiments under fast and ultra-fast MAS usually offer substantial gains in sensitivity. Solid-state heteronuclear multiple-quantum coherence (HMQC) experiments constitute an important class of indirect-detection correlation schemes. HMQC experiments involve transfer of *I*-spin polarization to heteronuclear coherences (excitation), time evolution of these coherences during indirect dimension, transfer back to *I*-spin single-quantum coherences (reconversion), and finally detection. Initially introduced and developed for ^{14}N ($S = 1$), indirect detection HMQC experiments[100,107,110,130,135–139] have been later extended to half-integer spins.[8,140–145]

Usually, excitation and reconversion periods contain a train of pulses or pulses and delays, with well-defined phases and durations, applied on *I* channel with the purpose of recoupling the *I*-*S* dipolar interaction. However, some time ago an *S* channel recoupling scheme was introduced, involving indirect detection of ^{14}N through ^{1}H or ^{13}C signals at moderate to high MAS.[114,132,146,147] Through long periods of RF irradiation on the ^{14}N channel, the polarization transfer is achieved from ^{1}H or ^{13}C to heteronuclear coherences involving single and double quantum ^{14}N terms. They have demonstrated that such a scheme affords good transfer efficiency and allows extraction of quadrupolar parameters via numerical simulation. Recently I. Hung and Z. Gan extended the above scheme to quadrupolar nuclei with half-integer spin, specifically ^{35}Cl ($S = 3/2$).[20] The pulse sequence exploits the **tra**nsfer of **p**opulations in **do**uble **r**esonance (TRAPDOR) mechanism[148-151] hence the acronym T-

HMQC. A schematic of TRAPDOR-HMQC[20] is shown in Figure 3.1. T-HMQC pulse sequence starts with a 90° excitation pulse on the proton channel followed by a long pulse on *S* (*^{35}Cl*) channel of duration of τ_{mix}. We refer the first long pulse irradiation on the *S* nuclei as first TRAPDOR irradiation. Subsequently, rotor synchronized t_1 evolution period follows, with an *I*-spin π pulse in the middle for refocusing the first order quadrupolar interactions under MAS, provided that the magic angle is adjusted precisely. The pulse sequence ends with a second TRAPDOR irradiation with the same duration, τ_{mix} followed by the detection of *I*-spin signal.

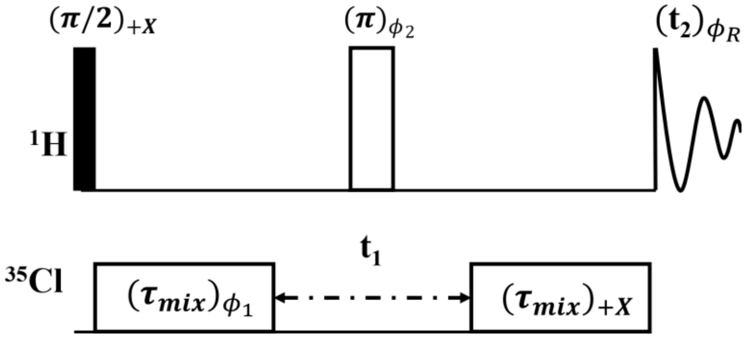

Figure 3.1: Schematic of the ^{1}H - ^{35}Cl T-HMQC pulse sequence. τ_{mix} refers to the duration of the TRAPDOR irradiation on ^{35}Cl channel. The phase cycle used to select the ^{35}Cl $\Delta p = \pm 1, \pm 3$ coherence transfer pathways is $\phi_1 = x, -x$, $\phi_2 = x, x, y, y, -x, -x, -y, -y$, $\phi_R = x, -x, -x, x$, and for $\Delta p = \pm 2$ it is $\phi_1 = x, y, -x, -y$, $\phi_2 = 4\{x\}, 4\{y\}, 4\{-x\}, 4\{-y\}$, $\phi_R = 2\{x, -x\}\ 2\{-x, x\}$where Δp *indicates the coherence order.*

For $S = 3/2$, the first period of irradiation of *S* spins leads to heteronuclear coherences involving single-quantum ($\Delta p = \pm 1$), double-quantum ($\Delta p = \pm 2$) and triple-quantum ($\Delta p = \pm 3$) *S*-spin terms. The conversion to *I*-spin single-quantum coherences for detection is performed by a second irradiation period. With appropriate phase cycling, coherences involving *S*-spin double-quantum terms were selected in indirect dimension, leading to high-resolution double-quantum ^{35}Cl spectra in the indirect dimension, due to the fact that double-quantum linewidths are considerably narrower than single or triple-quantum linewidths. The experiments were performed on active pharmaceutical ingredients (API) where remote ^{1}H's (*I*) are dipolar coupled to ^{35}Cl (*S*) nuclei. With double-quantum satellite-transition (DQ-ST) selection, it was possible to resolve signals coming from different ^{35}Cl sites. The simplicity of the experiment is to be noted in comparison to other HMQC type pulse sequences which, as mentioned, incorporate multi-pulse excitation and reconversion blocks on *I* spin channel. From the hardware point of view, similar to STMAS,[13,152] T-HMQC experiments involving single-and double-quantum satellite-transition coherences require precise setting of the magic angle and stable MAS rates, in order to refocus the first-order quadrupolar interaction.[20]

Subsequently, Bayzou et al. have presented an extensive experimental and theoretical study of T-HMQC.[21] Experiments were demonstrated on ^{1}H - ^{135}Pt/^{14}N/^{35}Cl systems with nuclear spin $S = 1/2, 1$ and $3/2$ respectively. A theoretical analysis of the experiments was provided within the Floquet theory[60,61,83] framework. For all systems, the Floquet calculations were performed in the jolting frame[153-154] in which the large anisotropic interaction (quadrupolar or CSA) is removed. The role of different terms in the Floquet effective Hamiltonian was discussed. For $S = 3/2$, the second order *I*-*S* term in the Floquet effective Hamiltonian was shown to lead to creation of heteronuclear coherences containing single, double, and triple-quantum *S*-spin terms when irradiating at one of the spinning sidebands of *S*. A truncation procedure was introduced in which only the projection of this second order *I*-*S* term on the first order term in the Floquet effective Hamiltonian was retained. It was shown that when irradiating the centerband, the second order *I*-*S* term is effectively truncated resulting in cancellation of the T-HMQC signal. It was also shown that recoupling due to the third-order I-S Floquet effective Hamiltonian may occur with irradiation in the midpoint between two consecutive spinning sidebands. Further, they have shown that a fourth-order *I*-*S* term may lead to T-HMQC signal when irradiating at $\nu_{1S} = (n + 1/3)\nu_R$. The theoretical conclusions, the dependence of T-HMQC on offset, recoupling time, RF amplitude, etc. were investigated using extensive numerical simulations. A similar analysis was performed for $S = 1/2$ and 1. For all systems it was derived analytically that the phase of the T-HMQC signals is independent of crystallite orientation, thus leading to more coherent signal addition in a powder.

In the work presented here we offer additional insights on the machinery of T-HMQC experiments for $S = 3/2$. We analyze spin dynamics during the two irradiation blocks of the T-HMQC experiment from two different perspectives. The first perspective involves finding correlations between various terms in an *exact* effective Hamiltonian and the buildup of various coherences during TRAPDOR irradiation. Analytical conclusions are derived and confronted with numerical simulations in which the exact effective Hamiltonian is evaluated with the *matrix logarithm* approach.[68] The second perspective considers the creation, evolution, and interconversion of coherences at arbitrary times during TRAPDOR irradiation. Evolution around avoided level crossings (for brevity ‘crossings’ hereafter) is considered within the approach established by A. J. Vega,[150-151] and the sudden, intermediate, and adiabatic regimes of the T-HMQC experiment are analyzed. Behaviour between consecutive crossings is described analytically.

3.2 Spin system

We consider a spin-3/2 ($S = 3/2$) nucleus subjected to irradiation at RF strength ω_{1S} and dipolar-coupled to a spin-1/2 ($I = 1/2$) nucleus. The *I*-*S* spin system undergoes magic angle spinning at angular frequency ω_R. First and second-order nuclear quadrupolar interactions of S are included in the Hamiltonian. We consider an axially-symmetric quadrupolar interaction (asymmetry parameter $\eta_Q = 0$) with Z axis of PAF of the quadrupolar tensor described by polar angles β_Q and $\gamma_Q$with respect to the rotor-frame coordinate system. The internuclear $I - S$ vector, $\boldsymbol{r}_{IS}$, is characterized by polar angles β_D and γ_D in the rotor frame. The angle between the Z principal axis of the quadrupolar tensor and internuclear $I - S$ vector is denoted by θ_{QD}. Under these conditions the Hamiltonian of the system can be written as

$$\mathcal{H}(t) = \Delta\omega_S S_Z + \omega_{1S} S_X + \mathcal{H}_Q^{(2)}(t,\beta_Q,\gamma_Q) + \omega_Q(t,\beta_Q,\gamma_Q)[3S_Z^2 - S(S+1)] + d(t,\beta_D,\gamma_D) 2I_Z S_Z, \qquad [3.1]$$

where $\omega_Q(t,\beta_Q,\gamma_Q)$ is the first-order quadrupolar frequency, $\mathcal{H}_Q^{(2)}(t,\beta_Q,\gamma_Q)$ is the second-order quadrupolar interaction, and $d(t,\beta_D,\gamma_D)$ is the dipolar coupling. Both first and second-order quadrupole interactions depend on quadrupolar coupling constant $C_Q = e^2Qq/\hbar$, where eQ is the quadrupole moment and eq is the principal component V_{ZZ} of electric field gradient tensor in the PAF. The dipolar interaction is characterized by dipolar coupling, $\omega_D = -\mu_o\gamma_I\gamma_S\hbar/4\pi r_{IS}^3$, where γ_I and γ_S are gyromagnetic ratios of I and S. The explicit expressions of the terms in Eq. [3.1] are provided in Appendix A3.1. When $\theta_{QD} = 0$, a common set of polar angles, β and γ, is used to characterize both quadrupolar and dipolar interactions. For simplicity, we have considered $\theta_{QD} = 0$ for all calculations presented.

3.3 Exact effective Hamiltonian

The effective Hamiltonian $\mathcal{H}_{\text{eff}}$ is defined as a time-independent Hamiltonian which satisfies $U(T_R, 0) = \exp(-i\mathcal{H}_{\text{eff}}T_R)$, where $U(T_R, 0)$ is the propagator over one rotor period associated with the Hamiltonian in Eq. [3.1]. Although almost obvious, it can be justified without any approximation (Appendix A3.2) that

$$\mathcal{H}_{eff} = \mathcal{H}^S_{eff} + A_S I_Z\,, \qquad [3.2]$$

where $\mathcal{H}^S_{eff}$ and A_S contain only *'pure S'* terms i.e., only *S*-spin operators. In addition, it is easy to show that the propagator corresponding to an arbitrary time, $U(t,0)$, is diagonal with respect to the Zeeman states of spin *I*, $|\alpha\rangle$ and $|\beta\rangle$. It follows that, starting with the initial condition $\rho(0) = I_X$ no *pure-S* coherences and no heteronuclear coherences involving I_Z are produced by TRAPDOR irradiation. This is numerically illustrated in Appendix A3.3.

In the following, Zeeman states of spin *S* are labeled as $|1\rangle = |3/2\rangle, |2\rangle = |1/2\rangle, |3\rangle = |-1/2\rangle,$ and $|4\rangle = |-3/2\rangle$. Subsequently, $\mathcal{H}_{eff}$, $\mathcal{H}^S_{eff}$, and $A_S I_Z$ are expanded into an operator basis containing products of Cartesian *I*-spin operators I_X, I_Y, I_Z and fictitious spin-1/2 operators[52] for spin *S* (S^{ij}_α with $\alpha = X, Y, Z$ and $i, j = 1,2,3,4$). S^{12}_α *and* S^{34}_α are satellite-transition single-quantum operators, S^{23}_α are central-transition single-quantum operators, S^{13}_α *and* S^{24}_α are satellite-transition double-quantum operators, and S^{14}_α are triple-quantum operators. The matrix representations of these spin operators are provided in Appendix A3.4. For example, $\mathcal{H}^S_{eff}$ may contain $S^{12}_X = \mathbf{1}_I[|1\rangle\langle 2| + |2\rangle\langle 1|]/2$, where $\mathbf{1}_I$is the *I*-spin unit operator; and $A_S I_Z$ may contain heteronuclear terms such as $S^{23}_X I_z$. If O_k is a given operator from the operator basis, the corresponding coefficient in $\mathcal{H}_{eff}$ is calculated as $\omega^{eff}_k = Tr[O_k \mathcal{H}_{eff}]/Tr[O^2_k]$. The same operator basis is utilized to expand the density operator, $\rho = \sum a_k O_k$, where $a_k = Tr[O_k \rho]/Tr[O^2_k]$. When dealing with specific examples of $\omega^{eff}_k$and a_k, the labeling described in Table 3.1 is used. In Table 3.1, $\mathbf{1}^{ij}_S$ represents the unit operator in the subspace of states $|i\rangle$ and $|j\rangle$.

k	$1ij,x$	$1ij,y$	$1ij,z$	$xij,1$	$yij,1$	$zij,1$	xij,x	xij,y	xij,z
O_k	$\mathbf{1}^{ij}_S I_X$	$\mathbf{1}^{ij}_S I_Y$	$\mathbf{1}^{ij}_S I_z$	$S^{ij}_X \mathbf{1}_I$	$S^{ij}_Y \mathbf{1}_I$	$S^{ij}_Z \mathbf{1}_I$	$S^{ij}_X I_X$	$S^{ij}_X I_Y$	$S^{ij}_X I_Z$
k	yij,x	yij,y	yij,z	zij,x	zij,y	zij,z			
O_k	$S^{ij}_Y I_X$	$S^{ij}_Y I_Y$	$S^{ij}_Y I_Z$	$S^{ij}_Z I_X$	$S^{ij}_Z I_Y$	$S^{ij}_Z I_Z$			

Table 3.1 Spin operators (O_k) and labeling of the coefficients $\omega^{eff}_k$and a_k.

Effective Hamiltonian, truncation, and amplitude of coherences

There are several ways to construct an effective Hamiltonian which can approximately describe the evolution due to a time-dependent Hamiltonian. Depending on the complexity of the system, multiple time dependencies etc., AHT and Floquet theory have been often and successfully employed in order to derive approximate effective Hamiltonians. For the spin system considered here, because of interference between the large time-dependent quadrupolar interaction and the RF field, an average Hamiltonian computed *numerically* in the jolting frame up to third order term in the Magnus expansion[56] was unable to reasonably predict the spin dynamics for different crystallite orientations. A detailed study of spin-dynamics associated with ^{1}H-^{14}N double cross polarization experiment[17] the *matrix logarithm* approach has been employed by Sajith et.al.[155] Since, as mentioned above, AHT was not capable to yield a fair quantitative description of the evolution, we have applied the *matrix logarithm* approach to evaluate numerically the effective Hamiltonian during TRAPDOR irradiation. The *matrix logarithm* method consists of two steps: (A) numerical calculation of the propagator $U(T_R, 0)$, and (B) construction of $\mathcal{H}_{\text{eff}}^{ln}$ via numerical evaluation of the *matrix logarithm*,

$$\mathcal{H}_{\text{eff}}^{ln} = \ln\big(U(T_R, 0)\big)/(-iT_R). \qquad [3.3]$$

All simulations discussed in the manuscript are performed using home-written MATLAB® **(**The Mathworks, Inc.) code**.**

The T-HMQC pulse sequence starts with a 90° excitation pulse on *I* channel followed by a long pulse on *S* channel of duration of $\tau_{mix} = n\tau_R$, where $\tau_R = 2\pi/\omega_R$ and n is an integer. We refer the first long pulse irradiation on the *S* nuclei as first TRAPDOR irradiation. Subsequently, rotor synchronized t_1 evolution period follows, with an *I*-spin π pulse in the middle for refocusing. The pulse sequence ends with a second TRAPDOR irradiation with the same τ_{mix} followed by detection of *I*-spin signal.

As the spin dynamics of the system is rich, initial simulations were performed to understand the connection between the structure of the effective Hamiltonian and the amplitudes of various coherences produced during first TRAPDOR irradiation. The experimental parameters ($\nu_R = 60$ kHz, $\nu_1 = 100$ kHz) are in the range considered in Ref. [20,21]. It was shown that the essential factor leading to efficient transfer is the presence of an offset, $\Delta\omega_S$.[20,21] In most simulations presented below we consider $\Delta\omega_S/2\pi = 10$ kHz. Towards the end we discuss the role of $\Delta\omega_S$ for efficient TRAPDOR transfer.

In Figure 3.2 various $\omega_k^{eff}/2\pi$ coefficients as well as amplitudes a_k of several coherences produced by first TRAPDOR irradiation are displayed as function of γ for a fixed

β angle. Since transfer efficiency strongly depends on crystallite orientation, the angle β was chosen to correspond to a *good transfer* from the initial state $\rho(0) = I_X$ to various heteronuclear coherences. It can be seen that both $\omega_k^{eff}/2\pi$ and a_k exhibit a complex dependence on γ. In addition and not unexpected (since the dipolar coupling is 1 kHz), coefficients $\omega_k^{eff}/2\pi$ of the *heteronuclear* terms in the effective Hamiltonian (Figure 3.2c) appear considerably smaller than the coefficients of *pure-S* terms (Figure 3.2b).

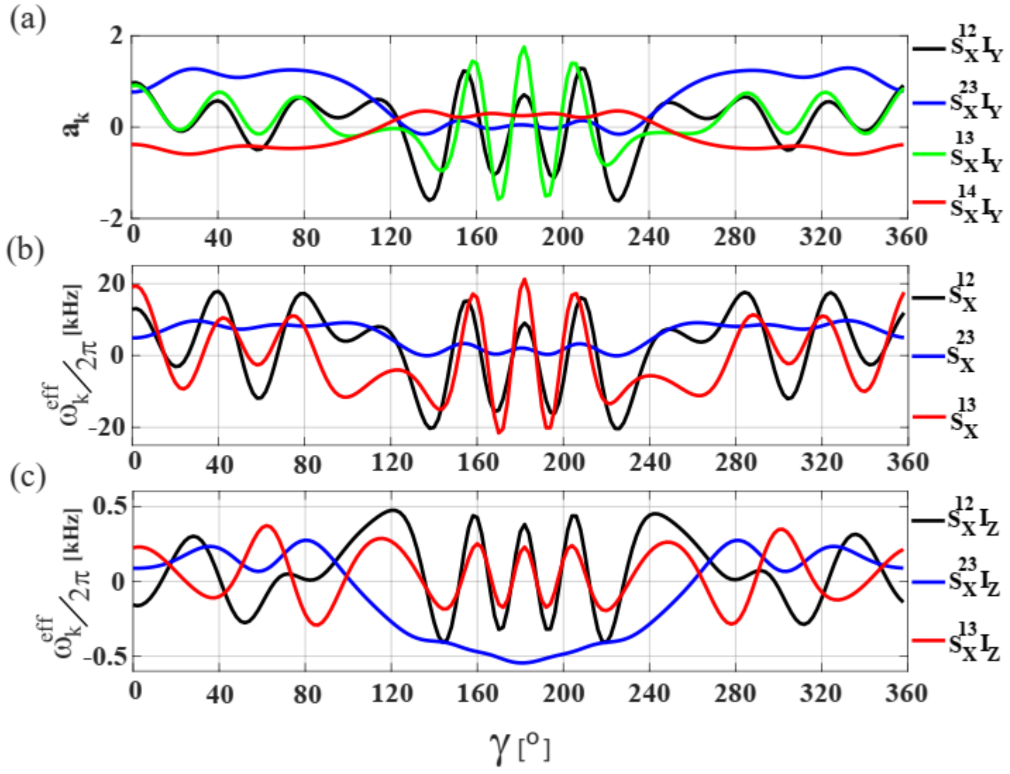

Figure 3.2 (a) Variation of the amplitude of several coherences at the end of first TRAPDOR block with γ angle. (b) Variation of several pure-S terms in $\mathcal{H}_{eff}$. (c) Variation of several heteronuclear terms in $\mathcal{H}_{eff}$. Numerical simulations are performed with $\beta = 50^o,\ C_Q = 2\,MHz,\ \nu_D = 1\,kHz,\ \nu_{1S} = 100\,kHz, \Delta\nu_S = 10\,kHz,$ and $\nu_R = 60\,kHz$. Duration of TRAPDOR irradiation is $100T_R$ (~1.67 ms). All the terms in Eq. [3.1] are considered.

This suggests to treat $A_S I_Z$ terms as a perturbation to $\mathcal{H}_{eff}^S$ such that, to first approximation; the effective Hamiltonian can be approximated as

$$\mathcal{H}_{eff} = \mathcal{H}_{eff}^S + A_S I_Z \cong \mathcal{H}_{eff}^S + A_S' I_Z, \qquad [3.4]$$

where $A_S{}'$ is that part of A_S which commutes with $\mathcal{H}_{eff}^S$. If $|\widetilde{m}\rangle$ denote the eigenstates of $\mathcal{H}_{eff}^S$, evaluation of A_S' may be performed as

$$A'_S = \sum_m |\widetilde{m}\rangle\langle\widetilde{m}|\langle\widetilde{m}|A_S|\widetilde{m}\rangle. \quad [3.5]$$

The truncation procedure may break down if some eigenvalues of $\mathcal{H}_{eff}^S$ are close enough and there are matrix elements of the non-commuting part of $A_S I_Z$ connecting the corresponding eigenstates. Therefore, it is expected that the truncation procedure will be less accurate at larger dipolar couplings (other possibilities for the breakdown of the truncation approximation are discussed later).

To test the validity of the truncation approximation we have performed extensive numerical simulations with dipolar coupling of 1, 10, 20 kHz, and for various crystallite orientations. For each orientation, $A_S{}'$ is evaluated numerically, the density operator is propagated with

$$U(NT_R, 0) = exp\left[-i\left(\mathcal{H}_{eff}^S + A_S I_Z\right)NT_R\right] \cong exp\left[-i\mathcal{H}_{eff}^S NT_R\right] exp\left[-iA_S{}' I_Z NT_R\right], \quad [3.6]$$

and, for comparison, with the exact propagator $exp\left[-i\left(\mathcal{H}_{eff}^S + A_S I_Z\right)NT_R\right]$. In Figure 3.3, amplitudes of various coherences, a_k, that are generated by first TRAPDOR irradiation are shown with (red) and without (black) the truncation approximation, as function of γ angle.

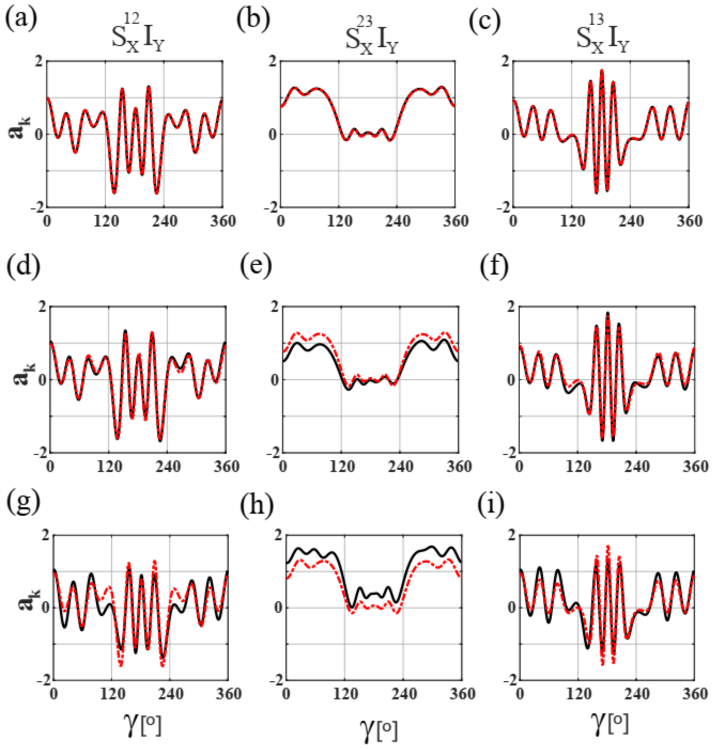

Figure 3.3 Amplitude of TRAPDOR coherences $S_X^{12}I_Y, S_X^{23}I_Y, S_X^{13}I_Y$ calculated with (red) and without (black) the truncation approximation as function of γ angle and for three different dipolar couplings, (a-c) $\nu_D = 1\ kHz$, (d-f) $10\ kHz$, and (g-i) $20\ kHz$ respectively. Other parameters used are $\beta = 50^o$, $C_Q = 2\ MHz$, $\nu_{1S} = 100\ kHz$, $\Delta\nu_S = 10\ kHz$, and $\nu_R = 60\ kHz$. The duration of TRAPDOR irradiation is $100T_R$ for (a-c), $10T_R$ for (d-f), and $5T_R$ for (g-i).

It can be seen that amplitudes calculated with Eq. [3.2] and [3.4] are in excellent agreement for the 1 kHz dipolar coupling and differ only marginally for dipolar couplings of 10 and 20 kHz (Figure 3.3d-i). Since for spin-3/2 nuclei coupled to protons short-range dipolar couplings are usually within a few kHz, we assume that the truncation approximation is accurate and we further proceed to investigate what inferences can be drawn from it.

As according to Eq. [3.5] A_S' is generally not proportional to $\mathcal{H}_{eff}^S$, this *truncation* procedure is more general than the *truncation* procedure adopted in Ref. [21] which projects heteronuclear terms in the Floquet effective Hamiltonian on the first-order Floquet effective Hamiltonian. A comparison between the two truncation procedures is presented in Appendix A3.5. Depending on crystallite orientation, predictions based on the two truncation procedures may be very similar, or may differ substantially. When they differ, predictions with truncation procedure adopted in Ref. [21] do not match the outcomes calculated without any truncation approximation (i.e., with the exact effective Hamiltonian).

When coefficients of different terms in ${A_S}'I_Z$ and amplitudes of different coherences are examined as function of crystallite orientation, a functional resemblance between certain $\omega_k^{eff}/2\pi$ and a_k^{IS} is observed according to which $\omega_{xpq,z}^{eff}/2\pi \rightarrow a_{xpq,y}^{IS}$ and $\omega_{ypq,z}^{eff}/2\pi \rightarrow a_{ypq,y}^{IS}$ for all coherences involving I_Y. This is illustrated in Figure 3.4 where a few amplitudes and the associated coefficients are displayed as function of γ. We justify this correspondence analytically utilizing the truncation approximation as shown below. By employing Eq. [3.6] the density operator after a period of irradiation NT_R is

$$\rho(NT_R) \cong exp[-i{A_S}'I_Z NT_R]I_X exp[i{A_S}'I_Z NT_R]. \qquad [3.7]$$

For small dipolar couplings (~1 kHz) the coefficients of various terms in ${A_S}'I_Z$ are below 100 Hz as seen in Figure 3.4. Therefore, for irradiation periods which are not very long, the exponential operators can be expanded in Taylor series and the density operator to first order in $NT_R$is

$$\rho(NT_R) \cong I_X - iA_S'[I_Z, I_X]NT_R = I_X + A_S' I_Y NT_R. \qquad [3.8]$$

From Eq. [3.8] it can be seen that the amplitudes of various coherences involving I_Y are proportional to the corresponding coefficients in ${A_S}'I_Z$, hence the $\omega_k^{eff}/2\pi \leftrightarrow a_k^{IS}$ functional resemblance is proved, at least for shorter irradiation times. For coherences involving I_X (not shown here) such a resemblance is not apparent. This can be comprehended as follows.

Coherences involving I_X develop at later times when the linear approximation involved in Eq. [3.8] is not sufficient. Adding to the density operator also the quadratic term, we obtain

$$\rho(NT_R) \cong I_X + A'_S I_Y N T_R - \frac{A'^2_S I_X N^2 T_R^2}{2}\,. \qquad [3.9]$$

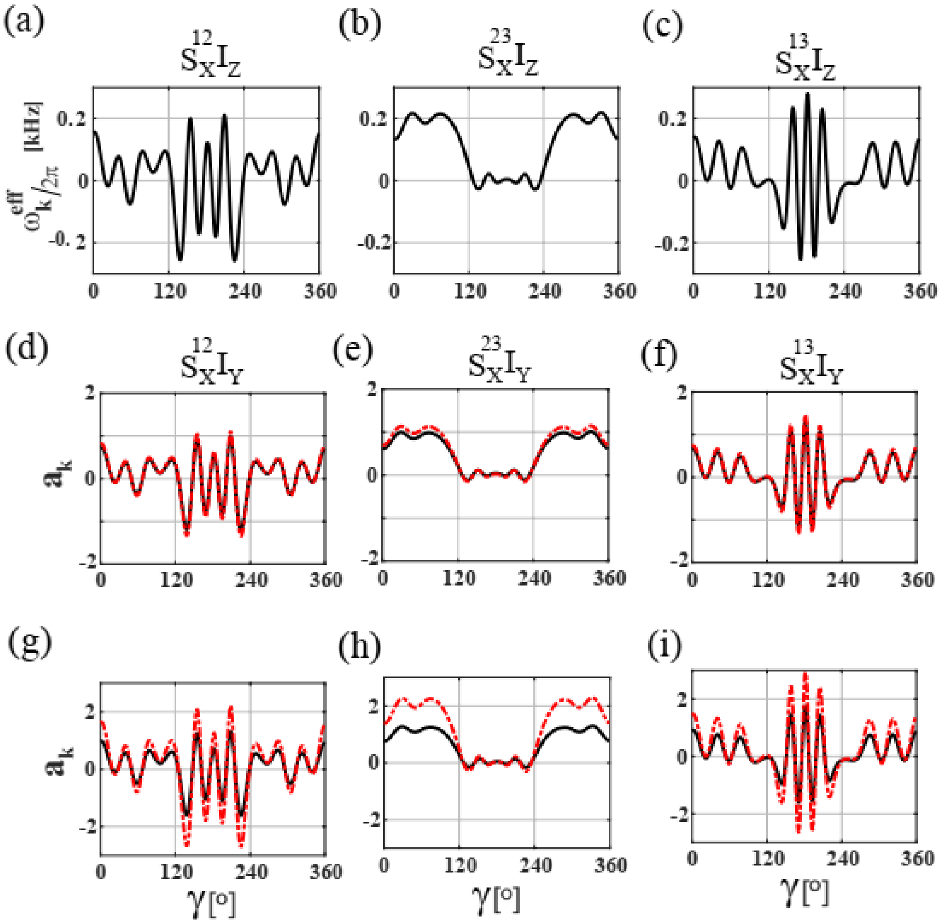

Figure 3.4 (a-c) Coefficients $\omega_k^{eff}/2\pi$ of various terms in $A_S{}'I_Z$, as function of γ angle. (d-f) Amplitudes of coherences $S_X^{12}I_Y$, $S_X^{23}I_Y$, and $S_X^{13}I_Y$ after $50T_R$ TRAPDOR irradiation. (g-i) The same after $100T_R$ TRAPDOR irradiation. In (d-i) amplitudes are evaluated with Eq. [3.7] (black) and with the quadratic expansion of Eq. [3.9] (red). Other parameters used are: $\beta = 50^o$, $C_Q = 2\ MHz$, $\nu_D = 1\ kHz$, $\nu_{1S} = 100\ kHz$, $\Delta\nu_S = 10\ kHz$, and $\nu_R = 60\ kHz$.

Since, according to Eq. [3.9], the coherences involving I_X are linked to A'^2_S, no simple functional resemblance between $\omega_k^{eff}/2\pi$ and a_k^{IS} occurs. From Figure 3.4 it can be seen that Eq. [3.9] is quite accurate for irradiation times up to $50T_R$ (~0.83 ms). With $100T_R$ (~1.67 ms) significant differences are noticed with Eq. [3.9], however the functional resemblance between $\omega_k^{eff}/2\pi$ and a_k^{IS} is still evident.

T-HMQC experiment: sign (phase) of signal and role of the π pulse

After deriving an initial insight on the features of the effective Hamiltonian and the connection with the amplitude of coherences created by the first TRAPDOR irradiation, we now consider the spin-dynamics associated with polarization transfer during the entire T-HMQC experiment. In the following, we consider the T-HMQC experiment with $t_1 = 0$ and, for the time being, with no *I*-spin π pulse between the two TRAPDOR blocks. We have seen in the previous sections that, at the end of first TRAPDOR irradiation, several heteronuclear coherences are present and thus it is important to examine the connection between the type of excited coherences and the phase of the detected *I*-spin signal. We denote by A_k^I that part of the *I*-spin signal which is due to coherence ‘k’ at the end of the first TRAPDOR irradiation. In Figure 3.5, *I*-spin signals corresponding to coherences involving *S*-spin double-quantum terms are presented as function of the β and γ angles.

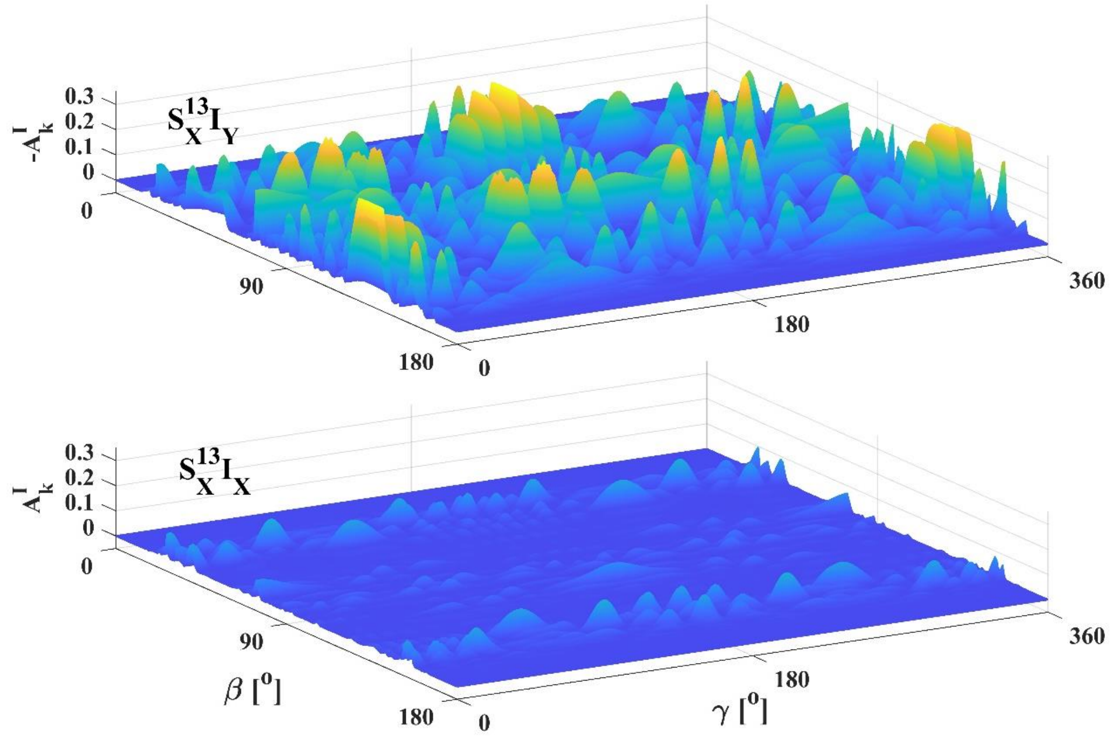

Figure 3.5 Top: T-HMQC experiment ($t_1 = 0$): dependence on β and γ of I-spin signal, A_k^I, corresponding to coherence $S_X^{13}I_Y$ produced by first TRAPDOR block. For better visibility $-A_k^I$ is displayed. Bottom: dependence on β and γ of I-spin signal, A_k^I, corresponding to coherence $S_X^{13}I_X$ produced by the first TRAPDOR block. Other parameters used are $C_Q = 2\ MHz$, $\nu_D = 1\ kHz$, $\nu_{1S} = 100\ kHz$, $\Delta\nu_S = 10\ kHz$, and $\nu_R = 60\ kHz$. Duration of excitation and reconversion TRAPDOR blocks is $100T_R$. No I-spin π pulse is applied between the two blocks.

Apart from the expected strong orientation dependence of the signals, it can be seen that the coherence involving I_X (I_Y) lead to positive (negative) signals for all β and γ angles.

It has been verified that this rule holds for all possible coherences present at the end of first TRAPDOR irradiation. Plots for coherences involving *S*-spin single-quantum terms (satellite and central transition) are presented in Appendix A3.6. Based on the truncation approximation this sign rule can be justified as follows.

Consider the *I*-spin signal corresponding to a given transfer pathway, $I_X \rightarrow a_X^{IS} O_S I_X \rightarrow a_X^{IS} a_X^{SI} I_X$ where O_S is a *pure-S* spin operator. The transfer amplitudes a_X^{IS} and a_X^{SI} are

$$a_X^{IS} = \frac{Tr\{U(\tau) I_X U^{+}(\tau) O_S I_X\}}{Tr\{[O_S I_X]^2\}}, \qquad [3.10]$$

$$a_X^{SI} = \frac{Tr\{U(\tau) O_S I_X U^{+}(\tau) I_X\}}{Tr\{[I_X]^2\}}, \qquad [3.11]$$

and using Eq. [3.6] we obtain

$$a_X^{IS} = \frac{Tr\{exp[-iA_S{}' I_Z \tau] I_X exp[+iA_S{}' I_Z \tau] O_S I_X\}}{Tr\{[O_S I_X]^2\}}, \qquad [3.12]$$

$$a_X^{SI} = \frac{Tr\{exp[+iA_S{}' I_Z \tau] I_X exp[-iA_S{}' I_Z \tau] O_S I_X\}}{Tr\{[I_X]^2\}}. \qquad [3.13]$$

Since $\left[\mathcal{H}_{eff}^{S}, A_S{}'\right] = 0$, $\mathcal{H}_{eff}^{S}$ and A_S' share the same eigenstates $\mathcal{H}_{eff}^{S}|\widetilde{m}\rangle = \epsilon_m|\widetilde{m}\rangle, A_S{}'|\widetilde{m}\rangle = \delta_m|\widetilde{m}\rangle$ where '*tilde*' signifies that $|\widetilde{m}\rangle$ are generally different from Zeeman spin-3/2 eigenstates. By using the basis $\{|\widetilde{m}\alpha\rangle = |\widetilde{m}\rangle|\alpha\rangle,\ |\widetilde{m}\beta\rangle = |\widetilde{m}\rangle|\beta\rangle\}$, the exponential operators in Eq. [3.12, 3.13] can be expressed as

$$exp[\pm iA_S{}' I_Z \tau] = \sum_m exp\left[\pm \frac{i\delta_m \tau}{2}\right] |\widetilde{m}\alpha\rangle\langle\widetilde{m}\alpha| + \sum_m exp\left[\mp \frac{i\delta_m \tau}{2}\right] |\widetilde{m}\beta\rangle\langle\widetilde{m}\beta|, \qquad [3.14]$$

and the transfer amplitudes become

$$a_X^{IS} = \frac{1}{2}\frac{\sum_m \cos(\delta_m \tau)\, \langle\widetilde{m}|O_S|\widetilde{m}\rangle}{Tr\{[O_S I_X]^2\}}, \qquad [3.15]$$

$$a_X^{SI} = \frac{1}{2}\frac{\sum_m \cos(\delta_m \tau)\, \langle\widetilde{m}|O_S|\widetilde{m}\rangle}{Tr\{[I_X]^2\}}. \qquad [3.16]$$

For pathway $I_X \rightarrow a_Y^{IS} O_S I_Y \rightarrow a_Y^{IS} a_Y^{SI} I_X$, proceeding in the same way as above we find

$$a_Y^{IS} = \frac{1}{2}\frac{\sum_m \sin(\delta_m \tau)\,\langle \widetilde{m}|O_S|\widetilde{m}\rangle}{Tr\{[O_S I_Y]^2\}}, \tag{3.17}$$

$$a_Y^{SI} = -\frac{1}{2}\frac{\sum_m \sin(\delta_m \tau)\,\langle \widetilde{m}|O_S|\widetilde{m}\rangle}{Tr\{[I_X]^2\}}. \tag{3.18}$$

Therefore $a_X^{IS}a_X^{SI} > 0$ and $a_Y^{IS}a_Y^{SI} < 0$ hence *I*-spin signal coming via heteronuclear coherences involving I_X (I_Y) is indeed positive (negative) regardless of crystallite orientation in accordance with the numerical calculations shown in Figure 3.5.

In the actual T-HMQC experiment a π pulse is applied on the *I*-spin channel in the middle of $t_1$evolution, for refocusing *I*-spin offsets/chemical shifts. The influence of this pulse in defining the sign of the signal is investigated here. Let us consider first a π_X pulse. We have

$$I_X \rightarrow a_X^{IS}O_S I_X \xrightarrow{\pi_X} a_X^{IS}O_S I_X \rightarrow a_X^{IS}a_X^{SI}I_X, \tag{3.19}$$

$$I_X \rightarrow a_Y^{IS}O_S I_Y \xrightarrow{\pi_X} -a_Y^{IS}O_S I_Y \rightarrow -a_Y^{IS}a_Y^{SI}I_X, \tag{3.20}$$

and hence the sign of the signal with a π_X pulse is always positive regardless of the coherence type. For a π_Y pulse we have

$$I_X \rightarrow a_X^{IS}O_S I_X \xrightarrow{\pi_Y} -a_X^{IS}O_S I_X \rightarrow -a_X^{IS}a_X^{SI}I_X, \tag{3.21}$$

$$I_X \rightarrow a_Y^{IS}O_S I_Y \xrightarrow{\pi_Y} a_Y^{IS}O_S I_Y \rightarrow a_Y^{IS}a_Y^{SI}I_X. \tag{3.22}$$

Therefore, the sign of the *I*-spin signal with a π_Y pulse is always negative regardless of the coherence type. This ensures coherent addition of signals from different crystallite orientation regardless of the coherence type. However, it does not guarantee distortion-free lineshapes (e.g., for the indirect-dimension central transition (CT) lineshape) because as seen from Figure 3.5, the transfer amplitudes exhibit a strong dependence on crystallite orientation.

3.4 Continuous creation and evolution of coherences during TRAPDOR irradiation

We have analyzed excitation of coherences with the aid of an effective Hamiltonian which is capable to predict the state of the system only at multiples of the rotor period. In this section we take a look at dynamics at arbitrary times within the rotor period during TRAPDOR irradiation.

Figure 3.6 shows creation and evolution of a few heteronuclear coherences during first few (three) rotor periods, for a given crystallite orientation ($\beta = 50°,\ \gamma = 0°$), along with plots displaying eigenvalues of the S-spin part of the Hamiltonian in Eq. [3.1] as function of time. From the eigenvalue plot (Figure 3.6a) it can be seen that within every rotor period there are two level crossings, occurring at about 0.4 and $0.6T_{\mathrm{R}}$. Abrupt changes in the amplitude and phase of various coherences take place around the crossings and close examination leads to the following observations.

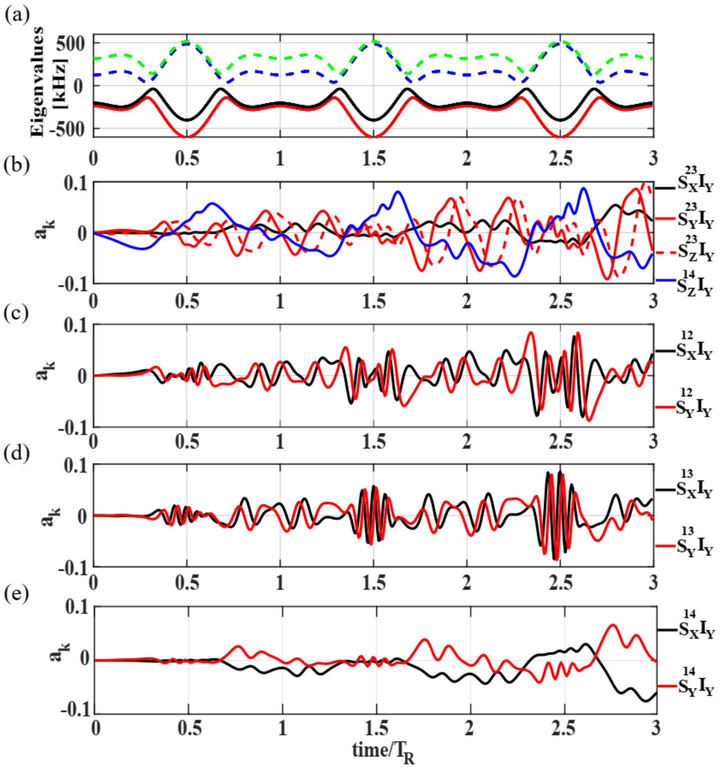

Figure 3.6 Creation of heteronuclear coherences at beginning ($0 - 3T_R$) *of TRAPDOR irradiation. (a) Eigenvalues of the S-spin part of the Hamiltonian in Eq. [3.1] over the same time period. (b-e) Time evolution of the amplitudes of various coherences. The parameters employed for simulation are:* $C_Q = 2\ MHz,\ \Delta\nu_S = 10\ kHz,\ \nu_D = 1\ kHz,\ \nu_{1S} = 100\ kHz,\ \nu_R = 60\ kHz,\ \beta = 50°, \gamma = 0°$.

O1. Till the first level crossing only one coherence, $S_Z^{14}I_Y$, (Figure 3.6b) is created with significant amplitude. Between any two consecutive crossings only $S_Z^{14}I_Y$ builds up visibly.

O2. At the first level crossing, central-transition, satellite-transition, and double-quantum coherences are produced at the expense of $S_Z^{14}I_Y$.

O3. Between consecutive level crossings, coherences exhibit a rather complex oscillatory pattern. At each crossing changes in the amplitude of these oscillations are noticeable.

O4. Amplitudes of central-transition, satellite-transition, and double-quantum coherences are comparable.

From Figure 3.6a, e it can be seen that coherences involving triple quantum S spin terms, $S_X^{14}I_Y$ and $S_Y^{14}I_Y$ are produced only after second crossing. This indicates that these coherences are not produced by interconversion of $S_Z^{14}I_Y$ at the level crossing but rather from other coherences.

Similar plots are displayed in Figure 3.7 and Figure 3.8 showing a window of evolution at much longer times ($\sim 100T_R$) where the amplitudes of various coherences are reaching maximal values. Though the behavior is complex, the following observations are noted.

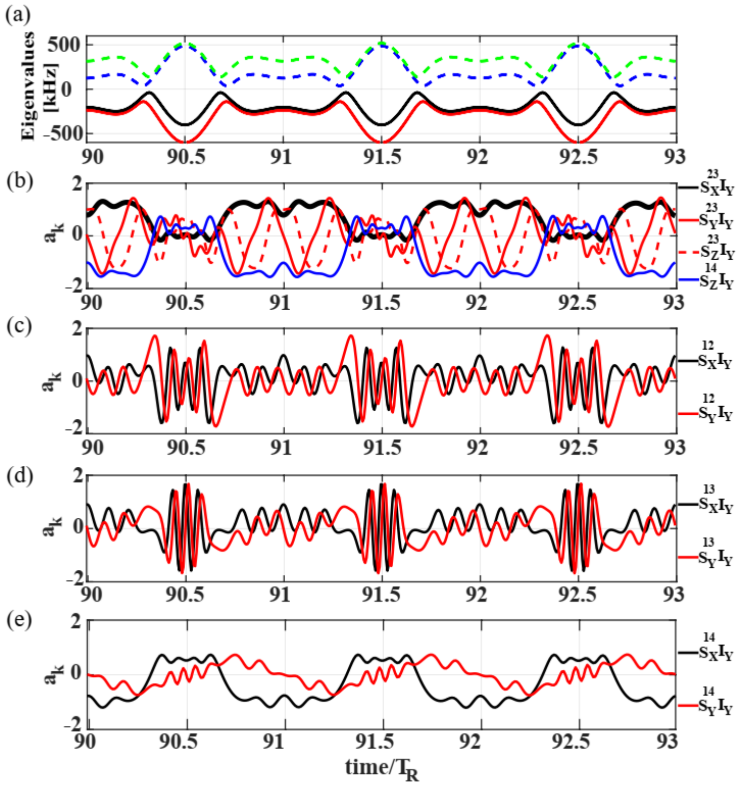

Figure 3.7 Heteronuclear coherences towards the end $(90 - 93T_R)$ *of TRAPDOR irradiation. (a) Eigenvalues of the S-spin part of the Hamiltonian in Eq. [3.1] over the same time period. (b-e) Evolution of amplitudes of various coherences. The parameters employed for simulation are:* $C_Q = 2\ MHz, \Delta\nu_S = 10\ kHz,\ \nu_D = 1\ kHz, \nu_{1S} = 100\ kHz, \nu_R = 60\ kHz, \beta = 50°, \gamma = 0°$.

O5. Coherences $S_Y^{23}I_Y$ and $S_Z^{23}I_Y$ seem to act in quadrature between crossings as seen in Figure 3.7b. The word *quadrature* is used here and later to indicate an exact or approximate 90° phase difference between the oscillations of two coherences.

O6. $S_X^{23}I_Y$ and $S_Z^{14}I_Y$ exhibits lesser variation than other coherences between crossings, Figure 3.7b.

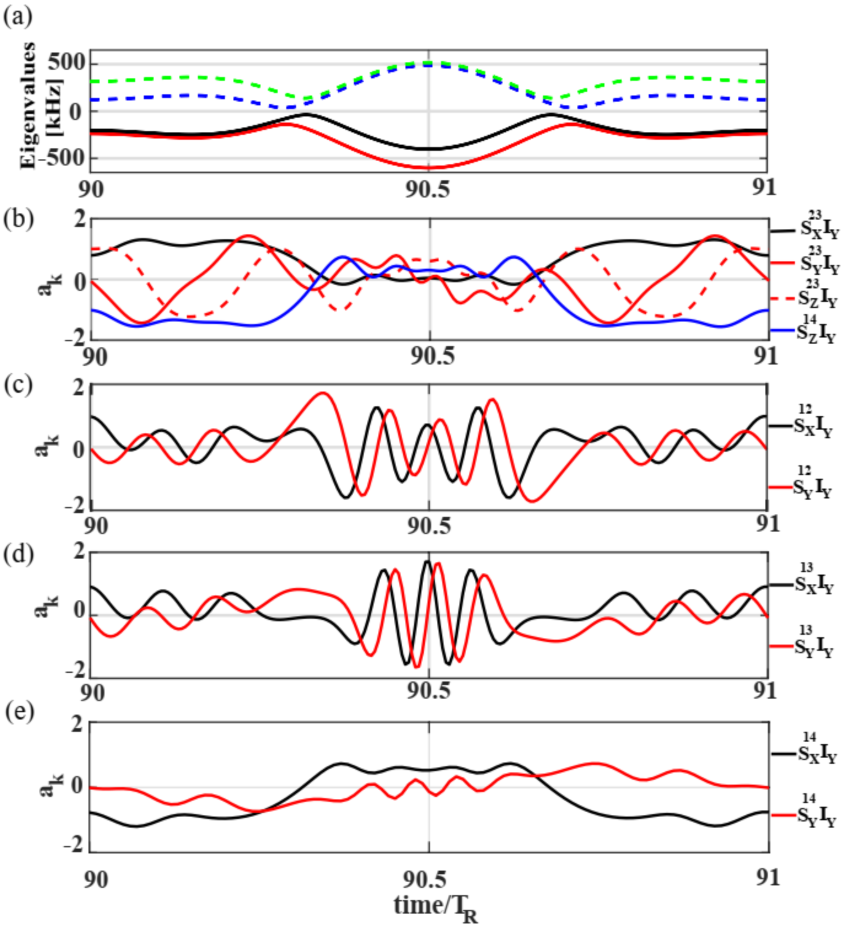

Figure 3.8 Expansion of Figure 3.7 showing evolution over one rotor period.

O7. Coherences $S_X^{12}I_Y$ and $S_Y^{12}I_Y$ seem to act in quadrature between crossings, Figure 3.7c and 3.8c.

O8. Coherences $S_X^{13}I_Y$ and $S_Y^{13}I_Y$ seem to act in quadrature between crossings, Figure 3.7d and 3.8d.

O9. Single-quantum satellite coherences and double-quantum coherences appear to interconvert between consecutive crossings, as seen from Figure 3.7c,d and 3.8c,d. This can be appreciated from the beat patterns of $S_X^{12}I_Y$, $S_Y^{12}I_Y$ versus $S_X^{13}I_Y$, $S_Y^{13}I_Y$ around $90.5T_R, 91.5T_R$, etc.

O10. The state of the system has entered an almost-periodic regime, $\rho(t) \cong \rho(t + kT_R)$ (with k not too large).

O11. Amplitudes for all coherences are comparable.

O12. Between two crossings $S_Z^{14}I_Y, S_X^{23}I_Y, S_Y^{23}I_Y, S_Z^{23}I_Y$ have either large or small amplitude as a group. When amplitudes in this group are large (small) amplitudes in a second group consisting of $S_X^{12}I_Y, S_Y^{12}I_Y, S_X^{13}I_Y, S_Y^{13}I_Y$ are small (large). This indicates systematic interconversions among the two groups at level crossings. However, $S_X^{14}I_Y$ and $S_Y^{14}I_Y$ do not seem to participate in this interconversion between the two groups.

Statements O1-O12 were introduced based on observations made for a particular β angle ($50°$) which corresponds to two level crossings per rotor period. Statements O1-O12 are observed, fully or partially, for most β angles capable of yielding reasonable T-HMQC signal. Statements O1-O5 seem to hold for all angles. However, 'quadrature' statements or interconversion statements may not be observed so easily for all β angles. Also, observation O12 may involve different sets of coherences. For β angles leading to four level crossings, due to smaller time intervals between crossings, quadrature and interconversion statements are more difficult to observe, Evolution of coherences for $\beta = 80°$, corresponding to four level crossings per rotor period, is presented in Appendix A3.7.

Theoretical description of evolution between consecutive level crossings

Most of the observations contained in O1-O12 are substantiated below within an approximate analytical approach. We consider first the evolution of coherences in time intervals between consecutive level crossings where, after the first of the consecutive crossings, heteronuclear coherences are already present. Since dipolar coupling considered here is small, for the time being, we neglect its effect. Also, for simplicity, we neglect $\mathcal{H}_Q^{(2)}$ (which is similar to an offset) and, dropping dependence on orientation in the notation, the time-dependent Hamiltonian is

$$\mathcal{H}(t) = \Delta\omega_S S_Z + \omega_{1S} S_X + \omega_Q(t)[3S_Z^2 - S(S+1)]. \qquad [3.23]$$

Between crossings eigenvectors of $\mathcal{H}(t)$ do not change significantly, allowing us to describe the time evolution via the time-independent Hamiltonian

$$\mathcal{H} = \Delta\omega_S S_Z + \omega_{1S} S_X + \bar{\omega}_Q[3S_Z^2 - S(S+1)], \qquad [3.24]$$

where $\bar{\omega}_Q = \frac{\int_{t_k}^{t_{k+1}} \omega_Q(t)dt}{t_{k+1}-t_k}$, and t_k and t_{k+1} are times of two consecutive crossings. The eigenvalues and eigenvectors of the static Hamiltonian in Eq. [3.24] have been described in Ref. [150-151]. For $\Delta\omega_S < \omega_{1S} < \bar{\omega}_Q$ it is allowed to neglect the satellite-transition RF terms, $S_X^{12}$and S_X^{34} (refer to eigenvector and eigenvalue description in Ref. [150] and a numerical investigation in Appendix A3.8). The Hamiltonian is then approximately the sum of two commuting terms

$$\mathcal{H}^{23} = \Delta\omega_S S_Z^{23} + 2\omega_{1S} S_X^{23} - 3\,\bar{\omega}_Q 1_S^{23}, \qquad [3.25]$$

and

$$\mathcal{H}^{14} = 3\Delta\omega_S S_Z^{14} + 3\,\bar{\omega}_Q 1_S^{14}. \qquad [3.26]$$

Defining $\omega_{eff} = \sqrt{\Delta\omega_S^2 + 4\omega_{1S}^2}$; $cos\phi = \Delta\omega_S/\omega_{eff}$; $sin\phi = 2\omega_{1S}/\omega_{eff}$ it is found (Appendix A3.9) that for initial central-transition coherences, evolution under the Hamiltonian in Eq. [3.25] gives

$$\begin{aligned} S_X^{23} I_Y \rightarrow & \left[\cos^2(\omega_{eff}t/2) - \sin^2(\omega_{eff}t/2) cos2\phi\right] S_X^{23} I_Y + \left[\sin(\omega_{eff}t)\, cos\phi\right] S_Y^{23} I_Y \\ & + \left[\sin^2(\omega_{eff}t/2) sin2\phi\right] S_Z^{23} I_Y, \end{aligned} \qquad [3.27]$$

$$\begin{aligned} S_Y^{23} I_Y \rightarrow & \left[\cos(\omega_{eff}t)\right] S_Y^{23} I_Y - \left[\sin(\omega_{eff}t)\, cos\phi\right] S_X^{23} I_Y \\ & + \left[\sin(\omega_{eff}t)\, sin\phi\right] S_Z^{23} I_Y, \end{aligned} \qquad [3.28]$$

$$\begin{aligned} & S_Z^{23} I_Y \\ & \rightarrow \left[\cos^2(\omega_{eff}t/2) + \sin^2(\omega_{eff}t/2) cos2\phi\right] S_Z^{23} I_Y + \left[\sin^2(\omega_{eff}t/2) sin2\phi\right] S_X^{23} I_Y \\ & - \left[\sin(\omega_{eff}t)\, sin\phi\right] S_Y^{23} I_Y. \end{aligned} \qquad [3.29]$$

For small offsets $\phi \cong \pi/2$ and setting $cos\phi \cong 0, cos2\phi \cong -1, sin\phi \cong 1, sin2\phi \cong 0$, it follows that $S_X^{23} I_Y \cong constant$ and that $S_Y^{23} I_Y$ and $S_Z^{23} I_Y$ are almost in quadrature. This justifies O5 and part of O6.

On the other hand, for an initial satellite-transition coherence $S_X^{12} I_Y$, it is found that

$$\begin{aligned} S_X^{12}I_Y \rightarrow \Big[& cos\left(6\overline{\omega}_Q t + \frac{3}{2}\Delta\omega_S t\right)\cos\left(\frac{\omega_{eff}t}{2}\right) \\ & + \sin\left(6\overline{\omega}_Q t + \frac{3}{2}\Delta\omega_S t\right)\sin\left(\frac{\omega_{eff}t}{2}\right) cos\phi\Big] S_X^{12}I_Y \\ & - \left[cos\left(6\overline{\omega}_Q t + \frac{3}{2}\Delta\omega_S t\right)\sin\left(\frac{\omega_{eff}t}{2}\right) cos\phi \right. \\ & \left. - \sin\left(6\overline{\omega}_Q t + \frac{3}{2}\Delta\omega_S t\right)\cos\left(\frac{\omega_{eff}t}{2}\right)\right] S_Y^{12}I_Y \\ & + \left[sin\left(6\overline{\omega}_Q t + \frac{3}{2}\Delta\omega_S t\right)\sin\left(\frac{\omega_{eff}t}{2}\right) sin\phi\right] S_X^{13}I_Y \\ & - \left[cos\left(6\overline{\omega}_Q t + \frac{3}{2}\Delta\omega_S t\right) sin\left(\frac{\omega_{eff}t}{2}\right) sin\phi\right] S_Y^{13}I_Y. \qquad [3.30a] \end{aligned}$$

For small offsets $\phi \cong \pi/2$ and setting $cos\phi \cong 0, cos2\phi \cong -1, sin\phi \cong 1, sin2\phi \cong 0$, Eq. [3.30a] becomes

$$\begin{aligned} S_X^{12}I_Y \rightarrow \cos\left(\frac{\omega_{eff}t}{2}\right) & \left[cos\left(6\overline{\omega}_Q t + \frac{3}{2}\Delta\omega_S t\right) S_X^{12}I_Y + \sin\left(6\overline{\omega}_Q t + \frac{3}{2}\Delta\omega_S t\right) S_Y^{12}I_Y\right] \\ & + \left[sin\left(6\overline{\omega}_Q t + \frac{3}{2}\Delta\omega_S t\right)\sin\left(\frac{\omega_{eff}t}{2}\right)\right] S_X^{13}I_Y \\ & - \left[cos\left(6\overline{\omega}_Q t + \frac{3}{2}\Delta\omega_S t\right) sin\left(\frac{\omega_{eff}t}{2}\right)\right] S_Y^{13}I_Y. \qquad [3.30b] \end{aligned}$$

This approximate equation exhibits quadrature between $S_X^{12}I_Y$ and $S_Y^{12}I_Y$ and at larger times (through $sin\left(\frac{\omega_{eff}t}{2}\right)$) creation of double-quantum coherences $S_X^{13}I_Y$ and $S_Y^{13}I_Y$. Similarly, starting with double-quantum coherence $S_X^{13}I_Y$ it is found that it evolves in quadrature with $S_Y^{13}I_Y$ and that at later times satellite transition $S_X^{12}I_Y$ and $S_Y^{12}I_Y$ are produced. Analogous behaviour is observed also with initial coherences $S_Y^{12}I_Y$ and $S_Y^{13}I_Y$. With this, statements contained in O7-O9 are justified.

Finally, for initial heteronuclear coherences involving S-spin triple-quantum terms we have

$$S_X^{14}I_Y \rightarrow cos(3\Delta_S t)S_X^{14}I_Y + sin(3\Delta_S t)S_Y^{14}I_Y, \qquad [3.31a]$$

$$S_Y^{14}I_Y \rightarrow cos(3\Delta_S t)S_Y^{14}I_Y - sin(3\Delta_S t)S_X^{14}I_Y. \qquad [3.31b]$$

Eq. [3.31] predict quadrature evolution. However, Figure 3.7, 3.8 do not reveal quadrature evolution for $S_X^{14}I_Y$ and $S_Y^{14}I_Y$. This may be due to the combination of two reasons: (a) comparable initial amplitudes of $S_X^{14}I_Y$ and $S_Y^{14}I_Y$, and (b) insufficient time spent between two consecutive crossings such that only incomplete oscillations of $S_X^{14}I_Y$ and $S_Y^{14}I_Y$ are performed. In fact, it is possible to reproduce qualitatively the behaviour in Figure 3.7 and 3.8 by using Eq. [3.31] with appropriate initial conditions for $S_X^{14}I_Y$ and $S_Y^{14}I_Y$.

Within the same approximation employed in Eq. [3.25, 3.26] we consider now the effect of the dipolar coupling in the time interval τ between $t = 0$ and the first level crossing. Introducing in a similar way the dipolar interaction averaged over τ, $\bar{d}2I_Z S_Z$, the Hamiltonian is then the sum of commuting parts

$$\mathcal{H}^{14} = 3\Delta\omega_S S_Z^{14} + 3\bar{\varpi}_Q \mathbf{1}_S^{14} + \bar{d}6I_Z S_Z^{14}, \qquad [3.32]$$

$$\mathcal{H}^{23} = \Delta\omega_S S_Z^{23} + \mathbf{2}\omega_{1S} S_X^{23} - 3\bar{\varpi}_Q \mathbf{1}_S^{23} + \bar{d}2I_Z S_Z^{23}. \qquad [3.33]$$

With the initial condition $\rho(0) = I_X$ it is found (Appendix A3.10) that the state of the system at some time *t* before first level crossing is

$$\begin{aligned}
\rho(t) = {} & \cos 3\bar{d}t\, \mathbf{1}_S^{14} I_X + \sin 3\bar{d}t\, 2S_Z^{14} I_Y \\
& + \left[\cos\left(\frac{\omega_+ t}{2}\right)\cos\left(\frac{\omega_- t}{2}\right) + \sin\left(\frac{\omega_+ t}{2}\right)\sin\left(\frac{\omega_- t}{2}\right)\cos(\phi_+ - \phi_-)\right]\mathbf{1}_S^{23} I_X \\
& + \left[\cos\phi_+ \sin\left(\frac{\omega_+ t}{2}\right)\cos\left(\frac{\omega_- t}{2}\right) - \cos\phi_- \cos\left(\frac{\omega_+ t}{2}\right)\sin\left(\frac{\omega_- t}{2}\right)\right] 2S_Z^{23} I_Y \\
& + \left[\sin\phi_+ \sin\left(\frac{\omega_+ t}{2}\right)\cos\left(\frac{\omega_- t}{2}\right) - \sin\phi_- \cos\left(\frac{\omega_+ t}{2}\right)\sin\left(\frac{\omega_- t}{2}\right)\right] 2S_X^{23} I_Y \\
& + \sin\left(\frac{\omega_+ t}{2}\right)\sin\left(\frac{\omega_- t}{2}\right)\sin(\phi_+ - \phi_-) 2S_Y^{23} I_Y, \qquad [3.34]
\end{aligned}$$

where $\cos\phi_\pm = \left(\Delta\omega_S \pm \bar{d}\right)/\omega_\pm, \sin\phi_\pm = 2\omega_{1S}/\omega_\pm,\ \omega_\pm = \sqrt{\left(\Delta\omega_S \pm \bar{d}\right)^2 + 4\omega_{1S}^2}$. If $\bar{d} \ll \Delta\omega_S \ll \omega_{1S}$ a simple expression for $\rho(t)$ is obtained,

$$\begin{aligned}
\rho(t) = {} & \cos 3\bar{d}t\, \mathbf{1}_S^{14} I_X + \sin 3\bar{d}t\, 2S_Z^{14} I_Y + \cos\left[\frac{(\omega_+ - \omega_-)t}{2}\right]\mathbf{1}_S^{23} I_X \\
& + \sin\left[\frac{(\omega_+ - \omega_-)t}{2}\right] 2S_X^{23} I_Y. \qquad [3.35]
\end{aligned}$$

From Eq. [3.35] it can be seen that heteronuclear coherences $S_Z^{14}I_Y$ and $S_X^{23}I_Y$ build up. However, due to the very small difference between ω_+ and ω_-, $S_X^{23}I_Y$ builds up very slowly in comparison with $S_Z^{14}I_Y$. We can see this by taking $\omega_{1S}/2\pi = 100$ kHz, $\Delta\omega_S/2\pi =$

10 kHz, $\bar{d}/2\pi = 0.5$ kHz and obtaining $\frac{1}{2}(\omega_+ - \omega_-)/2\pi = 25$ Hz, which is much smaller than $3\bar{d}/2\pi = 1.5$ kHz. We conclude that, for the *short* evolution time τ from $t = 0$ to first crossing, the major coherence created is $S_Z^{14}I_Y$, thus explaining observation O1. Starting with first level crossing other coherences are created by conversion from $S_Z^{14}I_Y$. From Figure 3.6 we see that the only coherence which builds up visibly *between* any two consecutive crossings is $S_Z^{14}I_Y$. The buildup of $S_X^{23}I_Y$ between consecutive crossings is not perceptible because of the same reason, the smallness of $(\omega_+ - \omega_-)$.

Transfer process and level crossings in quadrupolar systems revisited

An essential role in the transfer process is played by the behaviour of coherences during level crossings. According to A. J. Vega this behaviour depends on the swiftness of the passage of the system through the level crossings and three regimes are defined: the adiabatic, the intermediate, and the fast.[150,151] In this section we attempt to envisage the spin dynamics during TRAPDOR irradiation in the context of the three regimes.

In the adiabatic regime, if the system is initially in an eigenstate $|\epsilon(0)\rangle$ of the time-dependent Hamiltonian, it will evolve into the eigenstate $|\epsilon(t)\rangle$ at any time t. For $\Delta\omega_S < \omega_{1S} < \max(\omega_Q(t))$ the eigenstates away from the level crossings are approximately $|1\rangle, |c_+\rangle = (|2\rangle + |3\rangle)/\sqrt{2}, |c_-\rangle = (|2\rangle - |3\rangle)/\sqrt{2}, |4\rangle$, and during any level crossing they interchange as $|1\rangle \leftrightarrow |c_+\rangle, |4\rangle \leftrightarrow |c_-\rangle$.[150,151] With this it follows that various coherences will interchange according to well defined rules. Relevant for us is the $S_Z^{14} \leftrightarrow S_X^{23}$ interchange. Indeed, we have seen that before first crossing only $S_Z^{14}I_Y$ builds up significantly and therefore this coherence should pass into $S_X^{23}I_Y$ at the crossing. Between the first and second crossing $S_Z^{14}I_Y$ builds up again from I_X while $S_X^{23}I_Y$ does not change much. At second crossing $S_X^{23}I_Y$ and $S_Z^{14}I_Y$ interchange and so on. Other coherences do not participate to this 'exchange' process. Very important, heteronuclear coherences involving *S*-spin double-quantum terms cannot be created in the adiabatic case hence double-quantum T-HMQC would not be efficient. Moreover, the adiabatic case can be achieved only at very low spinning speeds, which will not work due to proton dephasing. The adiabatic case is illustrated in Figure 3.9.

From Figure 3.9 it can be seen that appreciable amplitudes of $S_X^{12}I_Y$, $S_X^{13}I_Y$, and $S_X^{14}I_Y$ occur as transients *during* the level crossings. *Between* crossings these amplitudes are always modest. When different crystallite orientations are considered, the position of the crossings will be different. Since the system spends considerably more time between crossings, few orientations will happen to have their crossings at the end of the TRAPDOR pulse and hence to lead to a large amplitude of $S_X^{12}I_Y$, $S_X^{13}I_Y$, and $S_X^{14}I_Y$. Therefore, we don't expect sizable signal via these coherences in a powder. The presence of $S_X^{12}I_Y$, $S_X^{13}I_Y$, and $S_X^{14}I_Y$ away from crossings indicates that the exact eigenstates of the Hamiltonian differ to some extent from the states $|1\rangle, |4\rangle, |c_+\rangle, and\ |c_-\rangle$. Finally, the absence of oscillations between consecutive crossings is a feature of the adiabatic process as under adiabatic conditions the density operator is commuting at any time with the time-dependent Hamiltonian.

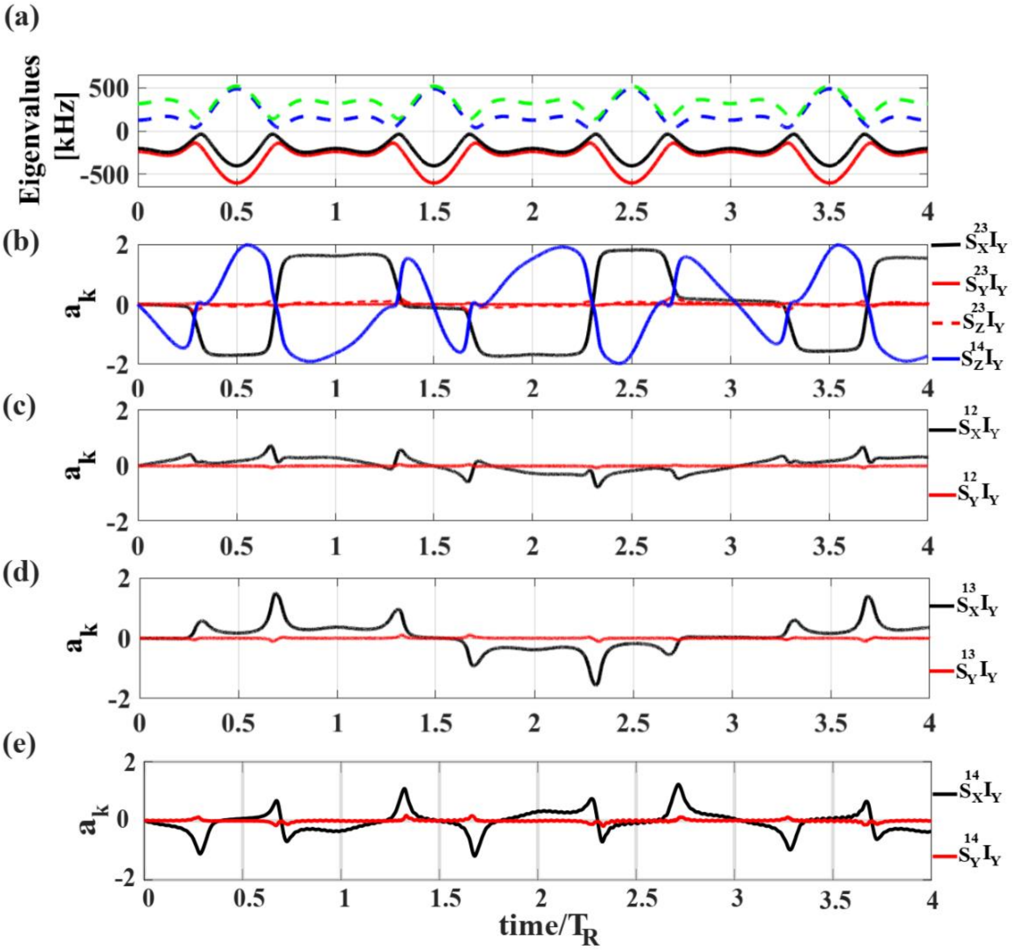

Figure 3.9 TRAPDOR evolution in the adiabatic regime at $\nu_R = 1\ kHz$. (a) Eigenvalues of the S-spin part of the Hamiltonian in Eq. [3.1] during first TRAPDOR irradiation pulse. (b-e) Creation and evolution of various coherences during the same period. Other parameters are: $C_Q = 2\ MHz$, $\Delta\nu_S = 10\ kHz$, $\nu_D = 1\ kHz$, $\nu_{1S} = 100\ kHz$, $\beta = 50°, \gamma = 0°$.

The parameters considered here, as well as in Ref. [20,21] correspond to the intermediate regime. In the intermediate regime, coherences interchange in a complex way during crossings. In Figure 3.6, at first crossing, $S_Z^{14}I_Y$ passes into a combination of heteronuclear coherences involving S-spin central-transition, satellite-transition, and double-quantum terms. With next crossings (Figure 3.6, 3.7, 3.8) the complex interchange results in production of different coherence types with comparable amplitude. Production of heteronuclear coherences involving *S*-spin double-quantum terms is possible and is indeed exploited in T-HMQC experiments.[20,21] However, an analytical description of dynamics during crossings is not available.

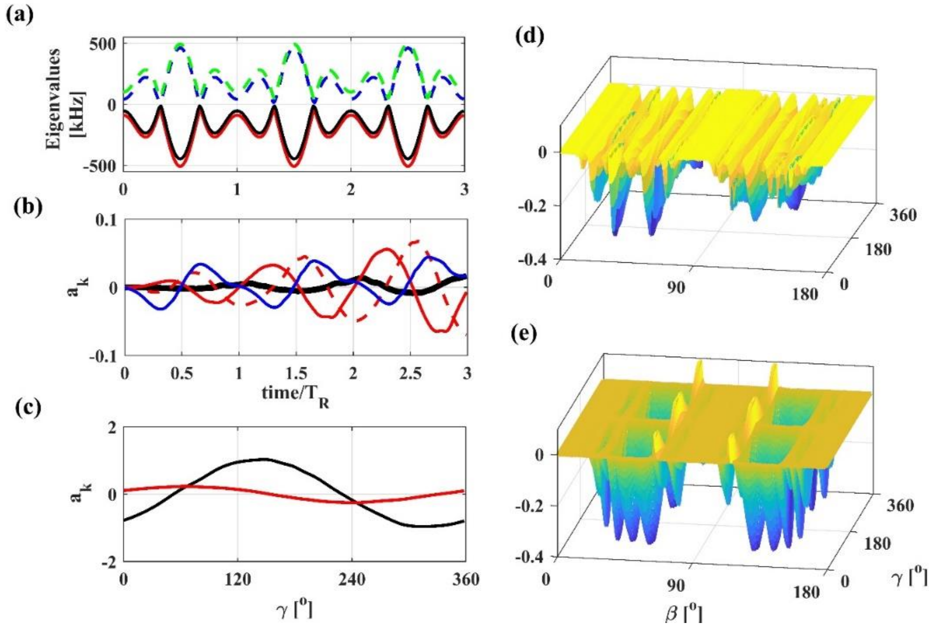

Figure 3.10 T-HMQC at rotary resonance. (a) Eigenvalues of S-spin part of the Hamiltonian as function of time for the first 3 rotor periods of TRAPDOR irradiation. (b) Creation of $S_X^{23}I_Y$ *(black),* $S_Y^{23}I_Y$ *(red),* $S_Z^{23}I_Y$ *(red dash), and* $S_Z^{14}I_Y$ *(blue) over the same period of time. (c) Amplitude of coherence* $S_Y^{23}I_Y$ *after* $100T_R$ *TRAPDOR irradiation, as function of* γ *for* $\beta = 65°$*. Calculations are performed with (red) and without (black) truncation approximation. (d) Amplitude of I-spin signal via* $S_X^{23}I_Y$ *pathway as function of* β *and* γ*. (e) Amplitude of I-spin signal via* $S_Y^{23}I_Y$ *pathway as function of* β *and* γ*. In (d) and (e) both TRAPDOR blocks have a duration* $100T_R$*. Other parameters common to all plots:* $C_Q = 2\ MHz$, $\Delta\nu_S = 10\ kHz$, $\nu_D = 1\ kHz$, $\nu_{1S} = 30\ kHz$*, and* $\nu_R = 60\ kHz$*.*

In the sudden regime the system passes so fast through crossings that any coherence present before crossing is found untouched after crossing. In this case the effective dipolar coupling $\bar{d}$ can be calculated by taking the average of $d(t)$ over one rotor period which yields $\bar{d} = 0$ and no transfer is produced. However, transfer can occur if a rotary resonance condition[73,156] can be achieved for the central transition, which is compatible with the sudden regime. For a spinning speed of 60 kHz the first rotary resonance condition $\omega_{1S} = \omega_R/2$ falls approximately in the sudden regime as it can be appreciated from Figure 3.10a and b where it can be seen that coherences involving central transition have little variation at the level crossings. Within first term in Magnus expansion, it was shown that the average Hamiltonian contains recoupled dipolar terms proportional to $S_Z^{23}I_Z$ and $S_Y^{23}I_Z$.[156] As a consequence, heteronuclear coherences involving central transition can be produced and utilized in a T-HMQC experiment. Within first term in Magnus expansion, no transfer is predicted to heteronuclear coherences involving S-spin double-quantum terms, and this feature is confirmed by simulations which indicate very low transfer efficiency to these coherences (not shown). In Figure 3.10c the amplitude of $S_Y^{23}I_Y$ at the end of first TRAPDOR irradiation is displayed as function of γ for $\beta = 65°$, and is evaluated with and without truncation approximation. The discrepancy clearly indicates the failure of truncation approximation for the chosen β angle. Simulations show similar behavior for other β in the range $60 - 70°$. In Figure 10d,e the I-spin T-HMQC signals ($t_1 = 0$) corresponding to $S_X^{23}I_Y$ and $S_Y^{23}I_Y$ are displayed as function of β and γ. It can be seen from Figure 10e that the sign of the signal due to $S_Y^{23}I_Y$ depends on β and γ. On the other hand, our proof that the sign of the signal is independent of the coherence type relies on the truncation approximation which, as we have shown above, is not valid at the rotary resonance. Moreover, the sign rule for the signal is violated for the same $60 - 70°$ range of β angle. Hence it appears that the constancy of the sign of the signal and the validity of truncation approximation may be closely related. Finally, we note that, for this rotary resonance condition, calculations performed with and without the time-dependent second-order quadrupolar Hamiltonian resulted in different outcomes, indicating the necessity of taking into account the full second-order quadrupolar Hamiltonian. On the other hand, for ν_{1S} in the range of interest, 90-110 kHz, simulations performed with and without the time-dependent second-order quadrupolar Hamiltonian led to extremely small differences for all crystallite orientations.

For the following discussion we reproduce again observation O1 according to which, (a) till the first level crossing, only $S_Z^{14}I_Y$ is created with significant amplitude and (b) only $S_Z^{14}I_Y$ builds up visibly between any two consecutive crossings. These two statements lead to the thought that $S_Z^{14}I_Y$ is a sort of driving coherence: it would build between consecutive crossings and then it would get converted to other coherences during crossings. We have tested this conjecture by *artificially* erasing a given coherence at any moment during TRAPDOR irradiation and monitoring how this influences creation and evolution of all the other coherences. For any coherence erased it was found that creation of all other coherences was suppressed to a certain degree. However, when the coherence continuously erased was $S_Z^{14}I_Y$, the suppression of other coherences was the most efficient (amplitudes of created coherences are one or two orders of magnitude smaller than when erasing any other coherence). This supports the conjecture that $S_Z^{14}I_Y$ is the driving coherence, in the sense discussed above. The fact that, when erasing *any* given coherence, the buildup of *all other* coherences gets quenched to a certain degree is easily explained. If a coherence converts to the erased coherence the reverse transfer does not take place and, due to the complex coherence interconversion in the intermediate regime, the erasure acts as an overall damping process.

Finally, we will briefly discuss the role of the *S*-spin offset. In Ref. [20,21] it was shown, within the Floquet effective Hamiltonian formalism, that recoupling is not efficient at offset zero (irradiation of the centerband) but it may occur at discrete values of the offset (irradiation at a given sideband, etc.). Their approach could not be used with arbitrary offset values. However, numerical simulations presented in Ref. [20,21] show a fairly broad dependence of transfer efficiency on offset, indicating there are no narrow recoupling conditions. Although not really shedding more light, we add here a few observations. Figure 3.11 shows the continuous buildup of a few coherences during TRAPDOR irradiation for offset zero and 1 kHz (second order quadrupolar interaction set to zero). With zero offset no steady buildup of coherences is observed (Figure 3.11a-e). On the other hand, dynamics is significantly altered even with the small offset of 1 kHz and coherences start to build up at different rates (Figure 3.11f-j). Among others, we have a sizable buildup of $S_X^{23}I_Y$. On the contrary, at offset zero, it can be seen that amplitude of $S_X^{23}I_Y$ is *strictly* zero at arbitrary times. We have a simple and interesting proof of this, based on the symmetry of the time-dependent Hamiltonian (Appendix A3.11). With increasing offset values, rather similar buildup rates are observed for all coherences (Appendix A3.12).

Most simulations presented in this work have been performed with an offset of 10 kHz which is considerably smaller than the RF strength (100 kHz). Simulations with $\Delta\nu_S$ in the 0-60 kHz range show a steady increase in T-HMQC signals up to 10 kHz and comparable signals in the 10-60 kHz range. Regarding the structure of the effective Hamiltonian no qualitative differences are noted for different offsets, except for the fact that, although heteronuclear terms in the effective Hamiltonian are comparable for all offsets considered, they are strongly suppressed by the truncation when $\Delta\nu_S \cong 0$ kHz. Regarding evolution during crossings and between consecutive crossings, statements O1-O9 have been based on simulations with the small offset $\Delta\nu_S = 10$ kHz, and an approximate theoretical explanation for some of them was provided. For larger offsets, simulations reveal a more complex behavior of coherences between consecutive crossings. For example, quadrature evolution of pairs of coherences becomes less evident. This is not surprising since Eq. [3.27-3.30] couple pairs of coherences only in the limit of small offsets.

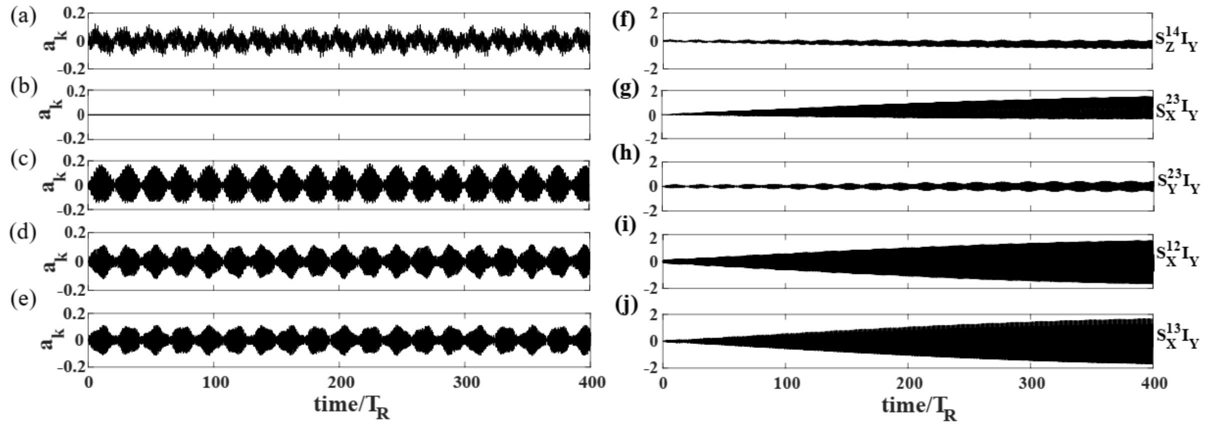

Figure 3.11 Amplitudes of several heteronuclear coherences during a period $400T_R$ *of TRAPDOR irradiation with (a-e)* $\Delta\nu_S = 0\ kHz$ *and (f-j)* $\Delta\nu_S = 1\ kHz$*. Other parameters employed are:* $C_Q = 2\ MHz,\ \nu_D = 1\ kHz, \nu_{1S} = 95\ kHz, \nu_R = 60\ kHz,\ \beta = 55°,$ *and* $\gamma = 0°$*. Second order quadrupolar interaction was set to zero.*

3.5 Conclusions

In this work we present a theoretical and numerical description of the T-HMQC experiment for a ^{1}H - ^{35}Cl (S = 3/2) spin system, with an emphasis on the dependence of signal on crystallite orientation and on the continuous creation, evolution, and inter-conversion of coherences at arbitrary times during TRAPDOR irradiation. This work can be seen as an addition to the approach and conclusions of Ref. [21].

To study the rich and complex spin dynamics due to the interference between the large time-dependent quadrupolar interaction and the RF field, an exact effective Hamiltonian was constructed numerically using the *matrix logarithm* approach. The different orders of magnitude of *pure-S* and *heteronuclear* terms in the exact effective Hamiltonian suggest a perturbative treatment or truncation of the later, as a first approximation. For the RF field strengths of interest, time-evolutions calculated with and without the truncation approximation are found to be in excellent agreement for dipolar couplings up to a few kHz, regardless of crystallite orientation. It is shown that, even with larger dipolar couplings (10-20 kHz), truncation approximation provides fair agreement with the calculations based on the exact effective Hamiltonian. The truncation procedure is similar to the procedure adopted in Ref. [21]. but is more general as it allows more heteronuclear terms to survive truncation.

When examining the structure of the exact effective Hamiltonian and of the amplitudes of various coherences produced by first TRAPDOR irradiation, we observe a functional resemblance between amplitudes of coherences and coefficients of various terms in the truncated effective Hamiltonian, as function of crystallite orientation. Utilizing the truncation approximation and a Taylor expansion of the propagator, we have justified the functional resemblance for coherences involving I_Y. However, for coherences involving I_X such a functional resemblance is not apparent. Coherences involving I_X develop at longer times, due to higher order terms in the Taylor expansion, resulting in complex dependence.

Subsequently, for the full T-HMQC experiment, the truncation approximation is utilized to derive analytically the dependence of the sign (phase) of the I-spin signal on the coherence type created by TRAPDOR irradiation. We show that, without a π pulse on I channel in the middle of the indirect dimension, sign of signals originating from different coherence types can be positive or negative, but for a given coherence it is independent of crystallite orientation. However, with the π pulse, we demonstrate that signals originating from *any* indirect-dimension coherences have the same sign. This overall sign depends on the phase of the π pulse.

An analysis of spin dynamics at arbitrary times during TRAPDOR irradiation has also been performed. Behaviour between consecutive crossings is described analytically within an approximation often used, which retains RF effects only in the central-transition subspace. Equations reveal 'quadrature' evolution of pairs of coherences and coherence interconversion e.g., between single-quantum satellite transition and double-quantum transition coherences. The adiabatic, sudden, and intermediate regimes for T-HMQC are discussed within the approach established by A. J. Vega, in which spin dynamics around crossings depends on the swiftness of the passage through crossing. Equations as well as numerical simulations suggest that there exists a driving coherence ($S_Z^{14} I_Y$) which builds up between consecutive crossings and then gets distributed among other coherences at crossings. Based on this observation, it is shown that coherences involving S-spin double-quantum terms are not efficiently produced in the adiabatic and sudden regimes. We have considered also the first rotary resonance condition, which falls in the sudden regime. In this case efficient creation of coherence involving central-transition terms is possible. Interestingly, we see that the truncation approximation fails at rotary resonance and at the same time the sign of certain T-HMQC signals is not anymore independent on crystallite orientation. It seems there exists a connection between these two features but the reason for this connection is not clear at present. In the intermediate regime redistribution of the driving coherence to other coherences is almost uniform such that coherences involving S-spin double-quantum terms may be efficiently produced as in fact demonstrated in Ref. [20,21].

Finally, we studied the continuous creation and evolution of heteronuclear coherences as function of the *S*-spin offset for individual crystallite orientations. With zero offset, most coherences are created during TRAPDOR irradiation but exhibit a low-amplitude beat pattern which prevents a steady buildup, resulting in overall low sensitivity for a powder. Introduction of small offsets (~1 kHz) leads to a radical change in the dynamics: different heteronuclear coherences exhibit a steady buildup, albeit at quite different rates. With larger offsets (~ 4 kHz or above) the buildup rates of most coherences are similar resulting in efficient transfer for most coherence types.

4

Summary and Discussion

The work presented in this thesis constitutes a theoretical and numerical investigation of the spin-dynamics in two recently demonstrated experiments, the ^{1}H-^{14}N double cross-polarization under fast MAS experiment by Carnevale et al.[17,18] and the ^{1}H-^{35}Cl TRAPDOR-HMQC[20,21] experiment of Hung et al. Both experiments involve long periods of RF irradiation on the quadrupolar nuclei channel. Creation and evolution of various coherences generated in these proton-detected experiments are investigated. To analyse the rich and complex spin dynamics due to interference between the large time-dependent quadrupolar interaction and the RF field, an exact effective Hamiltonian is constructed numerically using the *matrix logarithm* approach. Structure of the effective Hamiltonian is connected with transfer amplitudes to various coherences, the output signal, etc. and, when possible, characteristic features of the spin dynamics are derived theoretically. The analysis also provides insight on the efficiency of these experiments under different experimental conditions.

First part of the work described, in Chapter 2, deals with a comprehensive investigation of $1H(I) \rightarrow 14N(S)$ CP spin dynamics and in particular the efficient $1H \rightarrow 14N \rightarrow 1H$ CP transfer in double CP experiments in the context of Ref. [17,18]. The matrix logarithm approach and Floquet theory are employed to compute numerically the effective Hamiltonian associated to the time dependent Hamiltonian associated with CP. Certain common features related to construction of effective Hamiltonians by both approaches are discussed. The main observations related to ^{1}H-^{14}N CPMAS/double CP transfer are: (a) various spin terms of the effective Hamiltonian exhibit a strong dependence on the crystallite orientation; (b) significant CP transfer occurs only when magnitudes of the effective ^{1}H and ^{14}N RF strengths are comparable, and simultaneously all pure ^{14}N terms in the effective Hamiltonian are small, except for the longitudinal and the RF terms; (c) the sign of ^{14}N CPMAS signal follows the sign of ^{14}N effective RF strength; (d) sign of the double CP signal is largely independent of crystallite orientation. Matching conditions employing multiples of the spinning frequency or involving different ^{14}N RF strengths are predicted and verified. An analytical proof of (d) is provided together with a theoretical estimate for the ratio of ^{1}H-^{14}N and ^{14}N-^{1}H transfer amplitudes which is further substantiated through simulations. In addition, it is found that double CP signals include contributions from several single-quantum coherences present after the first CP process. The uneven contribution from different coherences leads to a reversal of signal at very short contact times, a feature noted experimentally by Carnevale et al. The connection between CPMAS transfer and efficient spin-lock is discussed and illustrated. The factors affecting second-order quadrupolar lineshapes in double CP experiment are examined.

Second part of the work described in the thesis, Chapter 3, investigates the spin dynamics associated with TRAPDOR- HMQC[20,21] type experiments. A theoretical and numerical description of spin dynamics associated with TRAPDOR-HMQC (T-HMQC) experiment for a ^{1}H–^{35}Cl (I-S) spin system under fast MAS is discussed. Towards this, an exact effective Hamiltonian describing the system is numerically constructed with the matrix logarithm approach. The different magnitudes of heteronuclear and pure S terms in the effective Hamiltonian allow us to suggest a truncation approximation, which is shown to be in excellent agreement with the exact time evolution of the spin system. Limitations of this approximation, especially at the rotary resonance condition, are discussed. The truncated effective Hamiltonian is further employed to monitor the build-up of various coherences during TRAPDOR irradiation. We observe and explain a functional resemblance between the magnitude of different terms in the truncated effective Hamiltonian and the amplitudes of various coherences during TRAPDOR irradiation, as function of crystallite orientation. Subsequently, the dependence of the sign (phase) of the T-HMQC signal on the coherence type generated is investigated numerically and justified analytically. Proceeding beyond effective Hamiltonian predictions, we examine the continuous creation and evolution of various coherences at *arbitrary* times during RF irradiation, i.e., during and between avoided level crossings. Behaviour between consecutive crossings is described analytically and reveals ‘quadrature’ evolution of pairs of coherences and coherence interconversions. The adiabatic, sudden, and intermediate regimes for T-HMQC experiments are discussed within the approach established by A. J. Vega. Equations as well as numerical simulations suggest the existence of a driving coherence which builds up between consecutive crossings and then gets distributed at crossings among other coherences. It is found that, in the intermediate regime, redistribution of the driving coherence to other coherences during avoided level crossings is almost uniform, enabling efficient production of coherences involving ^{35}Cl spin double-quantum terms.

Discussions and Future Directions

In this thesis we have illustrated the application of the matrix logarithm approach, not only for numerical simulations, but also for gaining insight into the relevant spin coherences.

With a single spin pair of ^{1}H-^{14}N, most experimental observations in double CP experiments were justified with the aid of an effective Hamiltonian constructed with the matrix logarithm approach. We believe that the methods employed and the insight provided in this thesis may help in developing new ^{1}H-^{14}N polarization transfer schemes.

In the analysis of TRAPDOR-HMQC experiments we have utilized a dual approach. On one hand, several important conclusions were reached via effective Hamiltonian calculations. On the other hand, a more intimate understanding of the transfer process was provided by analysis of spin dynamics at arbitrary times during RF irradiation. This dual approach may be useful for the study of other time-dependent problems.

Finally, we believe that the studies presented in this thesis demonstrate the potential of the matrix logarithm approach, in understanding the underlying spin dynamics, and may encourage its applications to other complex experiments in solid state NMR.

Appendix 1

A1.1 Rotation of spin operators

The unitary operator corresponding to rotation in spin space is given by $R_Z(\theta) = \mathrm{e}^{-i\theta I_Z}$ for a rotation by an angle θ about Z axis. Under this operation a component of the spin operator, say I_X transforms into

$$R_Z(\theta) I_X R_Z(\theta)^{-1} = \mathrm{e}^{-i\theta I_Z} I_X \mathrm{e}^{+i\theta I_Z}. \qquad \text{[A1.1]}$$

Expansion of the above expression using Taylor series yields

$$R_Z(\theta) I_X R_Z(\theta)^{-1} = \left(1 - i\theta I_Z - \frac{\theta^2}{2} I_Z^2 + \cdots\right) I_X \left(1 + i\theta I_Z - \frac{\theta^2}{2} I_Z^2 + \cdots\right)$$

$$= I_X - i\theta[I_Z, I_X] - \frac{\theta^2}{2}\left[I_Z, [I_Z, I_X]\right] + \frac{i\theta^3}{6}\left[I_Z, \left[I_Z, [I_Z, I_X]\right]\right] + \cdots \qquad \text{[A1.2]}$$

Using the identities corresponding to the cyclic permutation of the angular momentum operators,

$$[I_X, I_Y] = iI_Z, [I_Z, I_X] = iI_Y, [I_Y, I_Z] = iI_X, \qquad \text{[A1.3]}$$

the various commutators appearing above can be replaced as

$$I_X - i\theta[I_Z, I_X] - \frac{\theta^2}{2}\left[I_Z, [I_Z, I_X]\right] + \frac{i\theta^3}{6}\left[I_Z, \left[I_Z, [I_Z, I_X]\right]\right] + \cdots$$

$$= I_X + \theta I_Y - \frac{\theta^2}{2} I_X - \frac{i\theta^3}{6} I_Y + \cdots$$

$$= I_X\left(1 - \frac{\theta^2}{2} + \cdots\right) + I_Y\left(\theta - \frac{i\theta^3}{6} + \cdots\right) \qquad \text{[A1.4]}$$

after grouping and rearranging. Using the series expansions $\cos\theta = \left(1 - \frac{\theta^2}{2} + \cdots\right)$ and $\sin\theta = \left(\theta - \frac{i\theta^3}{6} + \cdots\right)$, the above expression can be simplified as

$$R_Z(\theta) I_X R_Z(\theta)^{-1} = I_X \cos\,\theta + I_Y \sin\,\theta \qquad \text{[A1.5a]}$$

Proceeding in the same way one obtains

$$R_Z(\theta) I_Y R_Z(\theta)^{-1} = I_Y \cos\theta - I_X \sin\theta. \qquad \text{[A1.5b]}$$

Since $R_Z(\theta)$ commutes with I_Z we have $R_Z(\theta) I_Z R_Z(\theta)^{-1} \;= I_Z$

For rotations about X axis,

$$R_X(\theta) I_X R_X(\theta)^{-1} \;= I_X,$$

$$R_X(\theta) I_Y R_X(\theta)^{-1} \;= I_Y \cos\theta + I_Z \sin\theta,$$

$$R_X(\theta) I_Z R_X(\theta)^{-1} \;= I_Z \cos\theta - I_Y \sin\theta. \qquad \text{[A1.5c]}$$

For rotations about Y axis,

$$R_Y(\theta) I_Y R_Y(\theta)^{-1} \;= I_Y,$$

$$R_Y(\theta) I_X R_Y(\theta)^{-1} \;= I_X \cos\theta - I_Z \sin\theta,$$

$$R_Y(\theta) I_Z R_Y(\theta)^{-1} \;= I_Z \cos\theta + I_X \sin\theta. \qquad \text{[A1.5d]}$$

A1.2 The spherical tensor formalism

The framework of irreducible spherical tensors is used to represent the Hamiltonians, and as it is illustrated, it has a spatial part and a spin part with characteristics that correspond to each interaction. The interactions are in their respective principal axis frames whereas the measurements are done in the lab frame. As a result, it must be translated into the lab frame using the Wigner rotation matrices illustrated here. As frame transformations require rotations, it will be more convenient to express Hamiltonians on a spherical basis, which transform in the same way as the spherical harmonics.

Frame transformations and form of the interaction Hamiltonian:

The general form of the Hamiltonian representing any internal interaction can be written as a scalar product of two irreducible spherical tensors

$$\boldsymbol{\mathcal{H}^{F}_{int}} = \left[\boldsymbol{C}\,\boldsymbol{I} \cdot \overleftrightarrow{\boldsymbol{A}} \cdot \boldsymbol{S}\right]^{\boldsymbol{F}}_{\boldsymbol{int}} \qquad \text{[A1.6a]}$$

$$\boldsymbol{\mathcal{H}^{F}_{int}} = \boldsymbol{C}_{int} \sum_{lm} A^{int,F}_{l,m} I_l S_m{}^{int} = \boldsymbol{C}_{int} \sum_{lm} A^{int,F}_{l,m} T^{int}_{l,m} = \boldsymbol{C}_{int} \sum_{l=0}^{2} \sum_{m=-l}^{l} (-1)^m A^{int,F}_{l,m} T^{int}_{l,-m}$$

[A1.6b]

where $\overleftrightarrow{\boldsymbol{A}}$: Second rank Cartesian tensor, describing the strength and anisotropy of the respective interaction Hamiltonian, denoted as 'int', $\boldsymbol{F}$: Frame considered, $\boldsymbol{I}, \boldsymbol{S}$: Cartesian spin operators corresponding to each interaction and $T_{l,m}^{int} = I_l S_m{}^{int}$: Composed of isotropic, symmetric and antisymmetric second rank cartesian tensors, $T_{iso} = \frac{1}{3} Trace\left(T_{l,m}^{int}\right) = \frac{1}{3} \sum_{l,m} T_{l,m}^{int} \, \delta_{l,m}, T_{asym} = \frac{1}{2}\left(T_{l,m}^{int} - T_{m,l}^{int}\right)$ and $T_{sym} = \frac{1}{2}\left(T_{l,m}^{int} + T_{m,l}^{int}\right) - T_{iso}$.

Chemical shift and J coupling interactions possess an isotropic part. The tensors representing the Hamiltonians of interest in this work are mostly symmetric (Dipolar and quadrupolar interactions). Antisymmetric part (chemical shift, J-coupling interactions) can be neglected as they have little effect on the NMR spectra. The interaction Hamiltonian in terms of the spatial and spin parts of a second rank tensor under spherical tensor formalism are enlisted below in Table A1.1.

Interaction	$\boldsymbol{I}$	$\overleftrightarrow{\boldsymbol{A}}$	$\boldsymbol{S}$	$\boldsymbol{\mathcal{H}_{int}} = \left[\boldsymbol{C}\,\boldsymbol{I} \cdot \overleftrightarrow{\boldsymbol{A}} \cdot \boldsymbol{S}\right]_{\boldsymbol{int}}$
Chemical shift	$(\boldsymbol{I_X}, \boldsymbol{I_Y}, \boldsymbol{I_Z})$	$\overleftrightarrow{\boldsymbol{\sigma}}$	$\gamma(\boldsymbol{0}, \boldsymbol{0}, \boldsymbol{B_0})$	$\mathcal{H}_{CS} = \gamma \boldsymbol{I} \cdot \overleftrightarrow{\boldsymbol{\sigma}} \cdot \boldsymbol{B}$
Dipolar: Heteronuclear	$(\boldsymbol{I_X}, \boldsymbol{I_Y}, \boldsymbol{I_Z})$	$\overleftrightarrow{\boldsymbol{D}}_{\boldsymbol{IS}}$	$(\boldsymbol{S_X}, \boldsymbol{S_Y}, \boldsymbol{S_Z})$	$\mathcal{H}_D{}^{IS} = \boldsymbol{I} \cdot \overleftrightarrow{\boldsymbol{D}}_{\boldsymbol{IS}} \cdot \boldsymbol{S}$
Quadrupolar	$(\boldsymbol{I_X}, \boldsymbol{I_Y}, \boldsymbol{I_Z})$	$\overleftrightarrow{\boldsymbol{Q}}$	$(\boldsymbol{I_X}, \boldsymbol{I_Y}, \boldsymbol{I_Z})$	$H_Q = \boldsymbol{I} \cdot \overleftrightarrow{\boldsymbol{Q}} \cdot \boldsymbol{I}$

Table A1.1 The spatial and spin parts of a second rank tensor under spherical tensor formalism are listed in terms of their Cartesian counterparts.

The various frame of references (Figure A1.1) mentioned in this thesis are: (1). Principal axis frame (PAF) in which the tensor describing the interaction will be diagonal, (2). Rotor frame (ROTOR) which is employed during MAS such that the Z-axis coincides with the rotor axis, (3). Laboratory frame (LAB) in which measurements are taken, where the Z-axis is parallel to the direction of the externally applied field. Under a frame transformation from F to F' for an interaction 'int' : $\left[\overleftrightarrow{\boldsymbol{A}^{(l)}}\right]^{int,F'} = \overleftrightarrow{\boldsymbol{A}^{(l)}}^{int,F} \boldsymbol{D}^{(l)}(\Omega_{FF'})$, where $\boldsymbol{D}^{(l)}(\Omega_{FF'})$ is the Wigner rotation matrix. The corresponding matrix elements transform according to : $\left[A_{l,m}\right]^{int,F'} = \sum_{m'=-l}^{l} A_{l,m'}{}^{int,F} D_{m'm}^{l}(\Omega_{FF'})$ where

$$D_{m'm}^{l}(\Omega_{FF'}) = \exp\{-im'\alpha_{FF'}\} d_{m'm}^{l}(\beta_{FF'}) \exp\{-im\gamma_{FF'}\},$$

are the matrix elements of the Wigner rotation matrix and $d^{l}_{m'm}$ are the matrix elements of the reduced Wigner rotation matrix and $\Omega_{FF'} = (\alpha_{FF'}, \beta_{FF'}, \gamma_{FF'})$ represent the Euler angles.

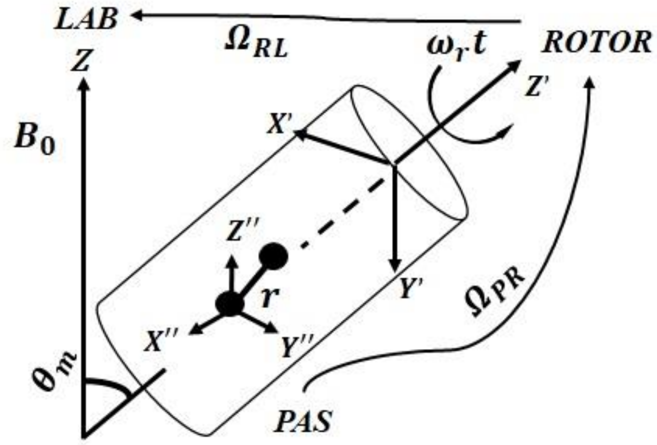

Figure A1.1 Various frames of references discussed in this thesis are schematized.

Wigner rotation matrices[157]

$$d^{(2)}_{00}(\beta) = \frac{1}{2}\,(3\cos^2\beta - 1) = P_2(\cos(\beta)),$$

$$d^{(2)}_{0\pm1}(\beta) = \pm\sqrt{\frac{3}{8}}\,\sin 2\beta,$$

$$d^{(2)}_{0\pm2}(\beta) = \sqrt{\frac{3}{8}}\,\sin^2\beta,$$

$$d^{(4)}_{00}(\beta) = \frac{1}{8}\,(35\cos^4\beta - 30\cos^2\beta + 3),$$

$$d^{(4)}_{0\pm1}(\beta) = \pm\sqrt{\frac{5}{16}}\,\sin\beta\,(7\cos^3\beta - 3\cos\beta),$$

$$d^{(4)}_{0\pm2}(\beta) = \sqrt{\frac{5}{32}}\,\sin^2\beta\,(7\cos^2\beta - 1),$$

$$d^{(4)}_{0\pm3}(\beta) = \pm\sqrt{\frac{35}{16}}\,\cos\beta\,\sin^3\beta,$$

$$d^{(4)}_{0\pm4}(\beta) = \sqrt{\frac{35}{128}}\,\sin^4\beta,$$

where $d^{(l)}_{mm'}(\beta) = (-1)^{m'} d^{(l)}_{m'm}(\beta)$.

Euler angles

$\Omega_{FF'} = (\alpha_{FF'}, \beta_{FF'}, \gamma_{FF'})$ represent the Euler angles transforming frame, F to F'. $\alpha_{FF'} \in (0,2\pi)$: rotation about the Z-axis, $\beta_{FF'} \in (0,\pi)$: rotation about new Y'-axis, $\gamma_{FF'} \in (0,2\pi)$: rotation about the new Z' −axis. Under the secular approximation, the Hamiltonians are invariant with respect to the rotation about the Z −axis. So, the γ angle transforming the principal axis frame to the laboratory frame can be omitted[32]. We have assumed that the orientations of the quadrupolar and dipolar interactions coincide for simplicity.

Using the idea described above, the expression for any interaction Hamiltonian in the laboratory frame can be derived starting from equation [A1.6a-b] as shown below:

$$\mathcal{H}_{int}^{LAB} = C_{int}\left[A_{0,0}^{int}\right]^{LAB}\left[T_{0,0}^{int}\right] + C_{int}\sum_{m=-1}^{1}(-1)^m\left[A_{1,-m}^{int}\right]^{LAB}\left[T_{1,m}^{int}\right]$$

$$+C_{int}\sum_{m=-2}^{2}(-1)^m\left[A_{2,-m}^{int}\right]^{LAB}\left[T_{2,m}^{int}\right]; \qquad \text{[A1.7]}$$

where $\left[A_{l,m}^{int}\right]^{LAB} = \sum_{m'=-l}^{l} D_{m',m}^{l}(\alpha,\beta,\gamma) R_{l,m'}^{int,PAF}$ and $R_{l,m'}^{int,PAF}$ denotes the spatial part in PAF (Table A1.2).

For $l = 0$: $\mathcal{H}_{int,l=0}^{PAF} = C_{int} R_{0,0}^{int,PAF}\left[T_{0,0}^{int}\right]$.

For $l = 1$: $\mathcal{H}_{int,l=1}^{PAF} = C_{int}\sum_{m=-1}^{1}(-1)^m R_{1,m}^{int,PAF}\left[T_{1,m}^{int}\right]$,

$$\mathcal{H}_{int,l=1}^{LAB} = C_{int}\sum_{m=-1}^{1}(-1)^m\left[A_{1,\mathrm{m}}^{int}\right]^{LAB}\left[T_{1,-m}^{int}\right].$$

As the antisymmetric part can be neglected as they have little effect on the NMR spectra, $l = 1$ terms are not considered.

For $l = 2$: $\mathcal{H}_{int,l=2}^{PAF} = C_{int}\sum_{m=-2}^{2}(-1)^m R_{2,m}^{int,PAF}\left[T_{2,m}^{int}\right]$,

$$\mathcal{H}_{int,l=2}^{LAB} = C_{int}\sum_{m=-2}^{2}(-1)^m\left[A_{2,m}^{int}\right]^{LAB}\left[T_{2,-m}^{int}\right],$$

$$\left[A_{2,m}^{int}\right]^{LAB} = \sum_{m'=-2}^{2} D_{m',m}^{2}(\alpha,\beta,\gamma) R_{2,m'}^{int,PAF}.$$

The spatial and spin parts of various internal interactions like chemical shift, dipolar, and quadrupolar Hamiltonians are written in the spherical tensor formalism as shown in Table A1.2.

Interaction Hamiltonian	***Spatial part (in PAF)***	***Spin part***
$\mathcal{H}_{CS}^{LAB} = \gamma \sum_{l=0}^{2} \sum_{m=-2}^{2} (-1)^m A_{l,m}^{CS} T_{l,-m}^{CS}$	$R_{0,0}^{CS,PAF} = -\frac{1}{\sqrt{3}} Tr[\sigma]$ $= -\sqrt{3}\sigma_{iso}$ $R_{1,0}^{CS,PAF} = 0$ *(symmetric)* $R_{1,\pm1}^{CS,PAF} = 0$ *(symmetric)* $R_{2,0}^{CS,PAF} = \sqrt{\frac{3}{2}}\delta_{CS}$ $R_{2,\pm2}^{CS,PAF} = \frac{1}{2}\eta_{CS}\delta_{CS}$	$T_{0,0}^{CS} = -\frac{1}{\sqrt{3}} I_z B_0$ $T_{1,0}^{CS} = 0$ $T_{1,\pm1}^{CS} = -\frac{1}{2} I_\pm B_0$ $T_{2,0}^{CS} = \sqrt{\frac{2}{3}} I_z B_0$ $T_{2,\pm1}^{CS} = \mp\frac{1}{2} I_\pm B_0$ $T_{2,\pm2}^{CS} = 0$
$\mathcal{H}_{D}^{LAB} = \omega_{D,IS} \sum_{m=-2}^{2} (-1)^m A_{2,m}^{D} T_{2,-m}^{D}$ $\omega_{D,IS} = -\frac{\mu_0 \gamma_I \gamma_S \hbar}{4\pi r_{IS}^3}$ *(For homonuclear case: I and S becomes* I_1 *and* I_2 *)*	$R_{0,0}^{D,PAF} = 0$ $R_{1,0}^{D,PAF} = 0$ $R_{1,\pm1}^{D,PAF} = 0$ $R_{2,0}^{D,PAF} = \sqrt{6}$ $R_{2,\pm1}^{D,PAF} = -\sqrt{6}$ $R_{2,\pm2}^{D,PAF} = \sqrt{6}$	$T_{0,0}^{D} = -\frac{2}{\sqrt{3}}\left[I_z S_z + \frac{1}{2}(I_+ S_- + I_- S_+)\right]$ $T_{1,0}^{D} = \frac{1}{\sqrt{2}}(I_- S_+ - I_+ S_-)$ $T_{1,\pm1}^{D} = (-I_\pm S_z + I_z S_\pm)$ $T_{2,0}^{D} = \sqrt{\frac{1}{6}}[3I_z S_z - (I \cdot S)]$ $T_{2,\pm1}^{D} = \mp\frac{1}{2}(I_z S_\pm + I_\pm S_z)$ $T_{2,\pm2}^{D} = \frac{1}{2} I_\pm S_\pm$
$\mathcal{H}_{Q}^{LAB} = \frac{2\pi C_Q}{2I(2I-1)} \sum_{m=-2}^{2} (-1)^m A_{2,m}^{Q} T_{2,-m}^{Q}$	$R_{0,0}^{Q,PAF} = 0$ $R_{1,\pm1}^{Q,PAF} = 0$ $R_{2,0}^{Q,PAF} = \sqrt{\frac{3}{2}}$ $R_{2,\pm1}^{Q,PAF} = 0$ $R_{2,\pm2}^{Q,PAF} = \frac{1}{2}\eta_Q$	$T_{0,0}^{Q} = -\frac{1}{\sqrt{2}}$ $T_{1,0}^{Q} = \sqrt{2} I_z$ $T_{1,\pm1}^{Q} = \mp I_\pm$ $T_{2,0}^{Q} = \sqrt{\frac{1}{6}}[3I_z^2 - I(I+1)]$ $T_{2,\pm1}^{Q} = \mp\frac{1}{2}(I_z I_\pm + I_\pm I_z)$ $T_{2,\pm2}^{Q} = \frac{1}{2} I_\pm^2$

Table A1.2 The spatial and spin parts of various internal NMR interactions are tabulated in terms of the spherical tensors.

Examples

Dipolar interaction

$$\mathcal{H}_D^{LAB} = 0 + 0 - \left(\frac{\mu_0}{4\pi}\right)\frac{\gamma_I\gamma_S\hbar}{r^3}\sum_{m=-2}^{2} (-1)^m\left[A_{2,-m}^{D}\right]^{LAB}\left[T_{2,m}^{D}\right] \qquad \text{[A1.8a]}$$

$$\left[A_{2,\mathrm{m}}^{int}\right]^{LAB} = \sum_{m\prime=-2}^{2} R_{2,m'}^{int,PAF} D_{m\prime m}^{2}(\Omega_{PL});): \Omega_{PL}(\alpha_{PL}=\phi, \beta_{PL}=\theta, \gamma_{PL}=0).$$

$$= \sum_{m\prime=-2}^{2} R_{2,m'}^{int,PAF} d_{m\prime m}^{2}(\beta_{PL})\, exp\{-im'\alpha_{PL}\}\, exp\{-i0\gamma_{PL}\}$$

$$= \sum_{m\prime=-2}^{2} R_{2,m'}^{int,PAF} d_{m\prime m}^{2}(\theta)\, exp\{-im'\phi\}\, exp\{-i0\gamma_{PL}\}$$

Expanding, grouping and rearranging yields:

$$\mathcal{H}_D^{LAB} = -\left(\frac{\mu_0}{4\pi}\right)\frac{\gamma_I\gamma_S\hbar}{r^3}\left[A + B + C + D + E + F\right] \qquad \text{[A1.8b]}$$

where $A = I_zS_z(3\cos^2\theta - 1), B = -\frac{1}{4}[I_+S_- + I_-S_+](3\cos^2\theta - 1),$

$\mathrm{C} = \frac{3}{2}[I_zS_+ + I_+S_z]\sin\theta\cos\theta e^{-i\phi}, D = \frac{3}{2}[I_zS_- + I_-S_z]\sin\theta\cos\theta e^{+i\phi},$

$E = \frac{3}{4}[I_+S_+]\sin^2\theta e^{-2i\phi}$ and $F = \frac{3}{4}[I_-S_-]\sin^2\theta e^{+2i\phi}.$

Under secular approximation ($\boldsymbol{m = 0}$)

$$H_{int,l=2}^{LAB} = C_{int}\left[A_{2,0}^{int}\right]^{LAB}\left[T_{2,0}^{int}\right], \left[A_{2,0}^{int}\right]^{LAB} = \sum_{m'=-2}^{2} D_{m',0}^{2}(\alpha,\beta,\gamma)R_{2,m'}^{int,PAF} \qquad \text{[A1.9]}$$

For the transformation of the principal axis frame to the laboratory frame using the Euler angle, $\Omega_{PL}(\alpha_{PL}, \beta_{PL}, \gamma_{PL} = 0)$ for an interaction, int under secular approximation ($m = 0$), we have

$$\left[A_{2,0}^{int}\right]^{LAB} = \sum_{m\prime=-2}^{2} R_{2,m'}^{int,PAF} D_{m\prime 0}^{2}(\Omega_{PL}) = \sum_{m\prime=-2}^{2} R_{2,m'}^{int,PAF} d_{m\prime 0}^{2}(\beta_{PL})\, exp\{-im'\alpha_{PL}\}$$

where $D_{m0}^{2}(\Omega_{PL}) = exp\{-im'\alpha_{PL}\}\, d_{m0}^{2}(\beta_{PL})\, exp\{-i0\gamma_{PL}\} = d_{m0}^{2}(\beta_{PL})\, exp\{-im\alpha_{PL}\}$ and the Euler angle rotation can be written in terms of the polar angles (θ, ϕ): $\Omega_{PL}(\alpha_{PL} = \phi, \beta_{PL} = \theta, \gamma_{PL} = 0)$.

Dipolar interaction *(Homonuclear)*

$$\left[A_{2,0}^{D}\right]^{LAB} = R_{2,0}^{D,PAF} D_{00}^{2}(\Omega_{PL}) = R_{2,0}^{D,PAS} d_{00}^{2}(\beta_{PL})\, exp\{-i0\alpha_{PL}\}, \Omega_{PL}(\alpha = \phi, \beta = \theta, \gamma = 0)$$

$$\left[A_{2,0}^{D}\right]^{LAB} = R_{2,0}^{D,PAF} d_{00}^{2}(\theta)=\sqrt{6}\tfrac{1}{2}\,(3\cos^2\theta - 1),$$

$$\left[T_{2,0}^{D}\right] = \sqrt{\tfrac{1}{6}}\,[3I_zS_z - (I \cdot S)] = \sqrt{\tfrac{1}{6}}\,(3I_{1z}I_{2z} - I_1 \cdot I_2)$$

$$\mathcal{H}_{D,I_1I_2}^{LAB} = \omega_{D,I_1I_2}\left[A_{2,0}^{D}\right]^{LAB}\left[T_{2,0}^{int}\right] = \omega_{D,I_1I_2}\sqrt{6}\frac{1}{2}\,(3\,cos^2\theta - 1)\sqrt{\frac{1}{6}}(3I_{1z}I_{2z} - I_1 \cdot I_2$$

$$= \omega_{D,I_1I_2}(3cos^2\theta - 1)(3I_{1z}I_{2z} - I_1 \cdot I_2) \qquad [A1.10a]$$

Dipolar interaction *(Heteronuclear)*

$$\left[A_{2,0}^{D}\right]^{LAB} = R_{2,0}^{D,PAF} D_{00}^{2}(\Omega_{PL}) = R_{2,0}^{D,PAF} d_{00}^{2}(\beta_{PL})\, exp\{-i0\alpha_{PL}\}, \Omega_{PL}(\alpha = \phi, \beta = \theta, \gamma = 0)$$

$$\left[A_{2,0}^{D}\right]^{LAB} = R_{2,0}^{D,PAF} d_{00}^{2}(\theta)=\sqrt{6}\tfrac{1}{2}\,(3\cos^2\beta - 1),\ \left[T_{2,0}^{D}\right] = \sqrt{\tfrac{1}{6}}\,2I_zS_z$$

$$\mathcal{H}_{D,IS}^{LAB} = \omega_{D,IS}\left[A_{2,0}^{D}\right]^{LAB}\left[T_{2,0}^{int}\right] = \omega_{D,IS}\sqrt{6}\frac{1}{2}\,(3\,cos^2\beta - 1)\sqrt{\frac{1}{6}}[2I_zS_z]$$

$$= \omega_{D,IS}(3cos^2\theta - 1)I_zS_z = \omega_{D,IS}P_2\big(cos\,(\theta)\big)2I_zS_z \qquad [A1.10b]$$

Quadrupolar interaction

$$R_{2,0}^{Q,PAF} = \sqrt{\frac{3}{2}}, R_{2,\pm 2}^{Q,PAF} = \frac{1}{2}\eta_Q, T_{2,0}^{Q} = \sqrt{\frac{1}{6}}[3I_z^2 - I(I+1)], C_{int} = \frac{2\pi C_Q}{2I(2I-1)}$$

$$\left[A_{2,0}^{Q}\right]^{LAB} = \sum_{m'=-2}^{2} R_{2,m'}^{Q,PAF} D_{m'0}^{2}(\Omega_{PL})$$

$$= R_{2,0}^{Q,PAF} D_{00}^{2}(\Omega_{PL}) + R_{2,0}^{Q,PAF} D_{-20}^{2}(\Omega_{PL}) + R_{2,2}^{Q,PAF} D_{20}^{2}(\Omega_{PL})$$

$${H_Q}^{LAB} = \frac{\omega_Q}{4}\left[3\,cos^2\theta - 1 + \eta_Q\,sin^2\theta cos\ \ 2\phi\right][3S_z^2 - S(S+1)] \qquad [A1.11]$$

where $\omega_{\mathrm{Q}} = \frac{e^2qQ}{2S(2S-1)\hbar}$ is called the quadrupolar frequency.

Under MAS:

Introducing rotor frame in between principal axis frame and laboratory frames, we get

$$\left[A_{20}^{int}\right]^{LAB} = \sum_{m=-2}^{2} \left[A_{2m}^{int}\right]^{PAF} D_{0m}^{2}(\Omega_{PR}) D_{m0}^{2}(\Omega_{RL})$$

$$= \sum_{m=-2}^{2} \left[A_{2m}^{int}\right]^{PAF} D_{0m}^{2}(\Omega_{PR}) d_{m0}^{2}(\beta_{RL})\, exp\{im\omega_{r}t\}$$

$$= \sum_{m=-2}^{2} \left[A_{2m}^{int}\right]^{PAF} D_{0m}^{2}(\Omega_{PR}) d_{m0}^{2}(\theta_{m})\, exp\{im\omega_{r}t\}$$

where $D^{(2)}(\Omega_{PR})\{\alpha_{PR} = 0, \beta_{PR}, \gamma_{PR}\} = exp\{-i0\alpha_{PR}\}\, d_{m0}^{2}(\beta_{PR})\, exp\{-i\gamma_{PR}\}$

$$= d_{m0}^{2}(\beta_{PR})\, exp\{-i\gamma_{PR}\} \qquad \text{[A1.12]}$$

and $D^{(2)}(\Omega_{RL}(t))\ \{\alpha_{RL} = -\omega_{r}t, \beta_{RL} = \theta_{m}, \gamma_{RL} = 0\}$=$exp\{im\omega_{r}t\}\, d_{m0}^{2}(\theta_{m})\, exp\{-i0\gamma_{RL}\} = d_{m0}^{2}(\theta_{m})\, exp\{im\omega_{r}t\}$ represent the Wigner rotation matrices for the $PAF \rightarrow ROTOR$ and $ROTOR \rightarrow LAB$ transformations using Euler angles: Ω_{PR}: $\{\alpha_{PR} = 0, \beta_{PR}, \gamma_{PR}\}$ and $\Omega_{RL}(t)$: $\{\alpha_{RL} = -\omega_{r}t, \beta_{RL} = \theta_{m}, \gamma_{RL} = 0\}$.

For dipolar interaction, under secular approximation

$$[A_{20}^{\mathrm{D}}]^{LAB} = \sum_{m=-2}^{2} [R_{2m}^{\mathrm{D}}]^{PAF} d_{0m}^{2}(\beta_{D})\, exp\{-i\gamma_{D}\}\, d_{m0}^{2}(\theta_{m})\, exp\{im\omega_{r}t\}$$

Under MAS, the spatial part of the quadrupolar Hamiltonian becomes time-dependent

$$\left[A_{20}^{Q}\right]^{LAB} = \sum_{m=-2}^{2} R_{2m}^{Q,PAF} D_{0m}^{2}\left(\Omega_{PR}^{Q}\right) D_{m0}^{2}\left(\Omega_{RL}^{Q}\right)$$

$$= \sum_{m=-2}^{2} R_{2m}^{Q,PAF} D_{0m}^{2}\left(\Omega_{PR}^{Q}\right) d_{m0}^{2}\left(\beta_{RL}^{Q}\right) exp\{im\omega_{r}t\}$$

$$= \sum_{m=-2}^{2} R_{2m}^{Q,PAF} d_{0m}^{2}\left(\beta_{Q}\right) exp\left\{-i\gamma_{Q}\right\} d_{m0}^{2}(\theta_{m})\, exp\{im\omega_{r}t\}$$

where Ω_{PR}: $\left(\alpha = 0, \beta = \beta_{Q}, \gamma = \gamma_{Q}\right), \Omega_{RL}(t)$: $(\alpha = \omega_{R}t, \beta = \theta_{m} = 54.7^{0}, \gamma = 0)$. [A1.13]

A1.3 Application of Matrix Logarithm in Rotary Resonance Recoupling

As a simple illustration of the matrix logarithm approach, we consider the phenomenon of rotary resonance[73] for a heteronuclear spin system composed of two dipolar-coupled spins I and S ($I = S = 1/2$), with one spin (say S) subjected to continuous-wave irradiation. When the amplitude of the RF field satisfies $\omega_1 \cong \omega_R$ or $2\omega_R$, the dipolar interaction is recoupled and can be utilized to produce heteronuclear coherences. In the average Hamiltonian theory framework, we consider first the rotary resonance condition $\omega_1 \cong \omega_R$. Under MAS the Hamiltonian is given by

$$\mathcal{H}(t) = \omega_1 S_X + d(t) 2 I_Z S_Z, \qquad \text{[A1.14]}$$

where the time-dependent dipolar coupling

$$d(t) = \sum_{m=-2}^{2} d_m e^{i\omega_R t}, m \neq 0, \qquad \text{[A1.15]}$$

oscillates at ω_R and $2\omega_R$. In order to apply average Hamiltonian theory a new rotating frame is introduced by

$$U(t,0) = \exp[-i\omega_R t S_X]\, U_R(t,0). \qquad \text{[A1.16]}$$

The Hamiltonian corresponding to the new rotating frame is

$$\mathcal{H}_R(t) = (\omega_1 - \omega_R) S_X + d(t) 2 I_Z (S_Z \cos \omega_R t + S_Y \sin \omega_R t). \qquad \text{[A1.17]}$$

By expanding the cosine and sin in terms of $e^{\pm i\omega_R t}$ and retaining in $\mathcal{H}_R(t)$ only the time-independent terms we obtain the zeroth-order average Hamiltonian,

$$\bar{\mathcal{H}}_R = (\omega_1 - \omega_R) S_X + d_1^{Re} 2 I_Z S_Z + d_1^{Im} 2 I_Z S_Y. \qquad \text{[A1.18]}$$

When $\omega_1 - \omega_R$ is significant the first term in $\bar{\mathcal{H}}_R$ will quench the effect of the last two terms and no recoupling will be observed. However, at rotary resonance condition $\omega_1 = \omega_R$, we have

$$\bar{\mathcal{H}}_R = d_1^{Re} 2 I_Z S_Z + d_1^{Im} 2 I_Z S_Y = [d_1^{Re} S_Z + d_1^{Im} S_Y] 2 I_Z. \qquad \text{[A1.19]}$$

and dynamics of the system due to the two dipolar terms can proceed unhindered. In order to derive the evolution of the spin system, we express $\bar{\mathcal{H}}_R$ as

$$\bar{\mathcal{H}}_R = d_1^{eff} [\cos\theta\, S_Z + \sin\theta\, S_Y] 2 I_Z, \qquad \text{[A1.20]}$$

where $d_1^{eff} = \sqrt{(d_1^{Re})^2 + (d_1^{Im})^2}$, $\cos\theta = d_1^{Re}/d_1^{eff}$, $\sin\theta = d_1^{Im}/d_1^{eff}$. Then, with

$$\bar{\mathcal{H}}_R = e^{+i\theta S_X}\left\{d_1^{eff} 2S_Z I_Z\right\}e^{-i\theta S_X} \qquad \text{[A1.21]}$$

the propagator can be written as

$$\bar{U}_R(t,0) = e^{+i\theta S_X} e^{-id_1^{eff}t2S_ZI_Z} e^{-i\theta S_X}. \qquad \text{[A1.22]}$$

where $t = kT_R$. Starting with $\rho(0) = I_X \rightarrow \rho_R(0) = I_X$, the density operator at later time, $\rho_R(t) = \bar{U}_R\rho(0)\bar{U}_R^+$ becomes

$$\rho_R(t) = e^{+i\theta S_X} e^{-id_1^{eff}t2S_ZI_Z} e^{-i\theta S_X} I_X e^{+i\theta S_X} e^{+id_1^{eff}t2S_ZI_Z} e^{-i\theta S_X}. \qquad \text{[A1.23]}$$

After successive application of the exponential operators, we obtain

$$\rho_R(t) = I_X \cos\left(d_1^{eff}t\right) + 2I_Y[S_Z\cos\theta + S_Y\sin\theta]\sin\left(d_1^{eff}t\right). \qquad \text{[A1.24]}$$

Since $d_{\pm1} = -\omega_D \frac{1}{\sqrt{2}}\sin 2\beta_{IS}\, e^{\pm i\gamma_{IS}}$ we have

$$d_1^{Re} = -\omega_D\frac{1}{\sqrt{2}}\sin 2\beta_{IS}\cos\gamma_{IS}\,, d_1^{Im} = -\omega_D\frac{1}{\sqrt{2}}\sin 2\beta_{IS}\sin\gamma_{IS}$$

and $d_1^{eff} = \omega_D\frac{1}{\sqrt{2}}\sin 2\beta_{IS}$. As a result $\theta = \gamma_{IS} + \pi$ and one can write

$$\bar{\mathcal{H}}_R = -d_1^{eff}[\cos\gamma_{IS} S_Z + \sin\gamma_{IS} S_Y]2I_Z, \qquad \text{[A1.25]}$$

and

$$\rho_R(t) = I_X\cos\left(d_1^{eff}t\right) - 2I_Y[S_Z\cos\gamma_{IS} + S_Y\sin\gamma_{IS}]\sin\left(d_1^{eff}t\right). \qquad \text{[A1.26]}$$

Because of the sine and cosine of γ_{IS} the terms I_YS_Z and $I_YS_Y$are averaged to zero for a powder. However, they can be utilized in HMQC/HSQC experiments where equal excitation and reconversion periods lead to the appearance of $\cos^2\gamma_{IS}$ or $\sin^2\gamma_{IS}$ in the detected signal. The second rotary resonance condition $\omega_1 = 2\omega_R$ is treated in the same way. In this case both $\bar{\mathcal{H}}_R$ and $\rho_R(t)$ contain the cosine and sine of $2\gamma_{IS}$. More complicated equations for $\bar{\mathcal{H}}_R$ and $\rho_R(t)$ are obtained when ω_1 is away from ω_R or $2\omega_R$. They predict a decrease in the amplitude of the excited heteronuclear coherences away from the rotary resonance conditions. When an additional offset term, $\Delta\omega_S S_Z$, equations become even more complicated, and predict excitation of additional coherences, besides the reduction of I_YS_Z and I_YS_Y.

In the following, the effective Hamiltonian is computed numerically with the matrix logarithm approach at first rotary resonance condition. The basis set of operators, O_p, is here composed of I and S spin operators, and of their products (I_ZS_Z, I_XS_Y and so forth). The result presented in Fig. A1.2 shows the amplitudes A_p, of coherences excited at rotary resonance, as function of $\gamma_{IS}$for a fixed β_{IS}, as well as coefficients $\omega_p^{eff}/2\pi$ of those spin operators of the chosen basis which do not vanish in the effective Hamiltonian. Simulations are preformed with and without an offset term $\Delta\omega_S S_Z$ added to the Hamiltonian. When $\Delta\omega_S = 0$ coherences $I_Y S_Z$ and $I_Y S_Y$ are excited in accordance with Eq. [A1.13]. At the same time, the non-vanishing ω_p^{eff} correspond to spin operators $I_Z S_Z$ and $I_Z S_Y$ and match the dependence on γ_{IS} in Eq. [A1.12]. When $\Delta\omega_S \neq 0$ an additional term in the effective Hamiltonian is obtained containing $I_Z S_X$. At the same time an additional coherence $I_Y S_X$ is excited.

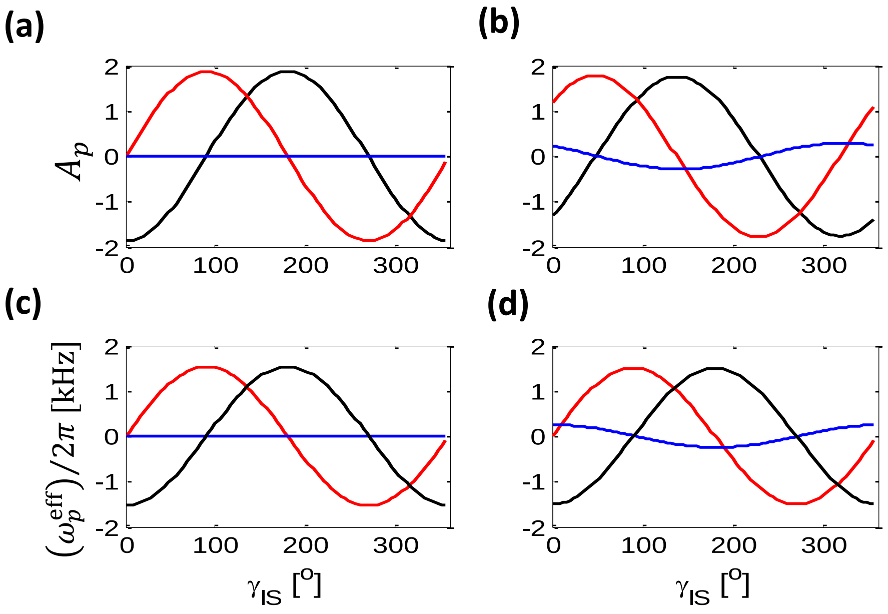

Figure A1.2 (a) Heteronuclear coherences $S_Z I_Y$ *(black),* $S_X I_Y$ *(blue),* $S_Y I_Y$ *(red) at exact rotary resonance condition* $\omega_1 = \omega_R$ *and with* $\Delta\nu_S = 0$*,after a recoupling period of* $15T_R$*. (b) The same but with* $\Delta\nu_S = 10\ kHz$*. (c) Coefficients of non-vanishing* $\mathcal{H}_{eff}$*terms* $S_Z I_Z$ *(black),* $S_X I_Z$ *(blue),* $S_Y I_Z$ *(red), for* $\Delta\nu_S = 0$*. (d) Coefficients of non-vanishing* $\mathcal{H}_{eff}$*terms for* $\Delta\nu_S = 10\ kHz$*. Other parameters used are* $\nu_R = 60\ kHz$*,* $\nu_1 = 60\ kHz$*,* $\nu_D = 5\ kHz$*. The simulation presents these quantitiy as function of* γ_{IS} *for* $\beta_{IS} = 30$ °.

Appendix 2

A2.1 System Hamiltonian

We consider a dipolar coupled $I - S$ spin pair ($S = 1, I = 1/2$), under magic angle spinning at angular frequency ω_R and subjected to irradiation at RF strengths ω_{1I} and ω_{1S} on I and S spin respectively. Chemical shifts are ignored in the following discussion. First and second-order nuclear quadrupolar interactions of S are included in the Hamiltonian. We consider an axially-symmetric quadrupolar interaction (asymmetry parameter, $\eta_Q = 0$) with the Z principal axis of the quadrupolar tensor described by polar angles β_Q and γ_Q with respect to the rotor-frame coordinate system. The internuclear $I - S$ vector, $\boldsymbol{r}_{IS}$, in the rotor frame is characterized by polar angles β_D and γ_D. The angle between the Z principal axis of the quadrupolar tensor and the internuclear $I - S$ vector is denoted by θ_{QD}.

The Hamiltonian of the system can be written as,

$$\mathcal{H}(t) = \omega_{1I} I_X + \omega_{1S} S_X + \Delta\omega_Q(\beta_Q) S_Z + \omega_Q(t, \beta_Q, \gamma_Q)[3S_Z^2 - S(S+1)] + d(t, \beta_D, \gamma_D) 2 I_Z S_Z \qquad \text{[A2.1]}$$

In the above equation,

$$\omega_Q(t, \beta_Q, \gamma_Q) = C_Q \left[\frac{1}{8}\sin^2(\beta_Q) cos(2\omega_R t + 2\gamma_Q) - \frac{1}{4\sqrt{2}}\sin(2\beta_Q)\cos(\omega_R t + \gamma_Q)\right], \qquad \text{[A2.2]}$$

where $C_Q = e^2 Qq/\hbar$ represents the quadrupolar coupling constant expressed in angular frequency units. In Eq. [A2.1], only the MAS-averaged second-order quadrupolar interaction is considered, which for $S = 1$ is given by

$$\Delta\omega_Q(\beta_Q) = \frac{C_Q^2}{8\omega_{oS}}(L + N), \qquad \text{[A2.3a]}$$

with

$$L = \frac{3}{5}, N = \frac{-27}{70}\left\{\frac{1}{8}\left(35\cos^4\beta_Q - 30\cos^2\beta_Q + 3\right)\frac{1}{8}\left(35\cos^4\theta_m - 30\cos^2\theta_m + 3\right)\right\}. \qquad \text{[A2.3b]}$$

Here ω_{0S} represents the Larmor frequency of the S spin and θ_m denotes the magic angle. Simulations with and without the time-dependent part of the second-order quadrupolar interaction showed very little difference, hence omission of the time-dependent part is justified for the RF strengths and spinning speed considered here.

The time-dependent spatial part of the dipolar interaction is given by,

$$d(t,\beta_D,\gamma_D) = \omega_D\left[\frac{\sin(2\beta_D)}{2\sqrt{2}}\cos(\omega_R t+\gamma_D) - \frac{\sin^2(\beta_D)}{4}\cos(2\omega_R t+2\gamma_D)\right], \qquad [A2.4]$$

where $\omega_D = -\mu_o\gamma_I\gamma_S\hbar/4\pi r_{IS}^3$, γ_I and γ_S are gyromagnetic ratios of I and S. When $\theta_{QD} = 0$, a common set of polar angles, β and γ, is used to characterize both quadrupolar and dipolar interactions. In numerical estimations, instead of angular frequency quantities, we utilize their frequency analogues, eg. ν_{1S}, ν_R, ν_D, etc.

A2.2 CPMAS in the absence of quadrupolar interaction

We consider the CPMAS transfer in the absence of quadrupolar interaction. In this case, the polarization transfer occurs at the usual Hartmann-Hahn conditions, $|\nu_{1I}| \pm |\nu_{1S}| = n\nu_R$. The CPMAS signal, as a function of β and γ, is shown in Figure A2.1.

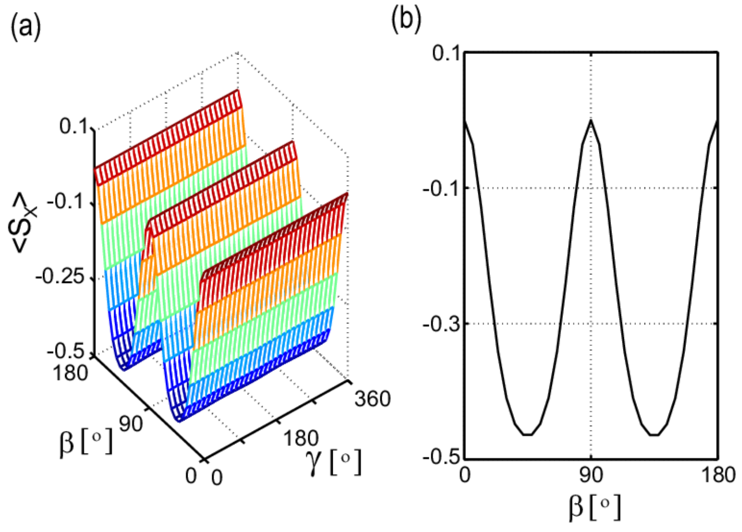

Figure A2.1 Brute force simulations showing (a) dependence of CPMAS signal on crystallite orientation in the absence of quadrupolar interaction. (b) Dependence of CPMAS signal on β for a fixed γ angle (0°). Parameters employed are $\nu_{1S} = 20\ kHz$, $\nu_{1I} = 40\ kHz$, $\nu_R = 60\ kHz$, $C_Q/2\pi = 0\ MHz$, $\eta_Q = 0$, $\nu_D = 10\ kHz$, and the contact time is 12 rotor periods.

We observe that, in the absence of quadrupolar interaction, the CPMAS signal is independent of γ, the signal has smooth variation with respect to β, and the sign of the signal is independent of crystallite orientation, thereby resulting in coherent addition of signals in a powder sample.

The CP contact time was 12 rotor periods and RF strengths employed were $\nu_{1I} = 40$ kHz and $\nu_{1S} = 20$ kHz, corresponding to $\nu_{1I} + \nu_{1S} = \nu_R$. For β around $0, 90,$ and $180°$ CP transfer is poor because the dipolar term oscillating at ν_R vanishes. These features are apparent in Figure A2.1.

A2.3 Matrix Representation of Operators

The effective Hamiltonians are expanded in terms of a set of Hermitian spin operators, O_p, which form a basis for the linear space of all 6×6 matrices. We choose to use a hybrid basis involving Hermitian linear combinations of spherical tensor operators.[95] This basis contains pure I operators, I_X, I_Y, I_Z, pure S operators, S_X, S_Y, S_Z, $S_XS_Z + S_ZS_X$, $S_YS_Z + S_ZS_Y$, $(3S_Z^2 - 2)$, $(S_+^2 + S_-^2)/2$, $(S_+^2 - S_-^2)/2i$, and IS terms like I_ZS_Z, $(S_YS_Z + S_ZS_Y)I_X$, etc. The corresponding matrix representations are given below. $S_+ = S_X + iS_Y, S_- = S_X - iS_Y$.

$$I_X = \frac{1}{2}\begin{bmatrix} 0 & 1 & 0 & 0 & 0 & 0 \\ 1 & 0 & 0 & 0 & 0 & 0 \\ 0 & 0 & 0 & 1 & 0 & 0 \\ 0 & 0 & 1 & 0 & 0 & 0 \\ 0 & 0 & 0 & 0 & 0 & 1 \\ 0 & 0 & 0 & 0 & 1 & 0 \end{bmatrix}, I_Y = \frac{1}{2}\begin{bmatrix} 0 & -i & 0 & 0 & 0 & 0 \\ i & 0 & 0 & 0 & 0 & 0 \\ 0 & 0 & 0 & -i & 0 & 0 \\ 0 & 0 & i & 0 & 0 & 0 \\ 0 & 0 & 0 & 0 & 0 & -i \\ 0 & 0 & 0 & 0 & i & 0 \end{bmatrix}, I_Z = \frac{1}{2}\begin{bmatrix} 1 & 0 & 0 & 0 & 0 & 0 \\ 0 & -1 & 0 & 0 & 0 & 0 \\ 0 & 0 & 1 & 0 & 0 & 0 \\ 0 & 0 & 0 & -1 & 0 & 0 \\ 0 & 0 & 0 & 0 & 1 & 0 \\ 0 & 0 & 0 & 0 & 0 & -1 \end{bmatrix}$$

$$S_X = \frac{1}{\sqrt{2}}\begin{bmatrix} 0 & 0 & 1 & 0 & 0 & 0 \\ 0 & 0 & 0 & 1 & 0 & 0 \\ 1 & 0 & 0 & 0 & 1 & 0 \\ 0 & 1 & 0 & 0 & 0 & 1 \\ 0 & 0 & 1 & 0 & 0 & 0 \\ 0 & 0 & 0 & 1 & 0 & 0 \end{bmatrix}, S_Y = \frac{1}{\sqrt{2}}\begin{bmatrix} 0 & 0 & -i & 0 & 0 & 0 \\ 0 & 0 & 0 & -i & 0 & 0 \\ i & 0 & 0 & 0 & -i & 0 \\ 0 & i & 0 & 0 & 0 & -i \\ 0 & 0 & i & 0 & 0 & 0 \\ 0 & 0 & 0 & i & 0 & 0 \end{bmatrix}, S_Z = \frac{1}{2}\begin{bmatrix} 1 & 0 & 0 & 0 & 0 & 0 \\ 0 & 1 & 0 & 0 & 0 & 0 \\ 0 & 0 & 0 & 0 & 0 & 0 \\ 0 & 0 & 0 & 0 & 0 & 0 \\ 0 & 0 & 0 & 0 & -1 & 0 \\ 0 & 0 & 0 & 0 & 0 & -1 \end{bmatrix}$$

$$3S_Z^2 - 2 = \begin{bmatrix} 1 & 0 & 0 & 0 & 0 & 0 \\ 0 & 1 & 0 & 0 & 0 & 0 \\ 0 & 0 & -2 & 0 & 0 & 0 \\ 0 & 0 & 0 & -2 & 0 & 0 \\ 0 & 0 & 0 & 0 & 1 & 0 \\ 0 & 0 & 0 & 0 & 0 & 1 \end{bmatrix},$$

$$S_XS_Z + S_ZS_X = \frac{1}{\sqrt{2}}\begin{bmatrix} 0 & 0 & 1 & 0 & 0 & 0 \\ 0 & 0 & 0 & 1 & 0 & 0 \\ 1 & 0 & 0 & 0 & -1 & 0 \\ 0 & 1 & 0 & 0 & 0 & -1 \\ 0 & 0 & -1 & 0 & 0 & 0 \\ 0 & 0 & 0 & -1 & 0 & 0 \end{bmatrix}, S_YS_Z + S_ZS_Y = \frac{1}{\sqrt{2}}\begin{bmatrix} 0 & 0 & -i & 0 & 0 & 0 \\ 0 & 0 & 0 & -i & 0 & 0 \\ i & 0 & 0 & 0 & i & 0 \\ 0 & i & 0 & 0 & 0 & i \\ 0 & 0 & -i & 0 & 0 & 0 \\ 0 & 0 & 0 & -i & 0 & 0 \end{bmatrix}$$

$$\frac{S_+{}^2+S_-{}^2}{2}=\begin{bmatrix}0&0&0&0&1&0\\0&0&0&0&0&1\\0&0&0&0&0&0\\0&0&0&0&0&0\\1&0&0&0&0&0\\0&1&0&0&0&0\end{bmatrix},\ \frac{S_+{}^2-S_-{}^2}{2i}=\begin{bmatrix}0&0&0&0&-i&0\\0&0&0&0&0&-i\\0&0&0&0&0&0\\0&0&0&0&0&0\\i&0&0&0&0&0\\0&i&0&0&0&0\end{bmatrix}$$

𝔄2.4: Removal of large IS terms via a rotating frame transformation

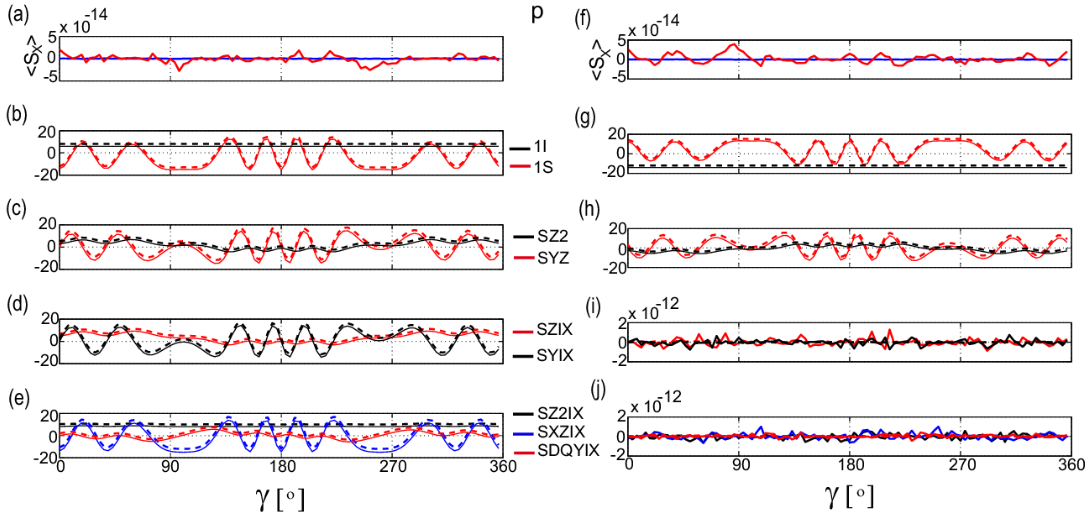

Figure A2.2 Dependence on γ of CPMAS signal (a, f) and of the ν_p^{eff} coefficients (b-e, g-j) calculated with Floquet theory (solid line) and the logarithm method (dashed line). Left: calculations starting from the Hamiltonian of Eq. [2.7]. Right: calculations starting from the Hamiltonian of Eq. [2.9]. The calculation assumes $\nu_D = 0\,kHz$ hence IS terms are not expected. Other parameters are: $\beta = 32^\circ, \nu_{1S} = 80\,kHz, \nu_{1I} = 46\,kHz, \nu_R = 60\,kHz, C_Q/2\pi = 1.5\,MHz, \eta_Q = 0$. The contact time is 10 rotor periods. For visibility, the plots with dashed line are shifted vertically. Labeling of the coefficients is according to Table 2.1. The coefficient $SZ2 \cong SDQX$, hence not shown. The coefficients ν_p^{eff} are expressed in kHz.

Simulations performed with RF irradiation on the I channel turned on, but with dipolar coupling turned off, starting with the time-dependent Hamiltonian given in Eq. [A2.1]. It is found that the effective Hamiltonians, and hence the ν_p^{eff} coefficients determined by the logarithm and Floquet methods are identical within numerical errors. Several ν_p^{eff}coefficients determined by both methods are presented in Figure A2.2(a-e). Since CP transfer is mediated by the dipolar interaction, as expected, the CP signal is absent (Figure A2.2(a)). However, from Figure A2.2(d,e) it can be seen that $\mathcal{H}_{\mathrm{eff}}$ contains a few large IS terms. Figure A2.2(f-j) represents the ν_p^{eff}coefficients determined by both methods starting with the time-dependent Hamiltonian given in Eq. [2.9]. It is visible that IS terms have been removed.

A2.5: Connection between two procedures for removal of large IS terms

From simulations summarized in Figure A2.2, we see that the effective Hamiltonian calculated in the old rotating frame, $\mathcal{H}_{\text{eff}}^{ln} = \mathcal{H}_{\text{eff}}^{\mathcal{F}}$ is different from the effective Hamiltonian calculated in the new rotating frame, $\widetilde{\mathcal{H}}_{\text{eff}}^{ln} = \widetilde{\mathcal{H}}_{\text{eff}}^{\mathcal{F}}$. This can be justified as follows. According to Eq. [2.8], the one-rotor-period propagators in the old and new rotating frames are related by

$$U(T_R, 0) = \exp(-i\omega_R T_R I_X)\, \widetilde{U}(T_R, 0) = -\widetilde{U}(T_R, 0). \qquad \text{[A2.5]}$$

Since $U(T_R, 0)$ and $\widetilde{U}(T_R, 0)$ are different, the associated Hamiltonians $\mathcal{H}_{\text{eff}}$ and $\widetilde{\mathcal{H}}_{\text{eff}}$ have to be different. From $U(T_R, 0) = \sum \exp\left(-i\epsilon_j T_R\right) |\epsilon_j\rangle\langle\epsilon_j|$, by adding $\pm\omega_R/2$ to all eigenvalues (or odd multiples of $\omega_R/2$), we obtain $-U(T_R, 0)$. Hence $\widetilde{\mathcal{H}}_{\text{eff}}^{ln}$ has to be connected to $\mathcal{H}_{\text{eff}}^{ln}$ by

$$\widetilde{\mathcal{H}}_{\text{eff}} = \sum(\epsilon_j \pm \omega_R/2)|\epsilon_j\rangle\langle\epsilon_j| = \mathcal{H}_{\text{eff}} + \sum(\pm\,\omega_R/2)|\epsilon_j\rangle\langle\epsilon_j|. \qquad \text{[A2.6]}$$

By construction, both $\mathcal{H}_{\text{eff}}$ and $\widetilde{\mathcal{H}}_{\text{eff}}$ have eigenvalues in the $(-\omega_R/2, \omega_R/2]$ interval, hence we must have

$$\widetilde{\mathcal{H}}_{\text{eff}} = \sum_{\epsilon_j > 0}(\epsilon_j - \omega_R/2)|\epsilon_j\rangle\langle\epsilon_j| + \sum_{\epsilon_j < 0}(\epsilon_j + \omega_R/2)|\epsilon_j\rangle\langle\epsilon_j|. \qquad \text{[A2.7]}$$

The eigenstates of the effective Hamiltonians $\widetilde{\mathcal{H}}_{\text{eff}}$ and $\mathcal{H}_{\text{eff}}$ are identical, but the energy levels pattern is different. This difference results in different expressions for the effective Hamiltonian in terms of the spin operators O_p.

This relation between $\mathcal{H}_{\text{eff}}$ and $\widetilde{\mathcal{H}}_{\text{eff}}$ suggests a second procedure to remove IS terms as follows. From the Floquet effective Hamiltonian in the old rotating frame, $\mathcal{H}_{\text{eff}}^{\mathcal{F}} = D\Lambda_0 D^{-1}$, we can obtain the Floquet effective Hamiltonian $\widetilde{\mathcal{H}}_{\text{eff}}^{\mathcal{F}}$ as

$$\widetilde{\mathcal{H}}_{\text{eff}}^{\mathcal{F}} = D\widetilde{\Lambda}_0 D^{-1},$$

where $\widetilde{\Lambda}_0$ is a new diagonal matrix, with elements

$$\tilde{\epsilon}_j = \begin{cases} \epsilon_j - \omega_R/2\,, \text{if}\, \epsilon_j > 0 \\ \epsilon_j + \omega_R/2\,, \text{if}\, \epsilon_j < 0 \end{cases}$$

It is seen that the effective Hamiltonian in the new rotating frame is obtained by a *simple rearrangement* of the eigenvalues of the effective Hamiltonian in the old rotating frame. It would be interesting to investigate whether this shifting procedure can be extended to more general frame transformations.

𝕬2.6: Structure of the effective Hamiltonian and absence of *IS* terms

𝕬2.5.1 $S = 1/2\,, I = 1/2$

For two dipolar-coupled spin-1/2 nuclei under RF irradiation the Hamiltonian is

$$\mathcal{H}(t) = \omega_{1I} I_X + \omega_{1S} S_X + d(t) 2 I_Z S_Z. \qquad \text{[A2.8]}$$

Let us consider a particular setup with $\nu_{1S} = 20$ kHz, $\nu_{1I} = 50$ kHz, $\nu_R = 60$ kHz, $\nu_D = 1$ kHz. This setup is away from any CP match condition or other resonance condition and also the dipolar coupling is much smaller than the spinning frequency. Therefore, the Hamiltonian can be very well approximated by leaving out the time-dependent dipolar interaction. This new, time-independent, Hamiltonian would describe well evolution for any time interval and hence it can be also used as an effective Hamiltonian to describe evolution over multiples of the rotor period. Thus we can set,

$$\mathcal{H}_{\text{eff}} = \omega_{1I} I_X + \omega_{1S} S_X. \qquad \text{[A2.9]}$$

The corresponding eigenvalues and eigenvectors are,

$$\epsilon_{m_I m_S} = m_I \omega_{1I} + m_S \omega_{1S} \rightarrow |m_I, m_S\rangle_X,$$

where the index *X* signifies that these states are eigenstates of S_X and I_X. For our setup and in frequency units, the eigenvalues in descending order are 35, 15, -15, -35 kHz and correspond to eigenstates $|1/2,1/2\rangle_X, |1/2,-1/2\rangle_X, |-1/2,+1/2\rangle_X, |-1/2,-1/2\rangle_X$. The 35 and -35 values are outside the $(-\nu_R/2\,, +\nu_R/2)$ interval, hence the logarithm method will produce an effective Hamiltonian $\mathcal{H}_{\text{eff}}^{ln}$ for which these eiegnvalues are replaced by $35 - 60 = -25$ kHz and $-35 + 60 = 25$ kHz while the corresponding eigenstates remain unchanged. In this way the eigenvalues of $\mathcal{H}_{\text{eff}}^{ln}$ are $-25, 15, -15, +25$ kHz corresponding to the eigenstates $|1/2,1/2\rangle_X, |1/2,-1/2\rangle_X, |-1/2,+1/2\rangle_X, |-1/2,-1/2\rangle_X$ respectively.

It is easy to see that this Hamiltonian can be expressed as

$$\mathcal{H}_{\text{eff}}^{ln} = \omega_{1I}^{\text{eff}} I_X + \omega_{1S}^{\text{eff}} S_X.$$

Indeed, for the -25 and 15 kHz eigenvalues we demand

$$-25\text{ kHz} = \nu_{1I}^{\text{eff}}/2 + \nu_{1S}^{\text{eff}}/2,$$

$$+15\text{ kHz} = \nu_{1I}^{\text{eff}}/2 - \nu_{1S}^{\text{eff}}/2.$$

The solution of this system is given by $\nu_{1I}^{\text{eff}} = -10\text{ kHz}$ and $\nu_{1S}^{\text{eff}} = -40\text{ kHz}$ and it satisfies also the equations related to the other two eigenvalues. As such this Hamiltonian maintains the original spin-operator structure and does not contain any *IS* terms.

It can be shown that this property is maintained for any other RF strengths as follows. The effective Hamiltonian produced from the propagator $\exp(-i\mathcal{H}_{\text{eff}} T_R)$ by the logarithm method, where $\mathcal{H}_{\text{eff}}$ is given in Eq. [A2.9], is of the form

$$\mathcal{H}_{\text{eff}}^{ln} = \mathcal{H}_{\text{eff}} + \sum_j k_j \omega_R |\epsilon_j\rangle\langle\epsilon_j| \qquad \text{[A2.10]}$$

where $|\epsilon_j\rangle$ are the eigenvalues of $\mathcal{H}_{\text{eff}}$ and integers k_j, termed as folding coefficients, make sure that eigenvalues of $\mathcal{H}_{\text{eff}}^{ln}$ are in the $(-\omega_R/2, \omega_R/2]$ interval. More explicitly

$$\mathcal{H}_{\text{eff}}^{ln} = \sum_{m_I, m_S} (m_I \omega_{1I} + m_S \omega_{1S}) |m_I m_S\rangle\langle m_I m_S|_X + \sum_{m_I, m_S} k_{m_S m_I} \omega_R |m_I m_S\rangle\langle m_I m_S|_X \qquad \text{[A2.11]}$$

where the subscript *X* indicates that kets and bras are eigenstates of S_X and I_X. The energy level pattern of $\mathcal{H}_{\text{eff}}$ is symmetric, $\epsilon_{m_I, m_S} = -\epsilon_{-m_I, -m_S}$, hence

$$k_{1/2,1/2} + k_{-1/2,-1/2} = 0,\ k_{1/2,-1/2} + k_{-1/2,1/2} = 0. \qquad \text{[A2.12]}$$

Next, we investigate the conditions that result in the presence of *IS* terms in the $\mathcal{H}_{\text{eff}}^{ln}$. The initial effective Hamiltonian $\mathcal{H}_{\text{eff}}$ does not contain any *IS* terms. Using Eq. [A2.11], the coefficient of any *IS* spin operator O_p can be calculated as,

$$\text{Tr}(\mathcal{H}_{\text{eff}}^{ln} O_p)/Tr(O_p^2) = \frac{Tr\left\{O_p \sum_{m_I, m_S} k_{m_I m_S} \omega_R |m_I m_S\rangle\langle m_I m_S|_X\right\}}{Tr(O_p^2)}$$

$$= \sum_{m_I, m_S} k_{m_I m_S} \omega_R \left\langle m_I m_S \middle| O_p \middle| m_I m_S \right\rangle_X / Tr(O_p^2). \qquad \text{[A2.13]}$$

The condition that the operator O_p does not appear in $\mathcal{H}_{\text{eff}}^{ln}$ is then

$$\sum k_{m_I m_S} \langle m_I m_S | O_p | m_I m_S \rangle_X = 0. \qquad \text{[A2.14]}$$

For our spin system $\langle m_I m_S | O_p | m_I m_S \rangle_X = 0$ for all IS operators except $I_X S_X$. Hence IS operators different from $I_X S_X$ do not appear in $\mathcal{H}_{\text{eff}}^{ln}$. For $I_X S_X$ we have

$$\langle m_I m_S | I_X S_X | m_I m_S \rangle_X = m_I m_S,$$

and the sum in Eq. [A2.13] vanishes

$$k_{1/2,1/2} + k_{-1/2,-1/2} - k_{-1/2,1/2} - k_{1/2,-1/2} = 0$$

after taking into account Eq. [A2.12]. Therefore $I_X S_X$ also does not appear in $\mathcal{H}_{\text{eff}}^{ln}$. We conclude that for any given RF strengths no IS terms are present in $\mathcal{H}_{\text{eff}}^{ln}$. This conclusion is not valid when $S = 1, I = 1/2$ as demonstrated in the next section.

A2.5.2 $\boldsymbol{S = 1, I = 1/2}$

For S=1 and $\nu_Q = 0$, let us consider the same setup as in E1, with $\nu_{1S} = 20$ kHz, $\nu_{1I} = 50$ kHz, $\nu_R = 60$ kHz, $\nu_D = 1$ kHz. Following the same steps, the eigenvalues of $\mathcal{H}_{\text{eff}}$ in descending order are $45, 25, 5, -5, -25, -45$ kHz and correspond to eigenstates $|1/2,1\rangle_X, |1/2,0\rangle_X, |1/2,-1\rangle_X, |-1/2,1\rangle_X, |-1/2,0\rangle_X, |-1/2,-1\rangle_X$. The 45 and -45 kHz eigenvalues are outside the $(-\nu_R/2, +\nu_R/2]$ interval and the logarithm method will replace them by $45 - 60 = -15$ kHz and $-45 + 60 = 15$ kHz. In this way the eigenvalues of $\mathcal{H}_{\text{eff}}^{ln}$ are $-15, 25, 5, -5, -25, +15$ kHz and correspond to eigenvectors $|1/2,1\rangle_X, |1/2,0\rangle_X, |1/2,-1\rangle_X, |-1/2,1\rangle_X, |-1/2,0\rangle_X, |-1/2,-1\rangle_X$, respectively. An attempt to find ω_{1I}^{eff} and ω_{1S}^{eff} such that

$$\mathcal{H}_{\text{eff}}^{ln} = \omega_{1I}^{\text{eff}} I_X + \omega_{1S}^{\text{eff}} S_X$$

fails as follows. For the first and second eigenvalues we would have

$$-15 \text{ kHz} = \nu_{1I}^{\text{eff}}/2 + \nu_{1S}^{\text{eff}},$$

$$+25 \text{ kHz} = \nu_{1I}^{\text{eff}}/2,$$

which would yield $\nu_{1I}^{\text{eff}} = 50$ kHz and $\nu_{1S}^{\text{eff}} = -40$ kHz. However, for the third eigenvalue we would have $5 \text{ kHz} = \nu_{1I}^{\text{eff}}/2 - \nu_{1S}^{\text{eff}} = 25 + 40 = 65$ kHz which is contradictory. It follows that $\mathcal{H}_{\text{eff}}^{ln}$ cannot be written as $\omega_{1I}^{\text{eff}} I_X + \omega_{1S}^{\text{eff}} S_X$ and additional terms are needed. It can be shown that some of these additional terms are IS. After some algebra, the following non-zero ν_p^{eff}coefficients are found,

$$\nu_{1I}^{\text{eff}} = 10 \text{ kHz}, \nu_{1S}^{\text{eff}} = -10 \text{ kHz},$$

$$\nu_{SZ2IX}^{\text{eff}} = 10 \text{ kHz}, \nu_{DQXIX}^{\text{eff}} = -30 \text{ kHz}.$$

The last two coefficients belong to *IS* terms in the effective Hamiltonian.

However, whether $\mathcal{H}_{\text{eff}}^{ln}$ can be written as $\omega_{1I}^{\text{eff}} I_X + \omega_{1S}^{\text{eff}} S_X$ or not depends on the RF strengths and spinning frequency. For example, if $\nu_{1S} = 20$ kHz, $\nu_{1I} = 110$ kHz, $\nu_R = 60$ kHz it can be checked that

$$\mathcal{H}_{\text{eff}}^{ln} = \omega_{1I}^{\text{eff}} I_X + \omega_{1S}^{\text{eff}} S_X,$$

with $\nu_{1I}^{\text{eff}} = -10$ kHz and $\nu_{1S}^{\text{eff}} = 20$ kHz.

Similar to $S = 1/2$ case, we investigate the condition $\sum k_{m_I m_S} \langle m_I m_S | O_p | m_I m_S \rangle_X \neq 0$ which results in the presence of an *IS* term O_p in the $\mathcal{H}_{\text{eff}}^{ln}$. Taking into account the symmetry of the energy level pattern of $\mathcal{H}_{\text{eff}}$ we have

$$k_{1/2,1} + k_{-1/2,-1} = 0,\ k_{1/2,0} + k_{-1/2,0} = 0,\ k_{1/2,-1} + k_{-1/2,1} = 0.$$

With $\langle m_S | S_Y | m_S \rangle_X = \langle m_S | S_Z | m_S \rangle_X = 0$ and $\langle m_I | I_Y | m_I \rangle_X = \langle m_I | I_Z | m_I \rangle_X = 0$, it follows that all simple *IS* terms of the form $I_i S_j$, except $I_X S_X$, are automatically zero in $\mathcal{H}_{\text{eff}}^{ln}$. With $\langle m_I, m_S | I_X S_X \ | m_I, m_S \rangle = m_I m_S$, we obtain

$$\sum_{m_I, m_S} k_{m_I m_S} \langle m_I m_S | I_X S_X | m_I m_S \rangle_X = (k_{1/2,1} + k_{-1/2,-1} - k_{1/2,-1} - k_{-1/2,1})/2 = 0$$

such that also $I_X S_X$ term does not appear in $\mathcal{H}_{\text{eff}}^{ln}$, similar to S=1/2 case. Proceeding in a similar way it can be shown that all other *IS* terms are zero for any RF strengths, except for $I_X(3S_Z^2 - 2)$ and $I_X(S_+^2 + S_-^2)/2$. Taking into account that $\langle 1 | 3S_Z^2 - 2 | 1 \rangle_X = \langle -1 | 3S_Z^2 - 2 | -1 \rangle_X = -\langle 0 | 3S_Z^2 - 2 | 0 \rangle_X / 2 = -1/2$, we obtain for $I_X(3S_Z^2 - 2)$

$$\sum_{m_I, m_S} k_{m_I m_S} \langle m_I m_S | I_X (3S_Z^2 - 2) | m_I m_S \rangle_X = (-k_{1/2,1} + k_{-1/2,-1} + 2k_{1/2,0} - 2k_{-1/2,0} + k_{-1/2,1} - k_{1/2,-1})/4$$

This sum may be different from zero, in which case an $I_X(3S_Z^2 - 2)$ term will appear in $\mathcal{H}_{\text{eff}}^{ln}$. For example, if $\omega_R > \omega_{1S} + \omega_{1I}/2 > \omega_R/2 > \omega_{1S} - \omega_{1I}/2$, we have $k_{1/2,1} = -1, k_{-1/2,1} = 0, k_{1/2,0} = 0$ and the non-vanishing sum leads to an $I_X(3S_Z^2 - 2)$ term. On the other hand, if $\omega_R > \omega_{1S} + \omega_{1I}/2 > \omega_{1S} - \omega_{1I}/2 > \omega_R/2$, we have $k_{1/2,1} = -1, k_{-1/2,1} = -1, k_{1/2,0} = 0$ and the sum is zero, yielding no $I_X(3S_Z^2 - 2)$ term. In this way the presence or absence of

$I_X(3S_Z^2-2)$ term can be predicted for any RF configuration. A similar analysis performed for the $I_X(S_+^2+S_-^2)/2$ yields minus the sum obtained for $I_X(3S_Z^2-2)$ hence the two *IS* terms are simultaneously present or absent depending on RF strengths and ω_R. This is confirmed by numerical simulations.

A similar analysis can be performed in the presence of quadrupolar interaction as follows. In the absence of dipolar coupling the propagator factorizes into pure *S* and pure *I* contributions. As a result, an effective Hamiltonian can be written as $\mathcal{H}_{\text{eff}}=\mathcal{H}_{\text{eff}}^{S,0}+\omega_{1I}I_X$, where $\mathcal{H}_{\text{eff}}^{S,0}$ is the S-spin effective Hamiltonian determined by Floquet or logarithm approaches for $\omega_{1I}=0$. Denoting the eigenvectors and eigenvalues of $\mathcal{H}_{\text{eff}}^{S,0}$ by $|m_S^0\rangle$ and $\epsilon_{m_S}^0$, the total effective Hamiltonian can be written as

$$\mathcal{H}_{\text{eff}}=\sum_{m_I,m_S^0}(\epsilon_{m_S}^0+m_I\omega_{1I})|m_Im_S^0\rangle\langle m_Im_S^0|_X. \qquad \text{[A2.15]}$$

Subscript *X* indicates that the *I* part of kets and bras are eigenstates of I_X. This Hamiltonian does not contain *IS* terms, as expected. The effective Hamiltonian $\mathcal{H}_{\text{eff}}^{ln}$ obtained by taking the logarithm of the full propagator $\exp\left(-i\mathcal{H}_{eff}T_R\right)$ is then

$$\mathcal{H}_{\text{eff}}^{ln}=\mathcal{H}_{\text{eff}}+\textstyle\sum_{m_I,m_S^0}k_{m_Im_S^0}\omega_R|m_Im_S^0\rangle\langle m_Im_S^0|_X \qquad \text{[A2.16]}$$

where the folding coefficients $k_{m_Im_S^0}$ brings the eigenvalue $\epsilon_{m_S}^0+m_I\omega_{1I}$ into the $(-\omega_R/2,\omega_R/2]$ interval. The *change* in the ω_p^{eff} coefficient corresponding to basis operator O_p is

$$Tr\frac{\left\{O_p\sum_{m_I,m_S^0}k_{m_I,m_S^0}\omega_R|m_Im_S^0\rangle\langle m_Im_S^0|_X\right\}}{Tr\left(O_p^2\right)}$$
$$=\sum_{m_I,m_S^0}k_{m_Im_S^0}\omega_R\left\langle m_Im_S^0\middle|O_p\middle|m_Im_S^0\right\rangle_X/Tr\left(O_p^2\right) \qquad \text{[A2.17]}$$

If O_p represents an *IS* operator, the condition that O_p does not appear in $\mathcal{H}_{\text{eff}}^{ln}$ is then

$$\sum_{m_I,m_S^0}k_{m_Im_S^0}\left\langle m_Im_S^0\middle|O_p\middle|m_Im_S^0\right\rangle_X=0$$

Since $\langle m_I|I_X|m_I\rangle_X=m_I$ and $\langle m_I|I_Y|m_I\rangle_X=\langle m_I|I_Z|m_I\rangle_X=0$ it follows that only *IS* terms involving I_X may appear in $\mathcal{H}_{\text{eff}}^{ln}$. This is confirmed through numerical simulations. By construction, the eigenvalues $\epsilon_{m_S}^0$ are in the $(-\omega_R/2, \omega_R/2]$ interval and the folding coefficients $k_{m_I m_S^0}$ clearly depend on the magnitude of the proton RF strength. With nonzero quadrupolar coupling, the energy level pattern of $\mathcal{H}_{\text{eff}}^{S,0}$ and hence $\mathcal{H}_{\text{eff}}$ is only approximately symmetric, $\epsilon_{m_I,m_S^0} \cong -\epsilon_{-m_I,-m_S^0}$, the degree of asymmetry depending on crystallite orientation. Nevertheless, relations of the type $k_{m_I,m_S^0} = -k_{-m_I,-m_S^0}$ hold for most crystallite orientations. For example, assuming $k_{m_I,m_S^0} = -k_{-m_I,-m_S^0}$ and if $\omega_R > \epsilon_{m_S=1}^0 + \omega_{1I}/2 > \omega_R/2 > \epsilon_{m_S=1}^0 - \omega_{1I}/2$, we have $k_{1/2,1} = -1, k_{-1/2,1} = 0, k_{1/2,0} = 0$ and an O_p term will appear if $\langle 1/2,1|O_p|1/2,1\rangle_X - \langle -1/2,-1|O_p|-1/2,-1\rangle_X \neq 0$. Since $|m_S^0\rangle$ are linear combinations of the 'unperturbed' states $|m_S\rangle_X$, it is expected that more *IS* terms will appear than in the case with zero quadrupolar coupling. This is confirmed in Figure A2.2. The eigenstates $|m_S^0\rangle$ depend strongly on crystallite orientation. Therefore, if nonzero the magnitude of a given *IS* term depends on $\langle m_I m_S^0|O_p|m_I m_S^0\rangle_X$, and it will most probably exhibit a strong dependence on crystallite orientation.

It presents interest to determine the relation between the effective RF strengths in $\mathcal{H}_{\text{eff}}$ and $\mathcal{H}_{\text{eff}}^{ln}$. According to Eq. [A2.17] the proton effective RF strength in $\mathcal{H}_{\text{eff}}^{ln}$ is

$$\omega_{1I}^{\text{eff}} = \omega_{1I} + \sum_{m_I,m_S^0} k_{m_I m_S^0}\omega_R \langle m_I m_S^0|I_X|m_I m_S^0\rangle_X /Tr(I_X^2) \qquad [A2.18]$$

Or $$\omega_{1I}^{\text{eff}} = \omega_{1I} + \frac{\omega_R}{3}\sum_{m_S^0}(k_{1/2,m_S^0} - k_{-1/2,-m_S^0}).$$

Due to symmetry of the energy level pattern, $k_{m_I,m_S^0} = -k_{-m_I,-m_S^0}$ and

$$\omega_{1I}^{\text{eff}} = \omega_{1I} + \frac{2\omega_R}{3}\sum_{m_S^0} k_{1/2,m_S^0}.$$

It follows that ω_{1I}^{eff} and ω_{1I} may differ only by a multiple of $2\omega_R/3$. This feature was initially discovered by analyzing ω_{1I}^{eff} in simulations with different proton RF strengths. In a similar manner we could also determine the change in effective S spin RF strength. Following Eq. [A2.17] the change in ω_{1S}^{eff} is

$$\sum_{m_I,m_S^0} k_{m_I m_S^0}\omega_R \langle m_I m_S^0|S_X|m_I m_S^0\rangle_X /Tr(S_X^2) \qquad [A2.19]$$

Due to the strong dependence of $|m_S^0\rangle$ on crystallite orientation, the change in $\omega_{1S}^{\mathrm{eff}}$ will not have a simple form.

Next, we consider the appearence of IS terms when the effective Hamiltonian is calculated after performing a rotating frame transformation of type $U(t,0) = \exp(-i\omega_R t I_X)\,\widetilde{U}(t,0)$. Since only the I part of the Hamiltonian is affected, the effective Hamiltonian in the rotating frame is $\widetilde{\mathcal{H}}_{\mathrm{eff}} = \mathcal{H}_{\mathrm{eff}}^{S,0} + (\omega_{1I} - \omega_R)I_X$, with $\mathcal{H}_{\mathrm{eff}}^{S,0}$ unchanged. Taking the logarithm of exp $(-i\widetilde{\mathcal{H}}_{\mathrm{eff}}T_R)$ gives

$$\widetilde{\mathcal{H}}_{\mathrm{eff}}^{ln} = \mathcal{H}_{\mathrm{eff}}^{S,0} + (\omega_{1I} - \omega_R)I_X + \sum_{m_I,m_S^0} k_{m_I m_S^0}\omega_R |m_I m_S^0\rangle\langle m_I m_S^0|_X \qquad [\mathrm{A2.20}]$$

where, if needed, the coefficient $k_{m_I m_S^0}$ brings the modified eigenvalue $\epsilon_{m_S}^0 + m_I(\omega_{1I} - \omega_R)$ into the $(-\omega_R/2, \omega_R/2]$ interval. If ω_{1I} is comparable to ω_R, (as it was the case for most simulations), it is seen that the range spanned by the eigenvalues of $\widetilde{\mathcal{H}}_{\mathrm{eff}}$ is reduced and may fall well inside the $(-\omega_R/2, \omega_R/2]$ interval. In this case all $k_{m_I m_S^0}$ are zero hence $\widetilde{\mathcal{H}}_{\mathrm{eff}}^{ln} = \widetilde{\mathcal{H}}_{\mathrm{eff}}$. Therefore $\widetilde{\mathcal{H}}_{\mathrm{eff}}^{ln}$ does not contain any IS terms and moreover the pure S part $\mathcal{H}_{\mathrm{eff}}^{S,0}$ remains unaffected.

To summarize, we have shown that in the absence of dipolar coupling, for both $I = 1/2 = S$ and $I = 1/2, S = 1$ cases, an effective Hamiltonian $\mathcal{H}_{\mathrm{eff}}$ that does not contain any *IS* terms could be constructed. We have shown that the effective Hamiltonians $\mathcal{H}_{\mathrm{eff}}^{ln}$ (obtained by taking the logarithm of the full propagator) and $\mathcal{H}_{\mathrm{eff}}$ were related through folding coefficients k_{m_I,m_S} which fold the eigenvalues of $\mathcal{H}_{\mathrm{eff}}$ within the $(-\omega_R/2, \omega_R/2]$ interval. The folding coefficients depend on the *I* spin RF strength. It was shown that the presence or absence of an *IS* operator, O_p, in the effective Hamiltonian $\mathcal{H}_{\mathrm{eff}}^{ln}$ depends on k_{m_I,m_S} and on the matrix elements $\langle m_I m_S^0|O_p|m_I m_S^0\rangle_X$. After performing the rotating frame transformation, as before an effective Hamiltonian $\widetilde{\mathcal{H}}_{\mathrm{eff}}$ that does not contain any *IS* terms was constructed. In comparison with $\mathcal{H}_{\mathrm{eff}}$, the eigenvalues of $\widetilde{\mathcal{H}}_{\mathrm{eff}}$ are confined to a reduced interval. As before the effective Hamiltonian $\widetilde{\mathcal{H}}_{\mathrm{eff}}^{ln}$ obtained by taking the logarithm of the full propagator is related to $\widetilde{\mathcal{H}}_{\mathrm{eff}}$ through folding coefficients k_{m_I,m_S}. If the reduced eigenvalue interval of $\widetilde{\mathcal{H}}_{\mathrm{eff}}$ falls within $(-\omega_R/2, \omega_R/2]$, it follows that all folding coefficients vanish, resulting in $\widetilde{\mathcal{H}}_{\mathrm{eff}}^{ln} = \widetilde{\mathcal{H}}_{\mathrm{eff}}$ and hence the absence of *IS* terms. It was shown that, depending on ω_{1I} for fixed ω_{1S} and ω_R, non-vanishing folding coefficients in $\mathcal{H}_{\mathrm{eff}}^{ln}$ do not necessarily lead to *IS* terms, hence rotating frame transformation may not be needed.

A2.7: Dependence of CPMAS signal on proton RF strength

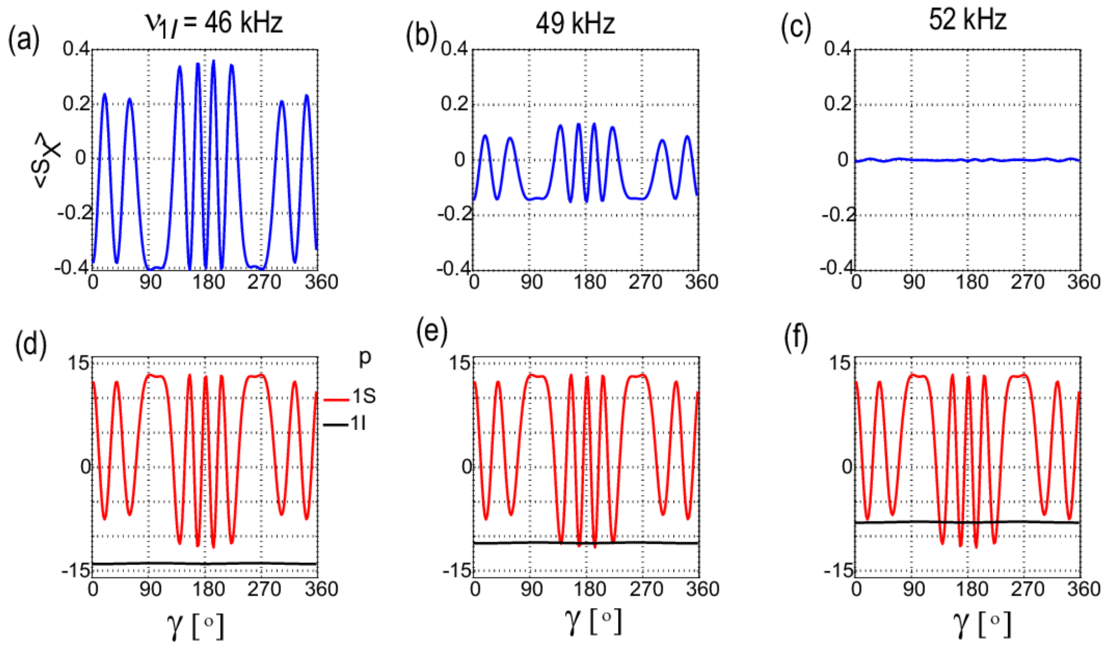

Figure A2.3 Dependence of CPMAS signal on γ *for (a)* $\nu_{1I} = 46$, *(b)* $\nu_{1I} = 49$, *(c)* $\nu_{1I} = 52\ kHz$. *(d-f) Dependence on* γ *of the corresponding* ν_{1S}^{eff} *(1S) and* ν_{1I}^{eff} *(1I) coefficients. Calculations start with the Hamiltonian of Eq. [2.9] and assume* $\nu_D = 10\ kHz$, $\beta = 32^{\circ}$, $\nu_{1S} = 80\ kHz$, $\nu_R = 60\ kHz$, $C_Q/2\pi = 1.5\ MHz$, $\eta_Q = 0$, $\theta_{QD} = 0$ *and* $\tau_{CP} = 10T_R$. *Labeling of the coefficients is given in Table 2.1. The coefficients* ν_{1S}^{eff} *and* ν_{1I}^{eff} *in (d-f) are expressed in kHz.*

Dependence of CPMAS signal on proton RF strength is and γ angle is shown in Figure A2.3. A good transfer occurs when $|\nu_{1I}^{\mathrm{eff}}|$ is slightly above the maximum of $|\nu_{1S}^{\mathrm{eff}}|$. Lower $|\nu_{1I}^{\mathrm{eff}}|$ results in a significant drop in the signal.

𝕬2.8: Dependence of CPMAS signal on β and γ for other matching conditions

All calculations and resulting conclusions upto Figure 2.5 correspond to a particular choice of RF strengths,$\nu_{1S} = 80$ kHz and $\nu_{1I} = 46$ kHz, a choice which yields good overall CP transfer in simulations and is also close to the optimized conditions employed in the experiments of Ref. [17].

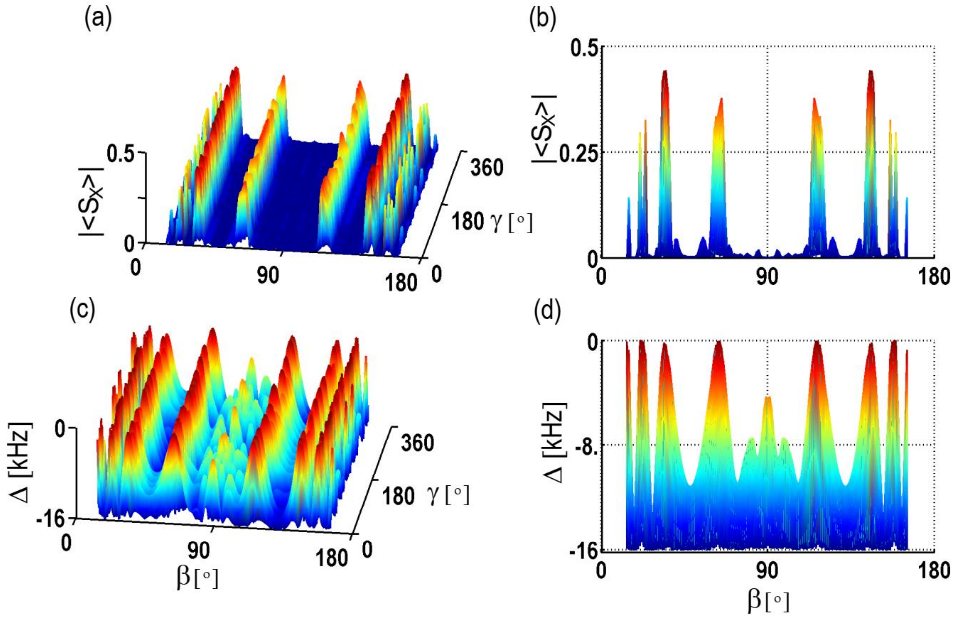

Figure A2.4 (a) Dependence of CP signal on β and γ. (b) Projection of (a) along γ. (c) Dependence on β and γ of the Δ parameter which reflects the difference between $|\nu_{1S}^{eff}|$ and $|\nu_{1I}^{eff}|$. (d) Projection of (c) along γ. Calculations start from the Hamiltonian of Eq. [2.9] and assume $\nu_D = 10\ kHz$, $\nu_{1S} = 80\ kHz$, $\nu_{1I} = 76\ kHz$, $\nu_R = 60\ kHz$, $C_Q/2\pi = 1.5\ MHz$, $\eta_Q = 0$, $\theta_{QD} = 0$. The contact time is 10 rotor periods.

The same reference presents CP mismatch plots, in which variation of the double CP signal is monitored as function of proton RF strength ν_{1I} and it is found that it exhibits maxima and minima. From the above arguments we can also predict other matching conditions as follows. The RF strengths $\nu_{1S} = 80$ kHz and $\nu_{1I} = 46$ kHz correspond to $\nu_{1I} + |\nu_{1S}^{\text{eff}}| \cong \nu_R$ with $|\nu_{1S}^{\text{eff}}| \cong 14$ kHz. One can speculate a new matching condition, $\nu_{1I} - |\nu_{1S}^{\text{eff}}| \cong \nu_R$, with the same $\nu_{1S} = 80$ kHz and arranging $\nu_{1I} \cong 74$ kHz. This is confirmed by simulations and shown in Figure A2.4, where an optimized value $\nu_{1I} = 76$ kHz is used. This is well in agreement with the double CP mismatch plot in Ref. [17] where it is found that two consecutive maxima of the signal occur at about $45 - 50$ kHz and $70 - 76$ kHz, when $\nu_{1S} = 80$ kHz.

In the same way other matching conditions can be determined, for example those involving $2\nu_R$. The matching conditions become $\nu_{1I} \cong 2\nu_R \pm \left|\nu_{1S}^{\text{eff}}\right|$ and yield 106 and 134 kHz for the proton RF strength. We have verified that significant CP transfer occurs at these values. Additional simulations show reduced CP transfer at other proton RF strengths between these values. For proton RF strengths in the 100 kHz range, identical effective Hamiltonians are obtained when starting from the Hamiltonian $\mathcal{H}(t)$ of Eq. [A2.1] or from a new rotating frame Hamiltonian, $\widetilde{\mathcal{H}}(t)$, given by

$$U(t,0) = \exp(-i2\omega_R t I_X)\,\widetilde{U}(t,0), \qquad \text{[A2.21]}$$

$$\begin{aligned}\widetilde{\mathcal{H}}(t)\\ &= (\omega_{1I} - 2\omega_R)I_X + \Delta\omega_Q(\beta_Q)S_Z + \omega_{1S}S_X + \omega_Q(t,\beta_Q,\gamma_Q)[3S_Z^2 - S(S+1)]\\ &+ 2d(t,\beta_D,\gamma_D)S_Z \exp(+2i\omega_R t I_X)\, I_Z \exp(-2i\omega_R t I_X). \qquad \text{[A2.22]}\end{aligned}$$

From Eq. [A2.21], $U(T_R,0) = \widetilde{U}(T_R,0)$ and it follows, from the *deterministic* action of the logarithm in Eq. [2.5], that $\mathcal{H}_{\text{eff}}^{ln} = \widetilde{\mathcal{H}}_{\text{eff}}^{ln}$ and hence transformation to the new rotating frame is not needed. The same holds for the Floquet approach and $\mathcal{H}_{\text{eff}}^{\mathcal{F}} = \widetilde{\mathcal{H}}_{\text{eff}}^{\mathcal{F}} = \mathcal{H}_{\text{eff}}^{ln} = \widetilde{\mathcal{H}}_{\text{eff}}^{ln}$.

It is clear that *the central quantity to determine the matching conditions is the nitrogen effective RF strength*. It therefore presents interest to investigate the CP transfer for other nitrogen RF strengths. Figure A2.5(a) displays $|\nu_{1S}^{\text{eff}}|$ as function of β and γ when the nitrogen RF strength is $\nu_{1S} = 40$ kHz. It is seen that $\left|\nu_{1S}^{\text{eff}}\right|$ peaks around 8 kHz. According to the simple reasoning above, matching will occur if $\left|\nu_{1S}^{\text{eff}}\right| \cong \left|\nu_{1I}^{\text{eff}}\right|$ which, given that $\nu_{1I}^{\text{eff}} \cong \nu_{1I} - \nu_R$, can be achieved when $\nu_{1I} \cong \nu_R \pm \left|\nu_{1S}^{\text{eff}}\right| \cong 52$ or 68 kHz. This is verified in Figure A2.5(b) which shows CP signal as function of β and γ for $\nu_{1I} \cong 52$ kHz. Similar CP transfer is achieved also with $\nu_{1I} \cong 68$ kHz.

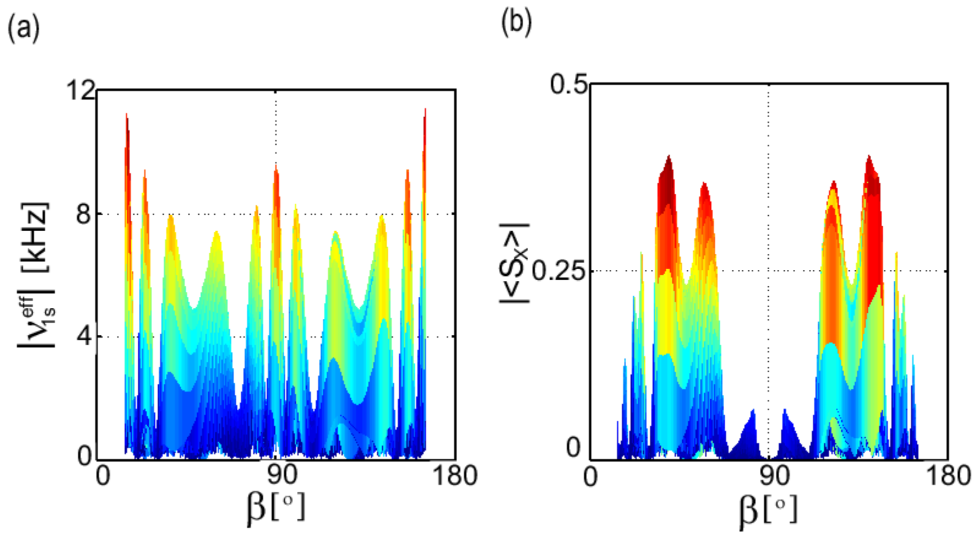

Figure A2.5 (a) Dependence of $\left|\nu_{1S}^{eff}\right|$ *on* β *and* γ*, for a smaller RF strength of S spin,* $\nu_{1S} = 40\ kHz$*. (b) Dependence of the CP signal on* β *and* γ*. The plots are projections along* γ *direction. Calculations start from the Hamiltonian of Eq. [2.9] and assume* $\nu_{1I} = 52\ kHz$*,* $\nu_R = 60\ kHz$*,* $C_Q/2\pi = 1.5\ MHz$*,*$\eta_Q = 0$*,* $\nu_D = 10\ kHz$*,* $\theta_{QD} = 0$*, and* $\tau_{CP} = 10T_R$*.*

𝔄2.9: Effective Hamiltonian with ramp-CP

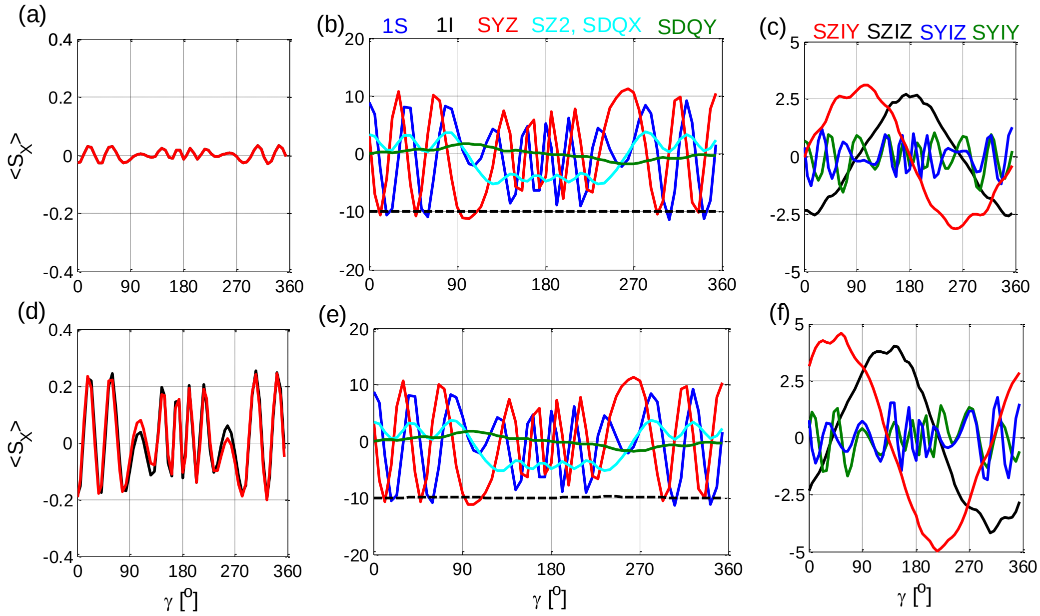

Figure A2.6 Dependence on γ *of CPMAS signal and of a few* ν_p^{eff} *coefficients (a-c) without and (d-f) with a ±3% linear ramp on the* ^{1}*H RF amplitude. Calculations start with the Hamiltonian of Eq. [2.12] and assume* $\nu_D = 10\ kHz$*,* $\beta = 39^\circ$*,* $\nu_{1S} = 80\ kHz$*,* $\nu_{1I} = 50\ kHz$*,* $\nu_R = 60\ kHz$*,* $C_Q/2\pi = 1.5\ MHz$*,* $\eta_Q = 0$*,* $\theta_{QD} = 0$ *and* $\tau_{CP} = 20T_R$*. Labeling of the coefficients is given in Table 2.1. In (a) and (d) signal is calculated with Eq. [2.13] (black) and with* $exp(-i\mathcal{H}_{eff}NT_R)$ *(red). The coefficients* ν_p^{eff} *are expressed in kHz.*

A2.10: Effective Hamiltonian in terms of fictitious spin-1/2 operators

We approximate the Hamiltonian of Eq. [2.26], $\mathcal{H}' = \omega_S S_Z + \omega_{1I}^{\mathrm{eff}} I_Z + \mathcal{H}'_{IS}$, by keeping off-diagonal terms only within, (2,3), (4,5) subspaces. We introduce fictitious spin-1/2 operators

$$Z_{23} = \frac{1}{2}[|2\rangle\langle 2| - |3\rangle\langle 3|],\ X_{23} = \frac{1}{2}[|2\rangle\langle 3| + |3\rangle\langle 2|],\ Y_{23} = \frac{1}{2i}[|2\rangle\langle 3| - |3\rangle\langle 2|]\,,$$

along with the unit operator $\mathbf{1}_{23} = |2\rangle\langle 2| + |3\rangle\langle 3|$ for the $(2,3)$ subspace, and similar operators for the $(1,6)$ and $(4,5)$ subspaces. The Hamiltonian $\mathcal{H}'$ can be written approximately as

$$\mathcal{H}' \cong \mathcal{H}'_{16} + \mathcal{H}'_{23} + \mathcal{H}'_{45}, \tag*{[A2.23]}$$

where $\mathcal{H}'_{16}, \mathcal{H}'_{23}$, and $\mathcal{H}'_{45}$ are to be expressed in terms of the fictitious spin-1/2 operators associated with subspaces$(1,6)$, $(2,3)$, and$(4,5)$. For the $(1,6)$ subspace we have

$$\mathcal{H}'_{16} = \Sigma_{16}\mathbf{1}_{16} + 2(\omega_S + \omega_{1I}/2 + \Delta_{16})Z_{16}, \tag*{[A2.24]}$$

where Σ_{16} and Δ_{16} are linear combinations of matrix elements $\langle 1|\mathcal{H}'_{IS}|1\rangle$ and $\langle 6|\mathcal{H}'_{IS}|6\rangle$. The unit operator $\mathbf{1}_{16}$ has no effect within the subspace and is henceforth omitted. For the $(2,3)$ subspace

$$\mathcal{H}'_{23} = (\omega_S/2)\mathbf{1}_{23} + \Delta Z_{23} + (\mathcal{H}'_{IS})_{23}$$

with $\Delta = \omega_S - \omega_{1I}$. The unit operator $\mathbf{1}_{23}$ has no effect within the subspace and is henceforth omitted. The *IS* term has generally the form

$$(\mathcal{H}'_{IS})_{23} = z_{23}Z_{23} + x_{23}X_{23} + y_{23}Y_{23},$$

where the coefficients z_{23}, x_{23}, y_{23} depend on the matrix elements of $\mathcal{H}'_{IS}$ in the $(2,3)$ subspace. The Hamiltonian is then

$$\mathcal{H}'_{23} = \Delta'_{23}Z_{23} + x_{23}X_{23} + y_{23}Y_{23} \tag*{[A2.25]}$$

with $\Delta'_{23} = \Delta + z_{23}$. Similarly, for the $(4,5)$ subspace

$$\mathcal{H}'_{45} = (-\omega_S/2)\mathbf{1}_{45} + \Delta Z_{45} + (\mathcal{H}'_{IS})_{45}$$

and, after dropping $\mathbf{1}_{45}$ and expressing $(\mathcal{H}'_{IS})_{45}$, we obtain

$$\mathcal{H}'_{45} = \Delta'_{45}\mathrm{Z}_{45} + \mathrm{x}_{45}\mathrm{X}_{45} + \mathrm{y}_{45}\mathrm{Y}_{45}, \qquad \text{[A2.26]}$$

with $\Delta'_{45} = \Delta + z_{45}$. The Hamiltonian $\mathcal{H}'_{23}$ can be further expressed as

$$\mathcal{H}'_{23} = e^{-i\phi_Z^{23}Z_{23}}e^{i\phi_Y^{23}Y_{23}}[\Omega_{23}X_{23}]e^{-i\phi_Y^{23}Y_{23}}e^{i\phi_Z^{23}Z_{23}}, \qquad \text{[A2.27]}$$

where $\Omega_{23} = \sqrt{(\Delta'_{23})^2 + x_{23}^2 + y_{23}^2}$ and

$$tan\phi_Z^{23} = y_{23}/x_{23},$$

$$tan\phi_Y^{23} = \Delta'_{23}\Big/\sqrt{x_{23}^2 + y_{23}^2}.$$

Similarly, $\mathcal{H}'_{45}$ can be expressed as

$$\mathcal{H}'_{45} = e^{-i\phi_Z^{45}Z_{45}}e^{i\phi_Y^{45}Y_{45}}[\Omega_{45}X_{45}]e^{-i\phi_Y^{45}Y_{45}}e^{i\phi_Z^{45}Z_{45}}, \qquad \text{[A2.28]}$$

where $\Omega_{45} = \sqrt{(\Delta'_{45})^2 + x_{45}^2 + y_{45}^2}$ and angles ϕ_Z^{45}, ϕ_Y^{45} are defined in a similar way as angles ϕ_Z^{23}, ϕ_Y^{23}.

Since $\mathcal{H}'$ is block-diagonal, the corresponding propagator V can be written as

$$V = e^{-i\mathcal{H}'nT_R} = e^{-i\mathcal{H}'_{16}nT_R} + e^{-i\mathcal{H}'_{23}nT_R} + e^{-i\mathcal{H}'_{45}nT_R} = V_{16} + V_{23} + V_{45}.$$

Here we have

$$e^{-i\mathcal{H}'_{23}nT_R} = \sum_{p,q=2,3} |p\rangle\langle p|e^{-i\mathcal{H}'_{23}nT_R}|q\rangle\langle q|,$$

and similar expressions for the other two exponential operators. Explicitly,

$$V_{16} = e^{-2i(\omega_S+\omega_{1I}/2+\Delta_{16})Z_{16}nT_R}, \qquad \text{[A2.29a]}$$

$$V_{23} = e^{-i\phi_Z^{23}Z_{23}}e^{i\phi_Y^{23}Y_{23}}e^{-\mathrm{i}\Omega_{23}X_{23}nT_R}e^{-i\phi_Y^{23}Y_{23}}e^{i\phi_Z^{23}Z_{23}}, \qquad \text{[A2.29b]}$$

$$V_{45} = e^{-i\phi_Z^{45}Z_{45}}e^{i\phi_Y^{45}Y_{45}}e^{-\mathrm{i}\Omega_{45}X_{45}nT_R}e^{-i\phi_Y^{45}Y_{45}}e^{i\phi_Z^{45}Z_{45}}. \qquad \text{[A2.29c]}$$

With an initial density operator $I_Z = Z_{16} - Z_{23} - Z_{45}$, one finds

$$\begin{aligned} VI_ZV^\dagger = Z_{16} - Z_{23}[&\cos^2\phi_Y^{23}\,cos(\Omega_{23}nT_R) + \sin^2\phi_Y^{23}] \\ &- Z_{45}[\cos^2\phi_Y^{45}\,cos(\Omega_{45}nT_R) + \sin^2\phi_Y^{45}] \\ &+\mathrm{A}_{23} + A_{45}, \end{aligned} \qquad \text{[A2.30]}$$

where

$$\begin{aligned}\mathrm{A}_{23} = X_{23}&\left[\frac{1}{2} sin2\phi_Y^{23} cos\phi_Z^{23}[1-\cos\,(\Omega_{23}nT_R)] + sin\phi_Z^{23} cos\phi_Y^{23} sin(\Omega_{23}nT_R)\right]\\ &+ Y_{23}\left[\frac{1}{2} sin2\phi_Y^{23} sin\phi_Z^{23}[1-\cos\,(\Omega_{23}nT_R)] - cos\phi_Z^{23} cos\phi_Y^{23} sin(\Omega_{23}nT_R)\right],\end{aligned}$$

[A2.31]

and A_{45} can be obtained by replacing '23' with '45' in the above equation.

To obtain the direct transfer amplitude A_{IS} we need to evaluate right hand side of Eq. [2.27], $A_{IS} = \frac{1}{4}\mathrm{Tr}\{VI_Z V^{\dagger} D^{\dagger} S_Z D\}$. Since D acts only on the S part of the basis states, $D^{\dagger} S_Z D$ does not contain X_{23}, Y_{23} or X_{45}, Y_{45} terms. Therefore, A_{23} and A_{45} terms *do not contribute* to the trace in Eq. [2.19] and hence

$$\begin{aligned}A_{IS} = \frac{1}{4}\mathrm{Tr}\Big\{\Big[&Z_{16} - Z_{23}[\cos^2\phi_Y^{23}\, cos(\Omega_{23}nT_R) + \sin^2\phi_Y^{23}]\\ &- Z_{45}[\cos^2\phi_Y^{45}\, cos(\Omega_{45}nT_R)\\ &+ \sin^2\phi_Y^{45}]\Big]\, D^{\dagger} S_Z D\Big\},\end{aligned} \qquad \text{[A2.32]}$$

which is Eq. [2.21].

To obtain the inverse transfer amplitude A_{SI} we need to evaluate the right hand side of Eq. [2.22], $A_{SI} == \frac{2}{3}\mathrm{Tr}\{V^{\dagger} I_Z V D^{\dagger} S_Z D\}$. Since $V^{\dagger} = e^{+i\mathcal{H}' nT_R} = e^{-i\mathcal{H}'(-nT_R)}$, we infer from Eq. [A2.32] that

$$\begin{aligned}V^{\dagger} I_Z V = Z_{16} &- Z_{23}[\cos^2\phi_Y^{23}\, cos(\Omega_{23}nT_R) + \sin^2\phi_Y^{23}]\\ &- Z_{45}[\cos^2\phi_Y^{45}\, cos(\Omega_{45}nT_R) + \sin^2\phi_Y^{45}] + B_{23} + B_{45},\end{aligned}$$

where the term $B_{23} + B_{45}$ can be obtained by substituiting $\Omega_{23}nT_R \rightarrow -\Omega_{23}nT_R$ and $\Omega_{45}nT_R \rightarrow -\Omega_{45}nT_R$ in $A_{23} + A_{45}$. However, since $B_{23} + B_{45}$ does not contribute to the trace,

$$\begin{aligned}A_{SI} = \frac{2}{3}\mathrm{Tr}\Big\{\Big[&Z_{16} - Z_{23}[\cos^2\phi_Y^{23}\, cos(\Omega_{23}nT_R) + \sin^2\phi_Y^{23}]\\ &- Z_{45}[\cos^2\phi_Y^{45}\, cos(\Omega_{45}nT_R)\\ &+ \sin^2\phi_Y^{45}]\Big]\, D^{\dagger} S_Z D\Big\},\end{aligned} \qquad \text{[A2.33]}$$

which is Eq. [2.33].

A2.11: Verification of the theoretical ratio $A_{IS}/A_{SI} = 3/8$

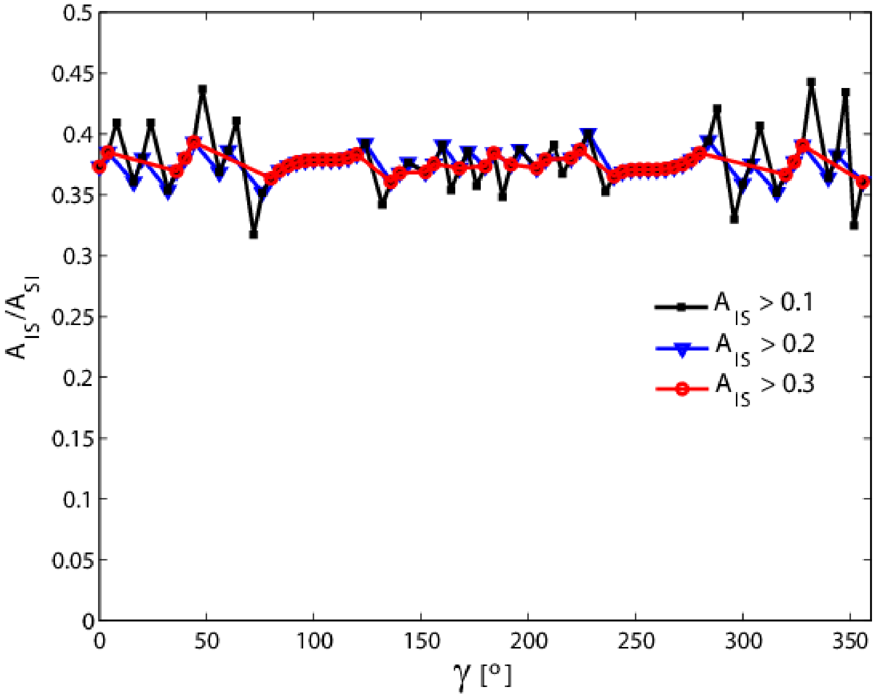

Figure A2.7 Dependence of the A_{IS}/A_{SI} on γ for a contact time $\tau_{CP} = 12T_R$. Simulations assume $\beta = 32^{\circ}, \nu_D = 10\ kHz, \nu_{1S} = 80\ kHz, \nu_{1I} = 46\ kHz, \nu_R = 60\ kHz, C_Q/2\pi = 1.5\ MHz, \eta_Q = 0, \theta_{QD} = 0$. The three different plots show ratios for those gamma angles for which A_{IS} is larger than 0.1(black), 0.2(blue), and 0.3(red). The average ratio A_{IS}/A_{SI} and the error were 0.376 ± 0.01, 0.375 ± 0.005, and 0.375 ± 0.003 respectively.

A2.12: Discussion of double CP powder lineshapes

It is seen that, for $\theta_{QD} = 0°$, regardless of CP duration, the singularity at 4.26 kHz has negligible intensity. This singularity corresponds to $\beta_Q = 90°$ and for $\theta_{QD} = 0°$, the ν_R component of the dipolar interaction vanishes resulting in negligible CP transfer. For nonvanishing θ_{QD} angles this component is non-zero leading to CP transfer and hence the presence of the singularity, as seen in Figure A2.8(b-d). For an ideal lineshape, another singularity occurs at 3.48 kHz corresponding to $\beta_Q \cong 49°$ and 131°. This singularity is slightly displaced to higher frequency values in the double CP spectra, regardless of CP duration or θ_{QD}. This can be predicted by inspection of Figure 2.6(d), which shows that, around $\beta_Q = 50°, 130^{o}$, the ^{14}N effective RF strength, ν_{1S}^{eff}, is far from the CP matching condition. The lineshapes in Figure A2.8(e-h) are obtained with other RF strengths: $\nu_{1S} = 85$ kHz, $\nu_{1I} = 50$ kHz. For almost all spectra, a singularity is present at 3.54 kHz, very close to the ideal-lineshape position. This is due to the fact that, with the new RF strengths, ν_{1S}^{eff} is approximately satisfying the matching condition around $\beta_Q = 50°, 130^o$. As before, the singularity corresponding to $\beta_Q = 90°$ is not visible for the $\theta_{QD} = 0$ geometry.

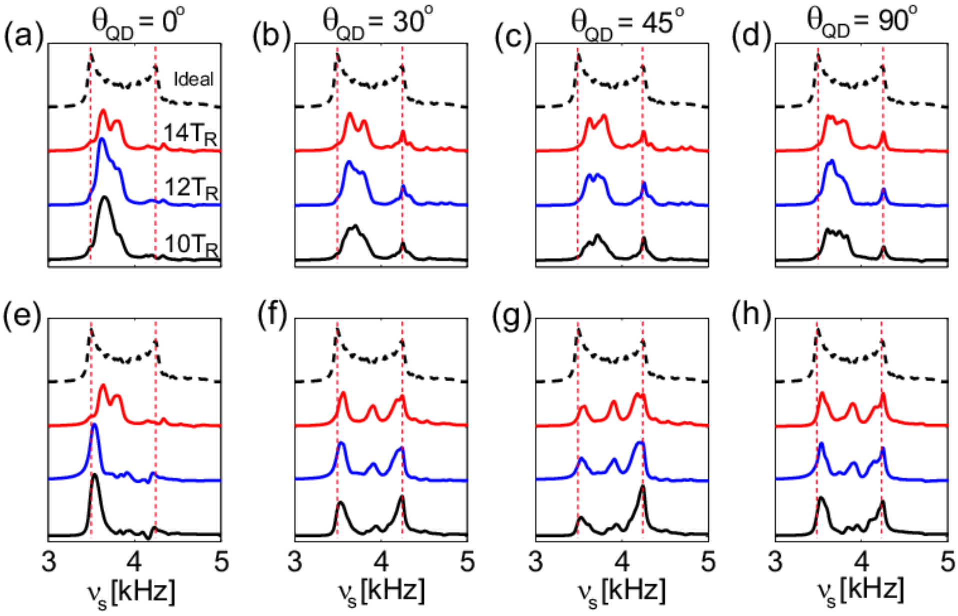

Figure A2.8 Double CP ^{14}N powder lineshapes simulated for different experimental conditions and with four different angles between the Z axes of the quadrupole and dipole PAFs. In (a-d) $\nu_{1S} = 80\ kHz$, $\nu_{1I} = 46\ kHz$ while in (e-h) $\nu_{1S} = 85\ kHz, \nu_{1I} = 50\ kHz$. Contact times are 10 (black), 12 (blue), 14 (red) rotor periods. The 4 columns, from left to right, correspond to a θ_{QD} angle of 0°, 30°, 45°, and 90°. Common parameters are $\nu_R = 60\ kHz$, $C_Q/2\pi = 1.5\ MHz$, $\eta_Q = 0$ $\nu_D = 10\ kHz$. An ideal ^{14}N powder lineshape corresponding to the above quadrupolar parameters (dashed line) is displayed for comparison. Vertical lines passing through the singularities of the ideal lineshape are also shown.

Appendix 3

A3.1: System Hamiltonian

The Hamiltonian defining the system is given by

$$\mathcal{H}(t) = \Delta\omega_S S_Z + \omega_{1S} S_X + \mathcal{H}_Q^{(2)}(t,\beta_Q,\gamma_Q) + \omega_Q(t,\beta_Q,\gamma_Q)[3S_Z^2 - S(S+1)] + d(t,\beta_D,\gamma_D)2I_Z S_Z. \qquad \text{[A3.1]}$$

In the above equation,

$$\omega_Q(t,\beta_Q,\gamma_Q) = \frac{C_Q}{3}\left[\frac{1}{8}sin^2(\beta_Q)cos(2\omega_R t + 2\gamma_Q) - \frac{1}{4\sqrt{2}}sin(2\beta_Q)\,cos\,(\omega_R t + \gamma_Q)\right]. \qquad \text{[A3.2]}$$

The explicit form of the second-order quadrupolar interaction is

$$H_Q^{(2)}(t,\beta_Q,\gamma_Q) = \frac{2(\omega_Q^2)}{9\omega_{oS}}(L + M + N) \qquad \text{[A3.3]}$$

where $\omega_Q = (3\pi C_Q)/2S(2S-1) = (\pi C_Q)/2$ and

$L = \frac{3}{5}\mathrm{Sz}\left\{3{S_z}^2 - \mathrm{S(S+1)}\mathbf{1}_S\right\}$,

$M = \frac{3}{56}\mathrm{Sz}\left\{12{S_z}^2 - 8\mathrm{S(S+1)}\mathbf{1}_S + 3\mathbf{1}_S\right\}\{M_1\,cos(\omega_R t + \gamma_Q) + M_2\,cos(2\omega_R t + 2\gamma_Q)\}$,

$N = \frac{9}{4480}\mathrm{Sz}\{-34{S_z}^2 + 18\mathrm{S(S+1)}\mathbf{1}_S - 51\mathbf{1}_S\}\{N_0 - 40N_1 cos(\omega_R t + \gamma_Q) + 20N_2\,cos(2\omega_R t + 2\gamma_Q) - 280N_3\,cos(3\omega_R t + 3\gamma_Q) + 35N_4\,cos(4\omega_R t + 4\gamma_Q)\}$,

$M_1 = -3\left(sin\,2\beta_Q\right)(sin\,2\theta_M), \qquad M_2 = 3\,(\sin^2\beta_Q)(\sin^2\theta_M)$,

$N_0 = \left(35\,cos^4\beta_Q - 30\,cos^2\beta_Q + 3\right)(35\cos^4\theta_m - 30\cos^2\theta_m + 3)$,

$N_1 = sin\,\beta_Q\left(7\,cos^3\beta_Q - 3\,cos\,\beta_Q\right)sin\,\theta_M\,(7\,cos^3\theta_M - 3\,cos\,\theta_M)$,

$N_2 = sin^2\beta_Q\left(7\,cos^2\beta_Q - 1\right)sin^2\theta_M\,(7\,cos^2\theta_M - 1)$,

$N_3 = cos\,\beta_Q\,sin^3\beta_Q\,cos\,\theta_M\,sin^3\theta_M$,

$N_4 = sin^4\beta_Q\,sin^4\theta_M$.

In the equations above $\mathbf{1}_S$ represents the S-spin unit operator.

We consider an axially-symmetric quadrupolar interaction (asymmetry parameter, $\eta_Q = 0$). The MAS-averaged second-order quadrupolar interaction can be obtained from Eq. [A3.3] by keeping only the time-independent terms and is given by

$$\mathcal{H}_Q^{(2)}(\beta_Q) = (2\omega_Q^2)/(9\omega_{0S})(L + N'), \qquad \text{[A3.4]}$$

where

$$N^{'} = \frac{9}{4480}\mathrm{Sz}\left\{-34{S_z}^2 + 18\mathrm{S}(\mathrm{S}+1)\mathbf{1}_S - 5\mathbf{1}_S\right\}N_0.$$

Here ω_{0S} represents the Larmor frequency of the S spin and θ_m denotes the magic angle. Simulations with and without the time-dependent part of the second-order quadrupolar interaction showed very little difference, hence omission of the time-dependent part is justified for the RF strength and spinning speed considered here.

The time-dependent spatial part of the dipolar interaction is given by,

$$d(t, \beta_D, \gamma_D) = \omega_D\left[\frac{\sin(2\beta_D)}{2\sqrt{2}}\cos(\omega_R t + \gamma_D) - \frac{\sin^2(\beta_D)}{4}\cos(2\omega_R t + 2\gamma_D)\right]. \qquad \text{[A3.5]}$$

𝔄3.2: Form of the effective Hamiltonian

The general form of the Hamiltonian under consideration (Eq. [A3.1]) is given by the expression:

$$\mathcal{H}(t) = \mathcal{H}_s(t) + d(t)I_Z S_Z, \qquad \text{[A3.6]}$$

where $\mathcal{H}_s(t)$ represent the various S terms appearing and $d(t)I_Z S_Z$ represents the dipolar part.

An effective Hamiltonian, $\mathcal{H}_{eff}$, is any time-independent Hamiltonian which satisfy

$$U(T_R, 0)=e^{-i\mathcal{H}_{eff}T_R}, \qquad \text{[A3.7]}$$

where $U(t_2, t_1)$ represents the propagator between times t_1 and t_2. The most general form for the *I*-*S* system is

$$\mathcal{H}_{eff}= \mathcal{H}_{eff}^{s}+ (A_s I_Z + B_s I_X + C_s I_Y) \qquad \text{[A3.8]}$$

where $\mathcal{H}_{eff}^{S}$ represents the '*pure-S*' part of the effective Hamiltonian and the remaining terms are heteronuclear terms of the effective Hamiltonian.

On the other hand, with $\hat{T}$ standing for Dyson's time-ordering operator,

$$U(T_R, 0) = \hat{T}exp\left[-i\int_0^{T_R}\mathcal{H}(t)dt\right],$$

which is equivalent to the time-ordered limit

$$U(T_R, 0) = \lim_{\Delta t\to 0}\prod_k e^{-i\mathcal{H}(t_k)\Delta t}. \qquad \text{[A3.9]}$$

For any exponential operator in the product above we have

$$\langle m_S, m_I|e^{-i\mathcal{H}(t_k)\Delta t}|m_S', m_I'\rangle = \sum_{n=0}^{\infty}\frac{(-i\Delta t)^n}{n!}\langle m_S, m_I|\mathcal{H}(t_k)^n\,|m_S', m_I'\rangle$$

and, since for any *n* we have $\langle m_S, m_I|\mathcal{H}(t_k)^n\,|m_S', m_I'\rangle = 0$ if $m_I \neq m_I'$, it follows that

$$\langle m_S, m_I|e^{-i\mathcal{H}(t_k)\Delta t}|m_S', m_I'\rangle = 0 \text{ if } m_I \neq m_I',$$

and that

$$\langle m_S, m_I|\prod_k e^{-i\mathcal{H}(t_k)\Delta t}\,|m_S', m_I'\rangle = 0 \text{ if } m_I \neq m_I'.$$

The equality above will hold also for the limit $\Delta t \to 0$ hence we have the exact result

$$\langle m_S, m_I|e^{-i\mathcal{H}_{eff}T_R}|m_S', m_I'\rangle = 0 \text{ if } m_I \neq m_I'. \qquad \text{[A3.10]}$$

Therefore, $\mathcal{H}_{eff}$ cannot contain $B_S I_X$ or $C_S I_Y$ terms since presence of such terms would violate Eq. [A3.10]. Hence, $\mathcal{H}_{eff} = \mathcal{H}_{eff}^{S} + A_S I_Z$. Numerical simulations are in agreement with this result (simulations show erratic $B_S I_X$ and $C_S I_Y$ terms of the order of 10^{-15}, obviously due to numerical computation errors).

𝔄3.3: Coherence types produced by TRAPDOR irradiation

Figure A3.1 illustrates the theoretical statement in the Chapter 3, according to which, starting form $\rho(0) = I_X$, the only coherences produced at the end of first TRAPDOR block are heteronuclear coherences involving I_X and I_Y.

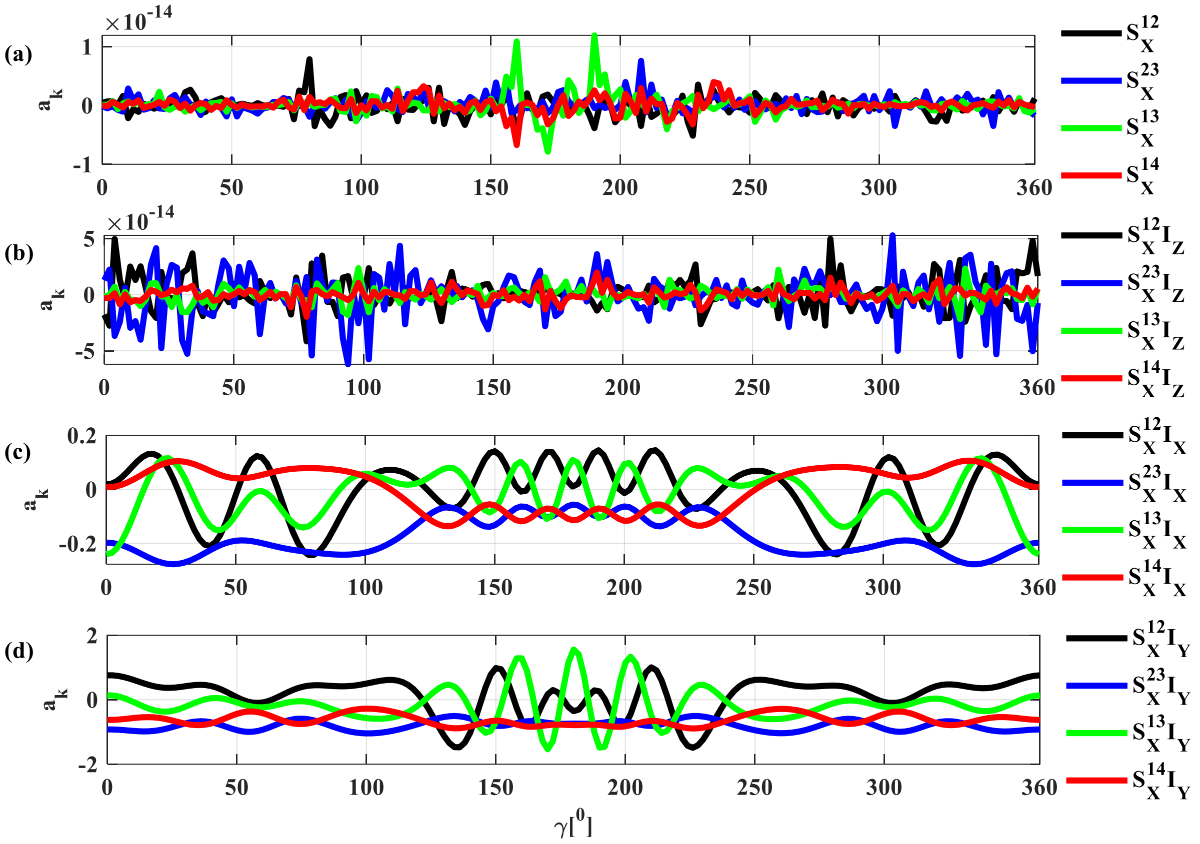

Figure A3.1 Variation, with γ *angle, of the amplitude of several coherences at the end of first TRAPDOR block with* $\rho(0) = I_X$ *corresponding to (a) pure S terms, (b) heteronuclear terms with* I_Z*, (c) heteronuclear terms with* I_X*, and (d) heteronuclear terms with* I_Y*. Numerical simulations are performed with* $\beta = 50^o$, $C_Q = 2\,MHz$, $\nu_D = 1\,kHz$, $\nu_{1S} = 90\,kHz$, $\Delta\nu_S = 10\,kHz$, *and* $\nu_R = 60\,kHz$*. Duration of TRAPDOR irradiation is* $100T_R$ *(~1.67 ms.). All the terms in Eq. [A3.1] are considered.*

𝔄3.4: Matrix Representation of Operators

Here, the Zeeman states of spin S are labelled as $|1\rangle = |3/2\rangle, |2\rangle = |1/2\rangle, |3\rangle = |-1/2\rangle$, and $|4\rangle = |-3/2\rangle$. Subsequently, $\mathcal{H}_{eff}$, $\mathcal{H}_{eff}^{S}$, and $A_S I_Z$ are expanded into an operator basis (8× 8 matrices) containing products of Cartesian I-spin operators I_X, I_Y, I_Z and fictitious spin-1/2 operators[52] for spin S (S_α^{ij} with $\alpha = X, Y, Z$ and $i, j = 1,2,3,4$). S_α^{12} *and* S_α^{34} are satellite-transition single-quantum operators, S_α^{23} are central-transition single-quantum operators, S_α^{13} *and* S_α^{24} are satellite-transition double-quantum operators, and S_α^{14} are triple-quantum operators. For example, $\mathcal{H}_{eff}^{S}$ may contain $S_X^{12} = \mathbf{1}_I[|1\rangle\langle 2| + |2\rangle\langle 1|]/2$, where $\mathbf{1}_I$ is the I-spin unit operator; and $A_S I_Z$ may contain heteronuclear terms such as $S_X^{23} I_Z$. The corresponding matrix representations are given below.

$$I_X = \frac{1}{2}\begin{bmatrix} 0 & 1 & 0 & 0 & 0 & 0 & 0 & 0 \\ 1 & 0 & 0 & 0 & 0 & 0 & 0 & 0 \\ 0 & 0 & 0 & 1 & 0 & 0 & 0 & 0 \\ 0 & 0 & 1 & 0 & 0 & 0 & 0 & 0 \\ 0 & 0 & 0 & 0 & 0 & 1 & 0 & 0 \\ 0 & 0 & 0 & 0 & 1 & 0 & 0 & 0 \\ 0 & 0 & 0 & 0 & 0 & 0 & 0 & 1 \\ 0 & 0 & 0 & 0 & 0 & 0 & 1 & 0 \end{bmatrix}, I_Y = \frac{1}{2}\begin{bmatrix} 0 & -i & 0 & 0 & 0 & 0 & 0 & 0 \\ i & 0 & 0 & 0 & 0 & 0 & 0 & 0 \\ 0 & 0 & 0 & -i & 0 & 0 & 0 & 0 \\ 0 & 0 & i & 0 & 0 & 0 & 0 & 0 \\ 0 & 0 & 0 & 0 & 0 & -i & 0 & 0 \\ 0 & 0 & 0 & 0 & i & 0 & 0 & 0 \\ 0 & 0 & 0 & 0 & 0 & 0 & 0 & -i \\ 0 & 0 & 0 & 0 & 0 & 0 & i & 0 \end{bmatrix}$$

$$I_Z = \frac{1}{2}\begin{bmatrix} 1 & 0 & 0 & 0 & 0 & 0 & 0 & 0 \\ 0 & -1 & 0 & 0 & 0 & 0 & 0 & 0 \\ 0 & 0 & 1 & 0 & 0 & 0 & 0 & 0 \\ 0 & 0 & 0 & -1 & 0 & 0 & 0 & 0 \\ 0 & 0 & 0 & 0 & 1 & 0 & 0 & 0 \\ 0 & 0 & 0 & 0 & 0 & -1 & 0 & 0 \\ 0 & 0 & 0 & 0 & 0 & 0 & 1 & 0 \\ 0 & 0 & 0 & 0 & 0 & 0 & 0 & -1 \end{bmatrix}, S_X^{23} = \frac{1}{2}\begin{bmatrix} 0 & 0 & 0 & 0 & 0 & 0 & 0 & 0 \\ 0 & 0 & 0 & 0 & 0 & 0 & 0 & 0 \\ 0 & 0 & 0 & 0 & 1 & 0 & 0 & 0 \\ 0 & 0 & 0 & 0 & 0 & 1 & 0 & 0 \\ 0 & 0 & 1 & 0 & 0 & 0 & 0 & 0 \\ 0 & 0 & 0 & 1 & 0 & 0 & 0 & 0 \\ 0 & 0 & 0 & 0 & 0 & 0 & 0 & 0 \\ 0 & 0 & 0 & 0 & 0 & 0 & 0 & 0 \end{bmatrix},$$

$$S_Y^{23} = \frac{1}{2}\begin{bmatrix} 0 & 0 & 0 & 0 & 0 & 0 & 0 & 0 \\ 0 & 0 & 0 & 0 & 0 & 0 & 0 & 0 \\ 0 & 0 & 0 & 0 & -i & 0 & 0 & 0 \\ 0 & 0 & 0 & 0 & 0 & -i & 0 & 0 \\ 0 & 0 & i & 0 & 0 & 0 & 0 & 0 \\ 0 & 0 & 0 & i & 0 & 0 & 0 & 0 \\ 0 & 0 & 0 & 0 & 0 & 0 & 0 & 0 \\ 0 & 0 & 0 & 0 & 0 & 0 & 0 & 0 \end{bmatrix}, S_Z^{23} = \frac{1}{2}\begin{bmatrix} 0 & 0 & 0 & 0 & 0 & 0 & 0 & 0 \\ 0 & 0 & 0 & 0 & 0 & 0 & 0 & 0 \\ 0 & 0 & 1 & 0 & 0 & 0 & 0 & 0 \\ 0 & 0 & 0 & 1 & 0 & 0 & 0 & 0 \\ 0 & 0 & 0 & 0 & -1 & 0 & 0 & 0 \\ 0 & 0 & 0 & 0 & 0 & -1 & 0 & 0 \\ 0 & 0 & 0 & 0 & 0 & 0 & 0 & 0 \\ 0 & 0 & 0 & 0 & 0 & 0 & 0 & 0 \end{bmatrix},$$

$$S_X^{12} = \frac{1}{2}\begin{bmatrix} 0 & 0 & 1 & 0 & 0 & 0 & 0 & 0 \\ 0 & 0 & 0 & 1 & 0 & 0 & 0 & 0 \\ 1 & 0 & 0 & 0 & 0 & 0 & 0 & 0 \\ 0 & 1 & 0 & 0 & 0 & 0 & 0 & 0 \\ 0 & 0 & 0 & 0 & 0 & 0 & 0 & 0 \\ 0 & 0 & 0 & 0 & 0 & 0 & 0 & 0 \\ 0 & 0 & 0 & 0 & 0 & 0 & 0 & 0 \\ 0 & 0 & 0 & 0 & 0 & 0 & 0 & 0 \end{bmatrix}, S_Y^{12} = \frac{1}{2}\begin{bmatrix} 0 & 0 & -i & 0 & 0 & 0 & 0 & 0 \\ 0 & 0 & 0 & -i & 0 & 0 & 0 & 0 \\ i & 0 & 0 & 0 & 0 & 0 & 0 & 0 \\ 0 & i & 0 & 0 & 0 & 0 & 0 & 0 \\ 0 & 0 & 0 & 0 & 0 & 0 & 0 & 0 \\ 0 & 0 & 0 & 0 & 0 & 0 & 0 & 0 \\ 0 & 0 & 0 & 0 & 0 & 0 & 0 & 0 \\ 0 & 0 & 0 & 0 & 0 & 0 & 0 & 0 \end{bmatrix},$$

$$S_X^{13} = \frac{1}{2}\begin{bmatrix} 0 & 0 & 0 & 0 & 1 & 0 & 0 & 0 \\ 0 & 0 & 0 & 0 & 0 & 1 & 0 & 0 \\ 0 & 0 & 0 & 0 & 0 & 0 & 0 & 0 \\ 0 & 0 & 0 & 0 & 0 & 0 & 0 & 0 \\ 1 & 0 & 0 & 0 & 0 & 0 & 0 & 0 \\ 0 & 1 & 0 & 0 & 0 & 0 & 0 & 0 \\ 0 & 0 & 0 & 0 & 0 & 0 & 0 & 0 \\ 0 & 0 & 0 & 0 & 0 & 0 & 0 & 0 \end{bmatrix}, S_Y^{13} = \frac{1}{2}\begin{bmatrix} 0 & 0 & 0 & 0 & -i & 0 & 0 & 0 \\ 0 & 0 & 0 & 0 & 0 & -i & 0 & 0 \\ 0 & 0 & 0 & 0 & 0 & 0 & 0 & 0 \\ 0 & 0 & 0 & 0 & 0 & 0 & 0 & 0 \\ i & 0 & 0 & 0 & 0 & 0 & 0 & 0 \\ 0 & i & 0 & 0 & 0 & 0 & 0 & 0 \\ 0 & 0 & 0 & 0 & 0 & 0 & 0 & 0 \\ 0 & 0 & 0 & 0 & 0 & 0 & 0 & 0 \end{bmatrix},$$

$$S_Z^{14} = \frac{1}{2}\begin{bmatrix} 1 & 0 & 0 & 0 & 0 & 0 & 0 & 0 \\ 0 & 1 & 0 & 0 & 0 & 0 & 0 & 0 \\ 0 & 0 & 0 & 0 & 0 & 0 & 0 & 0 \\ 0 & 0 & 0 & 0 & 0 & 0 & 0 & 0 \\ 0 & 0 & 0 & 0 & 0 & 0 & 0 & 0 \\ 0 & 0 & 0 & 0 & 0 & 0 & 0 & 0 \\ 0 & 0 & 0 & 0 & 0 & 0 & -1 & 0 \\ 0 & 0 & 0 & 0 & 0 & 0 & 0 & -1 \end{bmatrix}$$

It can easily be verified that $S_X = 2S_X^{23} + \sqrt{3}(S_X^{12} + S_X^{34}), S_Z = 3S_Z^{14} + S_Z^{23}$ and so on.

A3.5: Comparison of two truncation procedures

Comparison between amplitudes calculated with (A) $A'_S I_Z = \sum_m |\tilde{m}\rangle\langle\tilde{m}|\langle\tilde{m}|A_S|\tilde{m}\rangle\, I_Z$, where $|\tilde{m}\rangle$ denote the eigenstates of $\mathcal{H}_{eff}^S$, and (B) calculated with $A'_S I_Z = \mathcal{H}_{eff}^S I_Z tr\{A_S I_Z \mathcal{H}_{eff}^S I_Z\}/tr\left\{\left(\mathcal{H}_{eff}^S I_Z\right)^2\right\}$ which corresponds to the approach in Ref. [21]. Black curves correspond to simulations without any truncation approximation. Three β angles were chosen to illustrate various possibilities: full agreement between (A) and (B), partial agreement, and full disagreement.

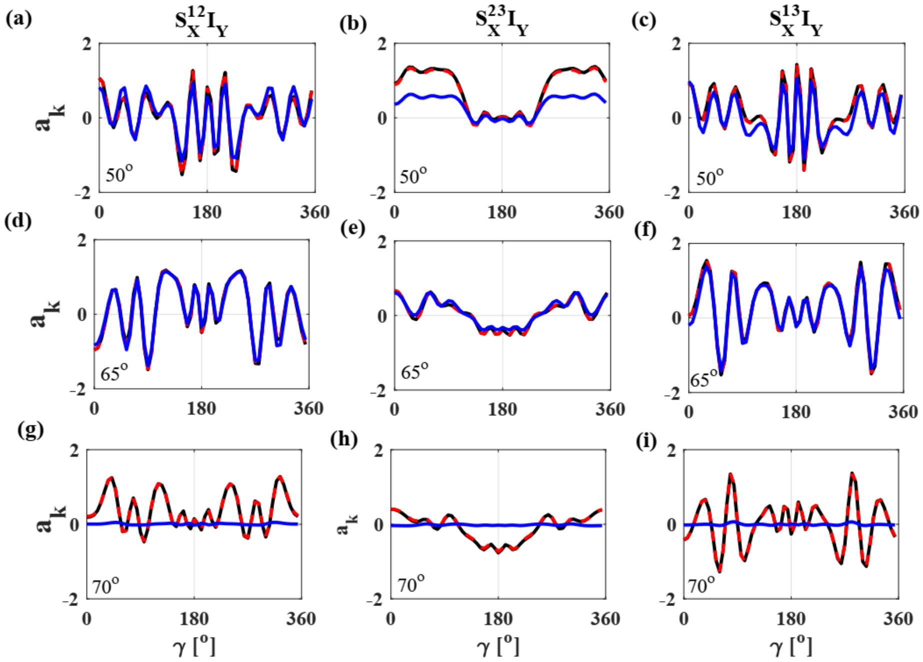

Figure A3.2 Variation of the amplitude of several coherences at the end of first TRAPDOR block with γ angle. The calculations are performed without truncation (black), truncation approximation based on Eq. [3.4] and [3.5] (red dash), and truncation approximation utilized in Ref. [21] *(blue). Numerical simulations are performed with $C_Q = 2\ MHz$, $\nu_D = 1\ kHz$, $\nu_{1S} = 100\ kHz$, $\Delta\nu_S = 10\ kHz$, and $\nu_R = 60\ kHz$. Duration of TRAPDOR irradiation is $100T_R$ (~1.67 ms). The β angle is indicated in each plot.*

A3.6: Sign (phase) of the signal

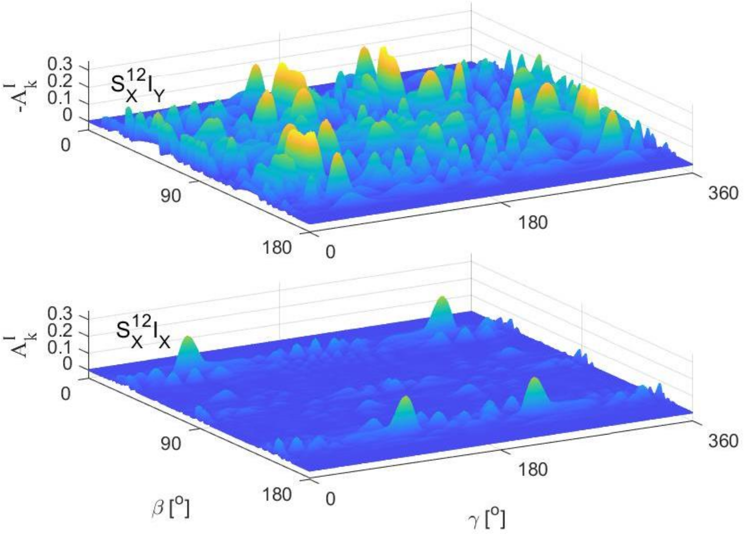

Figure A3.3 Top: T-HMQC experiment ($t_1 = 0$): dependence on β and γ of I-spin signal, A_k^I, corresponding to coherence $S_X^{12}I_Y$ produced by first TRAPDOR block. For better visibility $-A_k^I$ is displayed. Bottom: dependence on β and γ of I-spin signal, A_k^I, corresponding to coherence $S_X^{12}I_X$ produced by the first TRAPDOR block. Other parameters used are, $C_Q = 2\ MHz$, $\nu_D = 1\ kHz$, $\nu_{1S} = 100\ kHz$, $\Delta\nu_S = 10\ kHz$, and $\nu_R = 60\ kHz$. Duration of excitation and reconversion TRAPDOR blocks is $100T_R$. No I-spin π pulse is applied between the two blocks.

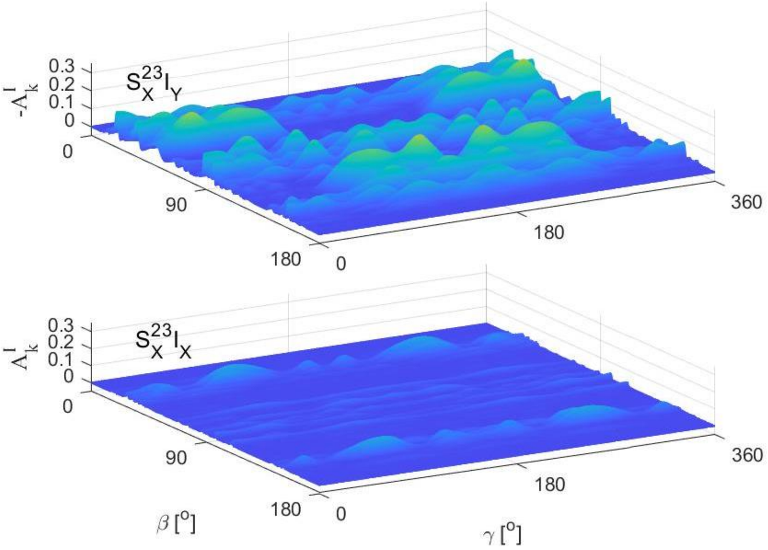

Figure A3.4 Top: T-HMQC experiment ($t_1 = 0$): dependence on β and γ of I-spin signal, A_k^I, corresponding to coherence $S_X^{23}I_Y$ produced by first TRAPDOR block. For better visibility $-A_k^I$ is displayed. Bottom: dependence on β and γ of I-spin signal, A_k^I, corresponding to coherence $S_X^{23}I_X$ produced by the first TRAPDOR block. Other parameters used are, $C_Q = 2\ MHz$, $\nu_D = 1\ kHz$, $\nu_{1S} = 100\ kHz$, $\Delta\nu_S = 10\ kHz$, and $\nu_R = 60\ kHz$. Duration of excitation and reconversion TRAPDOR blocks is $100T_R$. No I-spin π pulse is applied between the two blocks.

A3.7: Evolution with four level crossings per rotor period

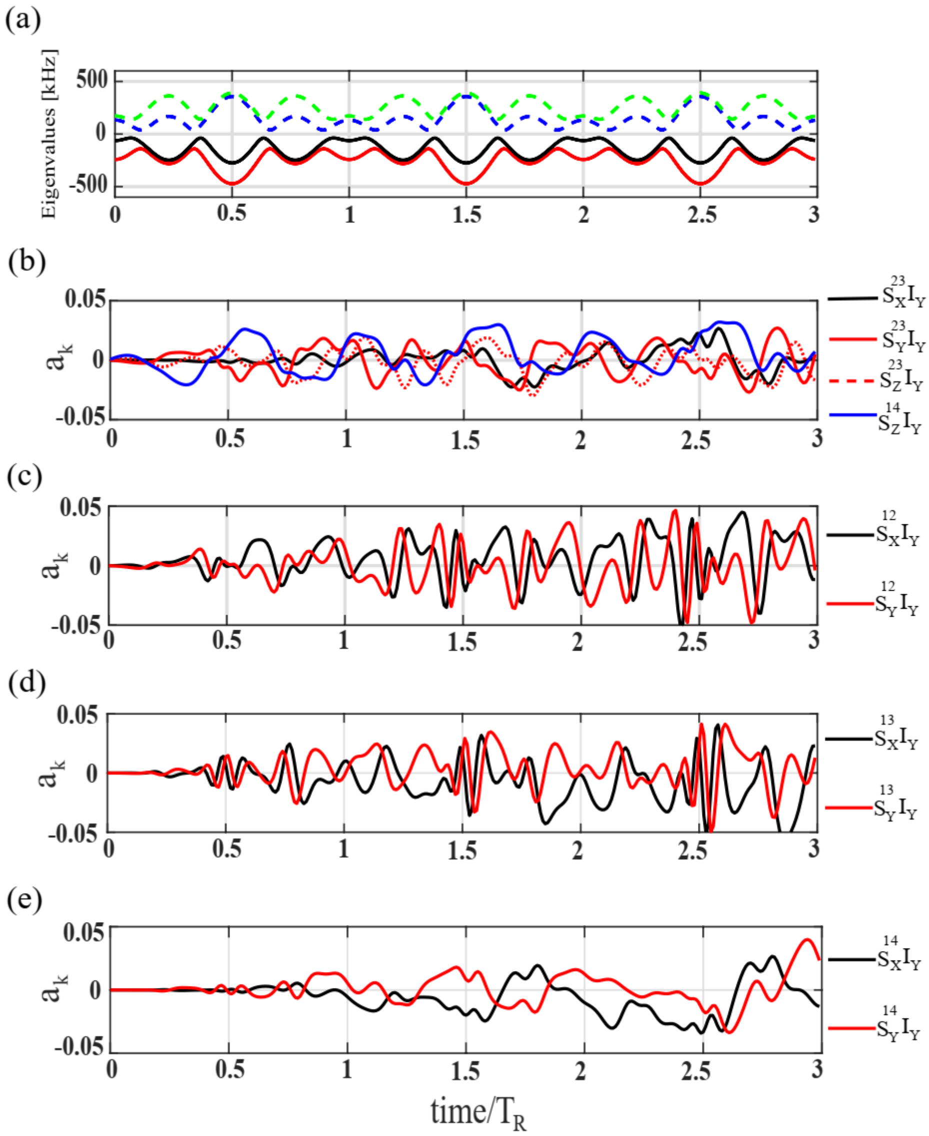

Figure A3.5 Creation of heteronuclear coherences at beginning $(0-3T_R)$ *of TRAPDOR irradiation. (a) Eigenvalues of the S-spin part of the Hamiltonian in Eq. [3.1] over the same time period. (b-d) Time evolution of the amplitudes of various coherences. The parameters employed for simulation are:* $C_Q = 2\ MHz$, $\Delta\nu_S = 10\ kHz$, $\nu_D = 1\ kHz$, $\nu_{1S} = 100\ kHz$, $\nu_R = 60\ kHz$, $\beta = 80°$, $\gamma = 0°$.

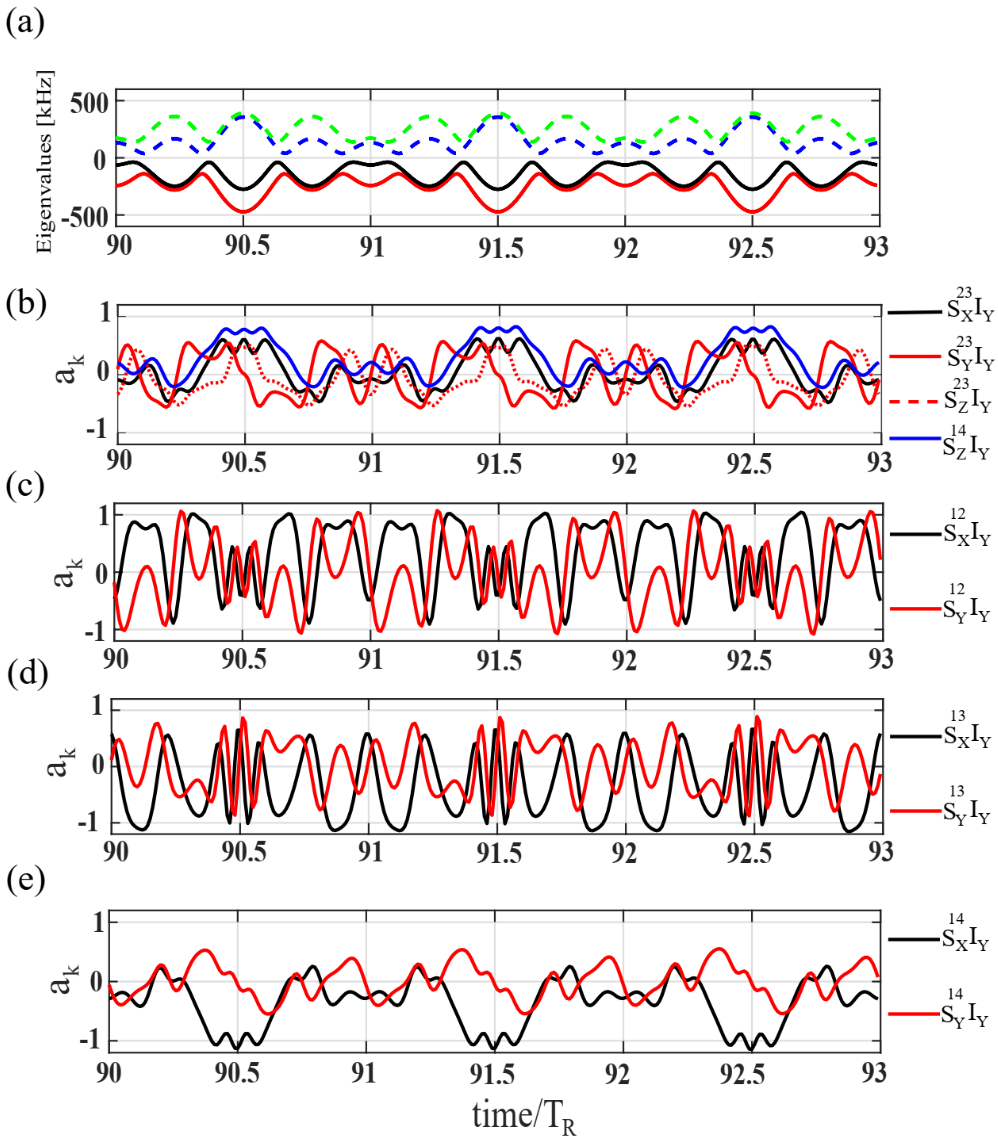

Figure A3.6 Heteronuclear coherences towards the end ($90 - 93T_R$) *of TRAPDOR irradiation. (a) Eigenvalues of the S-spin part of the Hamiltonian in Eq. [3.1] over the same time period. (b-d) Evolution of amplitudes of various coherences. The parameters employed for simulation are:* $C_Q = 2\ MHz$, $\Delta\nu_S = 10\ kHz$, $\nu_D = 1\ kHz$, $\nu_{1S} = 100\ kHz$, $\nu_R = 60\ kHz$, $\beta = 80°$, $\gamma = 0°$.

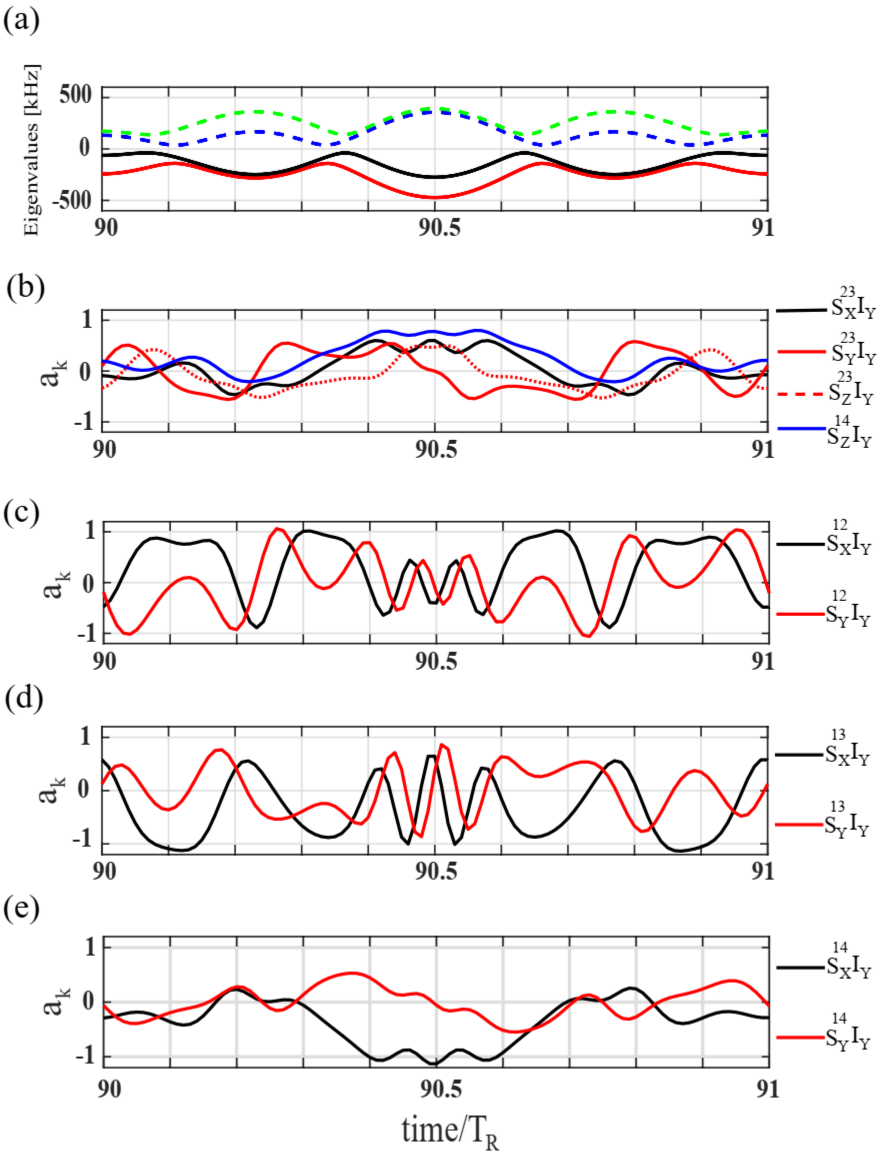

Figure A3.7 Expansion of Figure A3.6 showing evolution over one rotor period.

A3.8: Conditions for neglecting the satellite-transition RF terms

Spin evolution performed with $\mathcal{H} = \Delta\omega_S S_Z + \omega_{1S} S_X + \varpi_Q[3S_Z^2 - S(S+1)]$ versus $\mathcal{H} = \mathcal{H}^{23} + \mathcal{H}^{14}$ where $\mathcal{H}^{23} = \Delta\omega_S S_Z^{23} + \mathbf{2}\omega_{1S} S_X^{23} - 3\varpi_Q \mathbf{1}_S^{23}$ and $\mathcal{H}^{14} = 3\Delta\omega_S S_Z^{14} + 3\varpi_Q \mathbf{1}_S^{14}$ (Eq. [3.24] and Eq. [3.25,3.26]). Figures A3.8- A3.10 correspond to three different values of $\bar{\nu}_Q$ ($\bar{\nu}_Q = \varpi_Q/2\pi$), $\bar{\nu}_Q = 50, 100, 150$ kHz. The 50, 100, and 150 kHz values were chosen based on inspection of Figure 3.6a. Initial condition is $\rho(0) = S_X^{12}$.

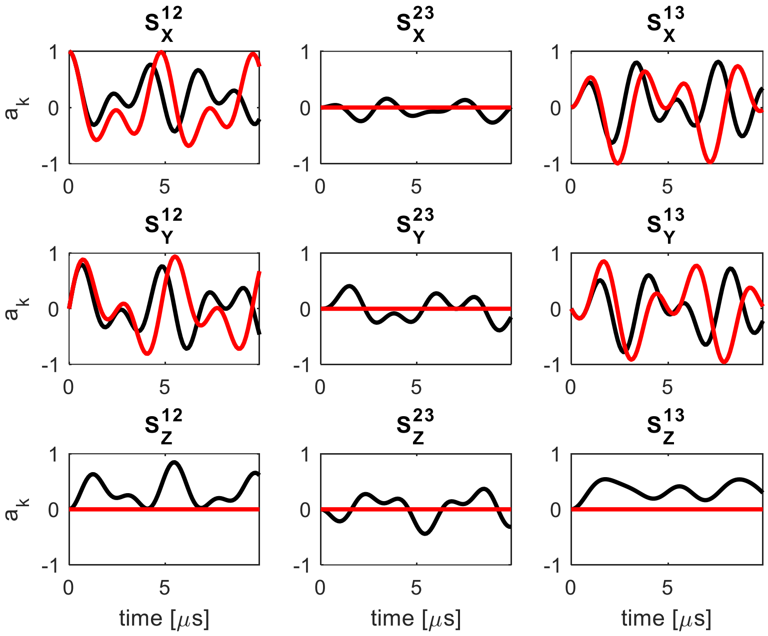

Figure A3.8 Simulations based on Eq. [3.24] (black) and Eq. [3.25,3.26] (red). The parameters are $\bar{\nu}_Q = 50\ kHz, \nu_{1S} = 100\ kHz, \Delta\nu_S = 10\ kHz$. *Initial condition is* $\rho(0) = S_X^{12}$.

It is clear that with $\bar{\nu}_Q = 50$ kHz and $\nu_{1S} = 100$ kHz neglection of satellite-transition RF terms is a poor approximation. Still, even without neglecting the satellite-transition RF terms, approximate $S_X^{12} \leftrightarrow S_Y^{12}$ quadrature and single- to double-quantum coherence interconversions can be suspected.

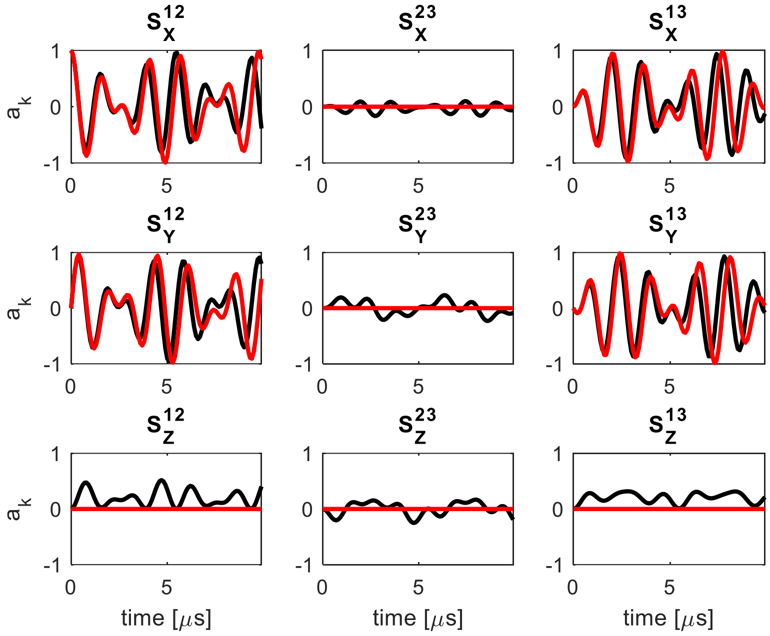

Figure A3.9 Simulations based on Eq. [3.24] (black) and Eq. [3.25,3.26] (red). The parameters are $\bar{\nu}_Q = 100\ kHz, \nu_{1S} = 100\ kHz, \Delta\nu_S = 10\ kHz$. *Initial condition is* $\rho(0) = S_X^{12}$.

With $\bar{\nu}_Q = 100$ kHz and $\nu_{1S} = 100$ kHz neglection of satellite-transition RF terms is reasonable, except for some of the coherences which vanish within the approximation. From Figure A3.9 interconversion between single-quantum (S_X^{12}, S_Y^{12}) and double-quantum (S_X^{13}, S_Y^{13}) satellite-transition coherences is fairly visible around $2.5, 5, 7.5\ \mu s$. Quadrature between $S_X^{12}$and S_Y^{12} is observed. Although less evident from Figure S9, quadrature between $S_X^{13}$and S_Y^{13} also holds.

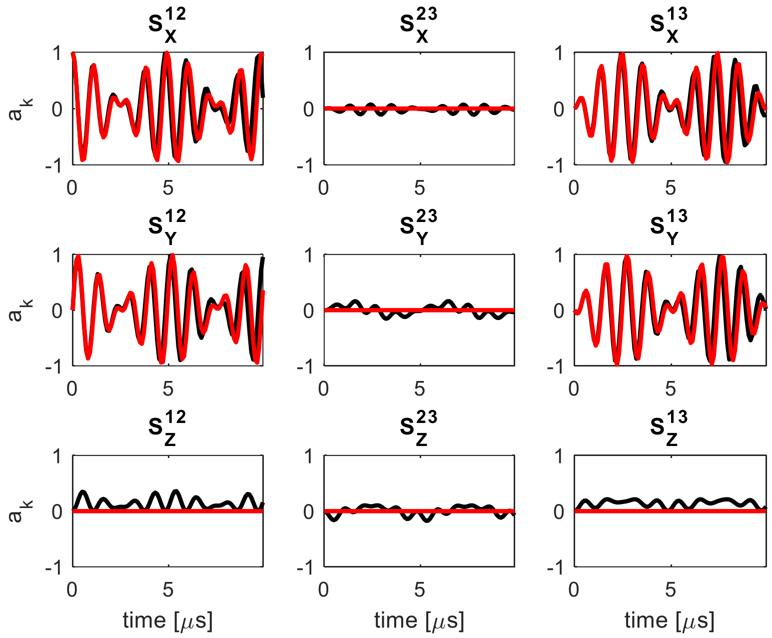

Figure A3.10 Simulations based on Eq. [3.24] (black) and Eq. [3.25,3.26] (red). The parameters are $\bar{\nu}_Q = 150\ kHz, \nu_{1S} = 100\ kHz, \Delta\nu_S = 10\ kHz$*. Initial condition is* $\rho(0) = S_X^{12}$.

With $\bar{\nu}_Q = 150$ kHz and $\nu_{1S} = 100$ kHz neglection of satellite-transition RF terms is reasonable for all coherences. From Figure A3.10 interconversion between single-quantum (S_X^{12}, S_Y^{12}) and double-quantum (S_X^{13}, S_Y^{13}) satellite-transition coherences is clearly visible around $2.5, 5, 7.5\ \mu s$. Quadrature between $S_X^{12}$and S_Y^{12} is observed. Although less evident from Figure A3.10, quadrature between $S_X^{13}$and S_Y^{13} also holds.

In the figure below spin dynamics starting from the central-transition initial condition, $\rho(0) = S_X^{23}$, is shown for $\bar{\nu}_Q = 150$ kHz.

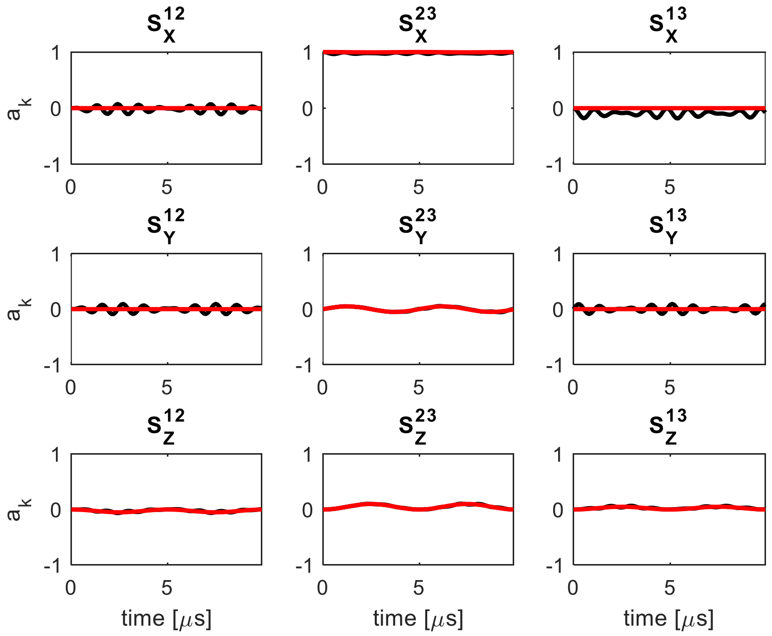

Figure A3.11 Simulations based on Eq. [3.24] (black) and Eq. [3.25,3.26] (red). The parameters are $\bar{\nu}_Q = 150\ kHz, \nu_{1S} = 100\ kHz, \Delta\nu_S = 10\ kHz$*. Initial condition is* $\rho(0) = S_X^{23}$.

In the figure below spin dynamics starting from the central-transition initial condition, $\rho(0) = S_Y^{23}$, is shown for $\bar{\nu}_Q = 150$ kHz.

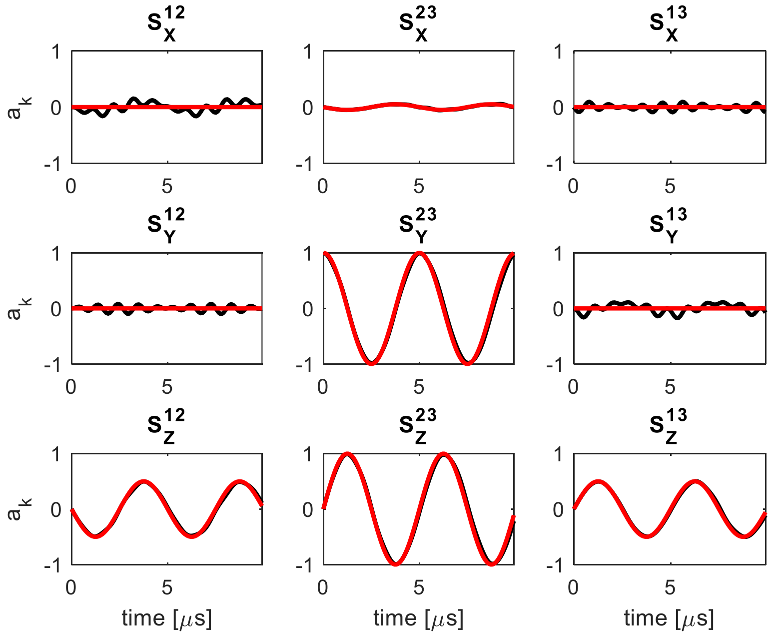

Figure A3.12 Simulations based on Eq. [3.24] (black) and Eq. [3.25,3.26] (red). The parameters are $\bar{\nu}_Q = 150\ kHz, \nu_{1S} = 100\ kHz, \Delta\nu_S = 10\ kHz$*. Initial condition is* $\rho(0) = S_Y^{23}$.

A3.9: Evolution of coherences in time intervals between consecutive crossings

Consider the evolution in time intervals between crossings. For the small dipolar coupling considered here we neglect, for the time being, the effect of the dipolar coupling. Also, for simplicity, we neglect $\mathcal{H}_Q^{(2)}$ (which is similar to an offset) and, dropping dependence on orientation in the notation, the Hamiltonian is:

$$\mathcal{H}(t) = \Delta\omega_S S_Z + \omega_{1S} S_X + \omega_Q(t)[3S_Z^2 - S(S+1)]. \qquad \text{[A3.11]}$$

Between crossings, eigenvectors of $\mathcal{H}(t)$ don't change significantly and this allows us to describe the time evolution via the time-independent Hamiltonian:

$$\mathcal{H} = \Delta\omega_S S_Z + \omega_{1S} S_X + \bar{\omega}_Q[3S_Z^2 - S(S+1)], \qquad \text{[A3.12]}$$

where $\bar{\omega}_Q = \frac{\int_{t_k}^{t_{k+1}} \omega_Q(t)dt}{t_{k+1} - t_k}$,and t_k and t_{k+1} are times of two consecutive crossings. For $\Delta\omega_S < \omega_{1S} < \bar{\omega}_Q$ (read the sign $<$ as 'considerably smaller/larger than') it is allowed to neglect the satellite-transition RF terms, S_X^{12} and S_X^{34}. The Hamiltonian is then approximately the sum of two commuting terms

$$\mathcal{H} \cong \mathcal{H}^{23} + \mathcal{H}^{14}, \qquad \text{[A3.13]}$$

where

$$\mathcal{H}^{23} = \Delta\omega_S S_Z^{23} + 2\omega_{1S} S_X^{23} - 3\bar{\omega}_Q \mathbf{1}_S^{23},\ \mathcal{H}^{14} = 3\Delta\omega_S S_Z^{14} + 3\bar{\omega}_Q \mathbf{1}_S^{14}. \qquad \text{[A3.14]}$$

Using

$$\omega_{eff} = \sqrt{\Delta\omega_S^2 + 4\omega_{1S}^2};\ cos\phi = \Delta\omega_S/\omega_{eff} \text{ and } sin\phi = 2\omega_{1S}/\omega_{eff}, \qquad \text{[A3.15]}$$

$\mathcal{H}^{23}$ can be written as

$$\mathcal{H}^{23} = \omega_{eff}[cos\phi S_Z^{23} + sin\phi S_X^{23}] - 3\bar{\omega}_Q \mathbf{1}_S^{23}.$$

Using the rotation operator for a spin-1/2 system[158]

$$\exp(i\phi \boldsymbol{n} \cdot \boldsymbol{I}) = \cos\frac{\phi}{2} + 2i\, \boldsymbol{n} \cdot \boldsymbol{I} \sin\frac{\phi}{2},$$

where the angle of rotation is ϕ around the axis given by unit vector $\boldsymbol{n}$**,** the propagator for the 2-3 subspace becomes

$$U^{23}(t,0) = \left\{cos\frac{\omega_{eff}t}{2}\mathbf{1}_S^{23} - 2i\,sin\frac{\omega_{eff}t}{2}[S_z^{23}\,cos\,\phi + S_x^{23}\,sin\,\phi]\right\}e^{i3\bar{\omega}_Q t}. \qquad [A3.16]$$

Action of this propagator on state $|2\rangle$ gives

$$U^{23}|2\rangle = \left\{cos\frac{\omega_{eff}t}{2}|2\rangle - i\,sin\frac{\omega_{eff}t}{2}cos\,\phi\,|2\rangle - i\,sin\frac{\omega_{eff}t}{2}sin\,\phi\,|3\rangle\right\}e^{i3\bar{\omega}_Q t}. \qquad [A3.17]$$

Similar expressions can be obtained for $U^{23}|3\rangle$, $\langle 2|U^{23^\dagger}$, $\langle 3|U^{23^\dagger}$ such that time-evolution of coherences involving states 2 and/or 3 can be evaluated. Since $\mathcal{H}^{14}$ is diagonal, we have

$$U^{14}(t,0) = e^{-i\left(3\bar{\omega}_Q+\frac{3}{2}\Delta\omega_S\right)t}|1\rangle\langle 1| + e^{-i(3\bar{\omega}_Q-\frac{3}{2}\Delta\omega_S)t}|4\rangle\langle 4|. \qquad [A3.18]$$

We consider the evolution of coherences in time intervals between consecutive level crossings where, after the first crossing, heteronuclear coherences are already present. For a starting coherence

$$\rho(0) = S_X^{23}I_Y = \frac{|2\rangle\langle 3|+|3\rangle\langle 2|}{2}I_Y \qquad [A3.19]$$

the state of the system at time t is

$$\rho(t) = U^{23}(t,0)\rho(0)U^{23^\dagger}(t,0). \qquad [A3.20]$$

Using Eq. [A3.16, A3.19, A3.20] we obtain

$$S_X^{23}I_Y \rightarrow \left[cos^2\left(\omega_{eff}t/2\right) - sin^2\left(\omega_{eff}t/2\right)cos2\phi\right]S_X^{23}I_Y + \left[sin\left(\omega_{eff}t\right)cos\phi\right]S_Y^{23}I_Y + \left[sin^2\left(\omega_{eff}t/2\right)sin2\phi\right]S_Z^{23}I_Y. \qquad [A3.21a]$$

Similarly for initial $S_Y^{23}I_Y$ and $S_Z^{23}I_Y$ coherences we obtain

$$S_Y^{23}I_Y \rightarrow \left[cos\left(\omega_{eff}t\right)\right]S_Y^{23}I_Y - \left[sin\left(\omega_{eff}t\right)cos\phi\right]S_X^{23}I_Y + \left[sin\left(\omega_{eff}t\right)sin\phi\right]S_Z^{23}I_Y, \qquad [A3.21b]$$

$$S_Z^{23}I_Y \rightarrow \left[\cos^2\left(\omega_{eff}t/2\right) + \sin^2\left(\omega_{eff}t/2\right)cos2\phi\right]S_Z^{23}I_Y + \left[\sin^2\left(\omega_{eff}t/2\right)sin2\phi\right]S_X^{23}I_Y - \left[\sin\left(\omega_{eff}t\right)sin\phi\right]S_Y^{23}I_Y. \qquad [A3.21c]$$

On the other hand, for initial heteronuclear coherences containing satellite transition terms, the time evolution has to be calculated by using both $U^{23}(t,0)$ and $U^{14}(t,0)$. For example, with

$$\rho(0) = S_X^{12} I_Y = \frac{|1\rangle\langle 2| + |2\rangle\langle 1|}{2} I_Y, \qquad \text{[A3.22]}$$

the state of the system at time t is

$$\rho(t) = U(t,0)\rho(0)U^{\dagger}(t,0) = \frac{1}{2} I_Y \Big(U^{14}|1\,\rangle\langle 2|U^{23^{\dagger}} + U^{23}|2\,\rangle\langle 1|U^{14^{\dagger}} \Big). \qquad \text{[A3.23]}$$

Using Eq. [A3.16, A3.18] yields

$$S_X^{12} I_Y \to \left[\cos\left(6\bar{\omega}_Q t + \frac{3}{2}\Delta_S t\right)\cos\left(\frac{\omega_{eff}t}{2}\right) + \sin\left(6\bar{\omega}_Q t + \frac{3}{2}\Delta_S t\right)\sin\left(\frac{\omega_{eff}t}{2}\right)\cos\phi\right] S_X^{12} I_Y$$

$$- \left[\cos\left(6\bar{\omega}_Q t + \frac{3}{2}\Delta_S t\right)\sin\left(\frac{\omega_{eff}t}{2}\right)\cos\phi - \sin\left(6\bar{\omega}_Q t + \frac{3}{2}\Delta_S t\right)\cos\left(\frac{\omega_{eff}t}{2}\right)\right] S_Y^{12} I_Y$$

$$+ \left[\sin\left(6\bar{\omega}_Q t + \frac{3}{2}\Delta_S t\right)\sin\left(\frac{\omega_{eff}t}{2}\right)\sin\phi\right] S_X^{13} I_Y$$

$$- \left[\cos\left(6\bar{\omega}_Q t + \tfrac{3}{2}\Delta_S t\right)\sin\left(\tfrac{\omega_{eff}t}{2}\right)\sin\phi\right] S_Y^{13} I_Y. \qquad \text{[A3.24a]}$$

Proceeding in the same way we obtain that, starting from $S_Y^{12} I_Y$,

$$S_Y^{12} I_Y \to \left[\cos\left(6\bar{\omega}_Q t + \frac{3}{2}\Delta_S t\right)\cos\left(\frac{\omega_{eff}t}{2}\right) + \sin\left(6\bar{\omega}_Q t + \frac{3}{2}\Delta_S t\right)\sin\left(\frac{\omega_{eff}t}{2}\right)\cos\phi\right] S_Y^{12} I_Y$$

$$+ \left[\cos\left(6\bar{\omega}_Q t + \frac{3}{2}\Delta_S t\right)\sin\left(\frac{\omega_{eff}t}{2}\right)\sin\phi\right] S_X^{13} I_Y$$

$$+ \left[\cos\left(6\bar{\omega}_Q t + \frac{3}{2}\Delta_S t\right)\sin\left(\frac{\omega_{eff}t}{2}\right)\cos\phi - \sin\left(6\bar{\omega}_Q t + \frac{3}{2}\Delta_S t\right)\cos\left(\frac{\omega_{eff}t}{2}\right)\right] S_X^{12} I_Y$$

$$+ \left[\sin\left(6\bar{\omega}_Q t + \tfrac{3}{2}\Delta_S t\right)\sin\left(\tfrac{\omega_{eff}t}{2}\right)\sin\phi\right] S_Y^{13} I_Y. \qquad \text{[A3.24b]}$$

For initial heteronuclear coherences involving *S*-spin double-quantum terms we obtain

$$S_X^{13} I_Y \to \left[\cos\left(6\bar{\omega}_Q t + \frac{3}{2}\Delta_S t\right)\cos\left(\frac{\omega_{eff}t}{2}\right) - \sin\left(6\bar{\omega}_Q t + \frac{3}{2}\Delta_S t\right)\sin\left(\frac{\omega_{eff}t}{2}\right)\cos\phi\right] S_X^{13} I_Y$$

$$+ \left[\sin\left(6\bar{\omega}_Q t + \frac{3}{2}\Delta_S t\right)\cos\left(\frac{\omega_{eff}t}{2}\right) + \cos\left(6\bar{\omega}_Q t + \frac{3}{2}\Delta_S t\right)\sin\left(\frac{\omega_{eff}t}{2}\right)\cos\phi\right] S_Y^{13} I_Y$$

$$+ \left[\sin\left(6\bar{\omega}_Q t + \frac{3}{2}\Delta_S t\right)\sin\left(\frac{\omega_{eff}t}{2}\right)\sin\phi\right] S_X^{12} I_Y$$

$$- \left[\cos\left(6\bar{\omega}_Q t + \tfrac{3}{2}\Delta_S t\right)\sin\left(\tfrac{\omega_{eff}t}{2}\right)\sin\phi\right] S_Y^{12} I_Y, \qquad \text{[A3.25a]}$$

$$S_Y^{13}I_Y \rightarrow \left[cos\left(6\varpi_Q t+\frac{3}{2}\Delta_S t\right)cos\left(\frac{\omega_{eff}t}{2}\right)-sin\left(6\varpi_Q t+\frac{3}{2}\Delta_S t\right)\sin\left(\frac{\omega_{eff}t}{2}\right)cos\phi\right]S_Y^{13}I_Y$$

$$+\left[cos\left(6\varpi_Q t+\frac{3}{2}\Delta_S t\right)sin\left(\frac{\omega_{eff}t}{2}\right)sin\phi\right]S_X^{12}I_Y$$

$$-\left[sin\left(6\varpi_Q t+\frac{3}{2}\Delta_S t\right)cos\left(\frac{\omega_{eff}t}{2}\right)+cos\left(6\varpi_Q t+\frac{3}{2}\Delta_S t\right)sin\left(\frac{\omega_{eff}t}{2}\right)cos\phi\right]S_X^{13}I_Y$$

$$+\left[sin\left(6\varpi_Q t+\frac{3}{2}\Delta_S t\right)sin\left(\frac{\omega_{eff}t}{2}\right)sin\phi\right]S_Y^{12}I_Y. \qquad \text{[A3.25b]}$$

Finally, for initial heteronuclear coherences involving S-spin triple-quantum terms we obtain

$$S_X^{14}I_Y \rightarrow cos(3\Delta_S t)S_X^{14}I_Y + sin(3\Delta_S t)S_Y^{14}I_Y, \qquad \text{[A3.26a]}$$

$$S_Y^{14}I_Y \rightarrow cos(3\Delta_S t)S_Y^{14}I_Y - sin(3\Delta_S t)S_X^{14}I_Y. \qquad \text{[A3.26b]}$$

𝔄3.10: Evolution of coherences in time intervals between consecutive crossings: effect of the dipolar interaction

Introducing the dipolar interaction averaged over the time from zero to the first level crossing, the Hamiltonian is:

$$\mathcal{H} = \Delta\omega_S S_Z + \omega_{1S}S_X + \varpi_Q[3S_Z^2 - S(S+1)] + \bar{d}2I_Z S_Z \qquad \text{[A3.27a]}$$

where $S_Z = 3S_Z^{14} + S_Z^{23}, S_X = 2S_X^{23} + \sqrt{3}(S_X^{12} + S_X^{34}),\ [3S_Z^2 - S(S+1)] = 3(\mathbf{1}_S^{14} - \mathbf{1}_S^{23}),$

$$\varpi_Q = \frac{\int_{t_k}^{t_{k+1}}\omega_Q(t)dt}{t_{k+1}-t_k}, \bar{d} = \frac{\int_{t_k}^{t_{k+1}}d(t)dt}{t_{k+1}-t_k}, \qquad \text{[A3.27b]}$$

and t_k and t_{k+1} are times of two consecutive crossings. For $\Delta\omega_S < \omega_{1S} < \varpi_Q$ it is allowed to neglect the satellite-transition RF terms, S_X^{12} and S_X^{34}. The Hamiltonian is then approximately the sum of two commuting terms:

$$\mathcal{H} \cong \mathcal{H}^{23} + \mathcal{H}^{14}. \qquad \text{[A3.28a]}$$

First consider the Hamiltonian in the 2-3 subspace

$$\mathcal{H}^{23} = \Delta\omega_S S_Z^{23} + 2\omega_{1S}S_X^{23} - 3\varpi_Q \mathbf{1}_S^{23} + \bar{d}2I_Z S_Z^{23}. \qquad \text{[A3.28b]}$$

With an initial density operator $\rho(0) = I_X = (\mathbf{1}_S^{14} + \mathbf{1}_S^{23})I_X = \rho^{14}(0) + \rho^{23}(0)$, the state of the system in the 2-3 subspace before the first level crossing is

$$\rho^{23}(t) = U^{23}(t,0)\rho^{23}(0){U^{23}}^{\dagger}(t,0) = \exp(-i\mathcal{H}^{23}t)\, I_X \exp(+i\mathcal{H}^{23}t), \qquad \text{[A3.29a]}$$

or, since $\mathcal{H}^{23}$ is diagonal with respect to the Zeeman states of the I spin,

$$\rho^{23}(t) = \tfrac{1}{2}\exp\{-i\mathcal{H}_+t\}\exp\{+i\mathcal{H}_-t\}I_+ + \tfrac{1}{2}\exp\{-i\mathcal{H}_-t\}\exp\{+i\mathcal{H}_+t\}I_-, \qquad \text{[A3.29b]}$$

where $\mathcal{H}_+ = \Delta\omega_S S_Z^{23} + 2\omega_{1S}S_X^{23} + \bar{d}S_Z^{23}$ and $\mathcal{H}_- = \Delta\omega_S S_Z^{23} + 2\omega_{1S}S_X^{23} - \bar{d}S_Z^{23}$. [A3.29c]

Evaluation of the exponentials proceeds in the same way as with Eq. [A3.14, A3.16] and after some straightforward algebra the final result is

$$\begin{aligned}
\rho^{23}(t) = {} & \left[\cos\left(\tfrac{\omega_+t}{2}\right)\cos\left(\tfrac{\omega_-t}{2}\right) + \sin\left(\tfrac{\omega_+t}{2}\right)\sin\left(\tfrac{\omega_-t}{2}\right)\cos(\phi_+ - \phi_-)\right]\mathbf{1}_S^{23}I_X + \\
& \left[\cos\phi_+\sin\left(\tfrac{\omega_+t}{2}\right)\cos\left(\tfrac{\omega_-t}{2}\right) - \cos\phi_-\cos\left(\tfrac{\omega_+t}{2}\right)\sin\left(\tfrac{\omega_-t}{2}\right)\right]2S_Z^{23}I_Y + \\
& \left[\sin\phi_+\sin\left(\tfrac{\omega_+t}{2}\right)\cos\left(\tfrac{\omega_-t}{2}\right) - \sin\phi_-\cos\left(\tfrac{\omega_+t}{2}\right)\sin\left(\tfrac{\omega_-t}{2}\right)\right]2S_X^{23}I_Y + \\
& \left[\sin\left(\tfrac{\omega_+t}{2}\right)\sin\left(\tfrac{\omega_-t}{2}\right)\sin(\phi_+ - \phi_-)\right]2S_Y^{23}I_Y, \qquad \text{[A3.30a]}
\end{aligned}$$

where

$$\omega_\pm = \sqrt{\left(\Delta\omega_S \pm \bar{d}\right)^2 + 4\omega_{1S}^2}, \cos\phi_\pm = \left(\Delta\omega_S \pm \bar{d}\right)/\omega_\pm, \sin\phi_\pm = 2\omega_{1S}/\omega_\pm. \qquad \text{[A3.30b]}$$

Turning our attention to the 1-4 subspace the corresponding propagator is

$$U^{14}(t,0) = e^{-i\left(3\bar{\varpi}_Q + \frac{3}{2}\Delta\omega_S + \frac{3}{2}\bar{d}2I_Z\right)t}|1\rangle\langle 1| + e^{-i\left(3\bar{\varpi}_Q - \frac{3}{2}\Delta\omega_S - \frac{3}{2}\bar{d}2I_Z\right)t}|4\rangle\langle 4|. \qquad \text{[A3.31]}$$

With an initial density operator $\rho^{14}(0) = \mathbf{1}_S^{14}I_X = \frac{|\alpha\rangle\langle\beta| + |\beta\rangle\langle\alpha|}{2}$ we have after simple algebra

$$\rho^{14}(t) = U^{14}(t,0)\mathbf{1}_S^{14}I_X{U^{14}}^{\dagger}(t,0) = cos\left(3\bar{d}t\right)\mathbf{1}_S^{14}\,I_X + \sin\left(3\bar{d}t\right)2S_Z^{14}I_Y \qquad \text{[A3.32]}$$

Adding the results for the 1-4 and 2-3 subspaces we finally obtain

$$\rho(t) = \cos 3\bar{d}t\, \mathbf{1}_S^{14} I_X + \sin 3\bar{d}t\, 2S_Z^{14} I_Y + \left[\cos\left(\frac{\omega_+ t}{2}\right)\cos\left(\frac{\omega_- t}{2}\right) + \sin\left(\frac{\omega_+ t}{2}\right)\sin\left(\frac{\omega_- t}{2}\right)\cos(\phi_+ - \phi_-)\right] \mathbf{1}_S^{23} I_X + \left[\cos\phi_+ \sin\left(\frac{\omega_+ t}{2}\right)\cos\left(\frac{\omega_- t}{2}\right) - \cos\phi_- \cos\left(\frac{\omega_+ t}{2}\right)\sin\left(\frac{\omega_- t}{2}\right)\right] 2S_Z^{23} I_Y + \left[\sin\phi_+ \sin\left(\frac{\omega_+ t}{2}\right)\cos\left(\frac{\omega_- t}{2}\right) - \sin\phi_- \cos\left(\frac{\omega_+ t}{2}\right)\sin\left(\frac{\omega_- t}{2}\right)\right] 2S_X^{23} I_Y + \left[\sin\left(\frac{\omega_+ t}{2}\right)\sin\left(\frac{\omega_- t}{2}\right)\sin(\phi_+ - \phi_-)\right] 2S_Y^{23} I_Y \qquad \text{[A3.33]}$$

𝔄3.11: Absence of coherence $S_X^{23} I_Y$ at zero offset

The time-dependent Hamiltonian of Eq. [3.1], with offset and second order quadrupolar interaction set to zero is invariant under rotation with $R = \exp[-i\pi(I_X + S_X)]$:

$$R\mathcal{H}(t)R^\dagger = \mathcal{H}(t).$$

As this holds at any time also the propagator is invariant

$$RU(t,0)R^\dagger = U(t,0). \qquad \text{[A3.34]}$$

We now suppose that there exists a nonzero $S_X^{23} I_Y$ term in the density operator at time *t*,

$$\rho(t) = U(t,0) I_X U(t,0)^\dagger = a S_X^{23} I_Y + r, \qquad \text{[A3.35]}$$

where r represents all other terms in $\rho(t)$. Taking into account Eq. [A3.34] and applying the rotation to left and right members of Eq. [A3.35] we obtain

$$RU(t,0) I_X U(t,0)^\dagger R^\dagger = U(t,0) I_X U(t,0)^\dagger = -a S_X^{23} I_Y + RrR^\dagger. \qquad \text{[A3.36]}$$

As $RrR^\dagger$ cannot contain any $S_X^{23} I_Y$ contribution, by comparing Eq. [A3.35] and Eq. [A3.36] it follows that $a = -a$, hence $a = 0$.

This line of proof cannot be used in case the offset and/or second order quadrupolar interaction is taken into account since then $R\mathcal{H}(t)R^\dagger \neq \mathcal{H}(t)$. Therefore, presence of $S_X^{23} I_Y$ cannot be ruled out.

A3.12: Evolution of coherences and impact of *S*-spin Offset

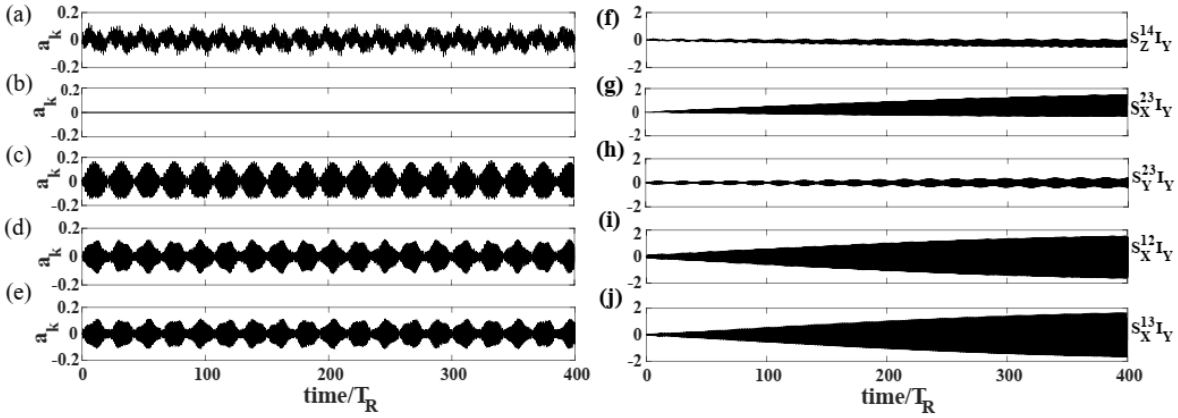

Figure A3.13 Amplitudes of several heteronuclear coherences during a period $400T_R$ *of TRAPDOR irradiation with (a-e)* $\Delta\nu_S = 0\ kHz$ *and (f-j)* $\Delta\nu_S = 1\ kHz$*. Other parameters employed are:* $C_Q = 2\ MHz,\ \nu_D = 1\ kHz, \nu_{1S} = 95\ kHz, \nu_R = 60\ kHz,\ \beta = 55°,$ *and* $\gamma = 0°$. *Second order quadrupolar interaction was set to zero. Figure A3.13 is the same as Figure 3.10.*

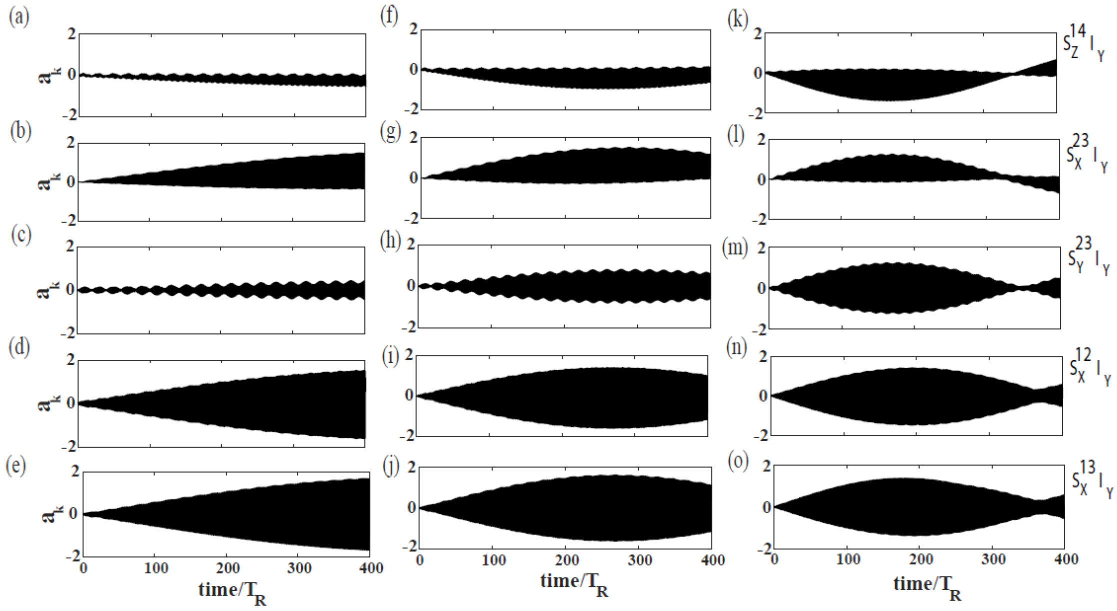

Figure A3.14 Offset dependence. Amplitudes of several heteronuclear coherences during a period $400T_R$ *of TRAPDOR irradiation and (a-e)* $\Delta\nu_S = 1\ kHz$*, (f-j)* $\Delta\nu_S = 2\ kHz$*, and (k-o)* $\Delta\nu_S = 4\ kHz$*. Other parameters employed for simulation are:* $C_Q = 2\ MHz,\ \nu_D = 1\ kHz,\ \nu_{1S} = 95\ kHz,\ \nu_R = 60\ kHz,\ \beta = 55°,$ *and* $\gamma = 0°$. *Second order quadrupolar interaction was set to zero.*

Bibliography

[1] F. Bloch, W. W. Hansen, M. Packard, Nuclear Induction, Phys. Rev. 69 (1946) 127-127. https://doi.org/10.1103/PhysRev.69.127

[2] E. M. Purcell, H. C. Torrey, R. V. Pound, Resonance absorption by nuclear magnetic moments in a solid, Phys. Rev. 69 (1946) 37-38. https://doi.org/10.1103/PhysRev.69.37

[3] A. A. Yee, A. Savchenko, A. Ignachenko, J. Lukin, X. Xu, T. Skarina, E. Evdokimova, C. S. Liu, A. Semesi, V. Guido, A. M. Edwards, C. H. Arrowsmith, NMR and X-ray crystallography, complementary tools in structural proteomics of small proteins, J. Am. Chem. Soc. 127 (2005) 16512-16517 . https://doi.org/10.1021/ja053565+

[4] E. R. Andrew, A. Bradbury, R. G. Eades, Nuclear magnetic resonance spectra from a crystal rotated at high speed, Nature 182 (1958) 1659. https://doi.org/10.1038/1821659a0

[5] E. R. Andrew, A. Bradbury, R. G. Eades, Removal of dipolar broadening of nuclear magnetic resonance spectra of solids by specimen rotation, Nature 183 (1959) 1802-1803. https://doi.org/10.1038/1831802a0

[6] I. J. Lowe, Free induction decays of rotating solids, Phys. Rev. Lett. 2 (1959) 285-287. https://doi.org/10.1103/PhysRevLett.2.285

[7] M. M. Maricq, J. S. Waugh, NMR in rotating solids, J. Chem. Phys. 70 (1979) 3300-3316. https://doi.org/10.1063/1.437915

[8] A. J. Rossini, M. P. Hanrahan, M. Thuo, Rapid acquisition of wideline MAS solid-state NMR spectra with fast MAS, proton detection, and dipolar HMQC pulse sequences, Phys. Chem. Chem. Phys. 18 (2016) 25284-25295. https://doi.org/10.1039/c6cp04279a

[9] J. P. Demers, V. Chevelkov, A. Lange, Progress in correlation spectroscopy at ultra-fast magic-angle spinning: Basic building blocks and complex experiments for the study of protein structure and dynamics, Solid State Nucl. Magn. Reson. 40 (2011) 101-113. https://doi.org/10.1016/j.ssnmr.2011.07.002

[10] J. W. Hennel, J. Klinowski, Magic-Angle Spinning: a Historical Perspective, Top. Curr. Chem. 2 (2005) 1-14. https://doi.org/10.1007/b98646

[11] K. T. Mueller, B. Q. Sun, G. C. Chingas, J. W. Zwanziger, T. Terao, A. Pines, Dynamic-angle spinning of quadrupolar nuclei, J. Magn. Reson. 213 (2011) 298-315. https://doi.org/10.1016/j.jmr.2011.08.034

[12] A. Medek, J. S. Harwood, L. Frydman, Multiple-Quantum Magic-Angle Spinning NMR: A New Method for the Study of Quadrupolar Nuclei in Solids, J. Am. Chem. Soc. 117 (1995) 12779-12787. https://doi.org/10.1021/ja00156a015

[13] Z. Gan, Isotropic NMR spectra of half-integer quadrupolar nuclei using satellite transitions and magic-angle spinning, J. Am. Chem. Soc. 122 (2000) 3242-3243. https://doi.org/10.1021/ja9939791

[14] S. R. Hartmann, E. L. Hahn, Nuclear double resonance in the rotating frame, Phys. Rev.128 (1962) 2042-2053. https://doi.org/10.1103/PhysRev.128.2042

[15] A. Pines, M. G. Gibby, J. S. Waugh, Proton-enhanced NMR of dilute spins in solids, J. Chem. Phys. 59 (1973) 569-590. https://doi.org/10.1063/1.1680061

[16] G. Wu, D. Rovnyak, R. G. Griffin, Quantitative multiple-quantum magic-angle-spinning NMR spectroscopy of quadrupolar nuclei in solids, J. Am. Chem. Soc. 118 (1996) 9326-9332. https://doi.org/10.1021/ja9614676

[17] D. Carnevale, X. Ji, G. Bodenhausen, Double cross polarization for the indirect detection of nitrogen-14 nuclei in magic angle spinning NMR spectroscopy, J. Chem. Phys. 147 (2017) 184201. https://doi.org/10.1063/1.5000689

[18] D. Carnevale, B. Grosjean, G. Bodenhausen, Dipolar couplings in solid polypeptides probed by 14N NMR spectroscopy, Chem. Commun.1 (2018) 1-27. https://doi.org/10.1038/s42004-018-0072-5

[19] D. Carnevale, M. Hollenstein, G. Bodenhausen, Self-Assembly of DNA and RNA Building Blocks Explored by Nitrogen-14 NMR Crystallography: Structure and Dynamics, Chem. Phys. Chem. 21 (2020) 1044-1051. https://doi.org/10.1002/cphc.201901214

[20] I. Hung, Z. Gan, High-Resolution NMR of S = 3/2 Quadrupole Nuclei by Detection of Double-Quantum Satellite Transitions via Protons, J. Phys. Chem. Lett. 11 (2020) 4734-4740. https://doi.org/10.1021/acs.jpclett.0c01236

[21] R. Bayzou, J. Trébosc, I. Hung, Z. Gan, O. Lafon, J. P. Amoureux, Indirect NMR detection via proton of nuclei subject to large anisotropic interactions, such as 14N, 195Pt, and 35Cl, using the T-HMQC sequence, J. Chem. Phys. 156 (2022) 064202. https://doi.org/10.1063/5.0082700

[22] N. J. Higham, Functions of Matrices Functions of Matrices Theory and Computation, SIAM Digital Library, 2008.

[23] B. H. Meier, Cross polarization under fast magic angle spinning: thermodynamical considerations, Chem. Phys. Lett. 188 (1992) 201-207. https://doi.org/10.1016/0009-2614(92)90009-C

[24] X. Wu, K. W. Zilm, Cross polarization with high-speed magic-angle spinning, J. Magn. Reson. A. 104 (1993) 154-165. https://doi.org/10.1006/jmra.1993.1203

[25] A. Abragam, The Principles of Nuclear Magnetism, Clarendon Press, Oxford, England, 1961.

[26] M. Mehring, Principles of High Resolution NMR in Solids, 2nd ed., Springer Berlin, Heidelberg, 1983. https://doi.org/10.1007/978-3-642-68756-3

[27] K. Schmidt-Rohr, H. W. Spiess, Multidimensional Solid-State NMR and Polymers, Academic Press, 1994. https://doi.org/https://doi.org/10.1016/C2009-0-21335-3

[28] M. J. Duer, Solid-state NMR spectroscopy: Principles and applications, Wiley-Blackwell Science Ltd, 2001. https://doi.org/10.1002/9780470999394

[29] J. Cavanagh, W. J. Fairbrother, A. G. Palmer, M. Rance, N. J. Skelton, Protein NMR Spectroscopy: Principles and Practice, 2nd ed., Academic Press, 2006. https://doi.org/10.1524/zpch.1997.202.part_1_2.297

[30] M. H. Levitt, Spin Dynamics: Basics of Nuclear Magnetic Resonance., 2nd ed., Wiley 2008.

[31] J. Keeler, Understanding NMR spectroscopy, 2nd ed., Wiley, 2010.

[32] D. Apperley, R. Harris, P. Hodgkinson, Solid-State NMR: Basic Principles & Practice, Momentum Press, 2012. https://doi.org/10.5643/9781606503522

[33] R. K. Harris, E. D. Becker, S. M. Cabral De Menezes, R. Goodfellow, P. Granger, NMR nomenclature: Nuclear spin properties and conventions for chemical shifts (IUPAC recommendations 2001), Concepts Magn. Reson. Part A Bridg. Educ. Res. 14 (2002) 1795-1818. https://doi.org/10.1002/cmr.10035

[34] R. R. Ernst, W. A. Anderson, Application of Fourier transform spectroscopy to magnetic resonance, Rev. Sci. Instrum. 37 (1966) 93. https://doi.org/10.1063/1.1719961

[35] R. R. Ernst, G. Bodenhausen, A. Wokaun, A. G. Redfield, Principles of Nuclear Magnetic Resonance in One and Two Dimensions, Clarendon Press, 1989. https://doi.org/10.1063/1.2811094

[36] F. J. Dyson, The radiation theories of Tomonaga, Schwinger, and Feynman, Phys. Rev.75 (1949) 486. https://doi.org/10.1103/PhysRev.75.486

[37] E. Nimerovsky, K. T. Movellan, X. C. Zhang, M. C. Forster, E. Najbauer, K. Xue, R. Dervişoğlu, K. Giller, C. Griesinger, S. Becker, L.B. Andreas, Proton detected solid-state nmr of membrane proteins at 28 tesla (1.2 ghz) and 100 khz magic-angle spinning, Biomolecules. 11 (2021) 752. https://doi.org/10.3390/biom11050752

[38] M. Bak, J. T. Rasmussen, N. C. Nielsen, SIMPSON: A General Simulation Program for Solid-State NMR Spectroscopy, J. Magn. Reson. 147 (2000) 296-330. https://doi.org/10.1006/jmre.2000.2179

[39] M. Eden, Computer simulations in solid-state NMR. III. Powder averaging, Concepts in Magn. Reson. 18A (2003) 24-55. https://doi.org/10.1002/cmr.a.10065

[40] G. E. Pake, Nuclear resonance absorption in hydrated crystals: Fine structure of the proton line, J. Chem. Phys. 16 (1948) 327. https://doi.org/10.1063/1.1746878

[41] J. Herzfeld, A. E. Berger, Sideband intensities in NMR spectra of samples spinning at the magic angle, J. Chem. Phys. 73 (1980) 6021-6030. https://doi.org/10.1063/1.440136

[42] M. Schledorn, A.A. Malär, A. Torosyan, S. Penzel, D. Klose, A. Oss, M. Org, S. Wang, L. Lecoq, R. Cadalbert, A. Samoson, A. Böckmann, B.H. Meier, Protein NMR Spectroscopy at 150 kHz Magic-Angle Spinning Continues To Improve Resolution and Mass Sensitivity, ChemBioChem. 21 (2020) 2540–2548. https://doi.org/10.1002/cbic.202000341

[43] M. Lee, W. I. Goldburg, Nuclear-magnetic-resonance line narrowing by a rotating rf field, Phys. Rev. 140 (1965) A1261. https://doi.org/10.1103/PhysRev.140.A1261

[44] J. S. Waugh, L. M. Huber, U. Haeberlen, Approach to high-resolution NMR in solids, Phys. Rev. Lett. 20 (1968) 180. https://doi.org/10.1103/PhysRevLett.20.180

[45] W. K. Rhim, D. D. Elleman, L. B. Schreiber, R. W. Vaughan, Analysis of multiple pulse NMR in solids. II, J. Chem. Phys. 4595 (1974) 4595-4604. https://doi.org/10.1063/1.1680944

[46] D. P. Burum, W. K. Rhim, Analysis of multiple pulse NMR in solids. III, J. Chem. Phys. 71 (1979) 944. https://doi.org/10.1063/1.438385

[47] D. P. Burum, M. Linder, R. R. Ernst, Low-power multipulse line narrowing in solid-state NMR, J. Magn. Reson. 44 (1981) 173-188. https://doi.org/10.1016/0022-2364(81)90200-6

[48] B. Chen, Fundamentals of Recoupling and Decoupling Techniques in Solid State NMR, AIP Publishing, 2020. https://doi.org/10.1063/9780735422209

[49] W. Kolodziejski, J. Klinowski, Kinetics of cross-polarization in solid-state NMR: A guide for chemists, Chem. Rev. 102 (2002) 613-628. https://doi.org/10.1021/cr000060n

[50] D. Rovnyak, Tutorial on analytic theory for cross-polarization in solid state NMR, Concepts Magn. Reson. Part A Bridg. Educ. Res. (2008) 254-276. https://doi.org/10.1002/cmr.a.20115

[51] C. A. Espinosa, P. Thureau, R. A. Shapiro, I. M. Litvak, R. W. Martin, Modulation of cross polarization in motionally averaged solids by variable angle spinning NMR, Chem. Phys. Lett. 508 (2011) 314-319. https://doi.org/10.1016/j.cplett.2011.04.043

[52] S. Vega, Fictitious spin 1/2 operator formalism for multiple quantum NMR, J. Chem. Phys. 68 (1977) 5518-5527. https://doi.org/10.1063/1.435679

[53] G. Metz, X. Wu, S. O. Smith, Ramped-Amplitude Cross Polarization in Magic-Angle-Spinning NMR, J. Magn. Reson. A. 110 (1994) 219-227. https://doi.org/10.1006/jmra.1994.1208

[54] S. Hediger, B. H. Meier, N. D. Kurur, G. Bodenhausen, R. R. Ernst, NMR cross polarization by adiabatic passage through the Hartmann-Hahn condition (APHH), Chem. Phys. Lett. 223 (1994) 283-288. https://doi.org/10.1016/0009-2614(94)00470-6

[55] U. Haeberlen, J. S. Waugh, Coherent averaging effects in magnetic resonance, Phys. Rev.175 (1968) 453. https://doi.org/10.1103/PhysRev.175.453

[56] U. Haeberlen, High Resolution NMR in Solids: Selective Averaging, Supplement to Advances in Magnetic Resonance, Academic Press, 1976. https://doi.org/https://doi.org/10.1016/B978-0-12-025561-0.X5001-1

[57] M. M. Maricq, Application of average Hamiltonian theory to the NMR of solids, Phys. Rev. B. 25 (1982) 6622-6632. https://doi.org/10.1103/PhysRevB.25.6622

[58] G. Floquet, Sur les équations différentielles linéaires à coefficients périodiques, Annales Scientifiques de l'École Normale Supérieure. 12 (1883) 47-88. https://doi.org/10.24033/asens.220

[59] J. H. Shirley, Solution of the Schrödinger Equation with a Hamiltonian Periodic in Time, Phys. Rev.138 (1965) B979. https://doi.org/10.1103/PhysRev.138.B979

[60] M. Leskes, P. K. Madhu, S. Vega, Progress in Nuclear Magnetic Resonance Spectroscopy Floquet theory in solid-state nuclear magnetic resonance, Prog. Nucl. Magn. Reson. Spectrosc. 57 (2010) 345-380. https://doi.org/10.1016/j.pnmrs.2010.06.002

[61] I. Scholz, J. D. Van Beek, M. Ernst, Operator-based Floquet theory in solid-state NMR, Solid State Nucl. Magn. Reson. 37 (2010) 39-59. https://doi.org/10.1016/j.ssnmr.2010.04.003

[62] K. L. Ivanov, K. R. Mote, M. Ernst, A. Equbal, P. K. Madhu, Floquet theory in magnetic resonance: Formalism and applications, Prog. Nucl. Magn. Reson. Spectrosc. 126-127 (2021) 17-58. https://doi.org/10.1016/j.pnmrs.2021.05.002

[63] D. Suter, K. V. Schenker, A. Pines, Theory of broadband heteronuclear decoupling in multispin systems, J. Magn. Reson. (1969). 73 (1987) 90-98. https://doi.org/10.1016/0022-2364(87)90227-7

[64] H. Liu, S. J. Glaser, G. P. Drobny, Development and optimization of multipulse propagators: Applications to homonuclear spin decoupling in solids, J. Chem. Phys. 93 (1990) 7543-7560. https://doi.org/10.1063/1.459386

[65] A. Bielecki, A. C. Kolbert, H. J. M. de Groot, R. G. Griffin, M. H. Levitt, Frequency-Switched Lee—Goldburg Sequences in Solids, in: Advances in Magnetic and Optical Resonance, 14 1990 111-124. https://doi.org/10.1016/B978-0-12-025514-6.50011-3

[66] S. J. Glaser, G. P. Drobny, Assessment and Optimization of Pulse Sequences for Homonuclear Isotropic Mixing, in: Advances in Magnetic and Optical Resonance, 14 1990 35-58. https://doi.org/10.1016/B978-0-12-025514-6.50007-1

[67] P. Robyr, M. Tomaselli, J. Straka, C. Grob-Pisano, U. W. Suter, B. H. Meier, R. R. Ernst, RF-driven and proton-driven NMR polarization transfer for investigating local order an application to solid polymers, Mol. Phys. 84 (1995) 995-1020. https://doi.org/10.1080/00268979500100691

[68] M. Eden, Y. K. Lee, M. H. Levitt, Efficient simulation of periodic problems in NMR. Application to decoupling and rotational resonance, J. Magn. Reson. A. 120 (1996) 56-71. https://doi.org/10.1006/jmra.1996.0099

[69] I. M. Haies, J. A. Jarvis, H. Bentley, I. Heinmaa, I. Kuprov, P. T. F. Williamson, M. Carravetta, 14 N overtone NMR under MAS: signal enhancement using symmetry-based sequences and novel simulation strategies, Phys. Chem. Chem. Phys. 17 (2015) 6577-6587. https://doi.org/10.1039/C4CP03994G

[70] P. Mansfield, Symmetrized pulse sequences in high resolution NMR in solids, J. Phys. C: Solid State Physics. 4 (1971) 1444-1452. https://doi.org/10.1088/0022-3719/4/11/020

[71] A. E. Bennett, R. G. Griffin, S. Vega, Recoupling of Homo- and Heteronuclear Dipolar Interactions in Rotating Solids, in: Solid-State NMR IV Methods and Applications of Solid-State NMR (1994) 1-77. https://doi.org/10.1007/978-3-642-79127-7_1

[72] T. Gullion and J. Schaefer, Rotational-Echo Double-Resonance NMR, J. Magn. Reson. 81 (1989) 196-200. https://doi.org/https://doi.org/10.1016/0022-2364(89)90280-1

[73] T. G. Oas, R. G. Griffin, M.H. Levitt, Rotary resonance recoupling of dipolar interactions in solid-state nuclear magnetic resonance spectroscopy, J. Chem. Phys. 89 (1988) 692-695. https://doi.org/10.1063/1.455191

[74] M. Ernst, Heteronuclear spin decoupling in solid-state NMR under magic-angle sample spinning, J. Magn. Reson. 162 (2003) 1-34. https://doi.org/10.1016/S1090-7807(03)00074-0

[75] E. T. Olejniczak, S. Vega, R. G. Griffin, Multiple pulse NMR in rotating solids, J. Chem. Phys. 81 (1984) 4804. https://doi.org/10.1063/1.447506

[76] A. Kubo, C. A. McDowell, One- and two-dimensional 31P cross-polarization magic-angle-spinning nuclear magnetic resonance studies on two-spin systems with homonuclear dipolar coupling and J coupling, J. Chem. Phys. 92 (1990) 7156. https://doi.org/10.1063/1.458255

[77] T. O. Levante, M. Baldus, B. H. Meier, R. R. Ernst, Formalized quantum mechanical floquet theory and its application to sample spinning in nuclear magnetic resonance, Mol. Phys. 86 (1995) 1195-1212. https://doi.org/10.1080/00268979500102671

[78] A. Schmidt, S. Vega, NMR line shape analysis for two-site exchange in rotating solids, J. Chem. Phys. 87 (1987) 6895. https://doi.org/10.1063/1.453384

[79] A. Schmidt, S. Vega, The Floquet theory of nuclear magnetic resonance spectroscopy of single spins and dipolar coupled spin pairs in rotating solids, J. Chem. Phys. 96 (1992) 2655-2680. https://doi.org/10.1063/1.462015

[80] G. J. Boender, S. Vega, H.J.M. De Groot, A physical interpretation of the Floquet description of magic angle spinning nuclear magnetic resonance spectroscopy, Mol. Phys. 95 (1998) 921-934. https://doi.org/10.1080/00268979809483226

[81] A. D. Bain, R. S. Dumont, Introduction to Floquet theory: The calculation of spinning sideband intensities in magic-angle spinning NMR, Concepts Magn. Reson. 13 (2001) 159-170. https://doi.org/10.1002/cmr.1006

[82] A. Llor, Equivalence between dynamical averaging methods of the Schrödinger equation: average Hamiltonian, secular averaging, and Van Vleck transformation, Chem. Phys. Lett. 199 (1992) 383-390. https://doi.org/10.1016/0009-2614(92)80136-Y

[83] O. Weintraub, S. Vega, Floquet Density Matrices and Effective Hamiltonians in Magic-Angle-Spinning NMR Spectroscopy, J. Magn. Reson. A. 105 (1993) 245-267. https://doi.org/10.1006/JMRA.1993.1279

[84] M. Ernst, H. Geen, B. H. Meier, Amplitude-modulated decoupling in rotating solids: A bimodal Floquet approach, Solid State Nucl. Magn. Reson. 29 (2006) 2-21. https://doi.org/10.1016/j.ssnmr.2005.08.004

[85] M. M. Maricq, Application of a folding transformation to the Magnus solution for the evolution of periodically time dependent systems, J. Chem. Phys. 85 (1986) 5167-5174. https://doi.org/10.1063/1.451710

[86] D. Marks, N. Zumbulyadis, S. Vega, Deuterium cross-polarization magic-angle spinning, J. Magn. Reson. A. 122 (1996) 16-36. https://doi.org/10.1006/jmra.1996.0170

[87] M. Chávez, M. Ernst, A continuous approach to Floquet theory for pulse-sequence optimization in solid-state NMR, J. Chem. Phys. 157 (2022) 184103. https://doi.org/10.1063/5.0109229

[88] M. A. Mehta, D. M. Gregory, S. Kiihne, D. J. Mitchell, M. E. Hatcher, J. C. Shiels, G. P. Drobny, Distance measurements in nucleic acids using windowless dipolar recoupling solid state NMR, Solid State Nucl. Magn. Reson. 7 (1996) 211-228. https://doi.org/10.1016/S0926-2040(96)01267-2

[89] S. R. Kiihne, K. B. Geahigan, N. A. Oyler, H. Zebroski, M. A. Mehta, G. P. Drobny, Distance measurements in multiply labeled crystalline cytidines by dipolar recoupling solid state NMR, J. Phys. Chem. A 103 (1999) 3890-3903. https://doi.org/10.1021/jp990719x

[90] I. Kuprov, Defeating the Matrix, J. Magn. Reson. 306 (2019) 75-79. https://doi.org/10.1016/j.jmr.2019.07.031

[91] C. P. Slichter, E. L. Hahn, Principles of Magnetic Resonance, 3rd ed., Springer Berlin, Heidelberg, 1990. https://doi.org/https://doi.org/10.1007/978-3-662-09441-9

[92] C. Bonhomme, J. Livage, Pictorial Representation of Anisotropy and Macroscopic Reorientations of Samples in Solid-State NMR: First-Order Interactions, J. Phys. Chem. A 102 (1998) 375-385. https://doi.org/10.1021/jp972525s

[93] C. Bonhomme, J. Livage, Pictorial Representation of Anisotropy and Macroscopic Reorientations of Samples in Solid-State NMR: Second-Order Interactions, J. Phys. Chem. A 103 (1999) 460-477. https://doi.org/10.1021/jp9830171

[94] A. Samoson, E. Kundla, E. Lippmaa, High resolution MAS-NMR of quadrupolar nuclei in powders, J. Magn. Reson. 49 (1982) 350-357. https://doi.org/10.1016/0022-2364(82)90201-3

[95] G. J. Bowden, W. D. Hutchison, Tensor operator formalism for multiple-quantum NMR. 1. Spin-1 nuclei, J. Magn. Reson. 67 (1986) 403-414. https://doi.org/10.1016/0022-2364(86)90378-1

[96] Hung, I., Altenhof, A. R., Schurko, R. W., Bryce, D. L., Han, O. H., & Gan, Z. (2021). Field-stepped ultra-wideline NMR at up to 36 T: On the inequivalence between field and frequency stepping, Magn. Reason. in Chem., 59 (2021), 951–960. https://doi.org/10.1002/mrc.5128

[97] L.A. O’Dell, R.W. Schurko, Fast and simple acquisition of solid-state 14N NMR spectra with signal enhancement via population transfer, J. Am. Chem. Soc. 131 (2009) 6658-6659. https://doi.org/10.1021/ja901278q

[98] B. M. Goodson, N. Whiting, A. M. Coffey, P. Nikolaou, F. Shi, B. M. Gust, M. E. Gemeinhardt, R. V. Shchepin, J. G. Skinner, J. R. Birchall, M. J. Barlow, E. Y. Chekmenev, Hyperpolarization methods for MRS, E. Mag. Res. 4 (2015) 797-810. https://doi.org/10.1002/9780470034590.emrstm1457

[99] R. Tycko, S. J. Opella, High-Resolution 14N Overtone Spectroscopy: An Approach to Natural Abundance Nitrogen NMR of Oriented and Polycrystalline Systems, J. Am. Chem. Soc. 108 (1986) 3531-3532. https://doi.org/10.1021/ja00272a071

[100] A. J. Pell, K. Sanders, S. Wegner, G. Pintacuda, C. P. Grey, Low-power broadband solid-state MAS NMR of 14 N, J. Chem. Phys. 146 (2017) 194202-25. https://doi.org/https://doi.org/10.1063/1.4983220

[101] K. J. Harris, A. Lupulescu, B. E. G. Lucier, L. Frydman, R. W. Schurko, Broadband adiabatic inversion pulses for cross polarization in wideline solid-state NMR spectroscopy, J. Magn. Reson. 224 (2012) 38-47. https://doi.org/10.1016/j.jmr.2012.08.015

[102] Ē. Kupče, R. Freeman, Adiabatic Pulses for Wideband Inversion and Broadband Decoupling, J. Magn. Reson. A. 115 (1995) 273-276. https://doi.org/10.1006/jmra.1995.1179

[103] H. Y. Carr, E. M. Purcell, Effects of diffusion on free precession in nuclear magnetic resonance experiments, Phys. Rev. 94 (1954) 630. https://doi.org/10.1103/PhysRev.94.630

[104] S. Meiboom, D. Gill, Modified spin-echo method for measuring nuclear relaxation times, Rev. Sci. Instrum. 29 (1958) 688. https://doi.org/10.1063/1.1716296

[105] L. A. O’Dell, R. W. Schurko, QCPMG using adiabatic pulses for faster acquisition of ultra-wideline NMR spectra, Chem. Phys. Lett. 464 (2008) 97-102. https://doi.org/10.1016/j.cplett.2008.08.095

[106] D. Carnevale, A. J. Perez Linde, G. Bauer, G. Bodenhausen, Solid-state proton NMR of paramagnetic metal complexes: DANTE spin echoes for selective excitation in inhomogeneously broadened lines, Chem. Phys. Lett. 580 (2013) 172-178. https://doi.org/10.1016/j.cplett.2013.06.052

[107] Z. Gan, Measuring amide nitrogen quadrupolar coupling by high-resolution 14N/13C NMR correlation under magic-angle spinning, J. Am. Chem. Soc. 128 (2006) 6040-6041. https://doi.org/https://doi.org/10.1021/ja0578597

[108] S. Cavadini, A. Lupulescu, S. Antonijevic, G. Bodenhausen, Nitrogen-14 NMR spectroscopy using residual dipolar splittings in solids, J. Am. Chem. Soc. 128 (2006) 7706-7707. https://doi.org/10.1021/ja0618898

[109] Z. Gan, 13C/14N heteronuclear multiple-quantum correlation with rotary resonance and REDOR dipolar recoupling, J. Magn. Reson. 184 (2007) 39-43. https://doi.org/10.1016/j.jmr.2006.09.016

[110] Z. Gan, J. P. Amoureux, J. Trébosc, Proton-detected 14N MAS NMR using homonuclear decoupled rotary resonance, Chem. Phys. Lett. 435 (2007) 163-169. https://doi.org/10.1016/j.cplett.2006.12.066

[111] M. H. Levitt, Symmetry-Based Pulse Sequences in Magic-Angle Spinning Solid-State NMR, E. Mag. Res. (2007) 1-31. https://doi.org/10.1002/9780470034590.emrstm0551

[112] M. Makrinich, M. Sambol, A. Goldbourt, Distance measurements between carbon and bromine using a split-pulse PM-RESPDOR solid-state NMR experiment, Phys. Chem. Chem. Phys. 22 (2020) 21022-21030. https://doi.org/10.1039/d0cp01162b

[113] K. Basse, S. K. Jain, O. Bakharev, N. C. Nielsen, Efficient Polarization Transfer between Spin-12 and in Solid-State MAS NMR Spectroscopy N Nuclei, J. Magn. Reson. 244 (2014) 85-89. https://doi.org/10.1016/j.jmr.2014.04.017

[114] J. A. Jarvis, I. M. Haies, P. T. F. Williamson, M. Carravetta, An efficient NMR method for the characterisation of 14N sites through indirect 13C detection, Phys. Chem. Chem. Phys. 15 (2013) 7613. https://doi.org/10.1039/c3cp50787d

[115] J. P. Amoureux, J. Trebosc, J. Wiench, M. Pruski, HMQC and refocused-INEPT experiments involving half-integer quadrupolar nuclei in solids, J. Magn. Reson. 184 (2007) 1-14. https://doi.org/10.1016/j.jmr.2006.09.009

[116] R. Bhattacharyya, L. Frydman, Quadrupolar nuclear magnetic resonance spectroscopy in solids using frequency-swept echoing pulses, J. Chem. Phys. 127 (2007) 194503. https://doi.org/10.1063/1.2793783

[117] J. V. Hanna, M. E. Smith, Recent technique developments and applications of solid state NMR in characterising inorganic materials, Solid State Nucl. Magn. Reson. 38 (2010) 1-18. https://doi.org/10.1016/j.ssnmr.2010.05.004

[118] V. Vitzthum, M. A. Caporini, S. Ulzega, J. Trébosc, O. Lafon, J.P. Amoureux, G. Bodenhausen, Uniform broadband excitation of crystallites in rotating solids using interleaved sequences of delays alternating with nutation, J. Magn. Reson. 223 (2012) 228-236. https://doi.org/10.1016/j.jmr.2012.05.024

[119] K. J. Harris, S. L. Veinberg, C. R. Mireault, A. Lupulescu, L. Frydman, R. W. Schurko, Rapid acquisition of 14N solid-state NMR spectra with broadband cross polarization, Eur. J. Chem. A 19 (2013) 16469-16475. https://doi.org/10.1002/chem.201301862

[120] R. W. Schurko, Ultra-Wideline Solid-State NMR Spectroscopy, Acc. Chem. Res. 46 (2013) 1985-1995. https://doi.org/https://doi.org/10.1021/ar400045t

[121] S. E. Ashbrook, M. J. Duer, Structural Information from Quadrupolar Nuclei in Solid State NMR, Concepts Magn. Reson. Part A 28 (1995) 183-248. https://doi.org/10.1002/cmr.a

[122] A. P. M. Kentgens, A practical guide to solid-state NMR of half-integer quadrupolar nuclei with some applications to disordered systems, Geoderma. 80 (1997) 271-306. https://doi.org/10.1016/S0016-7061(97)00056-6

[123] L. Müller, Proton-Deuterium polarization transfer in magic angle spinning polycrystalline solids in the rotating frame, Chem Phys. 61 (1981) 235-248. https://doi.org/10.1016/0301-0104(81)85064-1

[124] C. P. Grey, W. S. Veeman, A. J. Vega, Rotational echo 14N/13C/1H triple resonance solid-state nuclear magnetic resonance: A probe of 13C-14N internuclear distances, J. Chem. Phys. 98 (1993) 7711-7724. https://doi.org/10.1063/1.464579

[125] M. K. Pandey, M. S. Krishnan, Effective Floquet Hamiltonian for spin I = 1 in magie angle spinning NMR using contact transformation, in: J. Chem. Sci. (2007) 417-422. https://doi.org/10.1007/s12039-007-0054-0

[126] K. Gopalakrishnan, G. Bodenhausen, K. Gopalakrishnan, Cross polarization from spins I=1⁄2 to spins S=1 in nuclear magnetic resonance with magic angle sample spinning, J. Chem. Phys. 124 (2006) 194311. https://doi.org/https://doi.org/10.1063/1.2197827

[127] S. Wi, R. Schurko, L. Frydman, 1H-2H cross-polarization NMR in fast spinning solids by adiabatic sweeps, J. Chem. Phys. 146 (2017) 104201. https://doi.org/10.1063/1.4976980.

[128] S. Cavadini, S. Antonijevic, A. Lupulescu, G. Bodenhausen, Indirect detection of nitrogen-14 in solid-state NMR spectroscopy, Chem. Phys. Chem. 8 (2007) 1363-1374. https://doi.org/10.1002/cphc.200700049

[129] S. Cavadini, A. Abraham, G. Bodenhausen, Proton-detected nitrogen-14 NMR by recoupling of heteronuclear dipolar interactions using symmetry-based sequences, Chem. Phys. Lett. 445 (2007) 1-5. https://doi.org/10.1016/j.cplett.2007.07.060

[130] A. G. M. Rankin, J. Trébosc, P. Paluch, O. Lafon, Evaluation of excitation schemes for indirect detection of 14N via solid-state HMQC NMR experiments, J. Magn. Reson. 303 (2019) 28-41. https://doi.org/10.1016/j.jmr.2019.04.004

[131] E. O. Stejskal, J. Schaefer, J. S. Waugh, Magic-angle spinning and polarization transfer in proton-enhanced NMR, J. Magn. Reson. 28 (1977) 105-112. https://doi.org/10.1016/0022-2364(77)90260-8

[132] I. Hung, P. Gor'kov, Z. Gan, Efficient and sideband-free 1H-detected 14N magic-angle spinning NMR, J. Chem. Phys. 151 (2019) 154202. https://doi.org/10.1063/1.5126599

[133] S. Ding, C. A. McDowell, The equivalence between Floquet formalism and the multi-step approach in computing the evolution operator of a periodical time-dependent Hamiltonian, Chem. Phys. Lett. 288 (1998) 230-234. https://doi.org/10.1016/S0009-2614(98)00307-8

[134] O. W. Sørensen, Polarization transfer experiments in high-resolution NMR spectroscopy, Prog. Nucl. Magn. Reson. Spectrosc. 21 (1989) 503-569. https://doi.org/10.1016/0079-6565(89)80006-8

[135] S. Cavadini, A. Lupulescu, S. Antonijevic, G. Bodenhausen, Nitrogen-14 NMR spectroscopy using residual dipolar splittings in solids, J. Am. Chem. Soc. 128 (2006) 7706-7707. https://doi.org/10.1021/ja0618898

[136] S. Cavadini, S. Antonijevic, Indirect detection of nitrogen-14 in solids via protons by nuclear magnetic resonance spectroscopy, J. Magn. Reson. 182 (2006) 168-172. https://doi.org/10.1016/j.jmr.2006.06.003

[137] V. Vitzthum, M. A. Caporini, S. Ulzega, G. Bodenhausen, Broadband excitation and indirect detection of nitrogen-14 in rotating solids using Delays Alternating with Nutation (DANTE), J. Magn. Reson. 212 (2011) 234-239. https://doi.org/10.1016/j.jmr.2011.06.013

[138] M. Shen, J. Trébosc, O. Lafon, Z. Gan, F. Pourpoint, B. Hu, Q. Chen, J. P. Amoureux, Solid-state NMR indirect detection of nuclei experiencing large anisotropic interactions using spinning sideband-selective pulses, Solid State Nucl. Magn. Reson. 72 (2015) 104-117. https://doi.org/10.1016/j.ssnmr.2015.09.003

[139] R. Aleksis, A. J. Pell, Low-power synchronous helical pulse sequences for large anisotropic interactions in MAS NMR: Double-quantum excitation of 14N, J. Chem. Phys.153 (2020) 244202. https://doi.org/10.1063/5.0030604

[140] J. Trebosc, B. Hu, J. P. Amoureux, Z. Gan, Through-space R3-HETCOR experiments between spin-1/2 and half-integer quadrupolar nuclei in solid-state NMR, J. Magn. Reson. 186 (2007) 220-227. https://doi.org/10.1016/j.jmr.2007.02.015

[141] O. Lafon, Q. Wang, B. Hu, F. Vasconcelos, J. Tre, S. Cristol, F. Deng, J. Amoureux, Indirect Detection via Spin-1 / 2 Nuclei in Solid State NMR Spectroscopy: Application to the Observation of Proximities between Protons and Quadrupolar Nuclei, J. Phys. Chem. A (2009) 12864-12878. https://doi.org/10.1021/jp906099k

[142] X. Lu, O. Lafon, J. Trébosc, G. Tricot, L. Delevoye, F. Méar, L. Montagne, J. P. Amoureux, Observation of proximities between spin-12 and quadrupolar nuclei: Which heteronuclear dipolar recoupling method is preferable, J. Chem. Phys. 137 (2012) 144201. https://doi.org/10.1063/1.4753987

[143] M. K. Pandey, H. Kato, Y. Ishii, Y. Nishiyama, Two-dimensional proton-detected 35Cl/1H correlation solid-state NMR experiment under fast magic angle sample spinning: Application to pharmaceutical compounds, Phys. Chem. Chem. Phys. 18 (2016) 6209-6216. https://doi.org/10.1039/c5cp06042g

[144] A. Venkatesh, M. P. Hanrahan, A. J. Rossini, Proton detection of MAS solid-state NMR spectra of half-integer quadrupolar nuclei, Solid State Nucl. Magn. Reson. 84 (2017) 171-181. https://doi.org/10.1016/j.ssnmr.2017.03.005

[145] A. Venkatesh, F. A. Perras, A. J. Rossini, Proton-detected solid-state NMR spectroscopy of spin-1/2 nuclei with large chemical shift anisotropy, J. Magn. Reson. 327 (2021) 106-983. https://doi.org/10.1016/j.jmr.2021.106983

[146] J. A. Jarvis, I. Haies, M. Lelli, A. J. Rossini, I. Kuprov, M. Carravetta, P. T. F. Williamson, Measurement of 14N quadrupole couplings in biomolecular solids using

indirect-detection 14N solid-state NMR with DNP, Chem. Commun. 53 (2017) 12116-12119. https://doi.org/10.1039/c7cc03462h

[147] J. A. Jarvis, M. Concistre, I. M. Haies, R. W. Bounds, I. Kuprov, M. Carravetta, P. T. F. Williamson, Quantitative analysis of 14N quadrupolar coupling using 1H detected 14N solid-state NMR, Phys. Chem. Chem. Phys. 21 (2019) 5941-5949. https://doi.org/10.1039/c8cp06276e

[148] E. R. H. van Eck, R. Janssen, W. E. J. R. Maas, W. S. Veeman, A novel application of nuclear spin-echo double-resonance to aluminophosphates and aluminosilicates, Chem. Phys. Lett. 174 (1990) 428-432. https://doi.org/10.1016/S0009-2614(90)87174-P

[149] C. P. Grey, W. S. Veeman, The detection of weak heteronuclear coupling between spin 1 and spin 1 2 nuclei in MAS NMR; 14N/13C/1H triple resonance experiments, Chem. Phys. Lett. 192 (1992) 379-385. https://doi.org/10.1016/0009-2614(92)85486-T

[150] A. J. Vega, MAS NMR spin locking of half-integer quadrupolar nuclei, J. Magn. Reson. (1969). 96 (1992) 50-68. https://doi.org/10.1016/0022-2364(92)90287-H

[151] A. J. Vega, CPMAS of quadrupolar S = 3/2 nuclei, Solid State Nucl. Magn. Reson. 1 (1992) 17-32. https://doi.org/10.1016/0926-2040(92)90006-U

[152] C. Huguenard, F. Taulelle, B. Knott, Z. Gan, Optimizing STMAS, J. Magn. Reson. 156 (2002) 131-137. https://doi.org/10.1006/jmre.2002.2548

[153] P. Caravatti, G. Bodenhausen, R. R. Ernst, Selective pulse experiments in high-resolution solid state NMR, J. Magn. Reson. 55 (1983) 88-103. https://doi.org/10.1016/0022-2364(83)90279-2

[154] D. Rovnyak, M. Baldus, R. G. Griffin, Multiple-Quantum Cross Polarization in Quadrupolar Spin Systems during Magic-Angle Spinning, J. Magn. Reson. 142 (2000) 145-152. https://doi.org/10.1006/jmre.1999.1922

[155] S. V. Sajith, S. Jayanthi, A. Lupulescu, Effective Hamiltonian and 1H-14N cross polarization/double cross polarization at fast MAS, J. Magn. Reson. 320 (2020) 106832. https://doi.org/10.1016/j.jmr.2020.106832

[156] S. Wi, J. W. Logan, D. Sakellariou, J. D. Walls, A. Pines, Rotary resonance recoupling for half-integer quadrupolar nuclei in solid-state nuclear magnetic resonance spectroscopy, J. Chem. Phys.117 (2002) 7024-7033. https://doi.org/10.1063/1.1506907

[157] H. A. Buckmaster, Tables of angular momentum transformation matrix elements, Can. J. Phys. 42 (1964) 386-391. https://doi.org/10.1139/p64-036

[158] E. M. Landau, and L. D. Lifshitz, Quantum Mechanics, Course of Theoretical Physics, 3rd ed., Butterworth-Heinemann, 1996.